REPORT SERIES IN AEROSOL SCIENCE
N:o 236 (2021)

SNOWFALL MICROPHYSICS IN SURFACE-BASED AND RADAR OBSERVATIONS

JUSSI TIIRA

Institute for Atmospheric and Earth System Research
Faculty of Science
University of Helsinki
Helsinki, Finland

Academic dissertation

To be presented, with the permission of the Faculty of Science
of the University of Helsinki, for public criticism in Physicum hall E204,
Gustaf Hällströmin katu 2, on February 5th, 2021, at 12 o'clock noon.

Helsinki 2021

Author's Address: Institute for Atmospheric and Earth System Research
P.O. Box 64
FI-00014 University of Helsinki
jussi.tiira@helsinki.fi

Supervisor: Professor Dmitri Moisseev, Ph.D.
Institute for Atmospheric and Earth System Research
University of Helsinki

Reviewers: Senior researcher Luca Baldini, Ph.D.
Institute of Atmospheric Sciences and Climate
Consiglio Nazionale delle Ricerche

Research scientist Mariko Oue, Ph.D.
School of Marine and Atmospheric Sciences
Stony Brook University

Opponent: Associate Professor Alexis Berne, Ph.D.
Environmental Engineering Institute
Ecole polytechnique fédérale de Lausanne

ISBN 978-952-7276-53-2 (printed version)
ISSN 0784-3496
Helsinki 2021
Unigrafia Oy

ISBN 978-952-7276-54-9 (pdf version)
http://ethesis.helsinki.fi
Helsinki 2021
Helsingin yliopiston verkkojulkaisut

Acknowledgements

The research in this dissertation work was carried out in the radar group at the Institute for Atmospheric and Earth System Research in the University of Helsinki. Firstly, I would like to thank all the co-authors, collaborators and technical staff who made this PhD project possible. I thank the head of INAR, Academician Markku Kulmala, for providing work facilities. I would like to express my deep gratitude to Prof. Alexis Berne for accepting to act as my opponent in the public defence. I am grateful to both pre-examiners, Dr. Mariko Oue and Dr. Luca Baldini, for their time and valuable comments on this thesis.

I feel truly privileged for having Prof. Dmitri Moisseev as my supervisor during this work. His mindful and patient guidance led me towards topics and approaches through which I could best improve and use my skills, and helped avoid many pitfals along the way. It truly feels that the rationale in his way of supporting his students does not only concern how to get the job done, but what is best for us in our careers and lives overall.

I was lucky to share much of the PhD journey with Dr. Haoran Li. Sharing the laboratory office and the quirks and gimmicks of data analysis and writing papers with him, as well as going through many of the lectures, field courses and conferences together definitely made it all a much more pleasant experience. Further, thanks to his and Erkki Siivola's caretaking efforts, all my plants in the radar laboratory survived the long remote work phase during the pandemic. I thank M.Sc. Matti Leskinen for helping in interpreting and accessing measurement data, and for interesting stories that also brought historical context to the work. In the extended radar group, I've had the pleasure to work also with Annakaisa, Kalle, Davide, Brandon, Marta, Lorenzo, Tanel and Sybille.

I had an enjoyable time working at INAR. The thanks go to all my colleagues for creating such an inspiring working atmosphere. Academy of Finland and ATM-DP are gratefully acknowledged for funding my dissertation project. I wish to thank Oona Kinnunen for helping with the proofreading of the dissertation manuscript and for continuous interest in my work.

Finally, I want to thank my friends and family for their encouragement and for freeing my mind from the responsibilities of work. I am endlessly grateful for having a loving wife, Suvi, whom I want thank for her selfless support and for standing by me all these

years.

Jussi Tiira
Helsinki, January 2021

Jussi Tapani Tiira
University of Helsinki, 2021

Abstract

Snow has an important impact on hydrology, agriculture, climate and weather, infrastructure and different forms of both aerial and land transportation. The accumulation and properties of snow are inherently connected to the microphysical processes through which the falling ice particles grow. Furthermore, snow processes affect rainfall as well, since the vast majority of rain events originate as melted snow.

For monitoring precipitation, the spatial coverage and resolution of radar instrumentation are unmatched. The quality of quantitative precipitation estimation using radars depends on our ability to establish meaningful relations between microphysical and electromagnetic scattering properties of hydrometeors. Especially for snow particles, these properties are diverse and the relations between them complex involving prominent uncertainties and knowledge gaps. Furthermore, the properties are constantly evolving as the falling particles undergo series of microphysical processes including growth from vapour, aggregation and riming.

This dissertation work addresses these knowledge gaps by parametrizing microphysical properties of falling snow using ground-based measurements, investigating the links between the properties and ice processes, and further studying their manifestations in collocated and off-site radar observations.

A novel method is introduced for retrieving ensemble mean density of falling snow using a video disdrometer and a precipitation gauge. These retrievals are used in identifying triple-frequency radar signatures of rimed particles and low-density aggregates, and to develop a method for retrieving rime mass fraction. Based on the rime mass fraction retrievals, the effect of riming to snowfall is quantified. Using multi-frequency Doppler radar and scanning C band radar observations we show that the downward stretching of a melting layer is linked primarily to precipitation intensity and secondarily to riming.

Machine learning methods are employed in objectively documenting and automatically detecting known polarimetric fingerprints of ice microphysical processes in vertical profiles of radar variables. Automated ice process detection is anticipated to open the door for adaptive radar retrieval methods of snowfall rate.

Keywords: snowfall, precipitation, radar, ice processes

Contents

Nomenclature

Λ	slope parameter of gamma functional form of $N(D)$
Φ_{dp}	total differential phase shift
δ	backscatter differential phase shift
ϵ	measurement noise
λ	wavelength
μ	shape parameter of gamma functional form of $N(D)$
ϕ_{dp}	differential phase shift
$\bar{\rho}$	ensemble mean density
σ_b	backscattering cross section
a_v	prefactor of $v(D)$ relation
b_v	exponent of $v(D)$ relation
C	frequency band from 4 to 8 GHz
CCN	cloud condensation nuclei
D	diameter
D_0	median volume diameter
DFIR	Double Fence Intercomparison Reference
D_{veq}	volume equivalent diameter
DWR	dual wavelength ratio
$f_{\mathrm{H,V}}$	forward scattering amplitude at horizontal, vertical polarization
FR	rime mass fraction
G	snowfall accumulation

H-M	Hallett-Mossop process
HSRL	High Spectral Resolution Lidar
IN	ice nuclei
Ka	frequency band from 27 to 40 GHz
K_{dp}	specific differential phase
K_w	dielectric factor of liquid water
LWE	liquid water equivalent
m	mass
m_{ur}	mass of unrimed snow
MWACR	Marine W band ARM cloud radar
MWR	Microwave Radiometer
$N(D)$	particle size distribution function
N_0	intercept parameter of gamma functional form of $N(D)$
N_w	intercept parameter of normalized gamma functional form of $N(D)$
PCA	principal component analysis
PIP	Precipitation Imaging Package
PPI	plan position indicator
PSD	particle size distribution
QPE	quantitative precipitation estimation
r	distance
RHI	range height indicator
S	snowfall intensity
SVI	Snowflake Video Imager

v	terminal fall velocity
V_c	radar measurement volume
W	frequency band from 75 to 110 GHz
WBF	Wegener-Bergeron-Findeisen process
X	frequency band from 8 to 12 GHz
X/KaSACR	scanning dual-frequency (X, Ka) ARM cloud radar system
Z	reflectivity factor in dBZ
z	reflectivity factor in linear scale
Z_{DR}	differential reflectivity
Z_{e}	equivalent reflectivity factor
$Z_{\mathrm{H,V}}$	reflectivity factor at horizontal, vertical polarization

List of publications

This thesis consists of an introductory review, followed by five research articles. In the introductory part, these papers are cited according to their roman numerals.

I **Tiira, J.**, Moisseev, D., von Lerber, A., Ori, D., Tokay, A., Bliven, L. F., and Petersen, W., 2016: Ensemble mean density and its connection to other microphysical properties of falling snow as observed in Southern Finland, *Atmos. Meas. Tech.*, 9, 4825-4841, doi: 10.5194/amt-9-4825-2016.

II Kneifel, S., von Lerber, A., **Tiira, J.**, Moisseev, D., Kollias, P., and Leinonen, J., 2015: Observed relations between snowfall microphysics and triple-frequency radar measurements. *J. Geophys. Res. Atmos.*, 120, 6034–6055. doi: 10.1002/2015JD023156.

III Moisseev, D., von Lerber, A., and **Tiira, J.**, 2017: Quantifying the effect of riming on snowfall using ground-based observations, *J. Geophys. Res. Atmos.*, 122, doi: 10.1002/2016JD026272.

IV **Tiira, J.** and Moisseev, D., 2020: Unsupervised classification of vertical profiles of dual-polarization radar variables, *Atmos. Meas. Tech.*, 13, 1227–1241, doi: 10.5194/amt-13-1227-2020.

V Li, H., **Tiira, J.**, von Lerber, A., and Moisseev, D., 2020: Towards the connection between snow microphysics and melting layer: Insights from multi-frequency and dual-polarization radar observations during BAECC, *Atmos. Chem. Phys.*, 20, 9547–9562, doi: 10.5194/acp-20-9547-2020.

1 Introduction

In the mid and high latitudes, heavy snowfall is an important form of severe weather with high economic impact and, in the most severe cases, poses risks to human life. Reduced visibility due to snowfall, accumulating snow cover and icing can be hazardous conditions for ground transportation (Juga et al., 2012), aviation (Smith et al., 2012; Saltikoff et al., 2018), and infrastructure. Accurate forecasting of accumulation, timing and type of precipitation is increasingly important for maintenance, preparation and mitigation activities such as road and airport maintenance, re-routing of flights and removing snow from roofs to avoid collapsing under weight.

The quality and severity of these effects of snow are largely determined by the microphysical properties of the falling particles. For instance, snow density is strongly linked to visibility and the properties of the snow cover accumulating on surfaces. An ensemble of large fluffy aggregates has a larger impact on visibility than an ensemble of graupel particles with equal liquid equivalent water content. Compared to the more contained graupel particles, branched structures in the aggregates also make them stick and accumulate on tree branches more easily, increasing the risk of the trees falling onto power lines.

The microphysical properties, in turn, are determined by a chain of different snow processes along the paths of the falling particles according to the ambient conditions that drive them. The strong response of these processes to subtle changes in especially air temperature, humidity and the availability of condensation nuclei typically allows the evolution of a precipitation event in terms of intensity and particle types in temporal scales of minutes.

Not only snow, but also rainfall is affected by snow microphysical processes. Apart from drizzle, most of rainfall originates as melted snow particles in mid and high latitudes. The processes above the melting layer have a significant impact on rainfall intensity and drop size distribution (Lamb and Verlinde, 2011).

The global climate change is altering the climatology of precipitation through a wide range of environmental changes affecting atmospheric temperature profiles, moisture content and flow patterns. The most strongly affected are the polar regions due to arctic amplification (Serreze and Barry, 2011). Changes in the climatology of snow processes have a direct influence on water cycles (Rott et al., 2010). For example, the increase in seasonal snow cover in some areas may cause more severe spring time flooding. Mitigation of and preparing for such risks relies on accurate quantitative precipitation estimation (QPE; Berne and Krajewski, 2013) and realistic representation of the precipitation processes in numerical climate models (Briley et al., 2017). Especially winter precipitation remains one of the most significant sources of uncertainty in climate modelling (Schiermeier, 2010).

Surface base measurements are a fundamental bearing point for microphysical studies on snow and the related processes. They are the most viable method for performing continuous direct measurements of precipitation rate and microphysical properties of hydrometeors. Sometimes referred to as the "ground truth" in the remote sensing community, surface measurements are used as a verification and reference observations for radar retrievals. The observed microphysical properties of hydrometeors at the surface act as evidence for the processes through which the particles were formed aloft.

Historically, surface-based measurements have been performed manually and the hydrometeor properties have been studied on a particle-by-particle basis (e.g., Magono and Nakamura, 1965; Locatelli and Hobbs, 1974; Mitchell, 1996). Such studies have reached a high level of detail in describing the properties, but lack spatial and temporal coverage. At present, surface-based snow measurements are typically carried out using optical disdrometers capable of measuring a range of microphysical properties including the particle size distribution (PSD), and often also fall velocities and some aspects of particle shapes. Additionally, automatic precipitation gauges can be used for directly measuring liquid water equivalent (LWE) precipitation rate. Combining disdrometer and gauge measurements allows studying a range of snow microphysical properties in time series with temporal resolution of minutes.

The main limitation of surface-based observations, however, is their sparse spatial coverage (Pirazzini et al., 2018). This underlines the importance of remote sensing instrumentation capable of covering large areas and three-dimensional structure of cloud and precipitation systems at high spatial and temporal resolution. The use of polarimetry in modern weather radars allows retrieving evidence on hydrometeor shapes, sizes and dielectric properties manifested in the observed dual-polarization radar variables. Considering these capabilities, remote sensing instruments, especially weather radars, have enormous potential in identifying and locating precipitation processes. This ability can be utilized in improving both QPE and the representation of these processes in numerical weather and climate models.

Especially with snow, the connection between radar observations and the microphysical properties is often ambiguous. Difficulties arise from the diverse and irregular structure of the particles resulting in complex scattering properties. Furthermore, the particle properties are evolving continuously through microphysical processes, and multiple particle types and processes may even occur simultaneously in the same radar measurement volumes. A way forward in improving QPE and parametrization of snow microphysics in numerical models lies in better understanding of the microphysical properties and processes and their connection to radar observations. This dissertation work aims to address these challenges by

1. characterizing and parametrizing snow microphysical properties using surface-based observations (Paper **I**),
2. linking the retrieved properties to microphysical processes, namely aggregation and riming (Papers **II** and **III**),
3. studying interactions between different precipitation processes (Paper **V**),
4. based on the steps above, investigating the representation of the microphysical properties and processes in single and multi-frequency radar signatures (Papers **II**, **III** and **V**)
5. constructing an unsupervised classification of vertical profiles of polarimetric radar variables to allow automatic detection of ice process fingerprints in radar observations (Paper **IV**).

2 Snow microphysics

2.1 Microphysical quantities

The microphysical properties of snow are described with a number of quantities such as size, shape, density (or mass) and fall velocity, as well as their distributions over an ensemble of particles. The other microphysical quantities are conventionally expressed as a function of a chosen definition of particle **diameter** (D) or a **characteristic size** of an ensemble (Pruppacher and Klett, 2010). The choice of size definition is often related firstly to the used measurement techniques and limitations in their observation geometry, and secondly to the requirements posed by the retrieval methods of derived products. For instruments recording images of particles, the diameter of an equivalent area (Heymsfield et al., 2002; Paper **I**) or circumscribing sphere (Mitchell, 1996; Heymsfield et al., 2004; Heymsfield and Westbrook, 2010) is conventionally used. Conversions between different size definitions involve assumptions on characteristic particle shapes (Korolev and Isaac, 2003) and orientations (Matrosov et al., 2005). In Paper **I**, the disk equivalent diameter is converted to volume equivalent D_{veq} in order to compute volume flux weighted ensemble mean density. An approximation of D_{veq} is typically used also in studies employing instruments capable of imaging particles from multiple angles (Brandes et al., 2007; Wood et al., 2013; Huang et al., 2015).

Commonly used quantities describing characteristic sizes of hydrometeor ensembles include the mass weighted mean diameter (D_m) and the median volume diameter (D_0; Bringi and Chandrasekar, 2001). Half of the total volume is contributed by particles larger than D_0:

$$\int_0^{D_0} D^3 N(D)\,\mathrm{d}D = \int_{D_0}^{\infty} D^3 N(D)\,\mathrm{d}D\,, \tag{1}$$

where $N(D)$ is the size distribution function.

The size distribution function describes the **particle size distribution** (PSD), i.e. the distribution of different sizes of hydrometeors in a given volume. It is most commonly expressed in the units of $\mathrm{m}^{-3}\,\mathrm{mm}^{-1}$, as the measurement volume is given in cubic meters and particle sizes in millimeters. Some precipitation processes have a characteristic effect on the PSD, e.g. the generation of large snowflakes through aggregation results in a wide distribution (Brandes et al., 2007; Pettersen et al., 2020b; Yu et al., 2020). Radar observations can be sensitive to particle size distributions, as described further in Sect. 4. In order to express particle size distributions quantitatively, a gamma functional formulation is typically used (Ulbrich, 1983)

$$N(D) = N_0 D^{\mu} \exp(-\Lambda D), \tag{2}$$

where N_0 is the intercept parameter in $\mathrm{m}^{-3}\,\mathrm{mm}^{-1-\mu}$, μ is the shape parameter and Λ is the slope parameter of the gamma distribution. Due to instrumental limitations, this thesis mainly concerns ice particles larger than 0.2 mm. The effects of consequent PSD truncation are discussed in Paper **I**.

A fall velocity at which the gravitational force pulling a freely falling particle downwards is balanced with aerodynamic drag and buoyancy, is termed the **terminal velocity**. The net force on the object being zero, the terminal velocity is constant. The terminal velocity of hydrometeors in the atmosphere depends on their mass and shape, as well as the density of air, which increases with decreasing altitude. A lower air density allows higher terminal velocities and, on the other hand, dense particles fall faster than fluffy ones. An increase in vertically projected area increases drag, slowing the particle. If two particles of different sizes have very similar shapes and densities, the larger one will fall faster, as mass is proportional to the cube of the size while projected area is proportional to its square. In reality, snowflakes tend to become fluffier as they grow, causing fall speeds to saturate after the particle reaches a certain size (Barthazy and Schefold, 2006). Due to the low inertia of hydrometeors, especially snow particles, it can be safely assumed that the fall velocities equal their terminal velocities.

Due to recirculation in the particle wake and subsequent pressure distribution, snow particles tend to fall in **orientations** that maximize drag (Mandø and Rosendahl, 2010). The symmetry axis of falling particles is pointed vertically for plates and horizontally for columns. The complex structure of especially asymmetric aggregates may cause them to tumble or swing while falling. The aerodynamics also affect falling raindrop shapes by widening their horizontal dimension. Raindrops become more oblate as they grow larger.

In addition to aerodynamic effects, the orientation of an ice crystal is affected by a local electrostatic field. However, both theoretical calculations (Weinheimer and Few, 1987) and polarimetric radar observations (Williams et al., 2015) suggest that in most situations, the effect of an electric field to particle orientations is small compared to aerodynamics. Vertical orientation of small ice particles due to electrification is possible in convective thunderstorms. A commonly used measure of anisotropy of hydrometeors

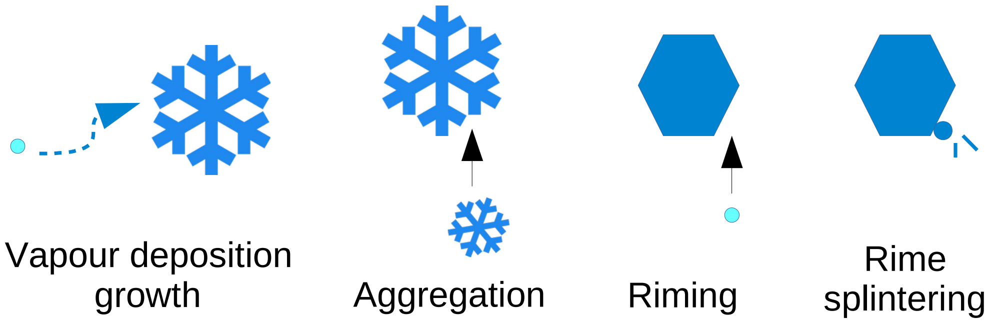

Figure 1: Types of ice processes.

is their **aspect ratio**, which in this context is defined as the ratio of the horizontal to the vertical axis. Characteristics in particle aspect ratios are especially useful in dual-polarization radar measurements as discussed further in Section 4.

2.2 Ice processes

In clouds with cloud top temperatures below the freezing point of $T_0 = 0\,°\mathrm{C}$, termed **cold clouds**, water is often present in three phases in parallel: ice, liquid and vapour. Transformations between these phases occur depending on ambient conditions, with humidity, temperature, and the availability of condensation nuclei being the most important ones. The liquid and solid phases are initiated by nucleation. In most cases, nucleation occurs heterogeneously, meaning that it is facilitated by aerosol particles acting as **cloud condensation nuclei (CCN)** or **ice nuclei (IN)**. Ice particles may also form through homogeneous nucleation without external agents by first condensing into liquid cloud drops, which then freeze. **Homogeneous nucleation** to liquid phase mainly occurs with very high supersaturations of over $300\,\%$, when insufficient amount of condensation nuclei are present, and is therefore improbable in the atmosphere (Lamb and Verlinde, 2011). A cloud droplet may freeze either heterogeneously when coming in contact with IN or homogeneously at temperatures below approximately $-38\,°\mathrm{C}$ (Pruppacher and Klett, 2010).

Fig. 1 illustrates notable examples of processes through which the generated ice particles grow, attach to each other and break apart. These processes are further described in the following paragraphs and are the main processes considered in this thesis.

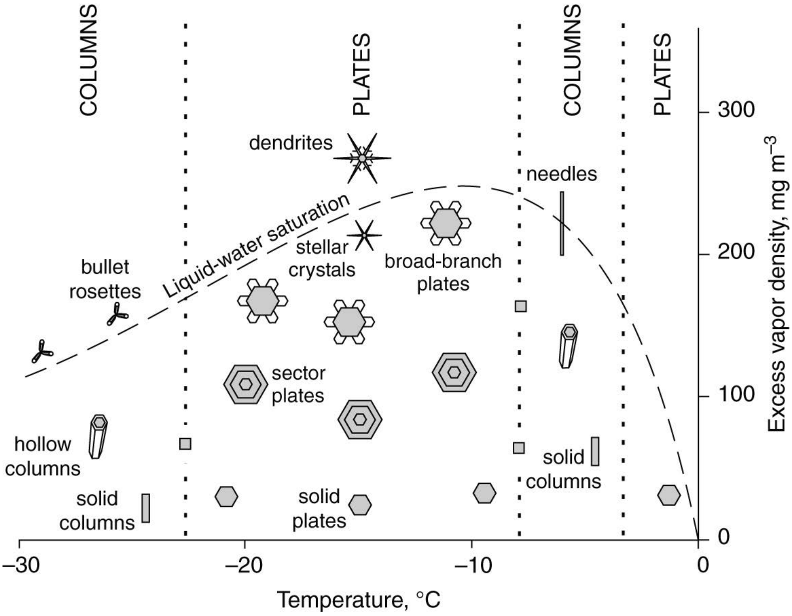

Figure 2: Snow crystal morphology. Reproduced from Lamb and Verlinde (2011) with permission.

The observed number concentration of ice particles often exceeds the number of IN, which has been explained by secondary ice production (Field et al., 2017). The proposed mechanisms include **Hallett-Mossop (H-M) rime splintering**, **collision fragmentation** of branched crystals with delicate structure and **shattering of cloud droplets** upon freezing (Hallett and Mossop, 1974; Vardiman, 1978; Rangno and Hobbs, 2001; Yano and Phillips, 2011; Rangno and Hobbs, 2005; Lawson et al., 2015).

Ice particles grow from vapour when there is vapour supersaturation in respect to ice. Equilibrium vapour pressure of ice is lower than that of liquid water. Therefore, coexistence of liquid and ice particles in a cloud leads to ice particles consuming water vapour faster than liquid droplets. This may continue to the point where there is no longer vapour saturation in respect to liquid. The situation where ice particles grow at the expense of evaporating liquid droplets is called the Wegener-Bergeron-Findeisen (WBF) process.

Depending on temperature, the growth of hexagonal crystals is greater either on the basal or the prism face leading to the growth of columnar or plate-like crystals, respectively. The preferential growth between these two main types of the **primary habit** alternate with temperature, as visualized in the ice crystal morphology diagram in Fig. 2. A sufficiently high ambient supersaturation leads to morphological instability in the growth of ice crystals. This means that changes in particle shapes affect the vapour field in a way that amplifies these changes. The effect is due to radial gradients in vapour concentration near the growing particle, and thus leads to preferential growth of features that stick out (Lamb and Verlinde, 2011). Such morphological features superimposed on the primary habit are termed the **secondary habit**. At high supersaturation, hexagonal plates have the tendency to grow branches at the corners of the hexagon resulting in **dendrites**. Dendritic growth is the preferential growth mechanism at high vapour supersaturations near $-15\,^{\circ}\mathrm{C}$.

Besides growth from vapour, ice particles can grow by collision and adhesion with other solid or liquid particles. Differences in mass and shape of cloud and precipitation particles lead to different fall velocities, allowing such collisions to occur. The collision and adhesion of solid particles is termed **aggregation**. The adhesion mechanisms involved in aggregation include mechanical interlocking, electrostatic effects and sintering. Mechanical interlocking is the most important mechanism from roughly $-15\,^{\circ}\mathrm{C}$ to $-12\,^{\circ}\mathrm{C}$ (Lamb and Verlinde, 2011). This mechanism is enhanced by the branched structure of dendrites growing efficiently at around $-15\,^{\circ}\mathrm{C}$. As a result, the maximum size of

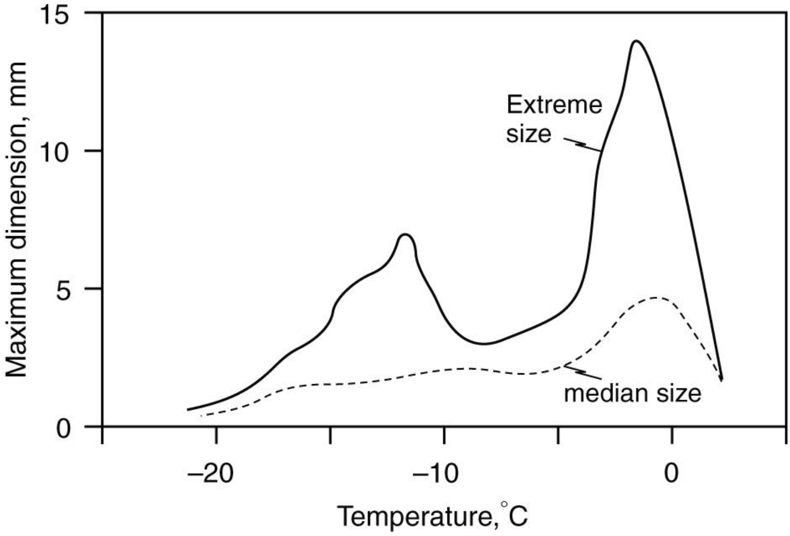

Figure 3: Sizes of snow aggregates as a function of temperature. Reproduced from Lamb and Verlinde (2011) with permission.

aggregates peaks at around those temperatures as seen in Fig. 3.

Sintering is an adhesion mechanism allowed by liquid-like properties of solid objects' surfaces especially near their melting points. This is why aggregation is a particularly important growth mechanism near 0 °C (Dias Neto et al., 2019), manifested as a corresponding peak in aggregate sizes as seen in Fig. 3. Surfaces of ice particles have such **quasi-liquid** properties also at colder temperatures, but sintering is less effective in such conditions. In aggregation, snow particles attach to each other in random arrangements often resulting in a loose structure. The porosity and hence bulk density of the aggregate depends on the primary particle habits. Due to the typical low density of unrimed aggregates, the dependence of fall velocity on size is smaller than with single crystals (Hanesch, 1999). Aggregation is linked to high precipitation rates (Moisseev et al., 2015), making it of particular interest in microphysical studies.

A snow particle falling through a supercooled liquid cloud layer is likely to collide with cloud droplets causing them to freeze instantaneously on its surface. This process, called **riming**, thus increases the mass of the particle and may also, depending on the initial habit and the stage of riming, affect its shape and size. With increased degree of riming, the crystalline structure of the particle is obscured and it becomes more

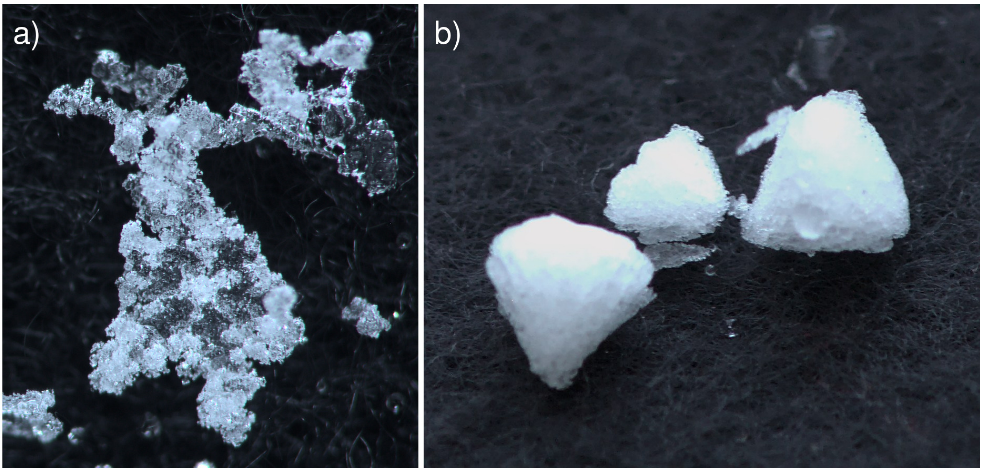

Figure 4: Snow particles with different stages of heavy riming: a) a heavily rimed aggregate and b) conical graupel.

roundish. However, the increase in particle size is small in proportion to the added mass, and consequently density and fall velocity are increased. Fig. 4 displays snow particles at different stages of riming: the original crystalline structure of the aggregate in pane a) is partly visible, while in the graupel particles in pane b) it is completely obscured.

In favourable conditions, the rime ice may release splinters upon freezing. There is strong evidence of the H-M process occurring in temperatures ranging from -8 to $-3\,^{\circ}\mathrm{C}$ in laboratory experiments (Hallett and Mossop, 1974; Choularton et al., 1980; Saunders and Hosseini, 2001), consistent with in situ measurements (e.g., Harris-Hobbs and Cooper, 1987; Taylor et al., 2016). However, there is no consensus on the physical explanation of the process. An early hypothesis has been that, upon impact, the supercooled liquid drops start freezing from their surface, surrounding the liquid core. The expansion of water on freezing increases pressure inside the core, which may cause the incompressible water to burst out and freeze, resulting in one or more secondary ice particles. At the temperature range favoured by the H-M process, ice tends to grow columnarly, resulting in needles at high supersaturations.

As the particles fall, they experience a continuum of changing conditions in terms of temperature, moisture and the presence of other particles. A falling ice particle will therefore likely go through a number of different processes before reaching the surface or the melting layer. In a given volume there may be particles originating from different altitudes, and have therefore gone through a different combination of conditions and processes. Consequently, a number of different habits may coexist in the same volume.

Observing snow microphysical processes using surface-based and radar observations always involves solving an inverse problem. In other words, physical properties have to be inferred from their indirect manifestations. In surface-based observations, only the final product of the microphysical processes is observed, and with radars we measure scattered microwave radiation in different polarizations and wavelengths. The following sections give a brief explanation on such measurements and how they can be used to study snow microphysical properties and processes aloft.

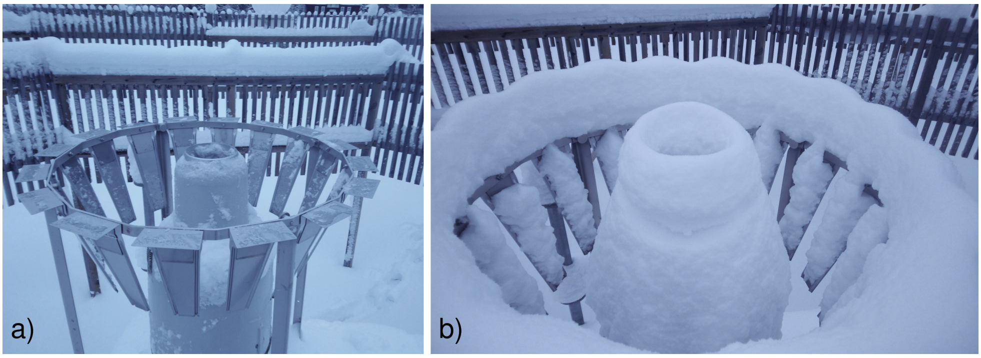

Figure 5: a) Precipitation gauge Pluvio^2 200 with Tretyakov wind shield inside the DFIR fence and b) the same gauge after a snowstorm on 28.-29.1.2019.

3 Surface-based snowfall measurements

In situ measurements of snowfall microphysics act as important validation reference for remote sensing observations. As an advantage over airborne measurements, surface-based in situ observations allow automated long-term continuous monitoring of snow microphysical properties at fixed locations.

Snowfall **accumulation** (G) and **intensity** (S) are often expressed in terms of their liquid water equivalents, and expressed in mm and $\mathrm{mm\,h^{-1}}$, respectively. The main types of automatic instruments for directly measuring precipitation rate and accumulation are gauges based on weighting or floating mechanisms, and tipping buckets (World Meteorological Organization, 2018). Out of these types, only the weighting mechanism is suitable for measuring all types of precipitation, while the other types are limited to liquid only. The main challenges and error sources in gauge measurements include evaporation and condensation, undercatch due to wind and piling of snow onto the orifice (Fig. 5; Michelson, 2004). The regular maintenance of the gauges includes manual emptying of the container, adding antifreeze liquid and suppressants for condensation and evaporation, as well as clearing possible blockages in case of piling snow. In Papers **I**, **II** and **III**, two OTT Pluvio^2 gauges were employed in the retrieval of $\bar{\rho}$. They are situated at the Hyytiälä measurement field surrounded by boreal forest, with the shortest distance between a gauge and trees being approximately 20 m. The gauges have different orifices and wind shielding. The Pluvio^2 200 with 200 $\mathrm{cm^2}$ orifice

Figure 6: Instrumentation at the Hyytiälä measurement station in February 2019.

is located inside the DFIR with a Tretyakov wind shield, and the Pluvio^2 400 outside the DFIR with Tretyakov and Alter wind shields.

A disdrometer is a surface-based instrument for measuring PSD, and in some device types also fall velocities and hydrometeor shapes. This data can be used for calculating hydrometeor volume flux, which in turn is useful in retrievals of density and precipitation rate. The information on shape, density and fall velocity are used in hydrometeor classification. Different disdrometer types include impact disdrometer such as the Joss-Waldvogel disdrometer (JWD; Joss and Waldvogel, 1967), and optical disdrometers based on either laser emitters and photodiodes as in the Particle Size Velocity (Parsivel; Löffler-Mang and Joss, 2000) disdrometer, or incoherent light and camera sensors such as in the Multi-Angle Snowflake Camera (MASC; Garrett et al., 2012), 2D-video disdrometer (2DVD; Kruger and Krajewski, 2002) and Precipitation Imaging Package (PIP; Pettersen et al., 2020a).

The variety of approaches in measuring particle shapes, sizes and fall velocities between the different camera-based disdrometers is rather wide. In the recently introduced MASC, the hydrometeors are photographed from three angles separated by 36° resulting in high resolution stereographic images. Fall velocity is measured from the detection time difference of two near-infrared emitter-detector pair arrays with vertical separation of 32 mm. The 2DVD, on the other hand, is based on two sets of horizontally aligned line scan cameras both recording the hydrometeor shadows in two orthogonal directions. Stacking these one-dimensional images as the particle falls through the measurement plane results in two-dimensional images of the hydrometeor in two angles. The sets of cameras are vertically separated by 6 mm to allow the retrieval of fall speed. PIP is a new generation of the Snowflake Video Imager (SVI; Newman et al., 2009). A two-dimensional greyscale video is recorded of the shadows of hydrometeors as they fall between a high frame rate camera and a light source. With the field of view at focus of 48 by 64 mm and a frame rate of 380 fps (frames per second), PIP is able to record multiple frames of the same particle, allowing its fall speed to be retrieved from the distance it fell between the frames.

In this research, PIP is the main disdrometer used. Its main benefits compared to the other disdrometers include open structure and large sampling volume. This allows for representative observations that are less affected by wind (Newman et al., 2009). PIP is also both mechanically and operationally robust, allowing deployment to remote locations with little maintenance (Souverijns et al., 2017). In Papers **I**, **II** and **III**, PIP was used together with precipitation gauge observations to retrieve time series of $\bar{\rho}$. Paper **I** linked the retrieved $\bar{\rho}$ to PIP-derived $v(D)$ relations and to PSD parameters. In Paper **II**, triple-frequency radar observations were compared to PIP snow particle images and $v(D)$ relations. Ensemble mean density and $v(D)$ relation were used in Paper **III** for computing the rime mass fraction (FR) of falling snow. In Paper **V**, FR was derived from PIP observations using the von Lerber et al. (2017) method. Additionally, a 2DVD was employed in Paper **V** for rain rate estimation and calibrating the X band radar reflectivity.

In the Hyytiälä measurement station, surface instrumentation are collocated with remote sensing instruments (Fig. 6; Petäjä et al., 2016). This allows combining direct observations of hydrometeor microphysical properties with indirect evidence of processes through which the particles were created aloft.

4 Radar measurements

Radars are the most widely used remote sensing instruments for precipitation measurements. The instrument transmits electromagnetic radiation at microwave frequencies typically in short pulses directed with a parabolic reflector resulting in a beam width in the order of 1°. The pulse propagates at the speed of light, and a fraction of the transmitted power is scattered from target objects back at the radar. The radar measures the properties of the backscattered radiation and the elapsed time from the transmission to the receiving. The location of the scatterers is solved from this time difference and the pointing azimuth and elevation angle of the antenna. The received power, typically converted to a quantity called reflectivity factor, depends on the size distribution and the dielectric properties of the targets in a measurement volume. Doppler radars, in addition, deduce the radial velocity of scatterers from the observed frequency shift. This Doppler velocity can be used to track storm movements, estimate wind speed and filter out stationary objects with scanning radar setups, or to study fall velocities with vertically pointing radars.

Apart from small cloud droplets, hydrometeors are not spherical, and have preferred orientations giving them different scattering properties depending on polarization. Therefore combining information of the received signals at the two perpendicular polarizations gives added information on particle shape, orientation, phase and distribution of sizes within the observation volume. Polarimetric measurements are used for hydrometeor classification, attenuation correction and improving QPE (Bringi and Chandrasekar, 2001).

The transmit wavelength (λ) of meteorological radars ranges between 3.2 mm and 11 cm. It is chosen considering the compromise between signal attenuation, measurement sensitivity and various system design aspects including size of the reflector and available power. Radars operating at millimetre wavelengths are often referred to as cloud radars as they are highly sensitive and can be used for observing cloud particles. On the other hand, cloud radar signal is heavily attenuated by moist air and droplets. Moreover, at shorter wavelengths it is more difficult to satisfy the Rayleigh criteria, meaning that particle size should be at least an order of magnitude smaller than the wavelength for the backscattered power to be proportional to the sixth power of the particle diameter. The most commonly used wavelengths in cloud radars are 3.2 mm (W band) and 8.6 mm (Ka band). Weather radars operate at 3.2 cm, 5.5 cm or 10.7 cm wavelengths falling to the X, C and S frequency bands, respectively, in order to be less affected by signal attenuation and to better meet the Rayleigh criteria for hydrometeors. In Papers **III**, **IV** and **V**, C band observations are analysed, and in Papers **II** and **V**, multi-frequency radar setups are used.

The **radar reflectivity factor** is defined for spherical liquid water droplets meeting the Rayleigh criteria as

$$z = \frac{1}{V_c} \sum_i D_i^6 , \tag{3}$$

where V_c is the contributing volume and D_i are the droplet diameters within the contributing volume (Rauber and Nesbitt, 2018). It can be rewritten using the particle size distribution as

$$z = \int_D D^6 N(D) \, \mathrm{d}D \, . \tag{4}$$

The reflectivity factor is conventionally expressed in $\mathrm{mm^6\,m^{-3}}$, but due to the wide range of values, typically displayed in decibels with respect to reference level of $1\,\mathrm{mm^6\,m^{-3}}$ (dBZ):

$$Z = 10 \log_{10} \left(\frac{z}{1\,\mathrm{mm^6\,m^{-3}}} \right) . \tag{5}$$

While the approximation of small spherical liquid water droplets is applicable for weather radar observations of rainfall, it may not be valid at higher frequencies, and certainly is not for ice particles or snowflakes of complex shapes. Therefore, it is often necessary to use the generalization of equivalent reflectivity factor (Bringi and Chandrasekar, 2001)

$$Z_\mathrm{e} = \frac{\lambda^4}{\pi^5 |K_w|^2} \int_D \sigma_b(D) N(D) \, \mathrm{d}D \, , \tag{6}$$

where $\sigma_b(D)$ is the backscattering cross section, and the dielectric factor of liquid water, $|K_w|^2$, is conventionally used as the true dielectric factor within the resolution volume is generally unknown.

Differential reflectivity, Z_DR, is defined as the ratio of the horizontal and vertical reflectivity factors in the logarithmic scale (Z_H and Z_V, respectively; Seliga and Bringi, 1976), and can thus be expressed as their difference

$$Z_\mathrm{DR} = Z_\mathrm{H} - Z_\mathrm{V} \tag{7}$$

in decibels. Differential reflectivity can thus be used to detect asymmetry in hydrometeor shapes. Relations linking raindrop sizes and aspect ratios can be used to infer a characteristic size from Z_{DR} signatures. Because of the strong size dependence of reflectivity, the magnitude of Z_{DR} is predominated by large particles. Being a ratio, Z_{DR} is independent of particle number concentrations and sensitive to the calibration of the two reflectivity factors.

The speed of electromagnetic waves in liquid water and ice is slower than in air. This is because the electric field interferes with the charges of the atoms, causing them to oscillate and emit their own electromagnetic waves which interact with the original wave slowing its phase speed. In a similar manner, an ensemble of hydrometeors interfere with radar microwave radiation slowing the phase speed. As a beam transmitted by a polarimetric radar propagates through an ensemble of oblate raindrops or statistically anisotropic ice particles, the electromagnetic waves effectively encounter more mass in one polarization than the other causing a corresponding difference in the phase speeds. The resulting phase shift between the polarizations is termed the **differential phase shift**, ϕ_{dp}. Given hydrometeors with statistically positive aspect ratios along the track of the beam, ϕ_{dp} increases with range. Rather than the absolute value of ϕ_{dp}, it is often more informative to estimate its rate of change along the beam. **Specific differential phase** is defined as

$$K_{\mathrm{dp}} = \frac{1}{2}\frac{\mathrm{d}\phi_{\mathrm{dp}}}{\mathrm{d}r}, \tag{8}$$

with units in $^\circ\,\mathrm{km}^{-1}$. It can be calculated for an ensemble of particles following the equation (Rauber and Nesbitt, 2018):

$$K_{\mathrm{dp}} = 10^3 \left(\frac{180\lambda}{\pi}\right) \int_D \Re\left(f_{\mathrm{H}} - f_{\mathrm{V}}\right) N(D)\,\mathrm{d}D\,, \tag{9}$$

where f_{H} and f_{V} are the forward scattering amplitudes describing the portion of electromagnetic wave scattering in the forward direction at horizontal and vertical polarizations, respectively. As their difference is related to the aspect ratios of scatterers, essentially, K_{dp} is a product of a factor related to the shapes of particles and number concentration. Specific differential phase is less sensitive to PSD than Z_{DR}. Further, it is independent of radar calibration and not affected by attenuation or partial beam blockage (Zrnić and Ryzhkov, 1996). These properties make K_{dp} valuable in snow microphysical analysis, quantitative rain estimation and radar calibration.

Specific differential phase or, strictly speaking, even ϕ_{dp} cannot be directly measured with a radar. Instead we measure the **total differential phase shift**:

$$\Phi_{\mathrm{dp}} = \phi_{\mathrm{dp}} + \delta + \epsilon, \tag{10}$$

where δ, termed the backscatter differential phase shift, is the differential phase shift due to non-Rayleigh scattering effects and ϵ is noise in the measured Φ_{dp}. Typically, the noise levels in Φ_{dp} are considerable, and the magnitude of δ can be difficult to estimate, complicating the retrievals of K_{dp}. Numerous algorithms have been developed aiming to overcome these difficulties (Hubbert et al., 1993; Hubbert and Bringi, 1995; Lang et al., 2007; Wang and Chandrasekar, 2009; Otto and Russchenberg, 2011; Vulpiani et al., 2012; Maesaka et al., 2012; Schneebeli et al., 2014), but nevertheless, often especially the effects of noise pose constraints on the use of low K_{dp} values.

4.1 Dual-polarization signatures of snow processes

As snow processes cannot be directly observed using radar measurements, we need ways to link radar observations to snow microphysical properties. This is based on identifying particle types in observations and understanding the scattering properties of ensembles of particles.

Even combined use of different dual-polarization radar variables leaves ambiguity to the interpretation of these properties and their cause, as is typical for inverse problems. As the snow particles go through the processes along their more or less vertical tracks, and with the high importance of ambient temperature for the processes, it is useful and often necessary to view changes in the polarimetric radar variables along the vertical axis in order to analyse the processes. For this, range height indicator (RHI) scans are ideal, as they provide high resolution vertical slices of radar observations in a chosen direction. For combining surface-based and remote sensing observations, it is useful to study the temporal evolution of these vertical observations over the location of interest as a series of vertical profiles in time-height format. A method for extracting vertical profiles of dual-polarization observations from RHI data was developed in Paper **IV**. A number of other vertical profile extraction methods exist for different scanning strategies and use cases, such as the quasi vertical profile method utilizing azimuthal averaging over high antenna elevation scans (Ryzhkov et al., 2016).

From profiles of dual-polarization radar variables, it is possible to analyse vertically extending patterns as fingerprints of precipitation processes, in contrast to performing hydrometeor classification based on individual radar volumes. Since the emergence of polarimetric radar technology, such fingerprints have been identified in observations.

Water deposition growth at the top of the cloud can be linked to the presence of planar crystals growing through the WBF process. The presence of these oblate crystals is characterized by high-Z_{DR} features near the cloud top (Williams et al., 2015; Oue et al., 2016).

As dense oblate crystals, dendrites are characterized polarimetric radar observations by an increase in Z_{DR} and, if number concentration is sufficiently high, an increase in K_{dp}. The presence of at least one of these characteristics near the $-15\,^{\circ}\mathrm{C}$ region is a likely indication of dendritic growth. A high number concentration of dendrites increases the likelihood of particle collisions and aggregation. Therefore, a K_{dp} signature around this temperature can also be treated as an indication of the onset of aggregation (Moisseev et al., 2015). Formation of such high concentrations of dendrites requires a high cloud top height, such that homogeneous nucleation can occur (Moisseev et al., 2015; Griffin et al., 2018). This type of K_{dp} fingerprints have been linked to heavy surface precipitation (Kennedy and Rutledge, 2011; Bechini et al., 2013), highlighting their importance. These properties of the radar fingerprints of dendritic growth were confirmed statistically in Paper **IV** using clustering of vertical profiles of polarimetric radar observations.

Similar K_{dp} bands have been reported at temperatures where the H-M process occurs and have been linked to the presence of needles consistent with the expected outcome of the process (Hogan et al., 2002; Grazioli et al., 2015; Sinclair et al., 2016; Kumjian et al., 2016; Giangrande et al., 2016). Unlike in dendritic growth zones, peak K_{dp} values in H-M zones seem to be consistently capped at 0.2 to $0.3\,^{\circ}\,\mathrm{km}^{-1}$, likely due to early onset of aggregation (Sinclair et al., 2016). This may pose challenges in automated radar-based detection of the process as found in Paper **IV**.

Riming and aggregation have highly similar polarimetric fingerprints, making it difficult to tell them apart in observations. Both are often characterized by K_{dp} and Z_{DR} decreasing downwards as the particles become more spherical by growing through collection. This coincides with an increase in reflectivity. Moisseev et al. (2015) found early aggregates to be oblate, contributing to K_{dp}, which may explain why K_{dp} peaks at a lower altitude than Z_{DR}. As the aggregates grow larger, they become more spherical, less dense and tend to tumble. As particles join together, the number concentration, and consequently K_{dp}, is decreased. The comparison of dual-polarization radar observations and retrievals of microphysical properties in Paper **III** suggest that the effect of riming on Z_{DR} depends on initial particle sizes indicating an underlying dependence on the initial habits. Apart from the use of polarimetry, the degree of riming may be inferred in remote sensing observations by the use of Doppler velocity (Mosimann, 1995; Mason et al., 2018) and LWP measurements.

4.2 Multi-frequency signatures

Estimation of snow microphysical properties such as PSDs using radar measurements at a single frequency involves considerable uncertainties, which further has a negative impact on QPE (Kulie and Bennartz, 2009; Hiley et al., 2011). Simultaneous use of collocated radar instrumentation at different frequencies has been found to significantly improve retrievals of these properties (Matrosov, 1998; Hogan et al., 2000; Matrosov et al., 2005). These methods are based on the relations between the effective reflectivity factor and a characteristic size of the PSD, such as D_0. The $Z_\mathrm{e}(D_0)$ relation is independent of the frequency as long as the Rayleigh approximation is valid, but becomes different when the size parameter approaches the resonance region and non-Rayleigh scattering becomes relevant. The dual wavelength method takes advantage of this difference by synergetic use of radars at two different frequencies. Typically, one wavelength is selected to be at or close to the Rayleigh regime (e.g. X, C or S band) and the other reasonably affected by non-Rayleigh effects (e.g. Ka or W; Matrosov, 1998; Hogan et al., 2000; Liao et al., 2005). The difference between the equivalent reflectivity factors at these two wavelengths, λ_1 and λ_2, is termed dual wavelength ratio (DWR)

$$\mathrm{DWR}(\lambda_1, \lambda_2) = Z_\mathrm{e}(\lambda_1) - Z_\mathrm{e}(\lambda_2). \tag{11}$$

Assuming snow particles as spheres or spheroids may not be sufficient for linking their microphysical and scattering properties due to the complex connection between these properties at high frequencies (Petty and Huang, 2010; Botta et al., 2010, 2011; Tyynelä et al., 2011). One possible approach in analysing the performance of such models is introducing a third frequency in the analysis, as demonstrated by Kneifel et al. (2011), who compared simulated DWRs at Ku, Ka and W bands from different scattering models. The study revealed a separation especially between the aggregate and spheroid models. In Paper **II**, triple-frequency radar observations are used in combination with ground-based in situ measurements to investigate connection between triple-frequency signatures and snow microphysical structure. The results verify these characteristic signatures of large aggregates in triple-frequency space, and further, triple-frequency fingerprints of rimed particles were discovered. These findings suggest a potential in using multi-frequency observations for snow type classification.

Instead of using a third frequency, another viable approach for inferring snow particle morphology and the related processes is through the combined use of DWR and Doppler velocity (Mason et al., 2018). The physical basis of such approach is, firstly, in the effect of particle densities and shapes on terminal velocity, and secondly, in the link between DWR and characteristic particle size. In Paper **V**, this approach is used for differentiating between rimed and unrimed snow aggregates using dual frequency Doppler radar in order to study the connection between snow processes and melting layer properties.

5 Machine learning methods

Machine learning methods can be used, among other applications, for detecting and objectively classifying recurring patterns, or filling gaps, in complex datasets such as time series of radar observations. Depending on the type of problem and characteristics of the data at hand, a machine learning approach is chosen from a large number of different algorithms and methods that have been developed up to this date. Machine learning methods can be categorized, firstly, between supervised, unsupervised and reinforcement learning, and secondly, between shallow and deep learning.

In the supervised learning paradigm, prelabeled training data are used to infer the function to map inputs to the correct outputs. In contrast, in unsupervised learning, previously undetected patterns are sought in the data with minimal human intervention. Reinforcement learning concerns finding balance between automated exploration and exploitation of current knowledge using reward and punishment mechanisms. Typical use cases for both supervised and unsupervised learning are classification problems (e.g., Junninen et al., 2007; Lindqvist et al., 2012) and filling data gaps (e.g., Kang et al., 2019; van den Heuvel et al., 2020).

Unsupervised classification methods rely on cluster analysis. Notable examples of clustering models are those based on centroids (k-means), connectivity, distributions and density. A clustering strategy should be selected based on the distribution of the features the cluster analysis is applied on. For example, a density based method that assumes clusters of similar density may perform badly if data is in fact Gaussian-distributed. Although less common, reinforcement learning can be employed for classification as well (Lin et al., 2020).

The depth of a machine learning architecture refers to the number of nonlinear feature transformation layers; shallow methods typically contain no more than one or two layers, whereas deep learning methods, such as deep neural networks, consist of several interconnected layers (Deng, 2014). Deep architectures are typically used in classification problems with intrinsic hierarchical complexity such as computer vision, which involves the transforming information hierarchically from the pixel matrix level to shape and texture detection levels, and further to the conception level. On simpler and well-constrained problems, shallow machine learning methods have been shown effective.

The use of shallow architectures often involves a separate feature extraction phase. Depending on how much domain knowledge is intended to be used at this stage, features to be extracted can be chosen completely manually, while there are also unsupervised methods such as principle component analysis (PCA) and factor analysis. In deep architectures, in contrast, feature extraction effectively occurs in the hidden layers, and a separate step is typically not needed.

In Paper **IV**, the widely used k-means clustering algorithm is employed for snow process detection based on features extracted using PCA. In the study, the benefits of using machine learning techniques for explorative data analysis on radar data are also demonstrated. The use of the clustering method revealed evidence that a second dendritic growth zone may sometimes be found in a strong inversion layer. It should be noted that similar use of machine learning in explorative data analysis may be useful even in studies that do not aim to use machine learning as their main analysis method.

6 Summary of results

Up to the present time, quantitative snowfall estimation has remained to a great extent an unsolved problem in radar meteorology. Further, the uncertainty in microphysical parametrization of falling snow has a negative impact on numerical weather and climate modelling. Combined use of multisensory data from heterogeneous sources at high temporal resolution is necessary for addressing these challenges. The focus of this work is in investigating the manifestations of snow processes in surface based measurements, and using this information for improving the physical basis of radar based snow retrievals. A machine learning based approach is presented for the analysis of ice processes in dual-polarization weather radar observations.

6.1 Retrieval of $\bar{\rho}$ in high temporal resolution

Surface-based in situ measurements of snow microphysical properties were conducted at the Hyytiälä measurement station, Finland. In this thesis, the video disdrometer PIP was diversely utilized for this purpose. Ensemble mean density, $\bar{\rho}$, was derived in Paper **I** using a combination of PIP-retrieved PSD and $v(D)$ relations with LWE precipitation rate from collocated gauge measurements. The temporal resolution of the Pluvio^2 gauge corrected accumulation product varied as a function of precipitation intensity. To fully leverage this, we used a variable integration time determined by the accumulation product resulting in a median resolution of 5 minutes. The derived density values, and the assumption of particle shape involved, were checked against snow depth measurements for validity. With RMSE of 0.30 cm, linear correlation coefficient of 0.88 and normalized bias of -0.06 between PIP-derived and directly measured snow depths, the agreement is good. The link between the retrieved $\bar{\rho}$ and other microphysical properties of snow were studied in Paper **I**, and the connection between the mean density and triple-frequency radar observations in Paper **II**. In Paper **III**, $\bar{\rho}$ was used for quantifying the effect of riming on snowfall.

6.2 Linking snow particle properties to microphysical processes

In Paper **I**, we found that parameters of normalized gamma PSD, D_0 and N_w, are correlated with $\bar{\rho}$. The dependence of D_0 on ensemble mean density can be expected as it is known that larger particles tend to be less dense (Brandes et al., 2007). The correlation between N_w and $\bar{\rho}$ was shown to stem from the link between D_0 and N_w. This indicates that aggregation is an important process in heavier precipitation.

The dependence of $v(D)$ relation on $\bar{\rho}$ was also investigated in Paper **I**. Both the prefactor a_v and the exponent b_v of the power law $v = a_v D^{b_v}$ were found to increase with density, which is in line with the conclusions of Barthazy and Schefold (2006). The positive correlation between $\bar{\rho}$ and a_v signifies that denser particles fall at higher terminal velocities.

In Paper **III**, the ice particle rime mass fraction was retrieved from $\bar{\rho}$ and PSD. For this purpose, a reference $m(D)$ relation was derived for unrimed snow. The derived rime mass fraction was used for analysing mass growth effects on snowfall. Riming was found to be responsible for 5 to 40 % of precipitation mass.

6.3 Investigating radar signatures of snow processes

Scattering signatures from triple-frequency radar observations have previously been shown to be sometimes consistent with spheroidal particle models and in others only explainable by complex models of aggregates. Comparisons of low-altitude triple-frequency signature with surface-based in situ observations of snow microphysical properties in Paper **II** revealed a bending away in (DWR(Ka, W), DWR(X, Ka)) space from the curve of spheroid models in the presence of large ($D > 5\,\mathrm{mm}$) aggregates. Riming was manifested as almost a horizontal line in the triple-frequency space.

In Paper **III**, the retrieved FR, $\bar{\rho}$ and simulated Z_e and Z_DR from scattering computations were compared to the low altitude reflectivity and differential reflectivity measured by the Ikaalinen C band radar. The results from the two cases studied suggest that the effect of riming on Z_DR depends on the initial snow particle habits, and whether riming affects their shapes or only increases particle densities.

Radar signatures at X and Ka bands were linked to FR in Paper **V**, and used for classifying rimed and unrimed snow. The classification results are consistent with a study by Zawadzki et al. (2005) using a single frequency. Observations using vertically pointing multi-frequency radar setup and RHI scans from C band weather radar revealed a strong link between snowfall intensity above melting layer and sagging, i.e., the descent and broadening, of the melting layer signature. Riming was found to have a secondary effect of increased sagging in moderate and heavy precipitation. A pronounced dip in Z_e above melting layer was linked to the presence of unrimed snow suggesting that aggregation may be suppressed by riming.

6.4 Automated analysis of snow process fingerprints in radar observations

A novel machine learning based method for objectively classifying vertical profiles of polarimetric radar variables in the solid precipitation medium is introduced in Paper **IV**. A dataset of almost 200 precipitation events with temporal resolution of 15 minutes collected year-round over 3.5 years was described using a total of 26 profile classes. The classes and features within were linked to known fingerprints of snow microphysical processes including dendritic growth, aggregation and the H-M process. Based on this, the profile classes were categorized into seven archetypes. The classification revealed evidence that strong temperature inversions may have an important role on the frequency of occurrence of some ice processes.

7 Review of papers and the author's contribution

Paper **I** investigates connections between ensemble mean snow density and microphysical properties of falling snow such as parameters of the particle size distribution. I performed the snowflake density retrievals, estimated the velocity-dimensional relations and PSD parameters. I was also responsible for the case studies and wrote the manuscript.

Paper **II** studies the relations between collocated triple-frequency radar signatures and ground based in situ measurements of snowfall microphysical properties. I was responsible for performing analysis of snowfall microphysical properties such as density retrievals and velocity-dimensional analysis. I also took part in the analysis of the case studies and preparation of the manuscript.

Paper **III** uses ground based observations to study the effect of riming on snowfall as well as its impact on dual-polarization radar variables. I took part in designing of the study, provided data for the retrieval of rime mass fraction and did meteorological analysis of the case studies. I contributed to the preparation of the manuscript.

Paper **IV** introduces a classification method for vertical profiles of polarimetric radar observations, and demonstrates its use for automated detection of ice processes. I had the main responsibility in designing and implementing the data analysis and on the writing process related to this paper.

Paper **V** investigates the link between melting layer properties and the ice processes taking place above it using a combination of ground based in situ measurements and multi-frequency radar observations. I was responsible for processing the C band radar data, and deriving the dual-polarization profile data used in the study. I also participated in the writing process.

8 Conclusions

Urbanization and the changing climate of precipitation highlight the increasing importance of accurate quantitative precipitation estimation for hydrology, agriculture, climate studies, aviation and other forms of transportation. In the extratropics, snow processes have an important impact on precipitation accumulations year-round. The spatial coverage and resolution enabled by weather radar technology and the ongoing progress in improving microwave remote sensing measurement techniques underline their current importance and potential in improving precipitation estimation.

Linking remote sensing observations to snow microphysical properties and processes has remained a grand challenge in the development of the estimation techniques. The main contribution of this thesis is in establishing these connections by developing retrieval methods for state of the art multi instrument setups, parametrizing microphysical properties of falling snow with surface-based in situ observations and analysing their links to snow growth processes and further to radar observations. Moreover, it is demonstrated how machine learning methods can pave the way for future development in precipitation estimation applications based on the known radar fingerprints of snow processes.

These investigations highlight the benefits of using versatile collocated surface-based in situ and remote sensing instrumentation together with off-site radar measurements in analysing snowfall microphysics. The studies in this thesis work employed two video disdrometers and two precipitation gauges for in situ precipitation observations, measurements of wind, temperature and snow depth, lidar and microwave radiometer measurements of liquid water, on-site triple-frequency radar measurements, and scanning C band weather radar measurements off-site.

From the point of view of a fixed location on the Earth's surface, changes in the dominating precipitation processes above often occur in time scales of minutes. In this thesis, time series of such properties are retrieved in high temporal resolution in order to study how they are affected by microphysical processes. Such quality-controlled datasets act as valuable validation basis for many studies. As an example, the ensemble mean density retrieved in Paper **I** was used as confirmation for triple-frequency retrievals in Paper **II**, and in Paper **III** to construct a method for retrieving rime mass fraction in order to quantify the effect of riming to snowfall.

Multi-frequency radar observations have shown a great potential in observing microphysical properties in snowfall. Backed by surface-based in situ retrievals, the value of triple-frequency measurements in inferring particle densities the characteristic size of the PSD, key elements for detecting aggregation and riming, were demonstrated in Paper **II**. In Paper **V**, multi-frequency Doppler radar observations were used to investigate the impact of precipitation intensity, aggregation, riming and dendritic growth to the properties of melting layer. Such methods and investigations have a great value in improving our understanding on, not only the effects of microphysics on scattering properties, but also the interactions between different precipitation processes as well as their climatology in order to improve their representation in numerical weather and climate prediction models.

From the point of view of more direct applications in precipitation estimation, the key focus should be in improving methods that are applicable for networks of scanning dual-polarization radars. In Paper **IV**, this need is addressed by demonstrating how machine learning methods can be employed in documenting and detecting fingerprints of precipitation processes in vertical profiles of polarimetric radar observations. Automated detection of ice processes may allow developing adaptive radar retrieval methods of snowfall rate in which parameters could be chosen based on the classification result. Classification models trained with vertical profiles of radar variables may also prove to be useful in extrapolating radar observations in situations where radar reception is partially blocked by obstacles.

References

Barthazy, E. and Schefold, R. (2006). Fall velocity of snowflakes of different riming degree and crystal types. *Atmospheric Research*, 82(1-2):391–398.

Bechini, R., Baldini, L., and Chandrasekar, V. (2013). Polarimetric Radar Observations in the Ice Region of Precipitating Clouds at C-Band and X-Band Radar Frequencies. *Journal of Applied Meteorology and Climatology*, 52(5):1147–1169.

Berne, A. and Krajewski, W. (2013). Radar for hydrology: Unfulfilled promise or unrecognized potential? *35th Year Anniversary Issue*, 51:357–366.

Botta, G., Aydin, K., and Verlinde, J. (2010). Modeling of Microwave Scattering From Cloud Ice Crystal Aggregates and Melting Aggregates: A New Approach. *IEEE Geoscience and Remote Sensing Letters*, 7(3):572–576.

Botta, G., Aydin, K., Verlinde, J., Avramov, A. E., Ackerman, A. S., Fridlind, A. M., McFarquhar, G. M., and Wolde, M. (2011). Millimeter wave scattering from ice crystals and their aggregates: Comparing cloud model simulations with X- and Ka-band radar measurements. *Journal of Geophysical Research*, 116:D00T04.

Brandes, E. A., Ikeda, K., Zhang, G., Schönhuber, M., and Rasmussen, R. M. (2007). A Statistical and Physical Description of Hydrometeor Distributions in Colorado Snowstorms Using a Video Disdrometer. *Journal of Applied Meteorology and Climatology*, 46(5):634–650.

Briley, L. J., Ashley, W. S., Rood, R. B., and Krmenec, A. (2017). The role of meteorological processes in the description of uncertainty for climate change decision-making. *Theoretical and Applied Climatology*, 127(3-4):643–654.

Bringi, V. N. and Chandrasekar, V. (2001). *Polarimetric Doppler Weather Radar : Principles and Applications*. Cambridge University Press, Cambridge, UNITED KINGDOM.

Choularton, T. W., Griggs, D. J., Humood, B. Y., and Latham, J. (1980). Laboratory studies of riming, and its relation to ice splinter production. *Quarterly Journal of the Royal Meteorological Society*, 106(448):367–374.

Deng, L. (2014). Deep Learning: Methods and Applications. *Foundations and Trends® in Signal Processing*, 7(3-4):197–387.

Dias Neto, J., Kneifel, S., Ori, D., Trömel, S., Handwerker, J., Bohn, B., Hermes, N., Mühlbauer, K., Lenefer, M., and Simmer, C. (2019). The TRIple-frequency and Polarimetric radar Experiment for improving process observations of winter precipitation. *Earth System Science Data*, 11(2):845–863.

Field, P. R., Lawson, R. P., Brown, P. R. A., Lloyd, G., Westbrook, C., Moisseev, D., Miltenberger, A., Nenes, A., Blyth, A., Choularton, T., Connolly, P., Buehl, J., Crosier, J., Cui, Z., Dearden, C., DeMott, P., Flossmann, A., Heymsfield, A., Huang, Y., Kalesse, H., Kanji, Z. A., Korolev, A., Kirchgaessner, A., Lasher-Trapp, S., Leisner, T., McFarquhar, G., Phillips, V., Stith, J., and Sullivan, S. (2017). Secondary Ice Production: Current State of the Science and Recommendations for the Future. *Meteorological Monographs*, 58:7.1–7.20.

Garrett, T. J., Fallgatter, C., Shkurko, K., and Howlett, D. (2012). Fall speed measurement and high-resolution multi-angle photography of hydrometeors in free fall. *Atmospheric Measurement Techniques*, 5(11):2625–2633.

Giangrande, S. E., Toto, T., Bansemer, A., Kumjian, M. R., Mishra, S., and Ryzhkov, A. V. (2016). Insights into riming and aggregation processes as revealed by aircraft, radar, and disdrometer observations for a 27 April 2011 widespread precipitation event: Insights into Riming and Aggregation. *Journal of Geophysical Research: Atmospheres*, 121(10):5846–5863.

Grazioli, J., Tuia, D., and Berne, A. (2015). Hydrometeor classification from polarimetric radar measurements: a clustering approach. *Atmospheric Measurement Techniques*, 8(1):149–170.

Griffin, E. M., Schuur, T. J., and Ryzhkov, A. V. (2018). A Polarimetric Analysis of Ice Microphysical Processes in Snow, Using Quasi-Vertical Profiles. *Journal of Applied Meteorology and Climatology*, 57(1):31–50.

Hallett, J. and Mossop, S. C. (1974). Production of secondary ice particles during the riming process. *Nature*, 249(5452):26–28.

Hanesch, M. (1999). *Fall velocity and shape of snowflakes*. PhD thesis, ETH Zurich.

Harris-Hobbs, R. L. and Cooper, W. A. (1987). Field Evidence Supporting Quantitative Predictions of Secondary Ice Production Rates. *Journal of the Atmospheric Sciences*, 44(7):1071–1082.

Heymsfield, A. J., Bansemer, A., Schmitt, C., Twohy, C., and Poellot, M. R. (2004). Effective Ice Particle Densities Derived from Aircraft Data. *Journal of the Atmospheric Sciences*, 61(9):982–1003.

Heymsfield, A. J., Lewis, S., Bansemer, A., Iaquinta, J., Miloshevich, L. M., Kajikawa, M., Twohy, C., and Poellot, M. R. (2002). A General Approach for Deriving the Properties of Cirrus and Stratiform Ice Cloud Particles. *Journal of the Atmospheric Sciences*, 59(1):3–29.

Heymsfield, A. J. and Westbrook, C. D. (2010). Advances in the Estimation of Ice Particle Fall Speeds Using Laboratory and Field Measurements. *Journal of the Atmospheric Sciences*, 67(8):2469–2482.

Hiley, M. J., Kulie, M. S., and Bennartz, R. (2011). Uncertainty Analysis for CloudSat Snowfall Retrievals. *Journal of Applied Meteorology and Climatology*, 50(2):399–418.

Hogan, R. J., Field, P. R., Illingworth, A. J., Cotton, R. J., and Choularton, T. W. (2002). Properties of embedded convection in warm-frontal mixed-phase cloud from aircraft and polarimetric radar. *Quarterly Journal of the Royal Meteorological Society*, 128(580):451–476.

Hogan, R. J., Illingworth, A. J., and Sauvageot, H. (2000). Measuring Crystal Size in Cirrus Using 35- and 94-GHz Radars. *Journal of Atmospheric and Oceanic Technology*, 17(1):27–37.

Huang, G.-J., Bringi, V., Moisseev, D., Petersen, W., Bliven, L., and Hudak, D. (2015). Use of 2D-video disdrometer to derive mean density–size and Ze–SR relations: Four snow cases from the light precipitation validation experiment. *Atmospheric Research*, 153:34–48.

Hubbert, J. and Bringi, V. N. (1995). An Iterative Filtering Technique for the Analysis of Copolar Differential Phase and Dual-Frequency Radar Measurements. *Journal of Atmospheric and Oceanic Technology*, 12(3):643–648. Publisher: American Meteorological Society.

Hubbert, J., Chandrasekar, V., Bringi, V. N., and Meischner, P. (1993). Processing and Interpretation of Coherent Dual-Polarized Radar Measurements. *Journal of Atmospheric and Oceanic Technology*, 10(2):155–164. Publisher: American Meteorological Society.

Joss, J. and Waldvogel, A. (1967). Ein Spektrograph für Niederschlagstropfen mit automatischer Auswertung. *Pure and Applied Geophysics PAGEOPH*, 68(1):240–246.

Juga, I., Hippi, M., Moisseev, D., and Saltikoff, E. (2012). Analysis of weather factors responsible for the traffic ‘Black Day’ in Helsinki, Finland, on 17 March 2005. *Meteorological Applications*, 19(1):1–9.

Junninen, H., Riipinen, I., Dal Maso, M., and Kulmala, M. (2007). An Algorithm for Automatic Classification of Two-dimensional Aerosol Data. In O’Dowd, C. D. and Wagner, P. E., editors, *Nucleation and Atmospheric Aerosols*, pages 957–961. Springer Netherlands, Dordrecht.

Kang, M., Ichii, K., Kim, J., Indrawati, Y. M., Park, J., Moon, M., Lim, J.-H., and Chun, J.-H. (2019). New Gap-Filling Strategies for Long-Period Flux Data Gaps Using a Data-Driven Approach. *Atmosphere*, 10(10):568.

Kennedy, P. C. and Rutledge, S. A. (2011). S-Band Dual-Polarization Radar Observations of Winter Storms. *Journal of Applied Meteorology and Climatology*, 50(4):844–858.

Kneifel, S., Kulie, M. S., and Bennartz, R. (2011). A triple-frequency approach to retrieve microphysical snowfall parameters. *Journal of Geophysical Research*, 116(D11):D11203.

Korolev, A. and Isaac, G. (2003). Roundness and Aspect Ratio of Particles in Ice Clouds. *Journal of the Atmospheric Sciences*, 60(15):1795–1808.

Kruger, A. and Krajewski, W. F. (2002). Two-Dimensional Video Disdrometer: A Description. *Journal of Atmospheric and Oceanic Technology*, 19(5):602–617.

Kulie, M. S. and Bennartz, R. (2009). Utilizing Spaceborne Radars to Retrieve Dry Snowfall. *Journal of Applied Meteorology and Climatology*, 48(12):2564–2580.

Kumjian, M. R., Mishra, S., Giangrande, S. E., Toto, T., Ryzhkov, A. V., and Bansemer, A. (2016). Polarimetric radar and aircraft observations of saggy bright bands during MC3E. *Journal of Geophysical Research: Atmospheres*, 121(7):3584–3607.

Lamb, D. and Verlinde, J. (2011). *Physics and Chemistry of Clouds*. Cambridge University Press, Cambridge.

Lang, T. J., Ahijevych, D. A., Nesbitt, S. W., Carbone, R. E., Rutledge, S. A., and Cifelli, R. (2007). Radar-Observed Characteristics of Precipitating Systems during NAME 2004. *Journal of Climate*, 20(9):1713–1733.

Lawson, R. P., Woods, S., and Morrison, H. (2015). The Microphysics of Ice and Precipitation Development in Tropical Cumulus Clouds. *Journal of the Atmospheric Sciences*, 72(6):2429–2445.

Liao, L., Meneghini, R., Iguchi, T., and Detwiler, A. (2005). Use of Dual-Wavelength Radar for Snow Parameter Estimates. *Journal of Atmospheric and Oceanic Technology*, 22(10):1494–1506.

Lin, E., Chen, Q., and Qi, X. (2020). Deep reinforcement learning for imbalanced classification. *Applied Intelligence*, 50(8):2488–2502.

Lindqvist, H., Muinonen, K., Nousiainen, T., Um, J., McFarquhar, G. M., Haapanala, P., Makkonen, R., and Hakkarainen, H. (2012). Ice-cloud particle habit classification using principal components. *Journal of Geophysical Research*, 117(D16).

Locatelli, J. D. and Hobbs, P. V. (1974). Fall speeds and masses of solid precipitation particles. *Journal of Geophysical Research*, 79(15):2185–2197.

Löffler-Mang, M. and Joss, J. (2000). An Optical Disdrometer for Measuring Size and Velocity of Hydrometeors. *Journal of Atmospheric and Oceanic Technology*, 17(2):130–139.

Maesaka, T., Iwanami, K., and Maki, M. (2012). Non-negative k dp estimation by monotone increasing ϕ dp assumption below melting layer. In *Extended Abstracts, Seventh European Conf. on Radar in Meteorology and Hydrology*.

Magono, C. and Nakamura, T. (1965). Aerodynamic Studies of Falling Snowflakes. *Journal of the Meteorological Society of Japan. Ser. II*, 43(3):139–147.

Mandø, M. and Rosendahl, L. (2010). On the motion of non-spherical particles at high Reynolds number. *Powder Technology*, 202(1-3):1–13.

Mason, S. L., Chiu, C. J., Hogan, R. J., Moisseev, D., and Kneifel, S. (2018). Retrievals of Riming and Snow Density From Vertically Pointing Doppler Radars. *Journal of Geophysical Research: Atmospheres*, 123(24).

Matrosov, S. Y. (1998). A Dual-Wavelength Radar Method to Measure Snowfall Rate. *Journal of Applied Meteorology*, 37(11):1510–1521. Publisher: American Meteorological Society.

Matrosov, S. Y., Reinking, R. F., and Djalalova, I. V. (2005). Inferring Fall Attitudes of Pristine Dendritic Crystals from Polarimetric Radar Data. *Journal of the Atmospheric Sciences*, 62(1):241–250.

Michelson, D. B. (2004). Systematic correction of precipitation gauge observations using analyzed meteorological variables. *Journal of Hydrology*, 290(3-4):161–177.

Mitchell, D. L. (1996). Use of Mass- and Area-Dimensional Power Laws for Determining Precipitation Particle Terminal Velocities. *Journal of the Atmospheric Sciences*, 53(12):1710–1723.

Moisseev, D. N., Lautaportti, S., Tyynela, J., and Lim, S. (2015). Dual-polarization radar signatures in snowstorms: Role of snowflake aggregation. *Journal of Geophysical Research: Atmospheres*, 120(24):12644–12655.

Mosimann, L. (1995). An improved method for determining the degree of snow crystal riming by vertical Doppler radar. *Atmospheric Research*, 37(4):305–323.

Newman, A. J., Kucera, P. A., and Bliven, L. F. (2009). Presenting the Snowflake Video Imager (SVI). *Journal of Atmospheric and Oceanic Technology*, 26(2):167–179.

Otto, T. and Russchenberg, H. W. J. (2011). Estimation of Specific Differential Phase and Differential Backscatter Phase From Polarimetric Weather Radar Measurements of Rain. *IEEE Geoscience and Remote Sensing Letters*, 8(5):988–992.

Oue, M., Galletti, M., Verlinde, J., Ryzhkov, A., and Lu, Y. (2016). Use of X-Band Differential Reflectivity Measurements to Study Shallow Arctic Mixed-Phase Clouds. *Journal of Applied Meteorology and Climatology*, 55(2):403–424.

Pettersen, C., Bliven, L. F., von Lerber, A., Wood, N. B., Kulie, M. S., Mateling, M. E., Moisseev, D. N., Munchak, S. J., Petersen, W. A., and Wolff, D. B. (2020a). The Precipitation Imaging Package: Assessment of Microphysical and Bulk Characteristics of Snow. *Atmosphere*, 11(8):785.

Pettersen, C., Kulie, M. S., Bliven, L. F., Merrelli, A. J., Petersen, W. A., Wagner, T. J., Wolff, D. B., and Wood, N. B. (2020b). A Composite Analysis of Snowfall Modes from Four Winter Seasons in Marquette, Michigan. *Journal of Applied Meteorology and Climatology*, 59(1):103–124.

Petty, G. W. and Huang, W. (2010). Microwave Backscatter and Extinction by Soft Ice Spheres and Complex Snow Aggregates. *Journal of the Atmospheric Sciences*, 67(3):769–787.

Petäjä, T., O'Connor, E. J., Moisseev, D., Sinclair, V. A., Manninen, A. J., Väänänen, R., von Lerber, A., Thornton, J. A., Nicoll, K., Petersen, W., Chandrasekar, V., Smith, J. N., Winkler, P. M., Krüger, O., Hakola, H., Timonen, H., Brus, D., Laurila, T., Asmi, E., Riekkola, M.-L., Mona, L., Massoli, P., Engelmann, R., Komppula, M., Wang, J., Kuang, C., Bäck, J., Virtanen, A., Levula, J., Ritsche, M., and Hickmon, N. (2016). BAECC A field campaign to elucidate the impact of Biogenic Aerosols on Clouds and Climate. *Bulletin of the American Meteorological Society.*

Pirazzini, R., Leppänen, L., Picard, G., Lopez-Moreno, J. I., Marty, C., Macelloni, G., Kontu, A., von Lerber, A., Tanis, C. M., Schneebeli, M., de Rosnay, P., and Arslan, A. N. (2018). European In-Situ Snow Measurements: Practices and Purposes. *Sensors*, 18(7):2016.

Pruppacher, H. and Klett, J. (2010). *Microphysics of Clouds and Precipitation*, volume 18 of *Atmospheric and Oceanographic Sciences Library*. Springer Netherlands, Dordrecht.

Rangno, A. L. and Hobbs, P. V. (2001). Ice particles in stratiform clouds in the Arctic and possible mechanisms for the production of high ice concentrations. *Journal of Geophysical Research: Atmospheres*, 106(D14):15065–15075.

Rangno, A. L. and Hobbs, P. V. (2005). Microstructures and precipitation development in cumulus and small cumulonimbus clouds over the warm pool of the tropical Pacific Ocean. *Quarterly Journal of the Royal Meteorological Society*, 131(606):639–673.

Rauber, R. M. and Nesbitt, S. W. (2018). *Radar meteorology: a first course*. Advancing weather and climate science series. John Wiley & Sons, Hoboken, NJ, first edition.

Rott, H., Yueh, S. H., Cline, D. W., Duguay, C., Essery, R., Haas, C., Hélière, F., Kern, M., Macelloni, G., Malnes, E., Nagler, T., Pulliainen, J., Rebhan, H., and Thompson, A. (2010). Cold Regions Hydrology High-Resolution Observatory for Snow and Cold Land Processes. *Proceedings of the IEEE*, 98(5):752–765.

Ryzhkov, A., Zhang, P., Reeves, H., Kumjian, M., Tschallener, T., Trömel, S., and Simmer, C. (2016). Quasi-Vertical Profiles—A New Way to Look at Polarimetric Radar Data. *Journal of Atmospheric and Oceanic Technology*, 33(3):551–562.

Saltikoff, E., Hagen, M., Juntti, H., Kaltenböck, R., and Pulkkinen, S. (2018). Nowcasting snow for airports at heterogeneous terrain. *Geophysica*, 53(1):29–41.

Saunders, C. and Hosseini, A. (2001). A laboratory study of the effect of velocity on Hallett–Mossop ice crystal multiplication. *Atmospheric Research*, 59-60:3–14.

Schiermeier, Q. (2010). The real holes in climate science. *Nature*, 463(7279):284–287.

Schneebeli, M., Grazioli, J., and Berne, A. (2014). Improved Estimation of the Specific Differential Phase Shift Using a Compilation of Kalman Filter Ensembles. *IEEE Transactions on Geoscience and Remote Sensing*, 52(8):5137–5149.

Seliga, T. A. and Bringi, V. N. (1976). Potential Use of Radar Differential Reflectivity Measurements at Orthogonal Polarizations for Measuring Precipitation. *Journal of Applied Meteorology*, 15(1):69–76.

Serreze, M. C. and Barry, R. G. (2011). Processes and impacts of Arctic amplification: A research synthesis. *Global and Planetary Change*, 77(1-2):85–96.

Sinclair, V. A., Moisseev, D., and von Lerber, A. (2016). How dual-polarization radar observations can be used to verify model representation of secondary ice. *Journal of Geophysical Research: Atmospheres*, 121(18):10,954–10,970.

Smith, W. L., Minnis, P., Fleeger, C., Spangenberg, D., Palikonda, R., and Nguyen, L. (2012). Determining the Flight Icing Threat to Aircraft with Single-Layer Cloud Parameters Derived from Operational Satellite Data. *Journal of Applied Meteorology and Climatology*, 51(10):1794–1810.

Souverijns, N., Gossart, A., Lhermitte, S., Gorodetskaya, I., Kneifel, S., Maahn, M., Bliven, F., and van Lipzig, N. (2017). Estimating radar reflectivity - Snowfall rate relationships and their uncertainties over Antarctica by combining disdrometer and radar observations. *Atmospheric Research*, 196:211–223.

Taylor, J. W., Choularton, T. W., Blyth, A. M., Liu, Z., Bower, K. N., Crosier, J., Gallagher, M. W., Williams, P. I., Dorsey, J. R., Flynn, M. J., Bennett, L. J., Huang, Y., French, J., Korolev, A., and Brown, P. R. A. (2016). Observations of cloud microphysics and ice formation during COPE. *Atmospheric Chemistry and Physics*, 16(2):799–826.

Tyynelä, J., Leinonen, J., Moisseev, D., and Nousiainen, T. (2011). Radar Backscattering from Snowflakes: Comparison of Fractal, Aggregate, and Soft Spheroid Models. *Journal of Atmospheric and Oceanic Technology*, 28(11):1365–1372.

Ulbrich, C. W. (1983). Natural Variations in the Analytical Form of the Raindrop Size Distribution. *Journal of Climate and Applied Meteorology*, 22(10):1764–1775.

van den Heuvel, F., Foresti, L., Gabella, M., Germann, U., and Berne, A. (2020). Learning about the vertical structure of radar reflectivity using hydrometeor classes and neural networks in the Swiss Alps. *Atmospheric Measurement Techniques*, 13(5):2481–2500.

Vardiman, L. (1978). The Generation of Secondary Ice Particles in Clouds by Crystal–Crystal Collision. *Journal of the Atmospheric Sciences*, 35(11):2168–2180. Publisher: American Meteorological Society.

von Lerber, A., Moisseev, D., Bliven, L. F., Petersen, W., Harri, A.-M., and Chandrasekar, V. (2017). Microphysical Properties of Snow and Their Link to Ze–S Relations during BAECC 2014. *Journal of Applied Meteorology and Climatology*, 56(6):1561–1582.

Vulpiani, G., Montopoli, M., Passeri, L. D., Gioia, A. G., Giordano, P., and Marzano, F. S. (2012). On the Use of Dual-Polarized C-Band Radar for Operational Rainfall Retrieval in Mountainous Areas. *Journal of Applied Meteorology and Climatology*, 51(2):405–425.

Wang, Y. and Chandrasekar, V. (2009). Algorithm for Estimation of the Specific Differential Phase. *Journal of Atmospheric and Oceanic Technology*, 26(12):2565–2578.

Weinheimer, A. J. and Few, A. A. (1987). The electric field alignment of ice particles in thunderstorms. *Journal of Geophysical Research*, 92(D12):14833.

Williams, E. R., Smalley, D. J., Donovan, M. F., Hallowell, R. G., Hood, K. T., Bennett, B. J., Evaristo, R., Stepanek, A., Bals-Elsholz, T., Cobb, J., Ritzman, J., Korolev, A., and Wolde, M. (2015). Measurements of Differential Reflectivity in Snowstorms and Warm Season Stratiform Systems. *Journal of Applied Meteorology and Climatology*, 54(3):573–595.

Wood, N. B., L'Ecuyer, T. S., Bliven, F. L., and Stephens, G. L. (2013). Characterization of video disdrometer uncertainties and impacts on estimates of snowfall rate and radar reflectivity. *Atmospheric Measurement Techniques*, 6(12):3635–3648.

World Meteorological Organization (2018). *Guide to meteorological instruments and methods of observation*. Number 8 in WMO. WMO, Geneva, 2018 edition. OCLC: 785715260.

Yano, J.-I. and Phillips, V. T. J. (2011). Ice–Ice Collisions: An Ice Multiplication Process in Atmospheric Clouds. *Journal of the Atmospheric Sciences*, 68(2):322–333.

Yu, T., Chandrasekar, V., Xiao, H., and Joshil, S. S. (2020). Characteristics of Snow Particle Size Distribution in the PyeongChang Region of South Korea. *Atmosphere*, 11(10):1093.

Zawadzki, I., Szyrmer, W., Bell, C., and Fabry, F. (2005). Modeling of the Melting Layer. Part III: The Density Effect. *Journal of the Atmospheric Sciences*, 62(10):3705–3723.

Zrnić, D. S. and Ryzhkov, A. (1996). Advantages of Rain Measurements Using Specific Differential Phase. *Journal of Atmospheric and Oceanic Technology*, 13(2):454–464.

Paper I

Atmos. Meas. Tech., 9, 4825–4841, 2016
www.atmos-meas-tech.net/9/4825/2016/
doi:10.5194/amt-9-4825-2016

Atmospheric Measurement Techniques
Open Access

Ensemble mean density and its connection to other microphysical properties of falling snow as observed in Southern Finland

Jussi Tiira[1], **Dmitri N. Moisseev**[1,2], **Annakaisa von Lerber**[2,3], **Davide Ori**[1,4], **Ali Tokay**[5,6], **Larry F. Bliven**[7], and **Walter Petersen**[8]

[1]Department of Physics, University of Helsinki, Helsinki, Finland
[2]Finnish Meteorological Institute, Helsinki, Finland
[3]School of Electrical Engineering, Aalto University, Finland
[4]Department of Biological Geological and Environmental Sciences and Department of Physics and Astronomy, University of Bologna, Bologna, Italy
[5]Joint Center for Earth Systems Technology, University of Maryland, Baltimore County, Baltimore, USA
[6]NASA Goddard Space Flight Center, Greenbelt, MD, USA
[7]NASA GSFC/Wallops Flight Facility, Wallops Island, VA, USA
[8]NASA-MSFC Earth Science Office, National Space Science and Technology Center, Huntsville, AL, USA

Correspondence to: Jussi Tiira (jussi.tiira@helsinki.fi)

Received: 1 June 2016 – Published in Atmos. Meas. Tech. Discuss.: 3 June 2016
Revised: 12 September 2016 – Accepted: 13 September 2016 – Published: 28 September 2016

Abstract. In this study measurements collected during winters 2013/2014 and 2014/2015 at the University of Helsinki measurement station in Hyytiälä are used to investigate connections between ensemble mean snow density, particle fall velocity and parameters of the particle size distribution (PSD). The density of snow is derived from measurements of particle fall velocity and PSD, provided by a particle video imager, and weighing gauge measurements of precipitation rate. Validity of the retrieved density values is checked against snow depth measurements. A relation retrieved for the ensemble mean snow density and median volume diameter is in general agreement with previous studies, but it is observed to vary significantly from one winter to the other. From these observations, characteristic mass–dimensional relations of snow are retrieved. For snow rates more than $0.2\,\mathrm{mm\,h^{-1}}$, a correlation between the intercept parameter of normalized gamma PSD and median volume diameter was observed.

1 Introduction

Due to a variety of ice particle types and shapes, representation of winter precipitation in models (Woods et al., 2007; Morrison and Milbrandt, 2015) and in ground, airborne and satellite remote sensing retrievals (Sekhon and Srivastava, 1970; Matrosov, 1997; Wood et al., 2013) is a topic of continuous interest. Both models and retrieval algorithms rely on a prior knowledge of snowflake mass (or density), shape and fall velocity, which are typically expressed as functions of a characteristic particle size (Pruppacher and Klett, 1996). Furthermore, information on possible particle size distributions (PSDs) is also required. Even though some of the microphysical properties of ice particles are not independent, e.g., fall velocity can be computed from particle mass and shape (Böhm, 1989; Khvorostyanov and Curry, 2005; Mitchell and Heymsfield, 2005; Heymsfield and Westbrook, 2010), the remaining degrees of freedom are rather numerous.

Historically, measurements of snowflake properties have been carried out on a particle-by-particle basis (e.g., Magono and Nakamura, 1965; Locatelli and Hobbs, 1974; Mitchell, 1996). While we may still regard such measurements as the more precise and detailed, these studies are limited to a relatively small number of observed ice particles due to the sheer amount of time needed for such experiments and corresponding data analysis. After the introduction of robust optical instruments capable of measuring particle size, shape and in some cases fall velocity, e.g., 2-D-video disdrometer (2-DVD; Hanesch, 1999; Schönhuber et al., 2007), particle size velocity (Parsivel) laser-optical disdrometer (Löffler-Mang and Joss, 2000; Löffler-Mang and Blahak, 2001), hydrometeor velocity size detector (HSVD; Barthazy et al., 2004), snow video imager (SVI; Newman et al., 2009) and multi-angle snowflake camera (MASC; Garrett et al., 2012), continuous recording of ice particle properties became possible. It should be noted that, in comparison to surface-based observations, aircraft measurements have a much longer history in determining ice particle microphysical properties and were carried out in different types of clouds and climate regimes (Pruppacher and Klett, 1996). A typical limitation of automatic observations of ice particle properties, however, is that only a subset of needed parameters is directly measured.

By combining optical disdrometer observations with other measurements, e.g., by radar or precipitation gauge, physical properties such as mean snow density can be derived. Huang et al. (2010) have used a C-band weather radar observations of equivalent reflectivity factor, Z_e, in combination with a 2-DVD to derive a snow density–dimensional relation and to infer more consistent Z_e–snowfall rate relations. Another method for snow density retrieval is based on solving aerodynamic equations to derive particle mass from observed fall velocity and particle effective projected area as proposed by Böhm (1989) and applied by Hanesch (1999) and more recently by Szyrmer and Zawadzki (2010) and Huang et al. (2015). Brandes et al. (2007), hereafter referred to as B07, used a combination of a weighing gauge and a 2-DVD to derive a relation between mean bulk density and median volume diameter and to document relations between PSD parameters for Colorado winter storms. Their approach is similar to the one used by Heymsfield et al. (2004), who have combined aircraft PSD and ice water content observations to derive mean snow density and average mass–dimensional relations for ice particles. Albeit using slightly different definitions, both B07 and Heymsfield et al. (2004) derive effective ice densities for ensembles of ice particles, but there is a difference in terminology. Heymsfield et al. (2004) and many others have used the term (particle) bulk density to refer to the density of individual ice or snow particles defined as the ratio of mass of a particle with a size D to its assumed volume: $\rho = \rho(D)$. In most of such cases, the word "bulk" is used to emphasize the inclusion of hollows within particles. The term "(mean) bulk density" is sometimes used also when referring to the mean density of an ensemble of particles representing the whole PSD, i.e., $\overline{\rho} = \overline{\rho}(D_0)$ (e.g., B07), whereas Heymsfield et al. (2004) used the term "population-mean effective density". In this study we derive the volume flux weighted snow density, similar to, e.g., B07, and refer to it as ensemble mean density, $\overline{\rho}$, to avoid possible confusion.

This paper documents the connection between ensemble mean density and other microphysical properties of snow as observed in Southern Finland. Using the estimated $\overline{\rho}$, average mass–dimensional relations characteristic to studied snowfall events are defined. In order to derive ensemble mean density, a method proposed by B07 was used. However, instead of a 2-DVD, a new generation of the SVI is employed. It is shown that, despite simpler construction compared to the 2-DVD, this instrument's data are suitable for such studies.

Even though this study is based on retrieval of ensemble mean snow density and not mass–dimensional relations directly, which could be more easily applied to radar retrievals and numerical weather prediction (NWP), there are a number of applications of such relations. Aikins et al. (2016) used $\overline{\rho}(D_0)$ to convert PSD observations to precipitation rate. Tong and Xue (2008), Dolan and Rutledge (2009), Matrosov et al. (2009), Huang et al. (2010) and Zhang et al. (2011) used mean snow density–median volume diameter relations for characterizing winter precipitation microphysics by radar. Kneifel et al. (2015) showed a connection between mean snow density and multi-frequency radar observations. Thompson et al. (2008) used the density relation by B07, and Iguchi et al. (2012) applied a similar density retrieval method to improve parametrization of snow microphysics in NWP models, for example.

2 Measurements

2.1 Measurement setup

Measurements were made at the University of Helsinki Hyytiälä Forestry Field Station, Finland (61°50′37″ N, 24°17′16″ E), during the Biogenic Aerosols Effects on clouds and Climate (BAECC) field campaign (Petäjä et al., 2016) and during the consecutive winter of 2014/15. BAECC was a joint experiment between the University of Helsinki, the Finnish Meteorological Institute (FMI) and the United States Department of Energy Atmospheric Radiation Measurement (ARM) program. From 1 February through 12 September 2014 the second ARM Mobile Facility (AMF2) was deployed to the measurement site. The measurement setup was designed for snowfall intensive observation period of BAECC, called BAECC Snowfall Experiment (SNEX), which was undertaken from 1 February though 30 April 2014 and focused on measurements of snow microphysics. However, in order to extend the dataset, the measurements were continued upon completion of BAECC. In total, 23 snowfall cases from winters 2013/14 and 2014/15 were used in this study as summarized in Table 1. The snowfall cases were selected based on measurements of liquid water equivalent (LWE) precipitation accumulation by a weighing gauge, snow depth using a laser sensor and temperature measured by the automatic weather station of the FMI located 500 m distance from the measurement site. Only precipitation cases,

Table 1. Liquid water equivalent precipitation accumulation measured with Pluvio^2 200 and 400, change in snow depth and maximum and minimum temperature, maximum and minimum relative humidity, mean and maximum wind speed and mean wind direction of the studied snow events. Events before the horizontal line are recorded during the BAECC campaign.

	LWE (mm)		ΔSD	Temp (°C)		RH (%)		Wind (m s^{-1}, °)		
Event	200	400	(cm)	min	max	min	max	mean	max	mean dir.
2014 Jan 31 21:00–Feb 01 06:00	7.4	7.3	5.1	−9.8	−8.9	84	91	1.6	2.9	138
2014 Feb 12 04:00–1:00	1.0	0.9	1.8	−1	0	96	98	0.6	2.0	170
2014 Feb 15 21:00–Feb 16 03:00	2.6	2.6	2.5	−2.1	−1	86	97	1.9	2.7	140
2014 Feb 21 16:00–Feb 22 05:00	5.5	5.2	3.6	−2.7	0	88	98	2.1	3.4	138
2014 Mar 18 08:00–19:00	4.4	4.0	7.3	−3.8	−1.8	76	96	1.2	2.7	155
2014 Mar 20 16:00–23:00	6.1	5.9	4.8	−4.3	−1.3	89	97	2.0	3.4	146
2014 Nov 06 19:00–Nov 07 14:30	10.5	–	10.3	−2.44	−1.6	95	97	0.8	1.9	238
2014 Dec 18 14:00–19:00	2.6	2.2	3.9	−2.3	−0.8	97	98	1.0	1.8	134
2014 Dec 24 08:30–13:00	1.3	1.2	1.2	−9.2	−8.9	90	91	0.7	1.5	204
2014 Dec 30 00:30–14:00	6.3	5.3	4.9	−10.4	−0.6	91	98	–	–	–
2015 Jan 3 09:00–23:50	7.3	7.3	11.9	−3.9	0	96	98	2.6	5.2	318
2015 Jan 7 01:00–20:10	5.4	4.8	2.2	−6.5	−0.8	92	97	1.3	2.8	181
2015 Jan 8 06:00–13:30	2.6	2.7	1.6	−1.9	0	97	99	1.0	2.2	155
2015 Jan 9 18:00–Jan 10 06:00	3.1	3.1	4.6	−3.7	−0.2	95	98	1.0	3.0	286
2015 Jan 10 22:00–Jan 11 09:00	0.7	0.6	0.7	−12.6	−4.4	88	95	1.6	3.4	207
2015 Jan 12 21:00–Jan 13 08:30	12.8	10.9	9.6	−15.7	−9.0	88	94	1.3	3.1	181
2015 Jan 13 22:00–Jan 14 07:00	–*	2.2	1.9	−8.0	−0.3	94	98	0.5	1.9	134
2015 Jan 16 01:30–07:30	–*	5.8	5.2	−1.3	−0.6	92	98	1.9	3.4	154
2015 Jan 18 16:00–21:00	1.9	1.9	2.7	−2.4	−0.3	95	97	1.2	2.6	300
2015 Jan 22 21:00–Jan 23 04:30	2.1	2.0	2.3	−13.3	−12.5	87	90	–	–	–
2015 Jan 23 15:00–23:00	1.4	1.2	1.4	−10.1	−8.8	91	93	0.3	1.0	205
2015 Jan 25 09:00–16:00	2.8	2.5	1.9	−2.4	−1.7	96	97	0.7	1.7	170
2015 Jan 31 12:00–Jan 31 23:15	7.0	6.6	5.7	−1.9	−0.4	92	97	1.2	2.6	175

* Pluvio^2 400 was used because data from Pluvio^2 200 were unavailable.

where temperature was below or equal to 0 °C, were chosen, and the data were omitted when occasionally the temperature during the event rose above 0 °C.

The experiments in both winters were organized in collaboration with the National Aeronautics and Space Administration (NASA) Global Precipitation Measurement (GPM) mission ground validation program. The surface precipitation measurements are carried out using a number of collocated instruments, such as NASA Particle Imaging Package (PIP), two OTT Pluvio^2 weighing gauges, two Parsivel^2 laser disdrometers (Tokay et al., 2014), a 2-DVD and a laser snow depth sensor by Jenoptik. To minimize effects of wind, a Double-Fence Intercomparison Reference (DFIR) wind protection (Rasmussen et al., 2012) was build on site as shown in Fig. 1 and discussed in more detail in Petäjä et al. (2016). Inside of the DFIR, the 2-DVD, one of the OTT Pluvio^{2}s and one of the Parsivel^2 disdrometers were placed. In addition to the precipitation sensors, 3-D anemometers were deployed. The wind measurements were carried out at the heights of precipitation instrument sampling volumes. In this study data from the NASA PIP disdrometer and both OTT Pluvio^2 gauges are used.

2.2 Particle Imaging Package

The NASA PIP is the new generation of the SVI. The PIP, like the SVI, consists of a halogen lamp and a charge-coupled device full frame camera with sensor resolution of 640 × 480 pixels. The main differences between PIP and SVI are the camera and improved software. The camera is now capable of imaging with a frame rate of 380 frames per second, enabling measurements of particle fall velocities. The distance between the lamp and the camera lens is approximately 2 m. The lens focus is set at 1.3 m, where the field of view (FOV) is 64 × 48 mm, and the image resolution thereby 0.1 × 0.1 mm. The main advantage of PIP, as well of SVI, over other disdrometers is the open particle catch volume, which minimizes effect of wind on quantitative precipitation measurements (Newman et al., 2009).

The instrument records shadows of particles as they fall through the observation volume. Given the camera frame rate, multiple images of a particle are recorded and used to estimate its fall velocity. The depth of field (DOF) is determined by the processing software either rejecting or not detecting particles that are out of focus. Thus, the observation volume is defined by the FOV and the DOF. The expected

Figure 1. Snow precipitation instruments on the measurement field in Hyytiälä. The Pluvio^2 200 is inside the wind protection on a platform and the PIP lamp can be seen at right on the ground. The view of the picture is to southwest and the distance from the platform to the treeline behind is approximately 20 m.

particle size error due to the blurring effect is 18 % (Newman et al., 2009). From the recorded particle images a number of parameters describing particle geometrical properties are calculated with National Instruments IMAQ software. The measured diameter is given as the equivalent area diameter, which is the diameter of a circle with the same area as the area of a particle shadow. Other parameters, such as particle orientation, and bounding box width and height are also recorded. The aspect ratio of a particle is derived by fitting an ellipse to the bounding box utilizing the orientation of the particle. The aspect ratio is the minor axis in respect to major maxis of the fitted ellipse. The major axis also defines the minimum circumscribing disk, and the area ratio is defined as total area of shadowed pixels in respect to area of the circumscribing disk.

2.3 Weighing gauges and anemometers

The measurement setup includes two OTT Pluvio^2 weighing gauges, one inside and one outside the DFIR, with orifices of 200 and 400 cm^2, respectively. There are differences in wind shielding as well. The Pluvio^2 200 is equipped with a Tretyakov wind shield and the Pluvio^2 400 with a combination of Tretyakov and Alter wind shields, as seen in the forefront in Fig. 1.

The gauges output several products of precipitation rate and accumulation. In this study, a non-real-time accumulation product is used as it is filtered for various sources of errors such as changes in the bucket mass due to evaporation, and as such should yield the most precise precipitation rate estimate among the output products. Because of the filtering, there is a 5 min delay in the recorded time series, which needs to be taken into account when comparing to other instruments. The precipitation accumulation values are recorded with a resolution of 0.001 mm, but non-real-time accumulation is output with a resolution of 0.05 mm.

The 3-D anemometer manufactured by Gill is located approximately at the height of the PIP on the field, respectively. The wind parameters, horizontal and vertical speed and horizontal direction, of Gill anemometer are measured every 10 s and averaged over 60 s. The mean and maximum of the 60 s wind speed averages and the mean wind direction for each event are given in the Table 1.

2.4 Snow depth sensor

The laser snow depth sensor, Jenoptik SHM30, is located on the measurement field, next to Pluvio^2 400. It is an optical sensor, which measures the snow depth by comparing signal phase information of the modulated visible laser light. It is a point measurement, and hence the piling of wind driven snow or random branches and leaves drifting on the snow pack can cause misreadings. To reduce this we have sheltered the measurement spot with a small wind fence and the instrument structure excluding the measurement pole is buried under the ground to prevent the piling of snow. The data are recorded every minute.

3 Retrievals of ensemble mean density, velocity–dimensional relations and PSD

Observations from the PIP and one of the weighing gauges are combined to retrieve snow ensemble mean density. Typically the gauge located inside of the DFIR, the Pluvio^2 200, is used for this retrieval. On a couple of days this gauge was not operational and data from the Pluvio^2 400 located outside of the DFIR were used instead. These dates are marked in Table 1 with asterisks in the LWE precipitation rate col-

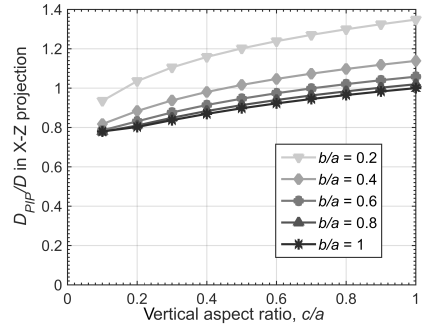

Figure 2. The ratio of the diameter observed by PIP, D_{PIP}, to volume equivalent diameter D.

umn. As seen in the Table 1 the differences in accumulated LWE recorded by the two Pluvio^{2}s are small, the largest being 15 %. Pluvio^2 200 inside the DFIR is typically measuring higher accumulations, which is expected because of the better wind protection. However, the observations do not show a clear indication that the observed precipitation accumulation difference depends on the wind speed. However, the difference seems to increase in respect to certain wind directions. There are two openings from the measurement field, one to a road crossing (approx. 130°) and the other to small field (approx. 180°). If the wind is blowing from these directions the difference between the two gauges seem to increase.

The retrieval procedure is described below and is similar to the one presented by B07, but with notable modifications. Prior to retrieval of $\overline{\rho}$, PSD and velocity–dimensional relations are estimated. It was found, however, that the density retrieval is highly sensitive to the integration time. To minimize this, a variable integration time determined by the precipitation accumulation is used. The same integration time was applied to compute PSD parameters and v–D relations.

3.1 Particle size distribution

The PSDs are calculated from the PIP records of particles that fell through the observation volume. The observed distributions are defined with respect to equivalent area diameter D_{PIP}, which is different from the apparent diameter of the 2-DVD and maximum particle dimensions used in other studies (e.g., Heymsfield et al., 2004). Wood et al. (2013) studied differences between diameter definitions and found that the diameter recorded by SVI is approximately 0.82 of maximum particle dimension. We performed a similar study by examining mean dimensions of rotated ellipsoids on a single projection, as shown in Fig. 2. The ellipsoids were defined by a long dimension a and a short dimension b lying nominally in the horizontal plane along the x and y-axes, respectively, and a short vertical dimension c lying nominally along the z-axis. The particle orientation was defined by Gaussian distribution of canting angles with a standard deviation of 9° (Matrosov et al., 2005a) and a uniform distribution of azimuth angles. The equivalent area diameters D_{PIP} of simulated particles were estimated from their projected areas onto the x–z plane and the resulting values were averaged over all orientations. The ratios of mean D_{PIP} to the particle volume equivalent diameter, i.e., the diameter for which the particle volume $V(D) = \frac{\pi}{6}D^3$, for a number of combinations of vertical and horizontal aspect ratios are shown in Fig. 2. Assuming spheroids (Matrosov, 2007) and taking the typical vertical aspect ratio $c/a = 0.6$ (Korolev and Isaac, 2003; Matrosov et al., 2005b), we found that D_{PIP} is roughly equal to 0.92 of a volume equivalent diameter. As can be seen, the conversion factor varies between 0.8 and 1. For ice particles with axis ratios smaller than 0.4, i.e., pristine ice crystals, this factor could approach 1.2. From this analysis we can conclude that the largest expected error is associated with observations of ice crystals. Dimensions of snowflake aggregates and graupel like particles are expected to be captured with a smaller error. In this study the same conversion factor of 0.92 is used for all the cases. As can be seen in Fig. 3 the median area and aspect ratios of the particles are 0.65 and 0.72, respectively. These observations also support our choice of a mean particle shape and the corresponding diameter transformation. Therefore, the results presented in the rest of the paper are using this volume equivalent diameter proxy.

Prior to calculations of PSD parameters, recorded PSD data are filtered to remove spurious observations of large particles. Following the procedure described in Leinonen et al. (2012), records of large particles were ignored if there was a gap of more than three consecutive PSD diameter bins. The bin size was set to 0.25 mm during the BAECC experiment and it was reduced to 0.2 mm for the winter 2014/2015. The PIP resolution is 0.1 mm and the minimum detectable particle diameter is approximately 0.3 mm (Newman et al., 2009). The smallest diameter bin used in calculations is 0.25 to 0.5 mm during BAECC and 0.2 to 0.4 mm in the following winter.

The PSD parameters were calculated using method of moments and assuming that PSD follows gamma functional form; see for example Ulbrich and Atlas (1998) and citations therein. The normalized gamma distribution $N(D)$ in $\mathrm{mm}^{-1}\,\mathrm{m}^{-3}$ was adopted following Testud et al. (2001), Bringi and Chandrasekar (2001) and Illingworth and Blackman (2002):

$$N(D) = N_{\mathrm{w}} f(\mu) \left(\frac{D}{D_0}\right)^{\mu} \exp(-\Lambda D), \tag{1}$$

$$f(\mu) = \frac{6}{3.67^4} \frac{(3.67+\mu)^{\mu+4}}{\Gamma(\mu+4)}, \tag{2}$$

$$\Lambda = \frac{3.67+\mu}{D_0}, \tag{3}$$

with N_{w} in $\mathrm{mm}^{-1}\,\mathrm{m}^{-3}$ being the intercept parameter, D_0 the median volume diameter in mm, Λ the slope parameter in

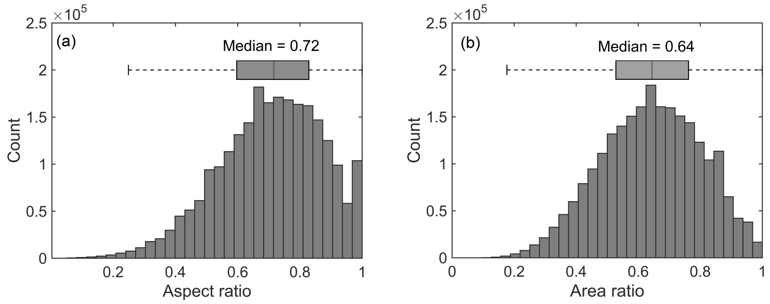

Figure 3. The distributions of snowflake **(a)** aspect ratio and **(b)** area ratio as observed using PIP with interquartile ranges visualized and median values shown.

mm^{-1} and μ the shape parameter. Using the second, fourth and sixth moments for the non-truncated gamma PSD, M_2, M_4 and M_6, the PSD parameters were estimated as follows:

$$\eta = \frac{M_4^2}{M_6 M_2}, \tag{4}$$

$$\mu = \frac{7 - 11\eta - \sqrt{\eta^2 + 14\eta + 1}}{2(\eta - 1)}, \tag{5}$$

$$\Lambda = \sqrt{\frac{M_2 \Gamma(\mu + 5)}{M_4 \Gamma(\mu + 3)}}, \tag{6}$$

$$D_0 = \frac{3.67 + \mu}{\Lambda}. \tag{7}$$

3.2 Ensemble mean density retrieval

The integration time, $\tau(t)$, of the ensemble mean density retrieval is driven by precipitation measurements of the Pluvio^2. The step of the non-real-time accumulation output is 0.05 mm, causing the output interval to be on the order of several minutes even at moderate snow rates. With a short fixed integration time in timescales of minutes or tens of minutes, the produced ensemble mean density estimation would hence be more unstable, the lower the precipitation rate. Therefore, variable length time intervals driven by the gauge output are used with a selected threshold value of 0.1 mm. This corresponds to a $\tau(t)$ of 6 min for a LWE precipitation intensity of $1\,\mathrm{mm\,h^{-1}}$. Effectively, the temporal resolution of the ensemble mean density retrieval is increased with increasing precipitation intensity, and in the analysis of the snowfall events in Table 1 the median $\tau(t)$ was 5 min.

As the integration time $\tau(t)$ is effectively driven by precipitation intensity, there is less variation in number of particles between intervals compared to a fixed time interval approach. With the selected accumulation threshold there are typically between 10^3 and 10^4 particles within a given integration time interval. However, with low precipitation intensities, $\tau(t)$ increases up to 1 h and retrieved $\overline{\rho}$ becomes less representative for the time interval in question. With LWE precipitation rates lower than $0.2\,\mathrm{mm\,h^{-1}}$, the resolution of Pluvio^2 LWE measurements is insufficient and calculations of $\overline{\rho}$ become overly sensitive to recorded number concentrations. Correspondingly, similar unwanted sensitivity to LWE precipitation accumulation occurs when the number of particles observed by PIP within $\tau(t)$ is less than 800. Therefore, time intervals with precipitation rates or particle counts lower than these thresholds are excluded from our analysis.

Given a population of solid precipitation particles with volume equivalent diameters D over the integration time $\tau(t)$, the liquid equivalent precipitation accumulation in millimeters is approximately

$$G(t) \approx \frac{\pi}{6} \times 10^{-6} \frac{\overline{\rho}}{\rho_\mathrm{w}} \int\limits_{t}^{t+\tau(t)} \int\limits_{D_\mathrm{min}}^{D_\mathrm{max}} D^3 v(D,t) N(D,t) \,\mathrm{d}D \mathrm{d}t, \tag{8}$$

where $\overline{\rho}$ is the volume flux weighted population mean snow density in $\mathrm{g\,cm^{-3}}$, $\rho_\mathrm{w} = 1\,\mathrm{g\,cm^{-3}}$ is the density of liquid water, $N(D,t)$ is mean particle number concentration over the integration time in $\mathrm{mm^{-1}\,m^{-3}}$, $v(D,t)$ is particle velocity relation in $\mathrm{m\,s^{-1}}$ and $[D_\mathrm{min}, D_\mathrm{max}]$ is the size range of snowflake observations from a disdrometer. From Eq. (8) we can estimate volume flux weighted snow density for each observation time interval as

$$\overline{\rho}(t) \approx \frac{6}{\pi} \times 10^{6} \rho_\mathrm{w} \frac{G(t)}{\int_t^{t+\tau(t)} \int_{D_\mathrm{min}}^{D_\mathrm{max}} D^3 v(D,t) N(D,t) \,\mathrm{d}D \mathrm{d}t}, \tag{9}$$

using liquid equivalent precipitation accumulation $G(t)$ as measured by the Pluvio^2 gauge, and retrieving averaged $N(D,t)$ and volume flux using fitted $v(D,t)$ based on measurements by the PIP as described in the following sections. It should be noted that, unlike in the retrieval of PSD parameters where gamma PSD was assumed, $\overline{\rho}$ was retrieved without making any assumptions on the shape of the PSD distribution and instead measured PSDs are used in the calculations.

3.3 Comparison of derived mean density to snow depth observations

The definition of ensemble mean density here is the same as for mean bulk density in B07. They determine the densities for 5 min precipitation volumes derived with a 2-DVD disdrometer observations together with precipitation mass measured by a weighing gauge. B07 defined the volume of a single particle by summing coin-shaped sub-volumes together, estimated separately for both orthogonal projections and taking geometrical mean. As the diameter used in our study is the estimated volume-equivalent diameter, our results are comparable to B07. In Heymsfield et al. (2004), the volume of a single particle is defined as a function of circumscribing maximum diameter, and the population mean effective density is determined from ice water content. The estimated ensemble mean snow density is volume-weighted and expected to have lower values than the velocity-weighted snow density. The difference is not generally prominent especially with low-density aggregates, whose velocity–dimensional dependence is weak.

It should be noted that the derived density is inversely proportional to the snow ratio, R_s, assuming that issues related to packing of snowflakes on the ground can be ignored. The snow ratio (Power et al., 1964; Ware et al., 2006) is used by operational weather services to estimate change in snow depth from LWE observations and can be defined as follows:

$$R_s(t) = \frac{1}{P \cdot C} \frac{\rho_w}{\overline{\rho}(t)}, \tag{10}$$

where $\overline{\rho}(t)$ is the volume flux weighted snow density derived as shown in Eq. (9), P is the packing efficiency of snowflakes and C is the snow compression. Assuming that the packing and compression terms, or their product, are close to unity, the derived density can be tested against the commonly used assumption that 1 mm of LWE accumulation corresponds to 1 cm change in snow depth. In Fig. 4 the combined distribution of estimated snow ratios on temporal scales defined by the gauge accumulation for all the 23 events analyzed in this study is shown. It can be seen that the mean and median values, equal to 10 and 9, respectively, are very close to the commonly assumed value.

This analysis assumes that packing efficiency of snowflakes is 100 % and compression of snow on the ground can be ignored or that snow compression counteracts reduction in snow density due to packing. The packing efficiency of snowflakes on the ground is not known. Random packing of the same size spheres has density of 64 % and dense packing of such spheres uses 74 % of the volume, corresponding to $P = 0.64$ and 0.74, respectively. Packing efficiency of equal spheroids depends on axis ratios, exceeding that of spheres, and could exceed 77 % (Donev et al., 2004). It is not unreasonable to expect that irregular shaped particles of variable sizes, such as snowflakes, would pack more efficiently than equal spheroids. At least, packing efficiency in excess of 90 % can be expected for spheres of several radii (de Laat et al., 2014). The packing efficiency of 70 % would mean that density of freshly fallen snow would be 30 % lower than that of falling snowflakes. The packing efficiency of 80 % would correspond to 20 % bias in estimated snowflake density from snow depth measurements or in 25 % underestimation of the snow depth change by using $\overline{\rho}(t)$. We do not know the exact value of the snow packing, but we could expect that in the worst case scenario it is about 70 % and probably closer to 80 % or even higher. It should also be noted that the snow compression would counteract this, but we are considering only freshly fallen snow and expect that the compression factor C is very close to unity.

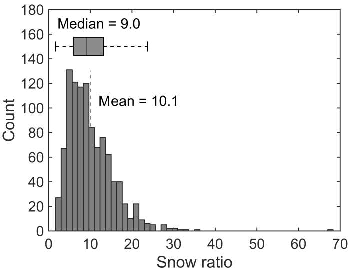

Figure 4. Distribution of snow ratios, ratio of snow depth change to LWE, calculated from retrieved ensemble mean densities with interquartile range, and median and mean values.

One of the major uncertainties in the density retrieval is the assumption about particle volume. In this study we have assumed that snowflakes are spheroids with axis ratios of 0.6. Given this assumption, a conversion factor relating volume equivalent and observed disc equivalent diameters was defined. Figure 2 shows that for a reasonable range of ellipsoid axis ratios this conversion factor can range between 0.8 and 1. This range of values implies that the uncertainty in the density estimation can range from an overestimation by as much as 50 % to an underestimation by about 20 %. This range of uncertainty is much larger than what is expected from a comparison of the retrieved volume-flux weighted density and snow depth measurements, as was discussed previously. Therefore, by comparing the PIP derived and the directly measured snow depths, the validity of the derived values of $\overline{\rho}$, and assumption of particle shape, can be checked. In Fig. 5 hourly change in the snow depth measured by the Jenoptik SHD30 is compared to the PIP derived snow depth. It can be seen that the agreement is good, with RMSE of 0.30 cm, linear correlation coefficient of 0.88 and normalized bias as low as −0.06. This comparison also gives confidence about the validity of the derived ensemble mean densities.

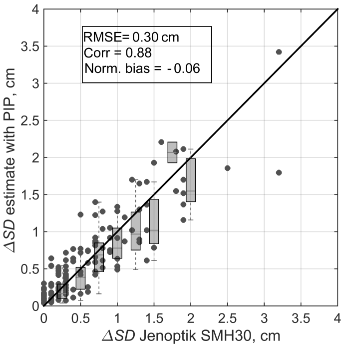

Figure 5. Scatterplot of the hourly change of snow depth measured with Jenoptik SMH30 and estimated from volume flux using PSD and fall velocities as measured by PIP. The data include all the studied cases except 10–11 January 2015.

3.4 Effect of PSD truncation on derived ensemble mean snow density

The observed PSDs are truncated on left and right sides (Ulbrich and Atlas, 1998). They are truncated on the right side because of the instrument finite sampling volume and because natural sizes of hydrometeors do not extend to infinity. The truncation on the left, on the small-diameter side, is due to instrumental limitations and possible wind effects (Moisseev and Chandrasekar, 2007). Ulbrich and Atlas (1998) have presented a comprehensive analysis on how the right-side truncation affects the derived gamma PSD parameters. A similar study on the effects of the left-side truncation and other instrumental effects was presented by Moisseev and Chandrasekar (2007). Here we apply the method presented by Moisseev and Chandrasekar (2007) to estimate impact of PSD truncation on the derived mean snow density.

To investigate the impact of the PSD truncation on retrieval of mean snow density, a simulation study was performed. To initiate the simulation, the PSD parameters N_w, D_0 and μ, together with parameters of m–D and v–D, are used. During the study it was found that the density estimation error is most sensitive to D_0 and μ and virtually independent of the other input parameters. Therefore, the results presented here assume that N_w is constant and equal to $10^4\,\mathrm{mm}^{-1}\,\mathrm{m}^{-3}$. Further, only one m–D relation representative of all BAECC cases, as presented in Sect. 4.3.1, is selected, and v–D representative of the snowfall with mean density ranging between 100 and $200\,\mathrm{g\,cm}^{-3}$ is utilized. The D_0 values were varied between 0.5 and 4 and μ values between -0.9 and 3.

At the first stage of the simulation, the number of observed particles was computed, assuming a Poisson distribution, with the expected number of particles being determined by PIP sampling volume and $\tau(t)$. Given this number of particles, their diameters were found by sampling a gamma probability density function, parameters of which are determined by the input PSD. To simulate the left-side truncation all particles with diameters smaller or equal to 0.25 mm, the PIP sensitivity threshold, were rejected. The right-side truncation was achieved by rejecting particles with sizes exceeding $3D_0$. For each D_0 and μ pair, 50 simulated PSDs were computed. Given the simulated truncated PSD the density is estimated in the same way as was presented above. This estimated density is compared to the one that is directly derived from the simulation input parameters and the results of their comparison is shown in Fig. 6. As one can see, the derived ensemble mean snow density is biased. The bias is largest for small D_0, which is explained by the left-side PSD truncation. For D_0 larger than 1 mm, the bias decreases and approaches 2 %. Given that the error associated with PSD truncation is rather small for $D_0 > 1$ mm, and that most of the observations fall within this range, the truncation error is not corrected in this study.

3.5 Velocity–dimensional analysis

For the retrieval of volume flux weighted snow density, velocity–dimensional relations of falling snow need to be estimated. For each integration time interval, $v(D) = a_\mathrm{v} D^{b_\mathrm{v}}$ is fitted for velocity–diameter data from the PIP. The $v(D)$ power-law fits to unfiltered data tend to be strongly biased by outliers. To address this problem, Gaussian kernel density estimation (KDE; Silverman, 1986) is used to find the most probable velocity for each diameter bin, and only observations with velocities within half width at half maximum from the bin peak KDE value are included in calculating the fit. Using the linear least squares method, a fit is performed for the data points in log–log scale to derive a power-law relation. It should be noted that using linear regression in log–log space does not optimally minimize residuals in linear space, but the method is used here as it does not overly emphasize the large end of the size spectrum. The retrieved velocity fits are shown for selected integration time intervals of the 18 March 2014 and the 22–23 January 2015 cases in the bottom of Figs. 7 and 8, respectively.

It should be noted that the power-law model, albeit widely used, may not necessary represent correctly velocities of ice particles over the complete range of diameters (Mitchell and Heymsfield, 2005). In many cases the fit can also be uncertain either because of narrow PSD or in presence of multiple particle types.

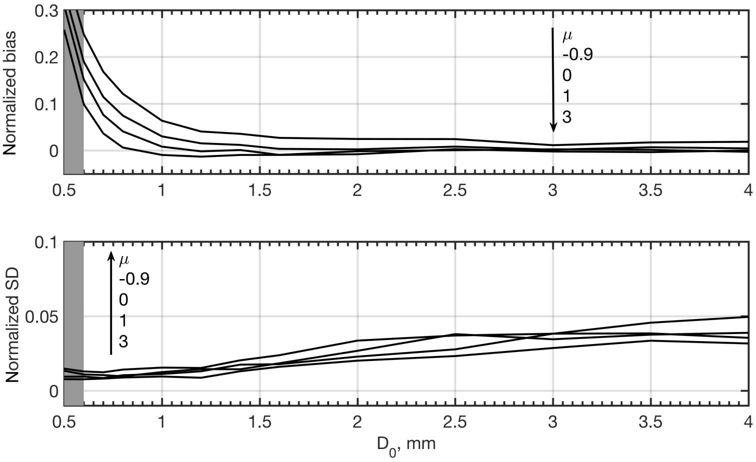

Figure 6. Computed normalized bias and standard deviation of estimated mean snow density as a function of μ and D_0. The shaded area indicates data that are not included in the analysis because derived D_0 is smaller than 0.6 mm. The increased values of bias at low D_0 values is due to left side truncation of the observed PSD, which is caused by the instrument sensitivity. At larger D_0 values the bias approaches value of 0.02.

4 Results

4.1 Case studies

4.1.1 18 March 2014

During the 18 March, Finland was covered in a continental polar air mass. In the morning, a warm occluded front associated with a weak low pressure center approached Southern Finland from the southwest, bringing light snowfall. In the afternoon, Hyytiälä was in the warm sector of the frontal system and the relative humidity dropped, halting the snowfall around 12:00 UTC. Later in the evening there was a 1 h snowfall from a squall line, associated with a cold front passing over Southern Finland.

Time series of LWE snow rate, ensemble mean density and PSD parameters for the 18 March case are shown in Fig. 7. The bottom panels show measured fall velocities for selected integration time intervals, representing observations with different ensemble mean densities. Between the red dotted lines is the region where KDE is higher than half maximum for a given particle size. The fits are applied for data points between these lines. There is considerable scatter in particle fall velocity throughout the case and a bimodal PSD is present momentarily in the morning as can be seen in fall velocity panel Fig. 7a.

During the snow shower in the evening, liquid equivalent precipitation rates were recorded on average roughly 3 times more intense than earlier during the day, allowing retrievals of $\overline{\rho}$ and PSD parameters at high time resolutions. Strong short timescale variations of $\overline{\rho}$ and PSD parameters are recorded during this shower. The lowest ensemble mean density value of the case, 0.035 $\mathrm{g\,cm^{-3}}$, is retrieved for time interval from 16:35 to 16:39, with concurrent D_0 value of 5.5 mm and N_w of roughly 700 $\mathrm{mm^{-1}\,m^{-3}}$. The corresponding fall velocity distribution visualized in Fig. 7b is characterized by low values of velocity fit coefficients a_v and b_v. Within the following 20 min, D_0 decreases down to roughly 2 mm, N_w increases to 2×10^4 $\mathrm{mm^{-1}\,m^{-3}}$ and retrieved values of $\overline{\rho}$ peak at over 0.2 $\mathrm{g\,cm^{-3}}$ between 16:54 and 16:58 and again from 17:05 to 17:08. Corresponding fall velocity distribution between 16:54 and 16:56, shown in Fig. 7c, is characterized by substantially higher values of a_v and b_v than 20 min earlier, which possibly indicates the onset of riming.

4.1.2 22–23 January 2015

During 22 January 2015, similarly to the 18 March 2014 event, a warm occluded front associated with a weak low moved northwards over the Gulf of Finland. However, due to a blocking high over northwestern Russia, the low and the associated front were sustained over Southern Finland for the whole day of 23 January, causing weak continuous precipitation in the area.

Time series of LWE snow rate, $\overline{\rho}$ and PSD parameters for the 22–23 January 2015 case, with velocity–diameter fits from selected time intervals, are shown in Fig. 8. The case is characterized by continuous snowfall at LWE precipitation rates lower than 1 $\mathrm{mm\,h^{-1}}$ throughout the case. The velocity distribution for a given time interval has substantially less scatter compared to the 18 March 2014 case. The evolution

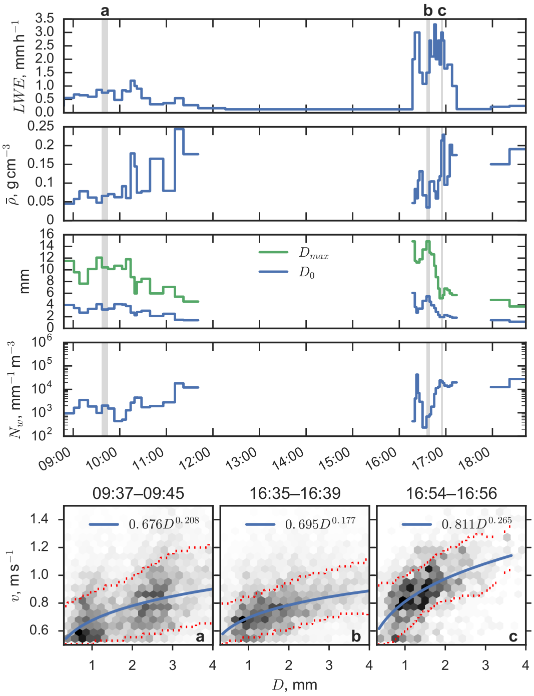

09:37–09:45 16:35–16:39 16:54–16:56

Figure 7. Evolution of snowfall intensity, ensemble mean density and particle size distribution parameters during 18 March 2015 with associated (v, D) from three selected time intervals (highlighted in gray). The red dashed lines mark the upper and lower velocity limits where for a given D the KDE value is higher than half maximum.

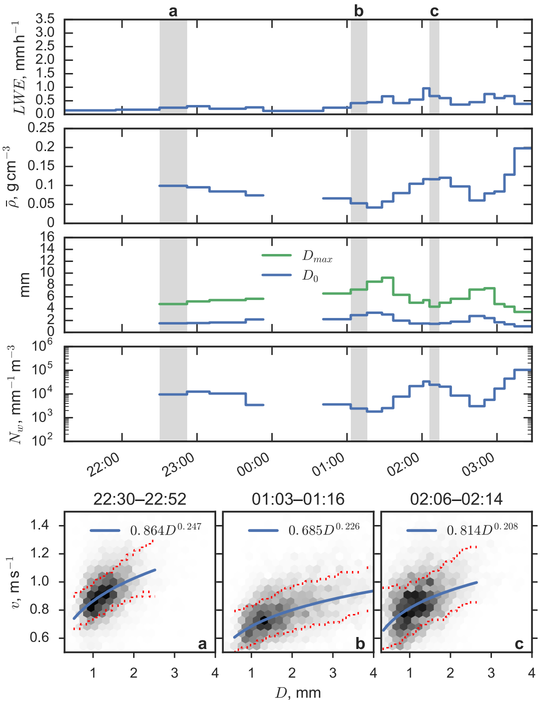

22:30–22:52 01:03–01:16 02:06–02:14

Figure 8. Evolution of snowfall intensity, ensemble mean density and particle size distribution parameters during the night between the 22 and 23 January 2015 with associated (v, D) from three selected time intervals (highlighted in grey). The red dashed lines mark the upper and lower velocity limits where for a given D, the KDE value is higher than half maximum.

of $\overline{\rho}$ and N_w, as shown in Fig. 8, shows considerable similarities, suggesting a strong correlation.

The velocity–diameter fits shown represent a low ensemble mean density ($\overline{\rho} = 0.05\,\mathrm{g\,cm^{-3}}$) time interval of 01:03–01:16 (Fig. 8b) and two intervals of 22:30–22:52 and 02:06–02:14 (Fig. 8a, c) with higher values of $\overline{\rho}$, 0.10 and $0.12\,\mathrm{g\,cm^{-3}}$, respectively. Notable is the higher modal fall velocities and the absence of particles larger than 3 mm in the high density time intervals compared to the distribution in Fig. 8b.

4.2 *v*–*D* and density

In Fig. 9, particle fall velocity versus diameter data points combined from all the cases in Table 1 are divided into three categories according to the snow ensemble mean density of the time interval during which particles were observed. A least squares fit is applied to observations in each $\overline{\rho}$ range using the same procedure as for velocity–dimensional fits for integration time intervals, as described in Sect. 3.5. The total number of observed particles is roughly 4 440 000, and for each density category numbers of particles included in the fitting process (within the red lines in Fig. 9) are approximately 1 140 000, 1 190 000 and 360 000, respectively. The fitted relations for ensemble mean density ranges are

$$v(D) = 0.834D^{0.217} \quad 0.0 < \overline{\rho} \leq 0.1\,\mathrm{g\,cm^{-3}}, \tag{11}$$

$$v(D) = 0.895D^{0.244} \quad 0.1 < \overline{\rho} \leq 0.2\,\mathrm{g\,cm^{-3}} \text{ and} \tag{12}$$

$$v(D) = 0.906D^{0.256} \quad \overline{\rho} \geq 0.2\,\mathrm{g\,cm^{-3}}, \tag{13}$$

with RMSE values of 0.30, 0.30 and $0.35\,\mathrm{m\,s^{-1}}$, respectively.

The coefficient is increased with density indicating higher fall velocities with more dense particles. There is also a clear increase in the slope of the fitted curve from the lowest density range to the 0.1–$0.2\,\mathrm{g\,cm^{-3}}$ range indicated by the increase in the power term. With particles in the highest density range the observed size distribution is narrow and hence the correlation between particle size and fall velocity is weak, and it is difficult to find an unambiguous relation between them. All things considered, the results are in line with the conclusion made by Barthazy and Schefold (2006) that

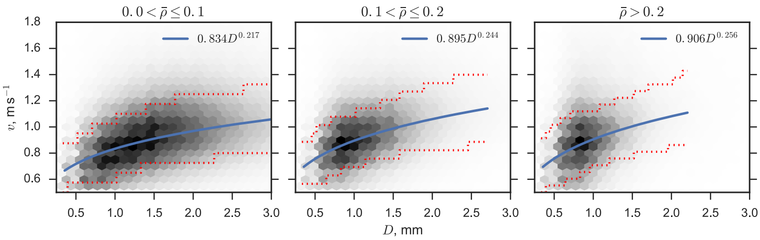

Figure 9. Probability densities of (D, v) in three ensemble mean density ranges ($[\overline{\rho}] = \mathrm{g\,cm^{-3}}$). Dashed lines mark the full width at half maximum KDE in each diameter bin. Power-law functions are fitted for data between those lines.

the prefactor and power terms increase with riming degree, which in turn are strongly connected with density (Power et al., 1964).

Considering the definition of the volume equivalent diameter, relations in the form of Eqs. (11)–(13) should be ideal for velocity–dimensional parametrization of radar observations as the average size of hydrometeors as observed by radar are largely defined by their volumes rather than their shapes.

4.3 Connection between PSD parameters and density

From the analysis of PSD parameters and their relations to ensemble mean density we have excluded data points representing integration time intervals where $D_0 < 0.6$ mm, as lower values of median volume diameter would imply that a substantial fraction of particles are too small to be observed with PIP. Applying this restriction, along with minimum thresholds set for particle count and LWE precipitation rate in density retrievals, as described in Sect. 3.2, all in all 101 time intervals were discarded from the total of 1141 intervals of observations, leaving 7173 min of snow observations for the analysis.

4.3.1 Density and D_0

In Fig. 10, observed distributions of D_0 for the three different density regimes are shown. For the low-density particles, the maximum D_0 value rarely exceeds 5 mm, which is in agreement with observations of snow aggregates presented by Lo and Passarelli Jr. (1982). It can also be seen that D_0 distribution depends on density. Low-density particles are generally larger and vice versa. This dependence of D_0 on ensemble mean density is not surprising, given that they are related as was previously shown by B07 and discussed in more detail below.

Relation between $\overline{\rho}$ and size (D_0) is illustrated in Fig. 11. The areas of individual data points are proportional to the particle counts of the corresponding observation time intervals. The overlaid black solid curve, a least squares fit applied for all cases in Table 1, is given by

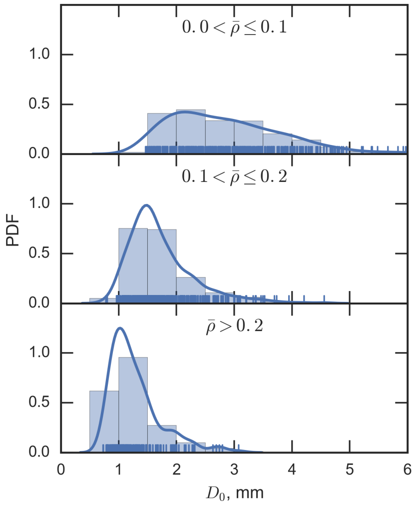

Figure 10. Normalized frequency (bars) and kernel density (line) of median volume diameter D_0 in three ensemble mean density ranges, $[\overline{\rho}] = \mathrm{g\,cm^{-3}}$.

$$\overline{\rho}(D_0) = 0.226 D_0^{-1.004}, \tag{14}$$

where D_0 is in mm and $\overline{\rho}$ is in g cm^{-3}. As the two examined winters were seen to have notable differences between each other in the snowfall type and average $\overline{\rho}$, corresponding relations were also calculated separately for the winters and are given by

$$\overline{\rho}(D_0) = 0.273 D_0^{-0.998} \quad \text{and} \tag{15}$$

$$\overline{\rho}(D_0) = 0.209 D_0^{-0.969} \tag{16}$$

for BAECC events and for events of winter 2014/15, respectively. A relation by B07, given by $\overline{\rho}(D) = 0.178 D_0^{-0.922}$, is plotted in Fig. 11 for comparison. As their definitions of particle diameter and $\overline{\rho}$ are close to ours, the relations are

Table 2. The prefactors and exponents of $m = a_\mathrm{m} D^{b_\mathrm{m}}$ derived for exponential PSD with different values of exponent b_v of velocity relation. The mass given in grams and the volume-equivalent diameter proxy in millimeters.

		a_m ($\times 10^{-5}$)		
Dataset	b_m	$b_\mathrm{v} = 0.217$	$b_\mathrm{v} = 0.244$	$b_\mathrm{v} = 0.256$
All cases	1.996	10.36	10.45	10.49
BAECC cases	2.002	12.54	12.64	12.69
Winter 2014–2015 cases	2.031	9.679	9.757	9.792

easy to compare. Especially Eq. (16) is in good agreement with B07's results. The ensemble mean density is on average higher for snow events recorded during BAECC, which suggests more riming occurred during those events. Indication to this is that the ARM AMF2 dual-channel microwave radiometer located on the same measurement field detected the presence of liquid water more than 80 % of the BAECC SNEX campaign time (Petäjä et al., 2016) and the presence of supercooled liquid layers could also be observed in the backscatter coefficient and circular depolarization ratio measurements of the co-located ARM HSRL (High Spectral Resolution Lidar) in the majority of the BAECC cases (Goldsmith et al., 2014). In general the BAECC winter was milder than the next winter 2014–2015, and the case duration weighted average of maximum recorded temperatures was almost 1 °C higher for BAECC events compared to the value for winter 2014–2015 cases. The temperatures closer to 0 °C could mean increased aggregation as stated in B07, and therefore decreased density values, as well as different snow habits compared to colder cases.

The mass–dimensional relation in power-law format $m = a_\mathrm{m} D^{b_\mathrm{m}}$ can be derived from the retrieved $\overline{\rho}$–D_0 relations (Eqs. 14–16) by assuming gamma PSD and describing the ensemble mean density approximately as

$$\overline{\rho} \approx \frac{\int_0^\infty m(D) v(D) N(D) \mathrm{d}D}{\int_0^\infty V(D) v(D) N(D) \mathrm{d}D}, \tag{17}$$

$$= \frac{\int_0^\infty a_\mathrm{m} (D)^{b_\mathrm{m}} a_\mathrm{v} D^{b_\mathrm{v}} N_0 D^\mu \exp(-\Lambda D) \mathrm{d}D}{\int_0^\infty \frac{\pi}{6} (0.1 D)^3 a_\mathrm{v} D^{b_\mathrm{v}} N_0 D^\mu \exp(-\Lambda D) \mathrm{d}D}, \tag{18}$$

$$= \frac{6}{\pi} 10^3 a_\mathrm{m} \frac{\Gamma(b_\mathrm{m} + b_\mathrm{v} + \mu + 1)}{\Gamma(b_\mathrm{v} + \mu + 4)} \left(\frac{1}{3.67} \right)^{b_\mathrm{m} - 3} D_0^{b_\mathrm{m} - 3}. \tag{19}$$

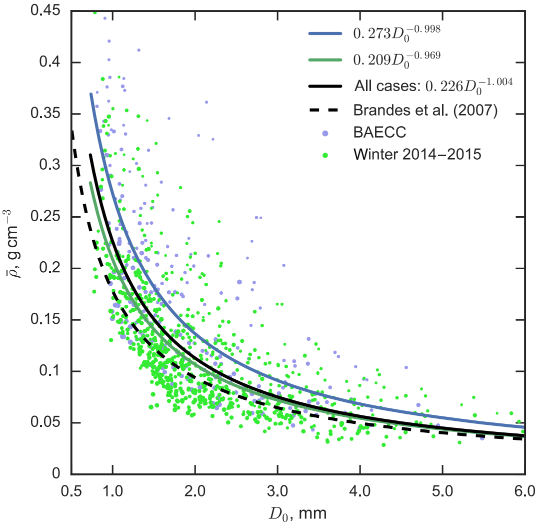

Figure 11. (D_0, $\overline{\rho}$) for all cases listed in Table 1. Area of each dot is proportional to the number of particles in corresponding integration time interval. Power-law fits are shown separately for BAECC winter cases (blue) and cases from the following winter (green).

The integration limits are defined from 0 to infinity for deriving the analytic solution, though the true range is narrower because of left and right truncation of the observed size spectrum. As shown in Fig. 6, the ensemble mean density is overestimated because of the truncation. The estimation bias of density ranges between 20 % for D_0 smaller than 0.75 mm and about 2 % for D_0 larger than 2 mm. Since for the estimation of the m–D relation most of the observed D_0 values are higher than approx. 1 mm as shown in Fig. 10, there is only minor contribution of the smaller D_0 values, and we assume our error in ensemble mean density to be close to 2 % because of truncation. This corresponds to an error of 2 % in the prefactor a_m as well, if it is assumed that the truncation does not introduce significant changes in the exponents of the $\overline{\rho}$–D_0 and m–D relations.

Taking the three velocity exponents from Eqs. (11)–(13), and assuming exponential PSD, the derived prefactors and exponents of mass relation are shown in Table 2, having the volume-equivalent diameter proxy in millimeters and mass given in grams. The factor 0.1 in Eq. (18) is derived from unit conversion, as $\overline{\rho}$ is in g cm^{-3}. The values of prefactor a_m are not sensitive to the changes in the velocity exponent b_v (changes in b_v are resulting less than 1 % deviation a_m values), though there is a small increase in a_m with increasing b_v. The prefactor is more sensitive to shape parameter μ of the gamma PSD; the value of a_m increases by 24 % as μ is increased from 0 to 1. With value of $\mu = 3$ the increase in the prefactor a_m value is 48 %. The shape factor of snow PSD is

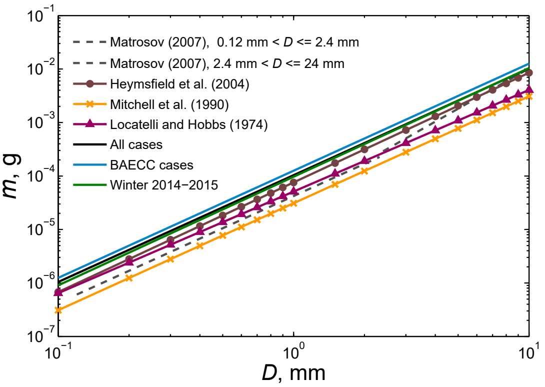

Figure 12. Derived m–D relations assuming exponential PSD in comparison relations presented in literature are shown in Table 3. A conversion of maximum dimension to volume equivalent diameter is done by assuming axis ratio of 0.6.

Table 3. The prefactors and exponents of $m = a_\mathrm{m} D^{b_\mathrm{m}}$ of literature values for comparison plotted in Fig. 12. A conversion from maximum dimension to volume equivalent diameter is done by assuming axis ratio of 0.6.

Study	b_m	a_m ($\times 10^{-5}$)
Matrosov (2007), 0.12 mm $< D \leq$ 2.4 mm	2.0	4.2172
Matrosov (2007), 2.4 mm $< D \leq$ 24 mm	2.5	3.2430
Heymsfield et al. (2004)	2.04	7.5814
Mitchell et al. (1990)	2.0	3.0926
Locatelli and Hobbs (1974)	1.9	5.1134

known to be noisy and thus often exponential distribution is assumed. With $b_\mathrm{v} = 0.217$ the derived mass–dimensional relations for all cases and for both studied winters separately are plotted against literature values in Fig. 12. The derived exponent b_m for the studied cases is in line with literature values, close to 2, but the prefactor a_m values are higher than in the presented relations in Table 3. The highest value of a_m is for the BAECC cases, indicating conditions of riming. The high prefactor values might manifest the Finnish winter conditions. Because of the vicinity of the Baltic Sea, the air is more moist than, for example, in continental conditions.

4.3.2 N_w and density

Distributions of observed N_w values also exhibit dependence of N_w on the ensemble mean density, as shown in Fig. 13; i.e., N_w increases with density. The modal values of N_w are approximately 5000, 40 000 and 80 000 $\mathrm{mm^{-1}\,m^{-3}}$ for ensemble mean density ranges 0.0–0.1, 0.1–0.2 and $> 0.2\,\mathrm{g\,cm^{-3}}$, respectively, with the vast majority of N_w values spanning less than 2 orders of magnitude for a given $\overline{\rho}$ range. This dependence of N_w on density is somewhat unexpected. There is no obvious reason to expect that N_w would depend on density. However, because D_0 and density are related, dependence of N_w on density potentially arises from the dependence of N_w on D_0.

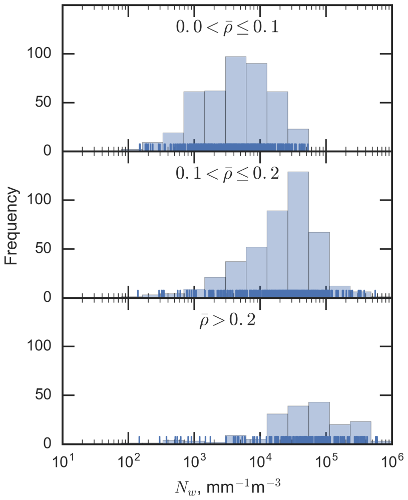

Figure 13. Frequency of N_w in three ensemble mean density ranges, $[\overline{\rho}] = \mathrm{g\,cm^{-3}}$.

To verify this, the partial correlation analysis of the relation between log values of N_w and density while controlling for log value of D_0 was carried out. It was found that there is a moderate negative partial correlation, -0.33, between N_w and density while controlling for D_0. However, the zero-order correlation between N_w and density is 0.52. The analysis confirms that the observed relation between N_w and density is due to their relation to D_0. It is not clear, however, what the meaning is of the found negative partial correlation between N_w and density.

A relation between N_w and snow particle size is shown in Fig. 14a. A linear least squares fit is applied for (D_0, $\log(N_\mathrm{w})$), and the corresponding relation between N_w and D_0 is given by

$$N_\mathrm{w} = 2.492 \times 10^5 \times 10^{-0.620 D_0}. \tag{20}$$

Bringi and Chandrasekar (2001) show that there is a weak tendency for N_w to decrease with increasing D_0 for rain (their Fig. 7.17), but to our knowledge this is the first attempt to find a climatological relation between D_0 and N_w for snow. It should be noted, however, that the observed relation is partially caused by data filtering, which removes low precipitation rate data. There is a high amount of scatter when $N_\mathrm{w} < 1 \times 10^3\,\mathrm{mm^{-1}\,m^{-3}}$. The data points in this area are more contained when D_0 is multiplied with $\overline{\rho}^{1/3}$ as shown in Fig. 14b. Making a fit to the resulting data points

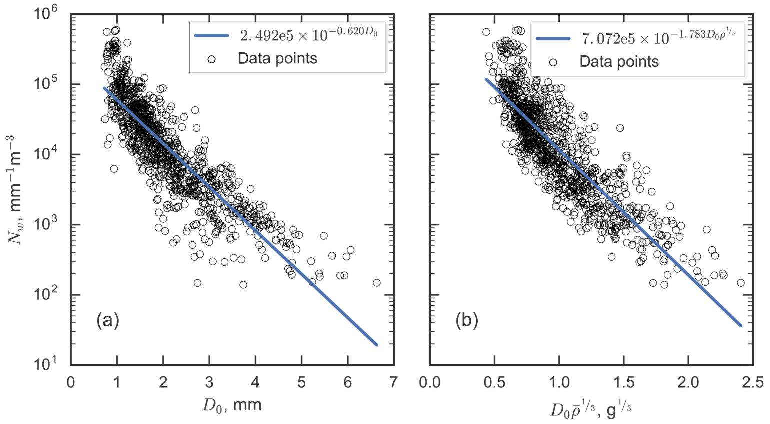

Figure 14. (D_0, N_w) and ($D_0\overline{\rho}^{1/3}$, N_w) with fitted relations.

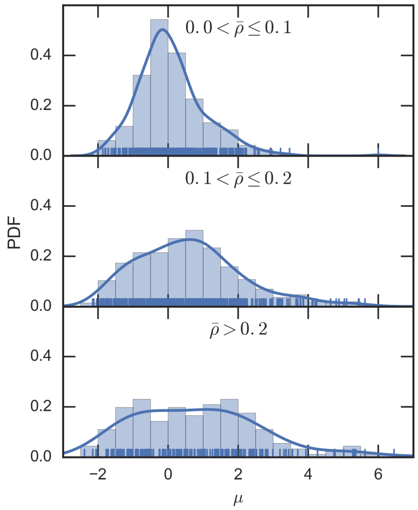

Figure 15. Normalized frequency (bars) and kernel density (line) of the gamma PSD shape factor μ in three ensemble mean density ranges, $[\overline{\rho}] = \mathrm{g\,cm^{-3}}$.

gives

$$N_\mathrm{w} = 7.072 \times 10^5 \times 10^{-1.783 D_0 \overline{\rho}^{1/3}}. \quad (21)$$

However, the difference in correlation coefficients for the fits in Fig. 14a and b, given by −0.87 and −0.85, respectively, is minimal. The lower scatter in Fig. 14b for N_w in the sub $10^3\,\mathrm{mm^{-1}\,m^{-3}}$ range seems to be compensated by slightly more scatter in the higher end of the distribution.

4.3.3 PSD shape parameter, μ

In Fig. 15 the normalized frequencies of the gamma PSD shape factor μ are visualized in the three ensemble mean density ranges. Unlike D_0 and N_w, μ does not seem to have a clear correlation with ensemble mean snow density, although a weak tendency for μ to increase with density is possible. Instead, the values of μ are scattered around approximately 0, with deviation increasing with density. In the ensemble mean density ranges 0.0 to 0.1 and 0.1 to $0.2\,\mathrm{g\,cm^{-3}}$ the kernel densities peak at −0.15 and 0.62, with standard deviations of 0.97 and 1.58, respectively. For the integration intervals with $\overline{\rho} > 0.2\,\mathrm{g\,cm^{-3}}$, the distribution of μ is more spread, with standard deviation of 2.0 and median of 0.76. The observations support the findings of B07 and Heymsfield et al. (2008), who have found that low-density particles generally have exponential or slightly super-exponential distributions. This suggests that the exponential PSD would be most appropriate for describing low-density aggregated snow and less so when strong riming occurs.

5 Conclusions

Microphysical properties of snow in Southern Finland were documented using observations from PIP and a weighing gauge. The data were collected during US DOE ARM funded BAECC campaign and the consecutive winter. It is shown that there is a detectable difference in measured snow properties between consecutive winters. Snow observed during BAECC is denser than during the next winter. The derived m–D relations from two winters are also different, and the difference is namely in the prefactor of the power-law relations.

It is found that D_0 and N_w parameters of gamma PSD are correlated with $\overline{\rho}$. While the relation between ensemble mean density and D_0 is not surprising, since these two parameters are related, the correlation between N_w and $\overline{\rho}$ is interesting. This correlation arises from the observed connection between N_w and D_0. It should be noted that this observed connection is partially due to data filtering that removes low precipitation rate data from the analysis. However, it indicates that for heavier precipitation aggregation is an important snow growth process. During snow growth by aggregation, N_w should decrease while D_0 increases, as was found by (Lo and Passarelli Jr., 1982). The shape parameter of the gamma PSD, μ, does not seem to depend on ensemble mean density and its average value is close to 0, which is in line with studies reported in literature.

Dependence of v–D relation on ensemble mean density was also studied. It was found that the prefactor of the v–D power law depends on density. It is higher for higher densities. This result is in agreement with the conclusion made by Barthazy and Schefold (2006): the coefficient and power terms increase with riming degree.

The presented study uses the newly developed instrument Particle Imaging Package, which is a new generation of SVI. It is shown that data collected by this instrument are adequate for such studies. While the instrument only observes particle shapes projected to single 2-D plane, as opposed to 2-DVD or MASC, it has a larger sampling volume and its observations are less affected by wind (Newman et al., 2009). Additionally, the instrument itself is operationally more robust and requires less maintenance, enabling deployment in sites with remote locations and harsh field conditions.

6 Data availability

The data of the video distrometer (PIP), the precipitation gauges and the snow depth sensor used in this study are available at http://www.arm.gov/campaigns/amf2014baecc#data or by request from D. Moisseev (dmitri.moisseev@helsinki.fi).

Acknowledgements. We would like to acknowledge the Hyytiälä station and University of Helsinki personnel for the daily tasks with measurements, in particular Matti Leskinen and Janne Levula. The research of Jussi Tiira and Dmitri N. Moisseev was supported by Academy of Finland (grant no. 263333) and the Academy of Finland Finnish Center of Excellence program (grant no. 272041). Annakaisa von Lerber was funded by grant of the Vilho, Yrjö and Kalle Väisälä Foundation and by SESAR Joint Undertaking Horizon 2020 grant agreement no. 699221 (PNOWWA). The instrumentation used in this study was supported by NASA Global Precipitation Measurement Mission ground validation program and by the Office of Science of the US Department of Energy ARM program.

Edited by: G. Vulpiani
Reviewed by: A. Heymsfield and two anonymous referees

References

Aikins, J., Friedrich, K., Geerts, B., and Pokharel, B.: Role of a Cross-Barrier Jet and Turbulence on Winter Orographic Snowfall, Mon. Weather Rev., 144, 3277–3300, doi:10.1175/MWR-D-16-0025.1, 2016.

Barthazy, E. and Schefold, R.: Fall velocity of snowflakes of different riming degree and crystal types, Atmos. Res., 82, 391–398, 2006.

Barthazy, E., Göke, S., Schefold, R., and Högl, D.: An Optical Array Instrument for Shape and Fall Velocity Measurements of Hydrometeors, J. Atmos. Ocean. Tech., 21, 1400–1416, doi:10.1175/1520-0426(2004)021<1400:AOAIFS>2.0.CO;2, 2004.

Brandes, E. A., Ikeda, K., Zhang, G., Schönhuber, M., and Rasmussen, R. M.: A statistical and physical description of hydrometeor distributions in Colorado snowstorms using a video disdrometer, J. Appl. Meteorol. Climatol., 46, 634–650, 2007.

Bringi, V. N. and Chandrasekar, V.: Polarimetric Doppler weather radar: principles and applications, Cambridge University Press, 2001.

Böhm, H. P.: A General Equation for the Terminal Fall Speed of Solid Hydrometeors, J. Atmos. Sci., 46, 2419–2427, doi:10.1175/1520-0469(1989)046<2419:AGEFTT>2.0.CO;2, 1989.

de Laat, D., de Oliveira, F., Fernando, M., and Vallentin, F.: Upper bounds for packings of spheres of several radii, Forum of Mathematics, Sigma, 2, e23 42 pp., doi:10.1017/fms.2014.24, 2014.

Dolan, B. and Rutledge, S. A.: A theory-based hydrometeor identification algorithm for X-band polarimetric radars, J. Atmos. Ocean. Tech., 26, 2071–2088, doi:10.1175/2009JTECHA1208.1, 2009.

Donev, A., Stillinger, F., Chaikin, P., and Torquato, S.: Unusually dense crystal packings of ellipsoids, Phys. Rev. Lett., 92, 255506, doi:10.1103/PhysRevLett.92.255506, 2004.

Garrett, T. J., Fallgatter, C., Shkurko, K., and Howlett, D.: Fall speed measurement and high-resolution multi-angle photography of hydrometeors in free fall, Atmos. Meas. Tech., 5, 2625–2633, doi:10.5194/amt-5-2625-2012, 2012.

Goldsmith, J., Ermold, B., and Eloranta, E.: High Spectral Resolution Lidar (HSRL), ARM Mobile Facility (TMP), University of Helsinki Research Station (SMEAR II), Hyytiälä, Finland, doi:10.5439/1025200, 2014.

Hanesch, M.: Fall velocity and shape of snowflakes, PhD thesis, Swiss Federal Institute of Technology, Zurich, 1999.

Heymsfield, A. and Westbrook, C.: Advances in the estimation of ice particle fall speeds using laboratory and field measurements, J. Atmos. Sci., 67, 2469–2482, 2010.

Heymsfield, A. J., Bansemer, A., Schmitt, C., Twohy, C., and Poellot, M. R.: Effective Ice Particle Densities Derived from Aircraft Data, J. Atmos. Sci., 61, 982–1003, doi:10.1175/1520-0469(2004)061<0982:EIPDDF>2.0.CO;2, 2004.

Heymsfield, A. J., Field, P., and Bansemer, A.: Exponential Size Distributions for Snow, J. Atmos. Sci., 65, 4017–4031, doi:10.1175/2008JAS2583.1, 2008.

Huang, G.-J., Bringi, V. N., Cifelli, R., Hudak, D., and Petersen, W. A.: A Methodology to Derive Radar Reflectivity–Liquid Equivalent Snow Rate Relations Using C-Band Radar and a 2D Video Disdrometer, J. Atmos. Ocean. Tech., 27, 637–651, doi:10.1175/2009JTECHA1284.1, 2010.

Huang, G.-J., Bringi, V., Moisseev, D., Petersen, W., Bliven, L., and Hudak, D.: Use of 2D-video disdrometer to derive mean density–size and Ze–SR relations: Four snow cases from the light precipitation validation experiment, Atmos. Res., 153, 34–48, doi:10.1016/j.atmosres.2014.07.013, 2015.

Iguchi, T., Matsui, T., Shi, J. J., Tao, W.-K., Khain, A. P., Hou, A., Cifelli, R., Heymsfield, A., and Tokay, A.: Numerical analysis using WRF-SBM for the cloud microphysical structures in the C3VP field campaign: Impacts of supercooled droplets and resultant riming on snow microphysics, J. Geophys. Res.-Atmos., 117, D23206, doi:10.1029/2012JD018101, 2012.

Illingworth, A. J. and Blackman, T. M.: The Need to Represent Raindrop Size Spectra as Normalized Gamma Distributions for the Interpretation of Polarization Radar Observations, J. Appl. Meteorol., 41, 286–297, doi:10.1175/1520-0450(2002)041<0286:TNTRRS>2.0.CO;2, 2002.

Khvorostyanov, V. I. and Curry, J. A.: Fall Velocities of Hydrometeors in the Atmosphere: Refinements to a Continuous Analytical Power Law, J. Atmos. Sci., 62, 4343–4357, doi:10.1175/JAS3622.1, 2005.

Kneifel, S., von Lerber, A., Tiira, J., Moisseev, D., Kollias, P., and Leinonen, J.: Observed relations between snowfall microphysics and triple-frequency radar measurements: TRIPLE-FREQUENCY SIGNATURES OF SNOWFALL, J. Geophys. Res.-Atmos., 120, 6034–6055, doi:10.1002/2015JD023156, 2015.

Korolev, A. and Isaac, G.: Roundness and aspect ratio of particles in ice clouds, J. Atmos. Sci., 60, 1795–1808, 2003.

Leinonen, J., Moisseev, D., Leskinen, M., and Petersen, W. A.: A Climatology of Disdrometer Measurements of Rainfall in Finland over Five Years with Implications for Global Radar Observations, J. Appl. Meteorol. Climatol., 51, 392–404, doi:10.1175/JAMC-D-11-056.1, 2012.

Lo, K. and Passarelli Jr., R.: The Growth of Snow in Winter Storms:. An Airborne Observational Study, J. Atmos. Sci., 39, 697–706, doi:10.1175/1520-0469(1982)039<0697:TGOSIW>2.0.CO;2, 1982.

Locatelli, J. D. and Hobbs, P. V.: Fall speeds and masses of solid precipitation particles, J. Geophys. Res., 79, 2185–2197, 1974.

Löffler-Mang, M. and Blahak, U.: Estimation of the equivalent radar reflectivity factor from measured snow size spectra, J. Appl. Meteor., 40, 843–849, doi:10.1175/1520-0450(2001)040<0843;EOTERR>2.0.CO;2, 2001.

Löffler-Mang, M. and Joss, J.: An optical disdrometer for measuring size and velocity of hydrometeors, J. Atmos. Ocean. Tech., 17, 130–139, doi:10.1175/1520-0426(2000)017<0130;AODFMS>2.0.CO;2, 2000.

Magono, C. and Nakamura, T.: Aerodynamic Studies of Falling Snowflakes, J. Meteorol. Soc. Jpn. Ser. II, 43, 139–147, 1965.

Matrosov, S., Reinking, R., and Djalalova, I.: Inferring fall attitudes of pristine dendritic crystals from polarimetric radar data, J. Atmos. Sci., 62, 241–250, doi:10.1175/JAS-3356.1, 2005a.

Matrosov, S. Y.: Variability of Microphysical Parameters in High-Altitude Ice Clouds: Results of the Remote Sensing Method, J. Appl. Meteor., 36, 633–648, doi:10.1175/1520-0450-36.6.633, 1997.

Matrosov, S. Y.: Modeling Backscatter Properties of Snowfall at Millimeter Wavelengths, J. Atmos. Sci., 64, 1727–1736, doi:10.1175/JAS3904.1, 2007.

Matrosov, S. Y., Heymsfield, A. J., and Wang, Z.: Dual-frequency radar ratio of nonspherical atmospheric hydrometeors, Geophys. Res. Lett., 32, L13816, doi:10.1029/2005GL023210, l13816, 2005b.

Matrosov, S. Y., Campbell, C., Kingsmill, D., and Sukovich, E.: Assessing snowfall rates from X-band radar reflectivity measurements, J. Atmos. Ocean. Tech., 26, 2324–2339, 2009.

Mitchell, D. L.: Use of Mass- and Area-Dimensional Power Laws for Determining Precipitation Particle Terminal Velocities, J. Atmos. Sci., 53, 1710–1723, doi:10.1175/1520-0469(1996)053<1710:UOMAAD>2.0.CO;2, 1996.

Mitchell, D. L. and Heymsfield, A. J.: Refinements in the Treatment of Ice Particle Terminal Velocities, Highlighting Aggregates, J. Atmos. Sci., 62, 1637–1644, doi:10.1175/JAS3413.1, 2005.

Mitchell, D. L., Zhang, R., and Pitter, R. L.: Mass-Dimensional Relationships for Ice Particles and the Influence of Riming on Snowfall Rates, J. Appl. Meteor., 29, 153–163, doi:10.1175/1520-0450(1990)029<0153:MDRFIP>2.0.CO;2, 1990.

Moisseev, D. N. and Chandrasekar, V.: Examination of the mu–Lambda Relation Suggested for Drop Size Distribution Parameters, J. Atmos. Ocean. Tech., 24, 847–855, doi:10.1175/JTECH2010.1, 2007.

Morrison, H. and Milbrandt, J. A.: Parameterization of Cloud Microphysics Based on the Prediction of Bulk Ice Particle Properties. Part I: Scheme Description and Idealized Tests, J. Atmos. Sci., 72, 287–311, doi:10.1175/JAS-D-14-0065.1, 2015.

Newman, A. J., Kucera, P. A., and Bliven, L. F.: Presenting the Snowflake Video Imager (SVI), J. Atmos. Ocean. Tech., 26, 167–179, doi:10.1175/2008JTECHA1148.1, 2009.

Petäjä, T., O'Connor, E. J., Moisseev, D., Sinclair, V. A., Manninen, A. J., Väänänen, R., von Lerber, A., Thornton, J. A., Nicoll, K., Petersen, W., Chandrasekar, V., Smith, J. N., Winkler, P. M., Krüger, O., Hakola, H., Timonen, H., Brus, D., Laurila, T., Asmi, E., Riekkola, M.-L., Mona, L., Massoli, P., Engelmann, R., Komppula, M., Wang, J., Kuang, C., Bäck, J., Virtanen, A., Levula, J., Ritsche, M., and Hickmon, N.: BAECC A field campaign to elucidate the impact of Biogenic Aerosols on Clouds and Climate, B. Am. Meteorol. Soc., doi:10.1175/BAMS-D-14-00199.1, online first, 2016.

Power, B. A., Summers, P. W., and D'Avignon, J.: Snow Crystal Forms and Riming Effects as Related to Snowfall Density and General Storm Conditions, J. Atmos. Sci., 21, 300–305, doi:10.1175/1520-0469(1964)021<0300:SCFARE>2.0.CO;2, 1964.

Pruppacher, H. and Klett, J.: Microphysics of Clouds and Precipitation, Atmospheric and Oceanographic Sciences Library, Springer Netherlands, https://books.google.fi/books?id=1mXN_qZ5sNUC, 1996.

Rasmussen, R., Baker, B., Kochendorfer, J., Meyers, T., Landolt, S., Fischer, A. P., Black, J., Thériault, J. M., Kucera, P., Gochis, D., Smith, C., Nitu, R., Hall, M., Ikeda, K., and Gutmann, E.: How Well Are We Measuring Snow: The NOAA/FAA/NCAR Winter Precipitation Test Bed, B. Am. Meteorol. Soc., 93, 811–829, doi:10.1175/BAMS-D-11-00052.1, 2012.

Schönhuber, M., Lammer, G., and Randeu, W. L.: One decade of imaging precipitation measurement by 2D-video-distrometer, Adv. Geosci., 10, 85–90, doi:10.5194/adgeo-10-85-2007, 2007.

Sekhon, R. S. and Srivastava, R. C.: Snow Size Spectra and Radar Reflectivity, J. Atmos. Sci., 27, 299–307, doi:10.1175/1520-0469(1970)027<0299:SSSARR>2.0.CO;2, 1970.

Silverman, B. W.: Density estimation for statistics and data analysis, vol. 26, CRC press, 1986.

Szyrmer, W. and Zawadzki, I.: Snow Studies. Part II: Average Relationship between Mass of Snowflakes and Their Terminal Fall Velocity, J. Atmos. Sci., 67, 3319–3335, doi:10.1175/2010JAS3390.1, 2010.

Testud, J., Oury, S., Black, R. A., Amayenc, P., and Dou, X.: The Concept of "Normalized" Distribution to Describe Raindrop Spectra: A Tool for Cloud Physics and Cloud Remote Sensing, J. Appl. Meteorol., 40, 1118–1140, doi:10.1175/1520-0450(2001)040<1118:TCONDT>2.0.CO;2, 2001.

Thompson, G., Field, P. R., Rasmussen, R. M., and Hall, W. D.: Explicit forecasts of winter precipitation using an improved bulk microphysics scheme, Part II: Implementation of a new snow parameterization, Mon. Weather Rev., 136, 5095–5115, doi:10.1175/2008MWR2387.1, 2008.

Tokay, A., Wolff, D. B., and Petersen, W. A.: Evaluation of the New Version of the Laser-Optical Disdrometer, OTT Parsivel2, J. Atmos. Ocean. Tech., 31, 1276–1288, doi:10.1175/JTECH-D-13-00174.1, 2014.

Tong, M. and Xue, M.: Simultaneous estimation of microphysical parameters and atmospheric state with simulated radar data and ensemble square root Kalman filter, Part I: Sensitivity analysis and parameter identifiability, Mon. Weather Rev., 136, 1630–1648, doi:10.1175/2007MWR2070.1, 2008.

Ulbrich, C. W. and Atlas, D.: Rainfall Microphysics and Radar Properties: Analysis Methods for Drop Size Spectra, J. Appl. Meteorol., 37, 912–923, doi:10.1175/1520-0450(1998)037<0912:RMARPA>2.0.CO;2, 1998.

Ware, E. C., Schultz, D. M., Brooks, H. E., Roebber, P. J., and Bruening, S. L.: Improving Snowfall Forecasting by Accounting for the Climatological Variability of Snow Density, Weather Forecast., 21, 94–103, doi:10.1175/WAF903.1, 2006.

Wood, N. B., L'Ecuyer, T. S., Bliven, F. L., and Stephens, G. L.: Characterization of video disdrometer uncertainties and impacts on estimates of snowfall rate and radar reflectivity, Atmos. Meas. Tech., 6, 3635–3648, doi:10.5194/amt-6-3635-2013, 2013.

Woods, C. P., Stoelinga, M. T., and Locatelli, J. D.: The IMPROVE-1 Storm of 1–2 February 2001, Part III: Sensitivity of a Mesoscale Model Simulation to the Representation of Snow Particle Types and Testing of a Bulk Microphysical Scheme with Snow Habit Prediction, J. Atmos. Sci., 64, 3927–3948, doi:10.1175/2007JAS2239.1, 2007.

Zhang, G., Luchs, S., Ryzhkov, A., Xue, M., Ryzhkova, L., and Cao, Q.: Winter precipitation microphysics characterized by polarimetric radar and video disdrometer observations in central Oklahoma, J. Appl. Meteorol. Climatol., 50, 1558–1570, doi:10.1175/2011JAMC2343.1, 2011.

Paper II

AGU PUBLICATIONS

JGR

Journal of Geophysical Research: Atmospheres

RESEARCH ARTICLE

10.1002/2015JD023156

Observed relations between snowfall microphysics and triple-frequency radar measurements

Stefan Kneifel[1], **Annakaisa von Lerber**[2], **Jussi Tiira**[3], **Dmitri Moisseev**[2,3], **Pavlos Kollias**[1], **and Jussi Leinonen**[4]

[1]Department of Atmospheric and Oceanic Sciences, McGill University, Montreal, Quebec, Canada, [2]Finnish Meteorological Institute, Helsinki, Finland, [3]Department of Physics, University of Helsinki, Helsinki, Finland, [4]Jet Propulsion Laboratory, California Institute of Technology, Pasadena, California, USA

Key Points:

- Triple-frequency radar compared to ground-based in situ snowfall measurements
- Strong relation between PSD/snowfall density and triple-frequency signatures
- Triple-frequency data also provide a very sensitive measure for riming

Correspondence to:
S. Kneifel,
skneifel@meteo.uni-koeln.de

Citation:
Kneifel, S., A. von Lerber, J. Tiira, D. Moisseev, P. Kollias, and J. Leinonen (2015), Observed relations between snowfall microphysics and triple-frequency radar measurements, *J. Geophys. Res. Atmos.*, *120*, 6034–6055, doi:10.1002/2015JD023156.

Received 23 JAN 2015
Accepted 20 MAY 2015
Accepted article online 26 MAY 2015
Published online 19 Jun 2015

Abstract Recently published studies of triple-frequency radar observations of snowfall have demonstrated that naturally occurring snowflakes exhibit scattering signatures that are in some cases consistent with spheroidal particle models and in others can only be explained by complex aggregates. Until recently, no in situ observations have been available to investigate links between microphysical snowfall properties and their scattering properties. In this study, we investigate for the first time relations between collocated ground-based triple-frequency observations with in situ measurements of snowfall at the ground. The three analyzed snowfall cases obtained during a recent field campaign in Finland cover light to moderate snowfall rates with transitions from heavily rimed snow to open-structured, low-density snowflakes. The observed triple-frequency signatures agree well with the previously published findings from airborne radar observations. A rich spatiotemporal structure of triple-frequency observations throughout the cloud is observed during the three cases, which often seems to be related to riming and aggregation zones within the cloud. The comparison of triple-frequency signatures from the lowest altitudes with the ground-based in situ measurements reveals that in the presence of large (>5 mm) snow aggregates, a bending away in the triple-frequency space from the curve of classical spheroid scattering models is always observed. Rimed particles appear along an almost horizontal line in the triple-frequency space, which was not observed before. Overall, the three case studies indicate a close connection of triple-frequency signatures and snow particle structure, bulk snowfall density, and characteristic size of the particle size distribution.

1. Introduction

Multifrequency measurements using millimeter-wavelength radars have been found to considerably improve retrievals of snowfall properties compared to single-frequency applications [e.g., *Matrosov*, 1998; *Hogan et al.*, 2000; *Matrosov et al.*, 2005]. These techniques are based on the fact that the effective radar reflectivity factor *Ze* (hereafter called reflectivity) from an ensemble of snow particles is a function of the characteristic size of the particle size distribution (PSD). A common measure of the characteristic size of the PSD is the median volume diameter D_0 defined as the diameter which partitions the PSD into two equal volume parts. However, the relation between *Ze* and D_0 will be different for different frequencies if non-Rayleigh scattering effects become relevant. *Matrosov* [1992] showed that one can derive D_0 using one radar wavelength in or close to the Rayleigh region (e.g., S or X band) and a second one which is sufficiently affected by non-Rayleigh scattering (e.g., Ka or W band).

Scattering simulations using spheroid particle models in combination with effective medium approximations, for example, the Maxwell-Garnett mixing rule [*Matrosov*, 1992, 1998], predict that the difference of the logarithmic *Ze* from two frequencies f_1 and f_2 (hereafter called dual wavelength ratio, $\mathrm{DWR}_{f_1,f_2} = Ze_{f_1} - Ze_{f_2}$) is not sensitive to snow density but only weakly dependent on the particle's aspect ratio. *Hogan et al.* [2012] confirmed that oblate spheroids can consistently represent scattering properties observed at 3 and 94 GHz and are also able to reproduce observed polarimetric signatures of nonprecipitating ice clouds.

Leinonen et al. [2011] extended the DWR methodology and demonstrated that if spheroid particle models are assumed to be correct, observations at two frequencies (e.g., C and W bands) can be used to compute reflectivity at a third frequency (for example, at Ka band). Studies of scattering properties of complex

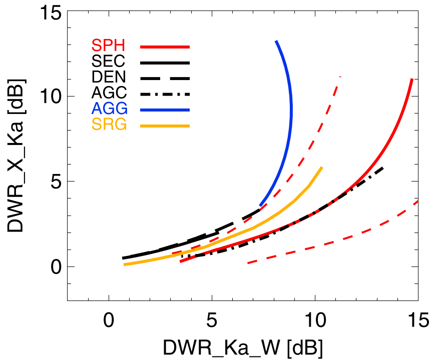

Figure 1. Exemplary simulated DWR$_{Ka,W}$ and DWR$_{X,Ka}$ for a selection of recently published PSDs and scattering models for snow particles (for a more detailed discussion see section 1): Sector snowflakes (SEC, black solid line) and dendrites (DEN, black dashed line) up to 5 mm particle size from the *Liu* [2008] database and rosette aggregates (AGC, black dashed-dotted line) [*Nowell et al.*, 2013] up to 12 mm particle size and exponential PSDs as used in *Kneifel et al.* [2011]. Average of an ensemble of dendrite aggregate structures (AGG, blue solid line), averaged (spheroidal shapes (SPH), solid red line), and 5%/95% percentiles (dashed red lines) obtained from spheroidal shapes assuming a homogeneous mixture of ice and air with different PSDs, axis ratios, and canting angles, as described by *Leinonen et al.* [2012]. Self-similar Rayleigh-Gans approximation (SRG, yellow solid line) using the parameters given for aggregates of bullet rosettes and columns by *Hogan and Westbrook* [2014] and assuming aggregates up to 20 mm maximum size and exponential PSDs as in *Kneifel et al.* [2011].

aggregate particles by, e.g., *Petty and Huang* [2010], *Botta et al.* [2010, 2011], and *Tyynelä et al.* [2011] have revealed that simple spheroid models of ice particles may not be sufficient for linking microphysical properties of snowflakes and their scattering signatures and may result in errors up to the order of 20 dB in calculations of W band reflectivities. This was further confirmed by *Ori et al.* [2014] and *Nowell et al.* [2013]. In a comprehensive analysis, *Kneifel et al.* [2011] compared simulated DWRs (Ku, Ka, and W bands) obtained from different scattering models including realistically shaped ice particles and aggregates to the DWRs calculated with spheroid models. For small D_0 (below 2 mm for DWR$_{Ku,Ka}$ and smaller than 1.5 mm for DWR$_{Ka,W}$) the differences between the scattering models are small and agree well with the findings of the aforementioned observational studies. However, the particle habit cannot be neglected for larger D_0: A combination of DWRs using all three frequencies (e.g., by plotting DWR$_{Ku,Ka}$ against DWR$_{Ka,W}$) revealed a separation especially between the aggregate models and the spheroid models. The DWRs from dendrite and needle aggregates which were based on scattering computations from *Petty and Huang* [2010] revealed a characteristic “hook” or “comma” shape in the triple-frequency space similar to the example shown in Figure 1. The typical hook feature in the triple-frequency space was also found by *Leinonen et al.* [2012], *Tyynelä and Chandrasekar* [2014], and *Leinonen and Moisseev* [2015] for snow aggregates composed of a variety of different primary crystal habits including needles, rosettes, hexagonal plates, dendrites, and fern-like dendrites. *Leinonen and Moisseev* [2015] analyzed in a comprehensive scattering modeling study the influence of habit and size of the primary crystal composing the aggregate on the triple-frequency signature: While the influence of the primary crystal habit is almost negligible, the primary crystal size influences the lowest DWR$_{Ka,W}$ value where the aggregates start to bend away from the spheroidal models. This might also partly explain the larger spread between the different aggregate types in the triple-frequency space found in *Kneifel et al.* [2011]: In order to change the size of the aggregates, *Petty and Huang* [2010] simply scaled the dipole structures which resulted in an unrealistic large exponent of the mass-size relation and also a likely overestimation of the size of the primary particles for large aggregate sizes.

Tyynelä et al. [2013] have shown that scattering properties from realistically shaped snowflakes can be calculated using Rayleigh-Gans theory with an accuracy comparable to other uncertainties inherent to radar measurements. Based on this study, *Leinonen et al.* [2013] have shown that the backscattering property of a snowflake can be directly linked to the mass distribution within the snowflake. *Hogan and Westbrook* [2014] have further developed this methodology and presented a simple analytic solution based on self-similarity of snowflakes. In contrast to the complex mass distribution found for snow aggregates, a homogeneous mixture of ice and air is usually assumed in “soft” spheroid approximations. This difference might partly explain the discrepancy between aggregate and spheroidal scattering models.

The first experimental proof of the existence of aggregate-like and spheroid-like triple-frequency signatures was recently found by *Leinonen et al.* [2012] and *Kulie et al.* [2014]. Despite the significant spatial averaging needed to correct, e.g., for radar beam width differences, these airborne observations confirm that at least two distinct scattering regimes in the triple-frequency space exist. Nevertheless, the lack of in situ observations has limited so far our ability to map the triple-frequency space to real snowfall properties.

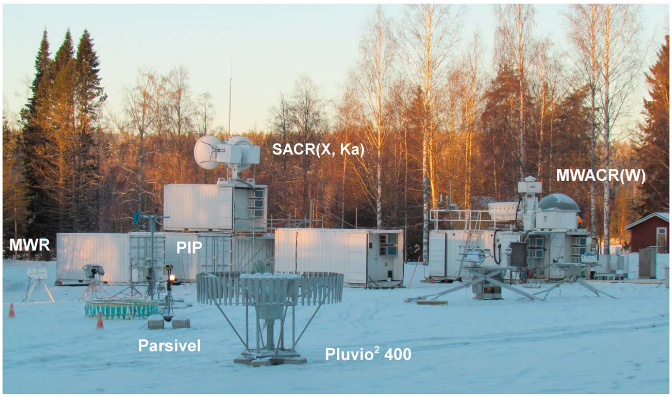

Figure 2. Part of the measurement site with in situ and remote sensing instruments deployed during the BAECC campaign 2014 at Hyytiälä, Finland. All radars (SACRs and MWACR) are mounted on top of the containers; the microwave radiometers (MWR) were installed close to the radars. On the field are the PIP video imager with its bright halogen lamp, the Parsivel 1-D disdrometer, and the Pluvio^2 weighing gauge. Other surface instruments are placed inside a wind fence (DFIR) about 30 m to the left from the containers (not shown).

In order to understand better the relation between physical snowfall properties and triple-frequency radar signatures, we analyze three case studies from collocated ground-based X, Ka, and W band zenith-pointing radar observations together with a comprehensive data set of in situ observations from the ground.

2. Data, Instruments, and Methods

The data used in this study were collected during the Biogenic Aerosols Effects on Clouds and Climate (BAECC) field campaign that took place at the University of Helsinki Hyytiälä Forestry Field Station, Finland (61°50′37.114′′N, 24°17′15.709′′E, 150 m above mean sea level). BAECC was organized in collaboration between the University of Helsinki, the Finnish Meteorological Institute, and the United States Department of Energy Atmospheric Radiation Measurement (ARM) program, which deployed the second Mobile Facility (AMF2) from 1 February to 12 September 2014. Between 1 February and 30 April 2014, an intensive observation period (IOP) was organized in collaboration with the National Aeronautics and Space Administration (NASA) Global Precipitation Measurement (GPM) ground validation program and Colorado State University focusing on winter precipitation; in total, 20 snowfall events were recorded during the IOP. The AMF2 and a part of the in situ precipitation sensors are shown in Figure 2.

The measurement field is a 60 by 70 m wide clearing surrounded by trees. Most of the precipitation instruments were located in the middle of the field at about 20 m distance from the nearest trees. The trees act as the first wind shield and make the site favorable for snow measurements. To achieve the best possible quality of snow measurements, a custom-designed Double-Fence Intercomparison Reference (DFIR) wind protection [*Rasmussen et al.*, 2012] was built at the site. The ground-based precipitation data set includes PSDs, terminal fall velocities, and particle shapes measured with 1-D and 2-D optical disdrometers and a 2-D imaging video camera. Furthermore, the liquid equivalent precipitation rate, total accumulation, and snow depth were measured. Wind conditions were obtained with 2-D and 3-D anemometers at the heights of the in situ instruments both inside the wind fence and on the measurement field.

The remote sensing instruments were collocated with the precipitation measurement equipment as can be seen in Figure 2. All ARM radars were mounted on top of containers; the ARM microwave radiometers (MWR) were installed on the field between the surface observations instruments and the radar containers. The atmospheric state was derived from radio soundings (RS) launched 4 times a day.

2.1. Cloud Radars

For this analysis we are using data from the scanning dual-frequency ARM cloud radar system (X/KaSACR) and from the Marine W band ARM cloud radar (MWACR). All radar observations used in this study were collected during zenith-pointing operations. For optimal volume matching, the radar beams need to be

Table 1. Technical Specifications and Settings of the AMF2 Cloud Radar Systems

Specifications	XSACR	KaSACR	MWACR
Frequency (GHz)	9.7	35.3	95.0
3 dB beam width (°)	1.27	0.33	0.38
Sensitivity at 1 km (dBZ)[a]	−30	−50	−50
Range gate spacing (m)	25	25	30
Nyquist velocity (m s^{-1})	5.9	6.1	6.0
Temporal sampling (s)	2	2	2

[a] Sensitivity for 2 s integration time and for nominal ARM radar settings.

properly aligned. The beam alignment can be assumed to be best for the X/KaSACR system for which both antennas are mounted on the same pedestal. The X/KaSACR performed alternating scans and zenith-pointing observations; the MWACR was continuously zenith pointing during the campaign. The MWACR system has been mounted on a different container in approximately 17 m distance from the X/KaSACR (Figure 2). All radars have been carefully aligned to zenith direction during installation of the AMF2 at the site.

The temporal and range resolution of the three radar systems has also been closely matched; differences between the center range gates are less then 16 m (Table 1). The half-power beam width of the MWACR and KaSACR are similar while the XSACR beam width is 3 to 4 times larger due to antenna size limitations required to allow scanning together with the KaSACR. In order to account for the slightly different center range gates and radar volumes, the radar observations are low-pass filtered using a boxcar averaging window over two range gates. Further, the data from KaSACR and MWACR have been averaged over three temporal sampling intervals (approximately 6 s) to compensate for the larger XSACR beam width.

2.2. Offset and Attenuation Correction

Absolute calibrations of the radar systems have been performed at the beginning of the campaign with a corner reflector (Nitin Bharadwaj, ARM radar engineer, personal communication). This study is based on DWR measurements at two frequency pairs (X-Ka and Ka-W bands); thus, the relative calibration of the three ARM radar systems is important. Before we consider instrument specific differences due to absolute calibration or radome attenuation, we first analyze atmospheric attenuation effects mainly due to water vapor, liquid water, and absorption by frozen hydrometeors.

We derived the two-way attenuation profile due to water vapor by using the measurements from the closest RS and the water vapor absorption model by *Rosenkranz* [1998] which includes also recently proposed modification of the water vapor continuum absorption [*Turner et al.*, 2009] and the 22 GHz line width modification proposed by *Liljegren et al.* [2005]. Due to the relatively moist atmosphere (vertically integrated water vapor amounts were in the range of 10–13 kg m^{-2}), water vapor attenuation especially affects the W band with two-way attenuation within the lowest 5 km of up to 1 dB, while at Ka band the water vapor attenuates the signal by less than 0.2 dB; at X band water vapor attenuation is below 0.02 dB and thus can be neglected.

Attenuation due to supercooled liquid water (SLW) strongly increases with frequency but also depends slightly on temperature. Although there are still uncertainties in the correct modeling of the absorption index of SLW, two-way attenuation due to a liquid water path (LWP) of 500 g m^{-2} (as, for example, observed during the snowfall case on 16 February) are in the range of 5 dB/1 dB/0.09 dB at W/Ka/X band, respectively [e.g., *Kneifel et al.*, 2014]. The attenuation effect at X band is within the noise level of the XSACR, and thus, we only correct for SLW attenuation at W and Ka band. For this, we use the LWP derived from the collocated two-channel MWR [*Cadeddu et al.*, 2013]. Ideally, we would need to know the vertical distribution of SLW in order to accurately calculate the SLW attenuation profile. Lidar and airborne in situ observations indicate the SLW to be often concentrated in distinct layers within snow clouds rather than following a continuous (adiabatic) SLW profile [e.g., *Verlinde et al.*, 2013]. Unfortunately, the lidar data cannot be used in our cases due to complete signal attenuation close to the ground caused by intense snowfall and/or SLW close to the surface. Lacking better information about the vertical SLW distribution, we assume the LWP to be homogeneously distributed within the cloud. We estimate the SLW absorption coefficient with a recent absorption model provided by *Ellison* [2007] and use the temperature profile from the closest RS. Given the observed LWP values during our three cases, we estimate the uncertainty of a different SLW profile due to the temperature dependence of the liquid water absorption coefficient to be in the range of 0.2 dB for W band and 0.4 dB for Ka band.

Average snowfall attenuation coefficients have been measured by *Nemarich et al.* [1988] using a horizontal radar link to be 0.9 dB km^{-1} $(\mathrm{g/m}^3)^{-1}$ at W band. At Ka band, attenuation due to snowfall is in general 1 order of magnitude lower [e.g., *Matrosov*, 2007]. For our attenuation correction, we calculate the vertical profiles of ice water content (IWC) using the XSACR observations and applying the Ze-IWC relation $\mathrm{IWC} = 0.015 Ze^{0.44}$ derived by *Boudala et al.* [2006] based on in situ observations and X band reflectivity observations for temperatures larger than −15°C. The attenuation profile due to snowfall has then be obtained with the IWC profiles and the attenuation coefficient measured by *Nemarich et al.* [1988]. The path integrated W band attenuation values found for our three cases are in the order of 1 dB which is similar to the findings for dry snowfall reported in *Matrosov* [2007]. Thus, only W band reflectivities are corrected for attenuation due to snowfall.

The remaining offsets due to radome attenuation or absolute calibration differences are derived by comparing the radar measurements in regions close to cloud top where we can expect the ice hydrometeors to be mostly Rayleigh scatterers, and thus, their reflectivity factors should be frequency independent [*Hogan et al.*, 2000]. In order to exclude potentially aggregated particles (indicated, e.g., by increased *Ze* and DWR values), we therefore only consider reflectivities smaller than −5 dBZ and only from cloud regions above 4 km height where DWR signatures are generally found below 1 dB. The relative offsets are derived assuming the XSACR data as our reference. Due to its lowest frequency of the three radar system and frequent tilting of the antenna during scanning periods, we expect radome attenuation effects by accumulated snow or liquid water to be smallest. The remaining offsets derived separately for every case are below 1.5 dB for the KaSACR-XSACR comparison and less than 3 dB for MWACR-XSACR. We also analyzed the noise floor at range gates without cloud particles, which can be expected to vary due to emission by liquid water included in a wet snow layer accumulating on the radome; during all three cases and for all three radars, the noise floor indicated no significant changes.

2.3. In Situ Sensors

One of the core instruments used in this study is the Particle Imaging Package (PIP), which is the next generation version of the Snow Video Imager (SVI) [*Newman et al.*, 2009]. As in the previous version, the measurement unit of PIP includes a halogen lamp and a video system of lens and a charge-coupled device full-frame camera. The frame rate of PIP is 380 frames per second enabling measurements of particle fall velocities. The distance between the camera and the lamp is approximately 2 m, and the focal plane is 1.3 m from the end of the lens; therefore, the field of view is 64×48 mm at this distance resulting in a resolution of 0.1×0.1 mm for the gray scale images. PIP records particle diameter D which is defined as an equivalent diameter of a disk that has the same area as the shadow of the particle. Further, terminal fall velocity and other particle image properties are derived according to the SVI particle detection algorithm described in *Newman et al.* [2009]. The particles which are out of focus are excluded according to thresholds based on increased blurring and reduced contrast values. The estimated error in sizing due to this effect is 18% [*Newman et al.*, 2009]. PIP measurements are minimally affected by wind-induced errors due to the open structure of the instrument. The average wind speed during the three case periods at the height of the PIP measured with Gill anemometer were 1.3, 1.8, and 2.1 m s^{-1} for 7, 16, and 24 February 2014, respectively.

In addition to the optical disdrometers, two Pluvio^2 weighing gauges were part of the instrumentation: The Pluvio^2-200 with an area of the orifice $A_G = 200$ cm^2 and Tretyakov wind shield were placed inside the DFIR wind fence; the Pluvio^2 400 with an orifice $A_G = 400$ cm^2 and a combination of Tretyakov and Alter wind shields were installed on the measurement field outside the DFIR fence. The differences of snowfall rate or snowfall accumulation measured with the two gauges are found to be on average smaller than 10%. The factory-made filtered data output of bucket nonreal-time accumulation is utilized. This output is selected because of its higher accuracy, though the data output has a time delay of 5 min from the occurring precipitation event. Due to problems with the proper synchronization of the system time of the data acquisition computer for the Pluvio^{2}s, the time shift due to the nonreal-time output and the drifting system time was obtained by cross correlating the Pluvio^2 time series of precipitation rate with the values derived from PIP for each case.

Prior to calculations of the PSD parameters, the PSDs recorded by PIP are filtered to exclude spurious measurements of large particles. Also, particles smaller than 0.375 mm are ignored, since these measurements are deemed to be unreliable. PIP sorts the observed particles into 105 bins ranging from 0.125 to 26.125 mm.

The PSDs observed during the three cases are close to an exponential distribution, and the derived PSD parameters agree well with the measured PSDs from a Parsivel on the site [*Löffler-Mang and Joss*, 2000; *Löffler-Mang and Blahak*, 2001; *Battaglia et al.*, 2010]. Characteristic parameters of the PSD are derived every minute and are then averaged over 6 min periods. The averaging time is selected to be long enough for the accumulation measured with the Pluvio^{2}s to reach the sensitivity limit of >0.1 mm and short enough to capture the transitions of snowfall properties (e.g., changes in degree of riming). The median volume diameter D_0 and total particle concentration N_T are calculated based on the 6 min averages; the maximum diameter $D_{\max}$ is the largest area-equivalent diameter observed during the 6 min period. From the nonaveraged 6 min observations of terminal fall velocities v and D, fall velocity-diameter power law relations in the form $v(D) = aD^b$ are calculated. Prior to carrying out the nonlinear regression fit with Levenberg-Marquardt algorithm, a two-dimensional probability density distribution of velocity-diameter observations is calculated with the kernel density estimation method [*Silverman*, 1986]. The main reason for selecting this method is to provide a consistent approach of reducing impacts of limited observations of the larger particles and outliers that are present in velocity observations of particles of all sizes. To minimize the influence of outliers on the v-D fit, but also to utilize the most of the reliable observations, for each diameter bin, the velocity observations that fall within the half width from each side of the peak of the measured velocity density function are used for the regression. It should be noted that the half widths are calculated for each side of the distribution, therefore, allowing for nonsymmetrical density functions.

The observed PSDs, velocity-diameter relations, and snowfall accumulation measurements from the Pluvio^{2}s are combined to calculate bulk densities of the observed snowfall for the 6 min averaging periods. The bulk snowfall density ρ_b in kg m^{-3} can be determined from the liquid equivalent precipitation accumulation G_{PIP} in mm estimated with PIP as

$$G_{\mathrm{PIP}}(T) = 10^{-6}\frac{\pi}{6}\frac{\rho_b}{\rho_w}\int_T^{T+6\mathrm{min}}\int_{D_{\min}}^{D_{\max}} D^3 v\,(D,t)\,N\,(D,t)\,\mathrm{d}D\,\mathrm{d}t, \tag{1}$$

where diameter D, minimum $D_{\min}$, and maximum $D_{\max}$-resolved diameter are in mm, the observed time interval t is in s, the fall velocity relation $v(D,t)$ is in m s^{-1}, and the PSD averaged over t, $N(D,t)$ is in mm^{-1} m^{-3}.

The value for ρ_b is retrieved by comparing G_{PIP} to the accumulation G_G measured with an OTT Pluvio^2 gauge

$$G_G(T) = 10\frac{1}{\rho_w A_G}\int_T^{T+6\mathrm{min}} m(t)\mathrm{d}t, \tag{2}$$

with bucket mass change in observed time interval $m(t)$ in kg s^{-1} and density of water $\rho_w = 1000$ kg m^{-3}.

A correlation of the found velocity-size relation and bulk snowfall density is detected, which is in accordance with previous studies [e.g., *Locatelli and Hobbs*, 1974; *Barthazy and Schefold*, 2006; *Garrett and Yuter*, 2014]. During certain time periods, especially on 16 February (Figure 10) between 00:44 and 00:56 UTC, a bimodal distribution of particles with different velocity-size distributions is observed; in these cases the derived velocity-size relation and the bulk snowfall density represent the average of both particle populations.

2.4. Time Lag Between Lowest Radar Ranges and Surface Level

For analyzing the relation between triple-frequency signatures and in situ properties of snowfall, we use the lowest 200 m observed by the three radars (380–580 m). Depending on the horizontal advection speed, we expect a temporal lag between the snowfall signatures measured at the lowest range gates and the according in situ signatures measured at the surface. We estimated the time lag with three different methods which are similar in some parts to the methods described in *Wood et al.* [2014]: The theoretical X band time series of reflectivity close to the surface is calculated using the sixth moment of the observed PSD. The time lag is derived by finding the best cross correlation between calculated surface X band reflectivity and observed XSACR reflectivities at the middle of the 200 m thick layer (480 m). In the second method, the temporal shift of the observed X band reflectivity time series within the lowest 200 m is estimated by cross correlation of the *Ze* time series of subsequent altitudes; the vertical profile of the time lag is then extrapolated toward the surface. In the third method, we use the profile of horizontal wind from the nearest RS and the observed mean Doppler velocity (MDV) as average terminal velocity of the snowfall. We simulate the resulting fall streak pattern in the radar time-height observation space similar to *Hogan and Kew* [2005]; and assume the height of the generating level close to cloud top. The time lag is estimated by extending the simulated fall streak down to surface level assuming the MDVs below the lowest radar range to be equal to the observed values at 380 m.

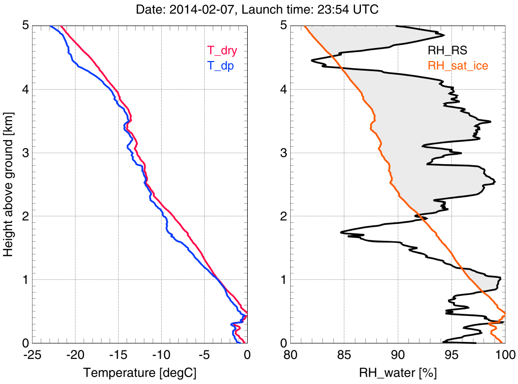

Figure 3. Vertical profiles of (left) air temperature (red), dew point (blue), and (right) relative humidity (black) from the radiosonde ascent launched at 23:54 UTC on 7 February 2014 in Hyytiälä. The red line in the right panel represents the relative humidity at which the air would be saturated with respect to ice; height layers with supersaturated conditions with respect to ice are shaded in light grey.

The time lag estimates obtained by the three methods differ by less than 0.5 min for the three analyzed cases. We shifted the averaging time window for the in situ data according to the average lag obtained by the three methods of 2.5, 3.8, and 1.0 min for 7, 16, and 21 February 2014, respectively (in all three cases the time shift is in the same direction, i.e., the snowfall signatures appear first in the lowest radar range gates and later in the in situ data).

3. Triple-Frequency Case Studies

In this section we present three snowfall case studies observed during February 2014 comprising different triple-frequency signatures, snowfall rates, and degrees of riming. A short description of the weather situation of each case will be followed by an analysis of the time-height 2-D structure observed by the triple-frequency radars. Finally, the in situ data collected at ground level are compared with triple-frequency signatures from the lowest radar range gates.

3.1. Case 1: 7 February 2014

3.1.1. Weather Situation and Radar Time-Height Structure

On 7 February 2014, a low pressure system over the Eastern Atlantic causes a southerly flow advecting relatively mild air (temperatures close to ground level between −5 and −0.5°C) over Hyytiälä. Between 12:00 and 20:30 UTC, only a thin mixed-phase cloud with cloud top at 2 km is present. At 20:30 UTC ice clouds from an approaching warm front are detected by the radars; the ice clouds steadily descend and finally merge with the underlying mixed phase cloud at 22:45 UTC.

We focus our analysis of triple-frequency signatures on the time period between 22:45 and 24:00 UTC, where a distinct snowfall band descends toward the ground. Temperatures at ground level are close to 0°C, increasing from −1°C at 22 UTC up to −0.3°C at 24 UTC. The vertical structure of temperature and relative humidity up to 5 km are shown from the closest RS at 23:54 UTC in Figure 3. The temperature profile reveals the first and strongest temperature inversion between 400 and 500 m above ground level (AGL) reaching largest values of 0.1°C. Due to the slightly positive temperature within this narrow layer, the ice and snow particles could experience slight melting. However, the vertical structure of *Ze* or MDV and also the time series of LWP does not show any significant enhancement that would be an indicator of melting (Figure 4). According to *Rasmussen and Pruppacher* [1982], it is quite likely that in this case the onset of melting is suppressed due to the slightly subsaturated (relative humidity only 96%) conditions at the level of 0.1°C. Therefore, we conclude that the snow particles are still unmelted while their sticking efficiency might be large due to the near 0°C temperatures, thus favoring formation of large aggregates [e.g., *Brandes et al.*, 2007].

The relative humidity profile is rather complex due to the merging of the two cloud systems. Based on the RS data, we also derived the relative humidity values that would be needed under the given temperature

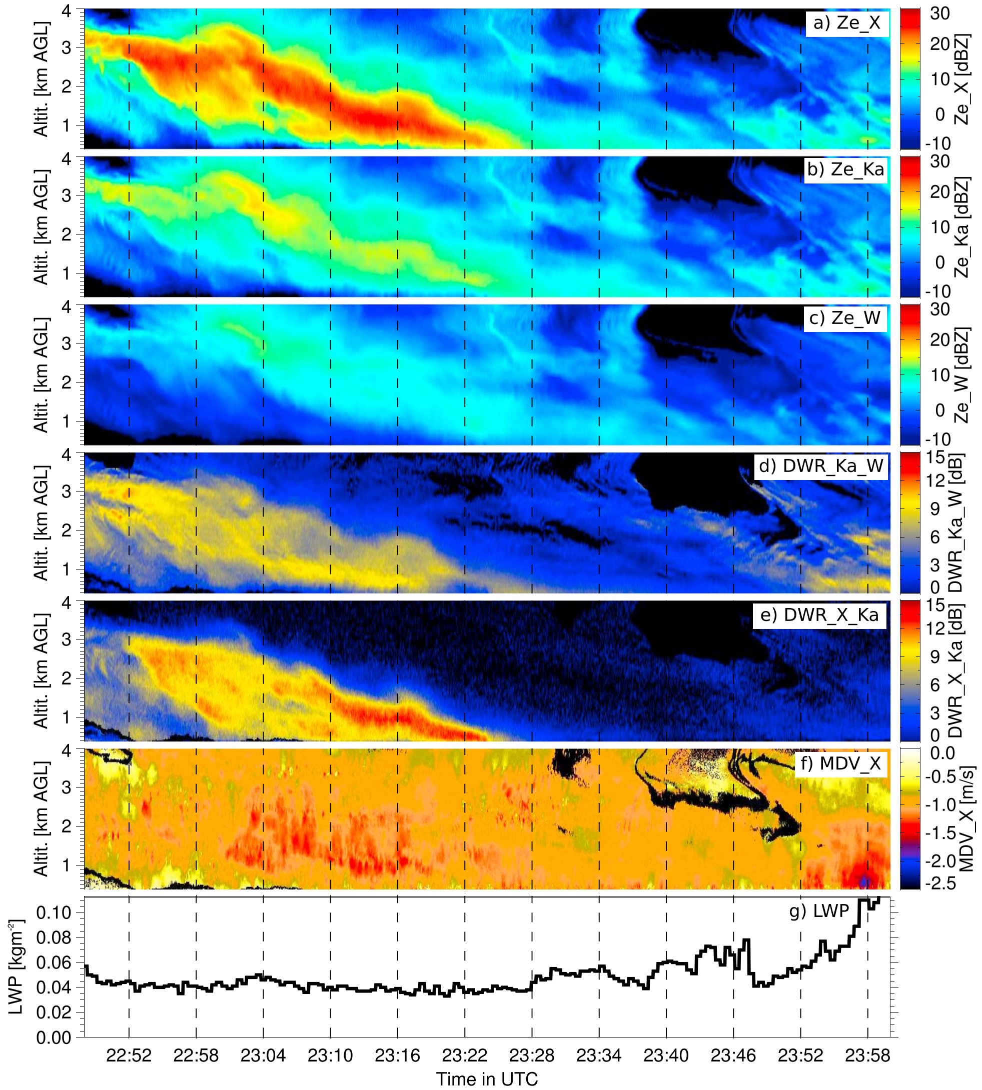

Figure 4. Radar and MWR observations from 7 February 2014 between 22:45 and 24:00 UTC. Radar reflectivities from vertically pointing (a) XSACR, (b) KaSACR, and (c) MWACR have been corrected for attenuation and calibration offsets (see more detailed description in the text). Time-height images of (d) $DWR_{Ka,W}$ and (e) $DWR_{X,Ka}$ have been derived from these corrected reflectivity fields. (f) Field of MDV from the XSACR. (g) Time series of LWP derived from the collocated two-channel MWR.

conditions to allow saturation with respect to ice. Combined with the ambient relative humidity profile, areas of saturated/subsaturated conditions with respect to ice favoring depositional growth or sublimation can be identified. Besides several areas close to liquid water saturation (e.g., 300 m and 1000 m AGL), we find a large layer saturated only with respect to ice (between 2.0 and 4.3 km) and distinct sub-saturated areas with respect to ice (e.g., between 1.2 and 2.0 km).

The most prominent structure visible in the time-height overview plots of radar reflectivities, DWRs, and MDV (Figure 4) is a band of high reflectivity starting at altitudes between 3 and 4 km steadily descending down to

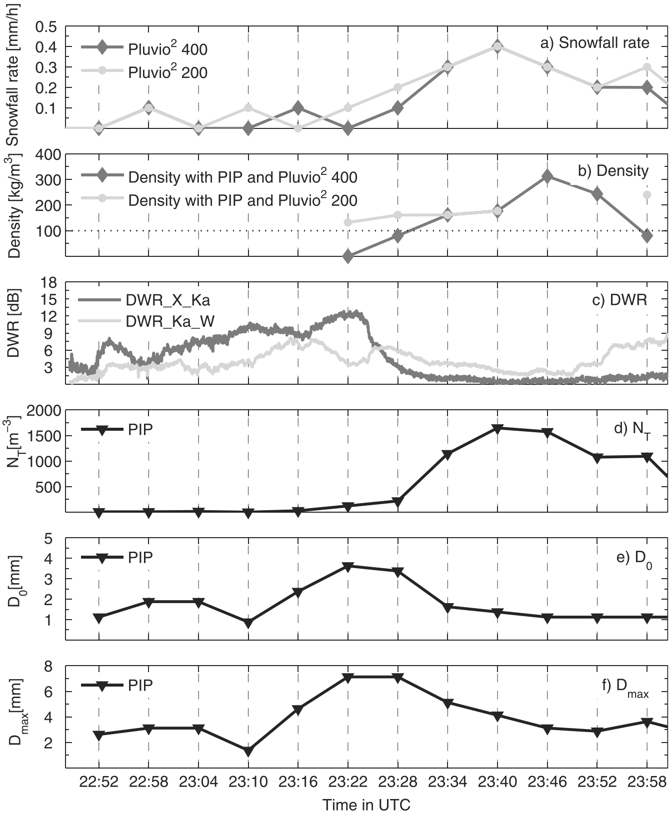

Figure 5. Time series of surface snowfall in situ observations derived from PIP and Pluvio^2 averaged over 6 min periods from 7 February 2014 between 22:45 and 24:00 UTC: (a) Liquid equivalent snowfall rate (mm $^{-1}$), (b) bulk snowfall density (kg m^{-3}), (c) dual-wavelength ratios (dB) averaged over the lowest 200 m radar ranges (380–580 m AGL), (d) total number concentration N_T (m^{-3}), (e) median volume diameter D_0 (mm), and (f) maximum particle diameter $D_{\max}$ (mm). Note that the time interval for the in situ averages has been shifted by the estimated time lag (see section 2.4) to be easier to compare with the radar observations.

ground. In the RS from 23:54 UTC (Figure 3) we find the temperature of the region where the snowfall band seems to form to be around −13 to −15°C. This temperature region together with high supersaturation is known to favor growth of dendritic ice particles, which are particularly effective at aggregating quickly due to their branched structure. The descending snowfall band causes significantly different reflectivities at the three radar frequencies: The maximum reflectivities at the center of the snowfall band are found at the X band, with maximum values of up to 25 dBZ, while the signal is weaker by up to 10 dB at the Ka band and by up to 14 dB at the W band. These strong differences can only be explained by non-Rayleigh scattering effects because after the intense snowfall band reaches the ground both $\mathrm{DWR}_{\mathrm{X,Ka}}$ and $\mathrm{DWR}_{\mathrm{Ka,W}}$ are close to 0 dB.

The observed MDVs are in the range of 0.8–1.4 m s^{-1}, which are typical terminal fall velocities of unrimed or only lightly rimed aggregates [*Barthazy and Schefold*, 2006]. Only at the end of the period do we find an increase of MDV up to 2 m s^{-1} within the lowest 1 km, coinciding with an increase of LWP up to 120 g m^{-2}. This signature is very likely connected to riming processes within this layer. Interestingly, this riming signature is slightly correlated with a significant increase of $\mathrm{DWR}_{\mathrm{Ka,W}}$ while the $\mathrm{DWR}_{\mathrm{X,Ka}}$ values remain below 3 dB.

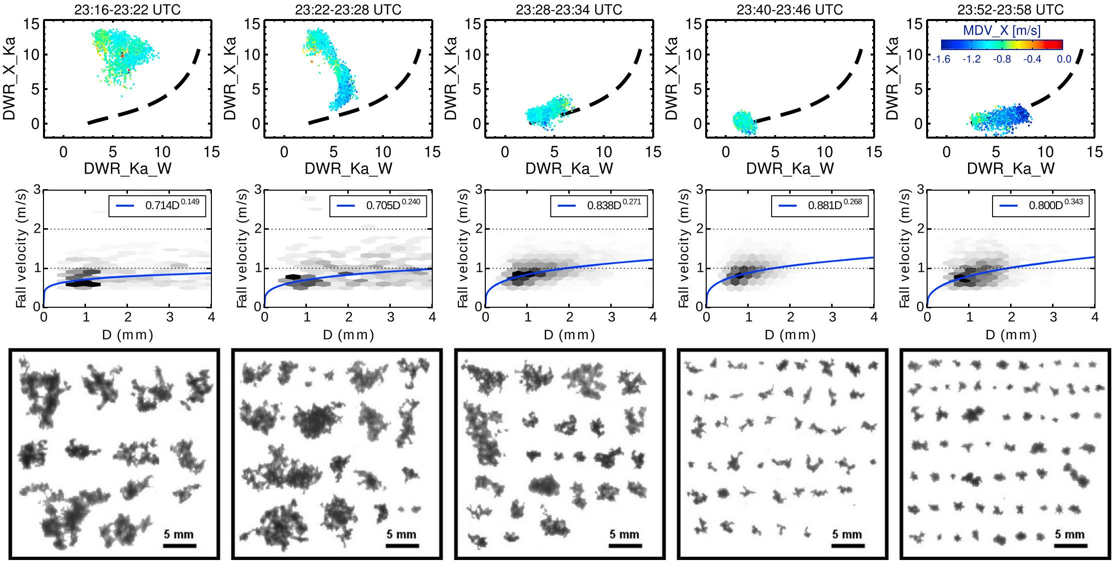

Figure 6. Comparison of low-level triple-frequency radar observations with surface measurements from the PIP for the case on 7 February 2014 shown in Figure 4: (top row) Plots of $\mathrm{DWR}_{\mathrm{Ka,W}}$ against $\mathrm{DWR}_{\mathrm{X,Ka}}$ for 6 min periods obtained from the lowest 200 m radar ranges (380–580 m AGL); the color scaling of every point indicates the MDV from the XSACR. All radar data have been restricted to observations with $Ze > -5$ dBZ in order to exclude potential DWR artifacts due to different radar sensitivities. The black dashed line indicates the average curve obtained from the spheroidal scattering model (same as the solid red curve in Figure 1). (middle row) Two-dimensional histograms of the PIP observed velocity-size relation together with the best power law fit to the distribution. (bottom row) Example images observed by the PIP during the 6 min time periods. Note that the time intervals for the in situ periods have been shifted by the estimated time lag (see section 2.4) to account for the altitude difference between the lowest radar gates and the surface level.

3.2. Comparison to Ground-Based In Situ Observations

The high-reflectivity band (Figure 4) approaches the lowest radar gates between 23:22 and 23:28 UTC. The in situ measurements (Figure 5) reveal during this time (note that the time of the in situ data have been shifted by the estimated time lag of 2.5 min between lowest range gates and surface level according to section 2.4) a low number concentration of large aggregates with D_0 and D_{max} of 3.5 mm and 7 mm, respectively. The low-bulk snowfall density and low concentration of snow particles result in only a light snowfall at the ground with less than 0.2 mm h^{-1} liquid equivalent snowfall rate. The actual maximum in snowfall rate of 0.4 mm h^{-1} is measured at the ground more than 10 min later at 23:40 UTC, concurrent with a higher number concentration (up to 1600 m^{-3}), decreasing D_0 (1 mm), smaller D_{max} (3.5 mm), and increasing bulk snow density (from 100 to 300 kg m^{-3}).

The triple-frequency data from the lowest 200 m layer (Figure 6) show also very different signatures before and after 23:28 UTC: During the time 23:16–23:28 UTC, we find very large $\mathrm{DWR}_{\mathrm{X,Ka}}$ values reaching up to 13 dB, while the $\mathrm{DWR}_{\mathrm{Ka,W}}$ values range between 3 and 10 dB. The observed signatures in the DWR space are quite similar to theoretical curves assuming aggregate scattering models (Figure 1), although some of the observations reveal an even stronger decrease of $\mathrm{DWR}_{\mathrm{Ka,W}}$ values than any of the aggregate models predict. It should be noted that the DWR values are independent of particle concentration and thus only dependent on D_0 and specific particle scattering behavior. The example PIP images (Figure 6, bottom) confirm the presence of large aggregates (sometimes up to 10 mm) with a very open or "fluffy" structure, i.e., an inhomogeneous and widespread distribution of ice within the particle's circumscribed volume. Due to the limited image resolution, it is, however, rather difficult to identify the primary particles that build the aggregates in this case.

After 23:28 UTC, both the triple-frequency signatures and in situ observations change considerably: While the total number concentration increases by a factor of eight accompanied by a steady increase of snowfall rate, D_0 and D_{max} drop to values below 2 mm and 5 mm, respectively. It is unlikely that the particles are strongly rimed considering that the LWP is still very small, and the terminal fall velocities seen by the PIP are

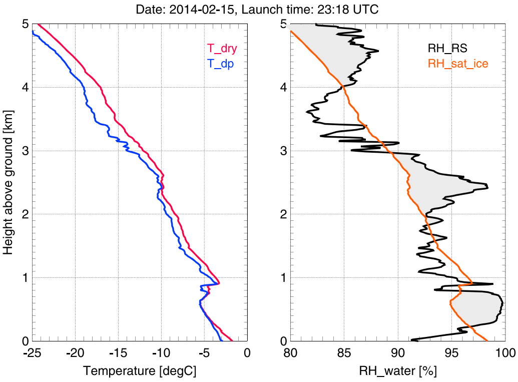

Figure 7. Same as Figure 3 but for the radio sounding on 15 February 2014, 23:18 UTC.

not significantly enhanced. In accordance with the decrease of particle sizes, the formerly very strong $\mathrm{DWR}_{\mathrm{X,Ka}}$ falls below 5 dB, while the $\mathrm{DWR}_{\mathrm{Ka,W}}$ values are found to range between 1 and 6 dB following closely the area predicted by scattering models of low-density particles with a homogenous ice-air mixture (soft spheroids). However, the PIP images only indicate a decrease of the overall aggregate size rather than a transition from open-structured aggregates to particles with more homogeneous ice-air mixture. In fact, in this area of low DWR values, different particle habits and their mixtures can produce very similar triple-frequency signatures [*Kneifel et al.*, 2011; *Leinonen et al.*, 2012; *Tyynelä and Chandrasekar*, 2014; *Leinonen and Moisseev*, 2015].

The DWR signatures almost completely disappear in the period between 23:35 and 23:50 UTC, while the total number concentration and snowfall rate reach their maximum within this period. The PIP images indicate the presence of small, open-structured aggregates rather than single crystals and small number of spherical, probably rimed particles. As expected, the DWR values seem to be independent on the increase in number concentration, while the decrease in both DWRs correlates well to the low D_0 and D_{max} values observed during this time.

After 23:50 UTC, $\mathrm{DWR}_{\mathrm{Ka,W}}$ increases up to 9 dB while $\mathrm{DWR}_{\mathrm{X,Ka}}$ remains below 3 dB. This increase in $\mathrm{DWR}_{\mathrm{Ka,W}}$ is well correlated with an increase in MDV up to 1.6 m s^{-1} (with larger MDV for larger $\mathrm{DWR}_{\mathrm{Ka,W}}$). At the same time the LWP increases by 60 g m^{-2}, and the slope of the velocity-size relation steepens which strongly indicates presence of rimed particles. Also, the PIP images indicate a change from small, open-structured aggregates to more compact, spheroidal habits.

3.3. Case 2: 16 February 2014

3.3.1. Weather Situation and Time-Height Structure

The atmospheric composition and cloud fields during the night of 15 to 16 February 2014 over Hyytiälä are influenced by a weakening low pressure system with its center at Northern Norway which moves further in northeasterly direction. A well-developed warm type occlusion associated with the cyclone moves from SW to NE, finally reaching the ground level at the SW corner of Finland at around 00 UTC on 16 February. Similar to 7 February case, a long-lasting thin mixed-phase cloud can be identified in the radar images of 15 February with its cloud top around 1 km AGL. At 12 UTC 15 February, first ice clouds at 6–8 km can be identified which continuously deepen with time, and finally at 21:15 UTC the ice particles fall into the lower mixed-phase cloud.

The RS from 23:18 UTC (Figure 7) shows the remaining cloud top temperature inversion and high relative humidity below 1 km associated with the former mixed-phase cloud layer. Most of the layers above 1 km are close to saturation with respect to ice but between 2 and 3 km, and also above 4 km the air is supersaturated with respect to ice. The temperature close to ground is only slightly lower compared to the 7 February case and varies between −0.7 and −1.2°C at our focus time between 00:00 and 01:00 UTC.

The radar observations (Figure 8) reveal a very complex precipitation pattern: When looking at the structure of the entire cloud (not shown), it seems the snowfall is initiated in cellular structures between 4 and 5 km.

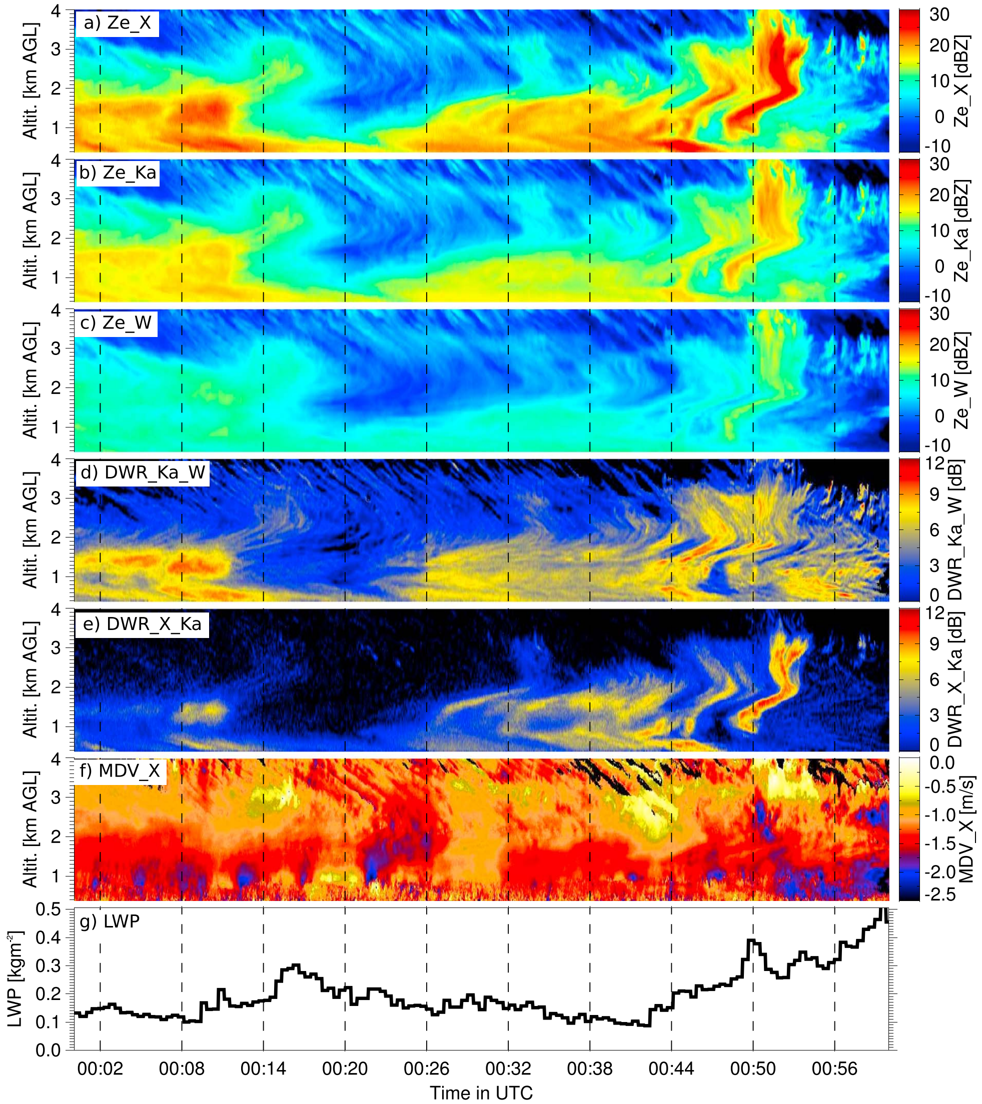

Figure 8. Same as Figure 4 but for 16 February 2014, 00:00–01:00 UTC.

The snow particles that fall out of these generating cells are advected by the horizontal wind which strongly varies with height. This variable wind shear leads to complex fall streak patterns with changing slopes in the time-height radar display (Figure 8). Generating cells and their corresponding fall streak structures is typical for snowfall clouds and have been observed since the early days of radar meteorology [e.g., *Marshall*, 1953; *Gunn and Marshall*, 1955]. The most prominent of these snowfall trails can be found around 00:50 UTC accompanied with a local peak in LWP and a maximum in reflectivity of 28 dBZ at the X band. It is plausible that the LWP increase is connected to a slight updraft, but the constant downward movement of the snow particles seen in the MDV indicates that the updraft must have been smaller than the typical average snowfall terminal velocity of 1 m s^{-1}.

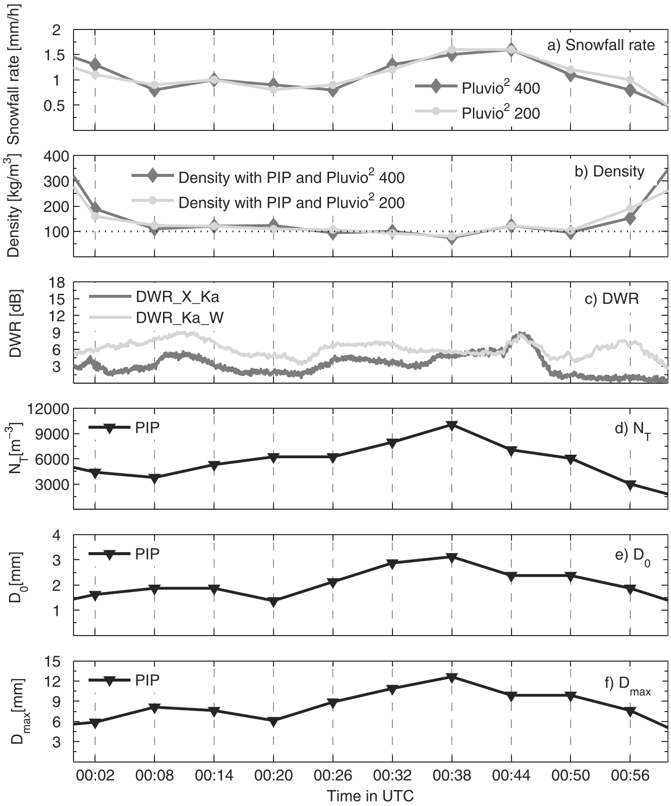

Figure 9. Same as Figure 5 but for 16 February 2014, 00:00–01:00 UTC.

The fall streak patterns appear also in the DWR fields: In the reflectivity differences of the two higher radar frequencies $\mathrm{DWR}_{\mathrm{Ka,W}}$, we find the fall streak structures starting just below the generating cells. This indicates that shortly after the particles are released from the generating cells, riming and/or aggregation processes must have taken place which were able to cause this differential scattering signatures between the W and Ka bands. Such rapid aggregation and riming processes connected to generating cell activity have also recently been observed with aircraft in situ probes and polarimetric radar observations [*Kumjian et al.*, 2014]. These fine fall streak structures starting at the generating cells cannot be observed in the $\mathrm{DWR}_{\mathrm{X,Ka}}$ (except the strong plume structures at the end of the period). The most significant increase in $\mathrm{DWR}_{\mathrm{X,Ka}}$, however, occurs in the lowest 2 km.

Detecting and evaluating the strength of riming is challenging in this case: The LWP ranges between 150 and 300 g m^{-2} during most of the hour. At the end of the period (00:42 until 01:00 UTC) the LWP increases up to 500 g m^{-2}. These LWP values are much higher than those observed for the 7 February case. The likelihood of riming can therefore be expected to be higher in this case which seems to be confirmed by the increase of MDV up to 2 m s^{-1} within the lowest 2 km after 00:42 UTC. However, the MDV during the entire hour reveals a rather complex pattern which seems to be connected to the overall reflectivity pattern only in certain areas. Clearly, microphysical processes like riming are superimposed over dynamical effects like the wave-like upward and downward motion detected in the MDV of the lowest 1 km during the first half of the focus period.

During the later period, when LWP further increases, we also note an increasing number of small, localized DWR maxima especially in the $\mathrm{DWR}_{\mathrm{Ka,W}}$ field. In some areas it seems like these maxima are related to the fall streak patterns where we can expect size sorting effects due to the wind shear and increased variability

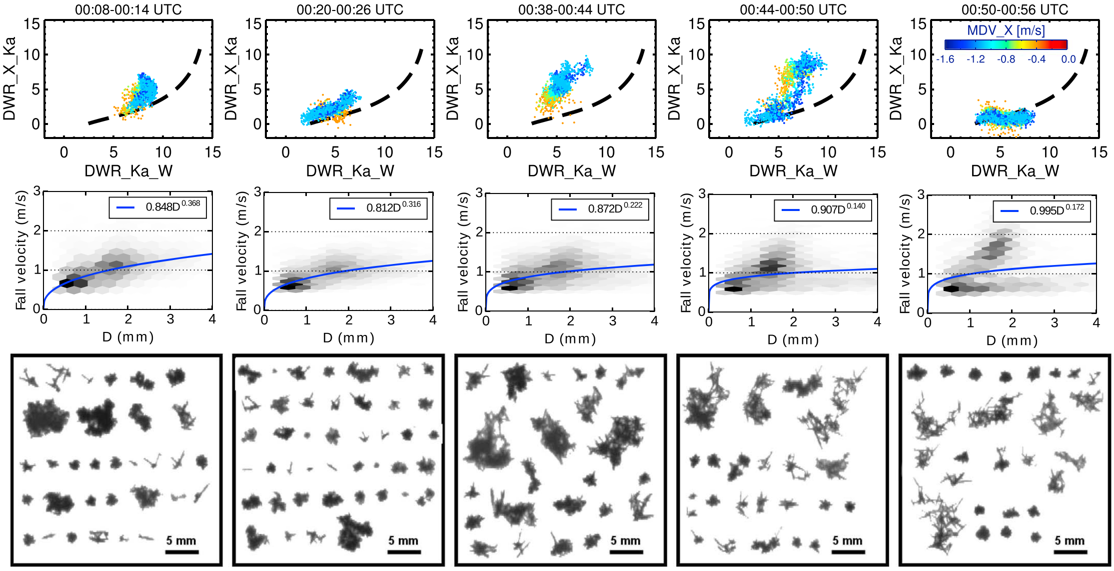

Figure 10. Same as Figure 6 but for 16 February 2014, 00:00–01:00 UTC.

in terminal fall velocities. This assumption is somewhat confirmed by the slightly different location of the maxima between $DWR_{X,Ka}$ and $DWR_{Ka,W}$ (for example, in the vicinity of the strongest plume-like structure around 00:50 UTC) which could be caused by size sorting of different particle populations within the fall streak which will then appear differently in the two DWRs.

3.4. Comparison to Ground-Based In Situ Observations

The observed snowfall rates at the surface (Figure 9) reach their maximum values of 1.6 mm h^{-1} during the second half of the focus period. During this second half also, D_0, D_{max}, and N_{tot} reach their maximum values of 3.4 mm, 12 mm, and 10^3 m^{-3}, respectively. The overall snow density, however, drops to a minimum value of 80 kg m^{-3} when the other parameters reach their peaks. This indicates that the period associated with the largest snowfall rate during this event was also composed of the “fluffiest,” i.e., least dense aggregates.

For the analysis of the relation between lowest radar range gate observations and in situ snowfall parameters, we again focus on five selected time periods were we find significant changes in the triple-frequency signatures (Figure 10). The time lag between the lowest radar range gates and ground level is estimated to be around 4 min.

The first time period between 00:08 and 00:14 UTC (Figure 10) is characterized by enhanced X/Ka-band reflectivity but low snowfall rate and only moderate values of $DWR_{X,Ka}$. As expected from the radar overview plot (Figure 8), we find the $DWR_{Ka,W}$ clearly enhanced up to 9 dB while $DWR_{X,Ka}$ ranges between 2 and 8 dB following mostly the average soft spheroid line; only a weak comma feature is found for the radar pixels with largest MDV (1.1–1.5 m s^{-1}) and largest $DWR_{Ka,W}$.

Visual analysis of the PIP images (Figure 10) reveals the presence of three major particle populations: Single needles (1–2 mm), small (1.5–2 mm) spherical aggregates, and a lower concentration of larger (> 2 mm) needle aggregates. This mixture of rimed particles, needles, and needle aggregates could be related to ice multiplication mechanism like rime splintering (Hallett-Mossop) process [*Hallett and Mossop*, 1974] in the layer below 800 m altitude: high values of relative humidity close to water saturation (Figure 7) might have favored the existence of SLW, and the temperatures are close to −5°C; these are both important condition for the Hallett-Mossop process to be effective. The measured histogram of particle velocity and diameter reveals at least two of these particle populations in different clusters of points. Despite the different particle populations, the velocity-size relation can be fitted surprisingly well using a single power law.

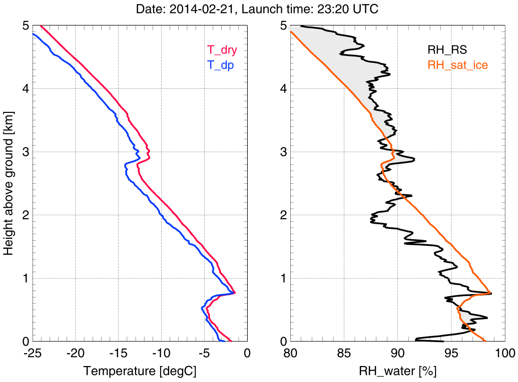

Figure 11. Same as Figure 3 but for the radio sounding on 21 February 2014, 23:20 UTC.

The DWRs during 00:20–00:26 UTC follow fairly well the curve predicted by the soft spheroids. It is also interesting that the radar pixels with MDV around 1 m s^{-1} are now almost equally distributed along the range of DWR values. The in situ time series (Figure 9) show that D_0 reaches its minimum values (1.7 mm) during this period. This might also explain why the DWR values are also very small: Only if all range gates within the 200 m layer during the 6 min are filled with similarly small particles with low differential scattering behavior can low DWR values be reached. In fact, when we split the radar data for this particular time period into shorter time periods, the DWR values are indeed be found to move along the line of the average spheroids reaching a minimum in both $\mathrm{DWR}_{\mathrm{X,Ka}}$ and $\mathrm{DWR}_{\mathrm{Ka,W}}$ at the time where the minimum in D_0 is observed at the ground.

The next time period we focus on is from 00:38 to 00:44 UTC: As mentioned before, during this period the maximum snowfall rate, particle concentration, and D_0 are reached while the bulk snowfall density is found to reach its minimum of 80 kg m^{-3}. Also the exponent of the power law fit for the velocity-size relation decreases from 0.32 to 0.22 which is likely to be connected to lower density particles. In accordance with the increase in D_0 and decrease in bulk snowfall density, the $\mathrm{DWR}_{\mathrm{X,Ka}}$ values increase to 10 dB, and the triple-frequency signatures bend away from the average spheroid line toward the area expected for aggregates. The PIP images show the presence of large needle aggregates of sometimes more compact and sometimes very open structure.

During the following time period (00:44 to 00:50 UTC), the overall aggregate signatures remain almost constant in the triple-frequency space. However, a new family of points with $\mathrm{DWR}_{\mathrm{X,Ka}}$ values below 3 dB, $\mathrm{DWR}_{\mathrm{Ka,W}}$ up to 6 dB but with MDV between 0.9 and 1.6 m s^{-1} appears during this period. The velocity-size scatterplot shows indeed evidence for a new, separated population of rimed particles with clearly enhanced terminal velocities reaching 1.3–1.5 m s^{-1} with sizes of only 1.0 to 2.0 mm. Similar to the end of the 7 February case, there seems to be a close connection of the presence of riming and an increase of $\mathrm{DWR}_{\mathrm{Ka,W}}$ together with low $\mathrm{DWR}_{\mathrm{X,Ka}}$ values (<3 dB).

Only 6 min later (00:50–00:56 UTC), the number of large aggregates further decreases, while the number of increasingly rimed particles with sizes of 1.5 to 2.0 mm and terminal velocities up to 2 m s^{-1} increases. As a result of the increasing density of the small particle population, the velocity-size scatterplot becomes progressively bimodal. The reduction in the number of larger aggregates also reduces the $\mathrm{DWR}_{\mathrm{X,Ka}}$ values below 3 dB while the $\mathrm{DWR}_{\mathrm{Ka,W}}$ measurements are still found up to 9 dB. This almost horizontal curve in the triple-frequency space and the presence of rimed particles is similar to the last time period observed at the 7 February case (Figure 6).

3.5. Case 3: 21 February 2014

3.5.1. Weather Situation and Time-Height Structure

The weather situation on 21 February is characterized by a weakened cyclone located over northeastern Scandinavia and a warm-type occlusion moving in northeasterly direction over Hyytiälä. Similar to the other two cases, a thin mixed-phase cloud with cloud top at 1 km exists almost continuously during the day. At 5 UTC, thicker ice clouds can be seen in the radar images between 4 and 7 km, slowly descending and deepening before they merge with the low mixed-phase cloud at 16 UTC. In the RS from 23:20 UTC (Figure 11) the

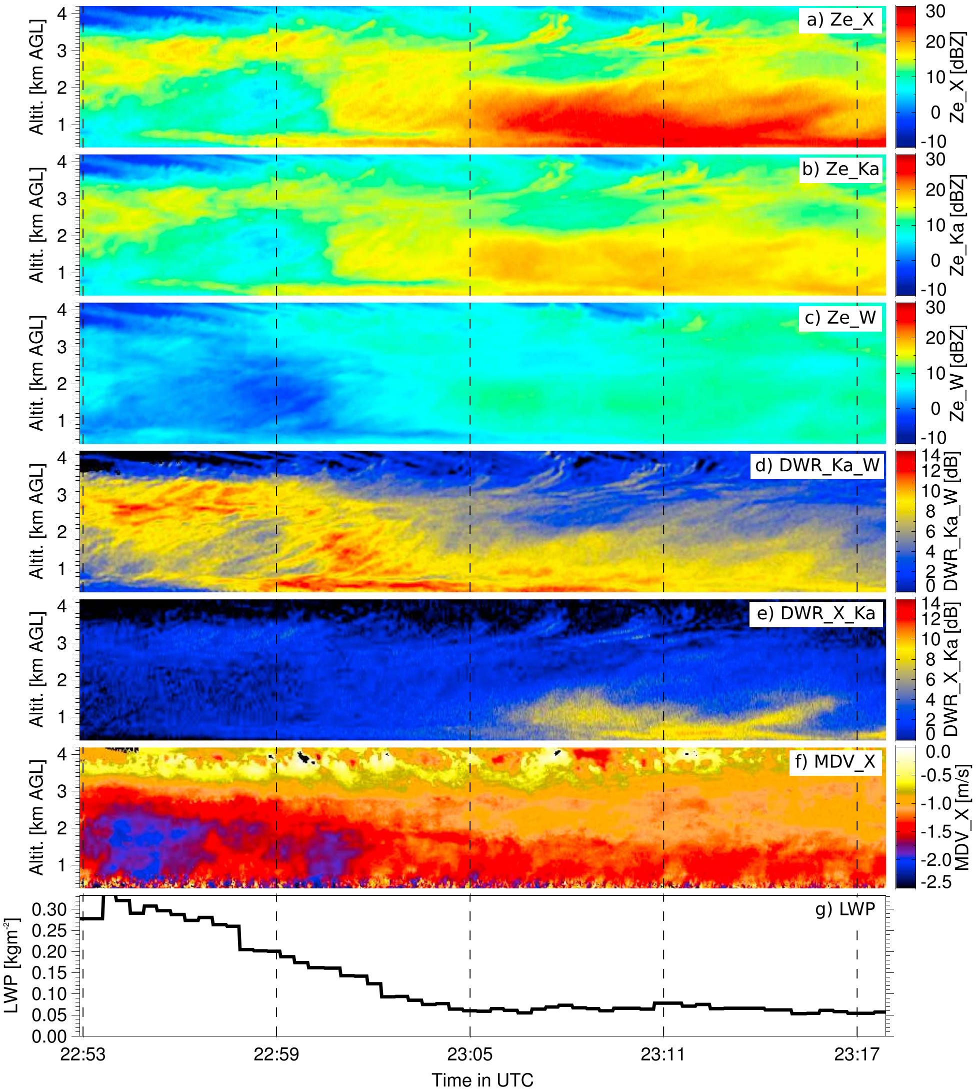

Figure 12. Same as Figure 4 but for 21 February 2014, 22:53–23:18 UTC.

signature of the mixed-phase cloud can still be detected in the temperature inversion at 800 m and the peak in relative humidity at the same height. A second temperature inversion together with a small peak in relative humidity is also visible at 2.9 km. The layer between 800 m and 2.3 km shows slightly subsaturated conditions with respect to ice in contrast to the ice supersaturated layer above. The temperatures close to surface during our focus time period were close to −2°C.

The selected focus time period from 22:53 to 23:18 UTC is shorter (25 min) compared to the other two cases because the X/KaSACR was frequently scanning during this day. In the radar reflectivity time-height image (Figure 12), the cloud appears to be relatively stratiform and only a few generating elements with their associated fall streaks can be found above 3 km. This case again exhibits significant signatures of riming and a

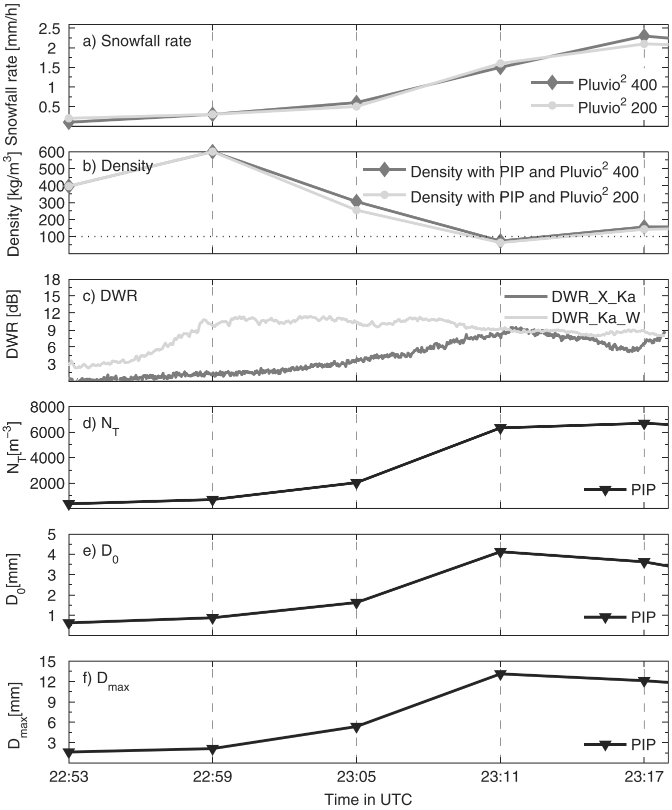

Figure 13. Same as Figure 5 but for 21 February 2014, 22:53–23:18 UTC.

transition from rimed small particles to aggregate snowfall: The enhanced MDV of up to 2.5 m s^{-1} corresponds well to the enhanced LWP (up to 350 g m^{-2}) during the first half of the focus period.

During the time period of enhanced MDV and LWP, we also find very large DWR$_{\mathrm{Ka,W}}$ values of up to 14 dB which are the largest values found in all three cases. In contrast, the DWR$_{\mathrm{X,Ka}}$ is found continually below 3 dB in most of these areas. The weak DWR$_{\mathrm{X,Ka}}$ signatures do, however, resemble the strong DWR$_{\mathrm{Ka,W}}$ structures. We expect a certain correlation of the two DWRs because they both generally increase with increasing D_0. It is thus likely that the strong DWR$_{\mathrm{Ka,W}}$ structures are not only a product of riming but also due to slightly increasing D_0.

After the LWP decreased to low values of 50 g m^{-2} (23:05 UTC), DWR$_{\mathrm{X,Ka}}$ increases in the lowest 2 km to 11 dB. The DWR$_{\mathrm{Ka,W}}$ values, on the other hand, continuously decrease especially above 2 km coinciding with a decline of MDV to values smaller than 1.5 m s^{-1}.

3.6. Comparison to Ground-based In Situ Observations

The in situ data (Figure 13) reveal a similar two-part separation of the snowfall event as found in the radar data: During the first half (before 23:05 UTC), the snowfall rate is relatively low (below 0.5 mm h^{-1}) and composed by a low concentration of small-sized ($D_{\mathrm{max}} < 3$ mm) particles with high density (estimated bulk snowfall density up to 600 kg m^{-3}). Although the density estimate has to be interpreted with care due to the low snowfall rate and particle concentration, the in situ data indicate the presence of heavily rimed particles with mostly spherical shape (Figure 14). A further confirmation of strong riming is the observed velocity-size relation during this time which resembles well those found for lump graupel [e.g., *Barthazy and Schefold*, 2006].

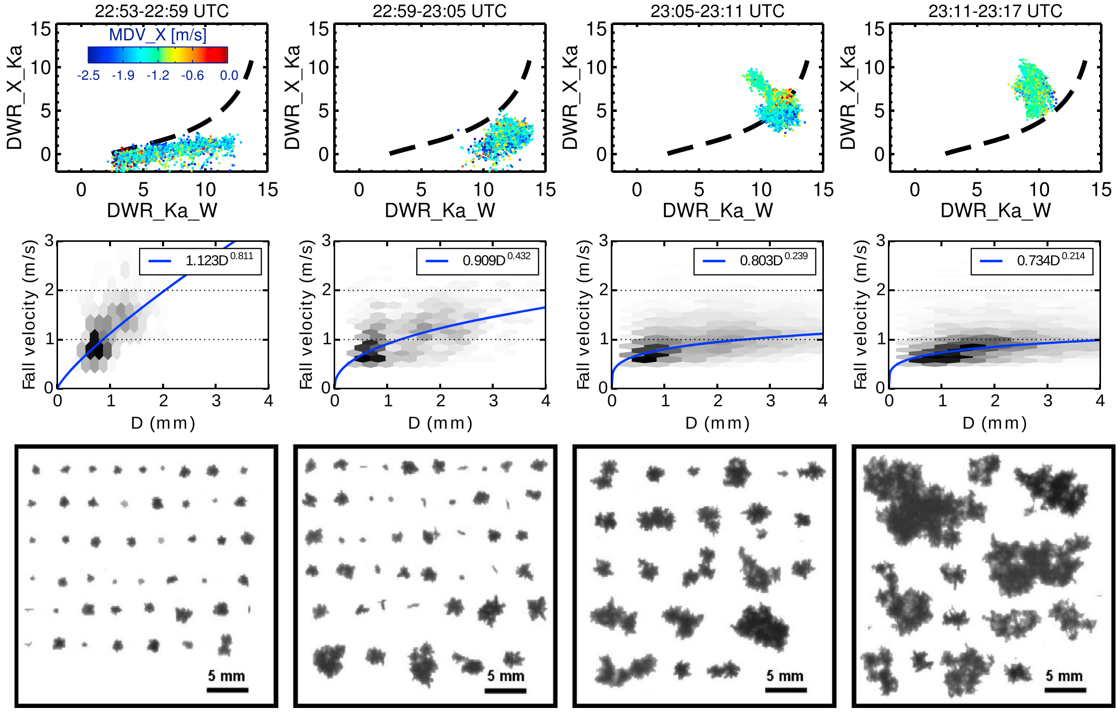

Figure 14. Same as Figure 6 but for 21 February 2014, 22:53–23:18 UTC.

The characteristics of the snowfall event are very different during the second period (23:05–23:18 UTC): The snowfall rate reaches its maximum of 2.2 mm h^{-1} around 23:17 UTC; this is the largest snowfall rate observed for all three cases. The peak in snowfall rate is connected to a strongly broadened PSD (D_0 up to 4.7 mm and $D_{max} > 12$ mm), increasing particle concentration, but also to a sharply decreased bulk snowfall density (90–150 kg m^{-3}).

This transition from light, graupel-like snowfall to moderate aggregate snowfall appears to be strongly correlated to changes in the triple-frequency space as can be seen in the temporal development of the low-level radar observations and in situ data (Figure 14): During the first 6 min (22:53–22:59 UTC), we find the $DWR_{Ka,W}$ values filling in the entire range between 2 and 12 dB; this means that the particle ensembles in the different low-level radar pixels must have been composed of very different realizations of D_0 and/or degree of riming. Visual analysis of the PIP images reveals the presence of mostly spherical particles mixed with a small number of columnar particles.

Only 6 min later (22:59–23:05 UTC), the velocity-size relation is significantly different (note the almost 50% smaller velocity-size exponent *b*) and aggregates with sizes up to 5 mm are found. The different PSD also changes the distribution in the triple-frequency space: The small $DWR_{Ka,W}$ values found in the previous period completely disappear and all $DWR_{Ka,W}$ values are now found between 8 and 14 dB. The $DWR_{X,Ka}$ slightly increased up to 5 dB which can be explained by the increasing D_0.

The increase of size and number of aggregates further intensifies during the following 6 min (23:05–23:11 UTC). During this time period, the maximum in X band reflectivity, $DWR_{X,Ka}$, D_0, and D_{max} are also reached. Unlike for 16 February, it is much more difficult in this case to identify the primary particles forming the aggregates. Although the aggregates' terminal velocities between 1 and 1.5 m s^{-1} are not strongly enhanced, they appear in the PIP images to be more dense compared to the former two cases. In the triple-wavelength space, the increasing number of large aggregates causes an increase of $DWR_{X,Ka}$ ranging

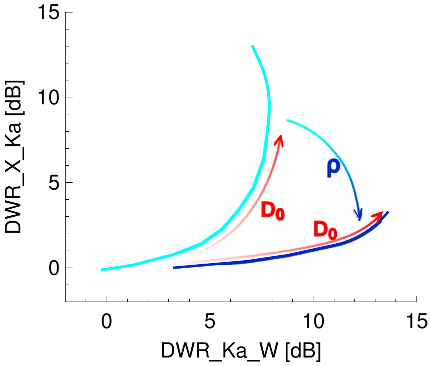

Figure 15. Schematic illustration of the effect of changes of PSD characteristic size D_0 and snow particle density ρ on triple-frequency signatures. The light blue and dark blue line represent the most extreme curves observed in this study for large, low-density aggregates (7 February) and heavily rimed particles (21 February), respectively.

now between 3 and 10 dB, while $\mathrm{DWR}_{\mathrm{Ka,W}}$ remains large similar to the previous time period. The data points appear to separate into two populations: One cloud of points is located around the average spheroid line and with most of the MDV being larger than 1.2 m s^{-1}. The second population bends away from the average spheroid line and shows MDV close to 1.2 m s^{-1}. An analysis of the DWR data from shorter time intervals reveals that the first population of spheroidal particles is associated with the first 3 min, while the bended cluster of points only appears during the second 3 min. Therefore, a fast transition of the snowfall from rimed, spheroidal particles to slower, aggregate-type scattering particles must have taken place during these 6 min.

During the last period (23:11–23:17 UTC), D_0 and also D_{max} of the aggregates remain almost constant while the exponent of the velocity-size relation further decreases. The extreme $\mathrm{DWR}_{\mathrm{Ka,W}}$ values disappear, and the triple-frequency data points bend further away from the average spheroid line; also, their MDV are now almost entirely below 1.2 m s^{-1} indicating a further transition from rimed to lower-density and aggregate-dominated snowfall. Although the increase in $\mathrm{DWR}_{\mathrm{X,Ka}}$ due to the broadened PSD (increase of D_0) is similar to the other two cases, the $\mathrm{DWR}_{\mathrm{Ka,W}}$ values between 8 and 12 dB are significantly larger than in the previous cases. Without being able to analyze the structure of the aggregates in more detail (e.g., investigating whether aggregates are composed of a mixture of heavily rimed particles and other unrimed aggregate components), it is difficult to fully explain the origin of these high $\mathrm{DWR}_{\mathrm{Ka,W}}$ values in this case.

4. Discussion and Conclusions

The long-term deployment of the AMF2 with its triple-frequency radar capabilities at the University of Helsinki Hyytiälä Forestry Field Station, Finland, combined with the availability of excellent in situ ground-based snow particle measurements, provided an unprecedented snowfall data set. The potential of this data set for snow studies is illustrated here using three events that cover light to moderate snowfall rates from 0.2 to 2.2 mm h^{-1} capturing a wide range of snow habits from low-density, open-structured aggregates to heavily rimed particles. All three snowfall cases were observed at a relatively narrow temperature range between −2 and 0°C close to ground.

The focus of this study was less on evaluating theoretical triple-frequency radar signatures but rather on connecting them to snow particle properties using the combination of remote-sensing and in situ observations. To this extend, the BAECC data set is a step forward compared to previous airborne data sets. The observed triple-frequency features found in this study clearly resemble the main triple-frequency features found in *Leinonen et al.* [2012] and *Kulie et al.* [2014]. The signatures from the current study are, however, more pronounced in terms of the magnitude of the triple-frequency signals, and they also appear to be less noisy, which can be explained by the smaller amount of averaging needed thanks to improved radar volume matching. A typical bending away from the average spheroid line was found to be connected to the presence of larger (>5 mm) aggregates in the in situ data. Besides the hook or comma feature associated with aggregates and the average spheroid region connected to compact, spheroidal aggregates, we were able to identify signatures of rimed particles. They appear in the triple-frequency space as nearly horizontal curves which were not observed before. These signatures agree well with scattering computations of graupel particles in *Tyynelä and Chandrasekar* [2014] using discrete dipole approximation. Also initial experiments with T matrix and different snow densities (not shown) revealed a tendency to a flatter curve with increasing density consistent to our observations. However, a more detailed analysis of the scattering signatures of increasingly rimed particles is

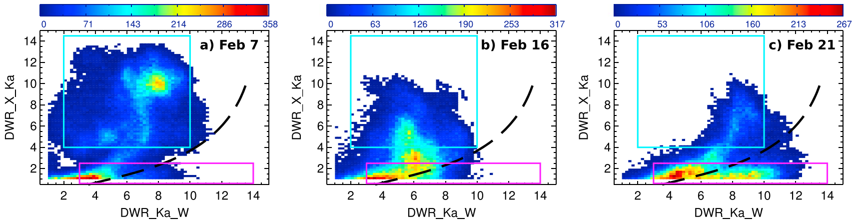

Figure 16. Two-dimensional histograms of triple-frequency signatures from all three cases including all heights below 4 km AGL. The color represents the absolute number of observations per pixel. The colored frames represent approximate areas in the triple-frequency space that were found to be related to the presence of large aggregates (light blue) or rimed particles (purple) in the surface in situ observations.

certainly needed to better understand the observed triple-frequency signatures and their relation to changes in shape and density.

As previously stated, the goal of this study is to remap part of the triple-frequency space to snowfall properties (e.g., density and characteristic size). While more observations and data analysis combined with scattering calculations are needed for a more comprehensive remap, a first attempt based on the data analyzed here is shown in (Figure 15). Considering the almost flat curve found for the largest bulk snowfall density at the beginning of the 21 February case (Figure 14) and the extreme bending of the low-density aggregates at the beginning of the 7 February case (Figure 6), we can conclude in a very schematic way that changes in snowfall density are recovered by a "rotation" in the triple-frequency space while the characteristic size is increasing along the specific particle curves (Figure 15).

Based on our comparison of the triple-frequency signatures close to the surface with in situ data, we believe that at least two basic hydrometeor regimes can be distinguished from triple-frequency observations (indicated by the colored boxes in Figure 16): A combination of $\mathrm{DWR}_{\mathrm{Ka,W}}$ values larger than 3 dB together with $\mathrm{DWR}_{\mathrm{X,Ka}}$ lower than 3 dB has been found to be connected to rimed particles. The region with $\mathrm{DWR}_{\mathrm{X,Ka}}$ values larger than 4 dB can be generally assigned to aggregates, while a combination with low $\mathrm{DWR}_{\mathrm{Ka,W}}$ indicates a decrease in aggregate density. The region with small DWR values at both frequency combinations reveals low values of D_0 (<2 mm). However, a distinction between single crystals, or rimed particles, seems not feasible based on the overlapping scattering properties in this region and limited radar sensitivity. It should be noted, however, that simulated DWR combinations including higher frequencies (e.g., 150 or 220 GHz) indicate a possible distinction of particle properties also in the low D_0 region [*Battaglia et al.*, 2014].

Therefore, the observations and recent scattering modeling studies suggest that triple-frequency observations bear the potential to derive two fundamental properties of snowfall microphysics: Bulk snowfall density and characteristic size of the PSD. These two important parameters can be potentially derived inside clouds even in regions were standard methods for identification of riming, e.g., using MDV, are infeasible due to large turbulence and intense vertical winds (e.g., within convective clouds).

A quantitative retrieval of these essential quantities from triple-frequency observations requires, however, a further increasing understanding of the overall connection of microphysical snowfall parameters to their scattering properties. Up to now, not only scattering approximations using effective medium theories (often called soft spheroid approximation) but also scattering computations using more realistic ice particles are unable to reproduce the whole space of observed triple-frequency signatures. Future improvements could be obtained by specifically designed closure studies including detailed in situ observation of the inner aggregate structure and snowfall PSD together with a large set of scattering computations which are increasingly available in recent years thanks to optimized scattering codes and increasing computing resources. The three case studies also reveal that mixtures of different snow particles can produce very similar triple-frequency signatures. Future studies will have to investigate whether it is important to quantify these particle populations separately or if bulk snowfall quantities can be derived independent of the overall snowfall composition.

Acknowledgments
We gratefully acknowledge the work of the Hyytiälä station and ARM AMF2 personnel for the daily tasks with measurements, especially mentioning Matti Leskinen and Janne Levula (UH). We thank the NASA GPM ground validation program and Walter Petersen for providing ground-based precipitation instrumentation used in this study. We also thank Larry Bliven from NASA GSFC/Wallops Flight Facility for advices with PIP data interpretation and Jarmo Koistinen from Finnish Meteorological Institute (FMI) for his assistance with the synoptic analysis of the case studies. Work carried out by S.K. was supported by a Postdoctoral Fellowship from the German Academic Exchange Service (DAAD); additional funding for S.K. and P.K. was provided by the U.S. Department of Energy Atmospheric System Research (ASR) program. The research of A.L. was funded by grants 3155/31/2009 of the Finnish Funding Agency for Technology and Innovation (TEKES) and 255718 of the Academy of Finland. D.M. and J.T. were supported by the Academy of Finland Finnish Center of Excellence program (grant 272041) and the Cluster for Energy and Environment through the Measurement, Monitoring, and Environmental Assessment (MMEA) research program. The research of J.L. described in this publication was carried out at the Jet Propulsion Laboratory, California Institute of Technology, under contract with the National Aeronautics and Space Administration. Peter Rodriguez from Environment Canada is acknowledged for sharing his ideas on snow measurement setup. We further thank Robin Hogan for his fruitful discussion and for providing his code to compute DWR using SSRG. We also acknowledge valuable discussions with Chris Westbrook, Jani Tyynelä, and Maria Cadeddu. All remote sensing and in situ data from the BAECC campaign used in this study are available from the ARM data archive at http://www.archive.arm.gov.

References

Barthazy, E., and R. Schefold (2006), Fall velocity of snowflakes of different riming degree and crystal types, *Atmos. Res.*, *82*, 391–398, doi:10.1016/j.atmosres.2005.12.009.

Battaglia, A., E. Rustemeier, A. Tokay, U. Blahak, and C. Simmer (2010), PARSIVEL snow observations: A critical assessment, *J. Atmos. Oceanic Technol.*, *27*, 333–344, doi:10.1175/2009JTECHA1332.1.

Battaglia, A., C. D. Westbrook, S. Kneifel, P. Kollias, N. Humpage, U. Löhnert, J. Tyynelä, and G. W. Petty (2014), G band atmospheric radars: New frontiers in cloud physics, *Atmos. Meas. Tech.*, *7*(6), 1527–1546, doi:10.5194/amt-7-1527-2014.

Botta, G., K. Aydin, and J. Verlinde (2010), Modeling of microwave scattering from cloud ice crystal aggregates and melting aggregates: A new approach, *IEEE Geosci. Remote Sens. Lett.*, *7*(3), 572–576, doi:10.1109/LGRS.2010.2041633.

Botta, G., K. Aydin, J. Verlinde, A. E. Avramov, A. S. Ackerman, A. M. Fridlind, G. M. McFarquhar, and M. Wolde (2011), Millimeter wave scattering from ice crystals and their aggregates: Comparing cloud model simulations with X- and Ka-band radar measurements, *J. Geophys. Res.*, *116*, D00T04, doi:10.1029/2011JD015909.

Boudala, F. S., G. A. Isaac, and D. Hudak (2006), Ice water content and precipitation rate as a function of equivalent radar reflectivity and temperature based on in situ observations, *J. Geophys. Res.*, *111*, D11202, doi:10.1029/2005JD006499.

Brandes, E. A., K. Ikeda, G. Zhang, M. Schoenhuber, and R. M. Rasmussen (2007), A statistical and physical description of hydrometeor distributions in Colorado snowstorms using a video disdrometer, *J. Appl. Meteorol. Climatol.*, *46*(5), 634–650, doi:10.1175/JAM2489.1.

Cadeddu, M. P., J. C. Liljegren, and D. D. Turner (2013), The Atmospheric radiation measurement (ARM) program network of microwave radiometers: Instrumentation, data, and retrievals, *Atmos. Meas. Tech.*, *6*(9), 2359–2372, doi:10.5194/amt-6-2359-2013.

Ellison, W. J. (2007), Permittivity of pure water, at standard atmospheric pressure, over the frequency range 0–25 THz and the temperature range 0–100 degrees C, *J. Phys. Chem. Ref. Data*, *36*, 1–18.

Garrett, T., and S. Yuter (2014), Observed influence of riming, temperature, and turbulence on the fallspeed of solid precipitation, *Geophys. Res. Lett.*, *41*, 6515–6522, doi:10.1002/2014GL061016.

Gunn, K. L. S., and J. S. Marshall (1955), The effect of wind shear on falling precipitation, *J. Meteorol.*, *12*(4), 339–349.

Hallett, J., and S. Mossop (1974), Production of secondary ice particles during riming process, *Nature*, *249*(5452), 26–28, doi:10.1038/249026a0.

Hogan, R. J., and S. F. Kew (2005), A 3D stochastic cloud model for investigating the radiative properties of inhomogeneous cirrus clouds, *Q. J. R. Meteorol. Soc.*, *131*(611, A), 2585–2608, doi:10.1256/qj.04.144.

Hogan, R. J., and C. D. Westbrook (2014), Equation for the microwave backscatter cross section of aggregate snowflakes using the self-similar Rayleigh-Gans approximation, *J. Atmos. Sci.*, *71*(9), 3292–3301.

Hogan, R. J., A. J. Illingworth, and H. Sauvageot (2000), Measuring crystal size in cirrus using 35- and 94-GHz radars, *J. Atmos. Ocean. Technol.*, *17*(1), 27–37.

Hogan, R. J., L. Tian, P. R. A. Brown, C. D. Westbrook, A. J. Heymsfield, and J. D. Eastment (2012), Radar scattering from ice aggregates using the horizontally aligned oblate spheroid approximation, *J. Appl. Meteorol. Climatol.*, *51*(3), 655–671.

Kneifel, S., M. S. Kulie, and R. Bennartz (2011), A triple-frequency approach to retrieve microphysical snowfall parameters, *J. Geophys. Res.*, *116*, D11203, doi:10.1029/2010JD015430.

Kneifel, S., S. Redl, E. Orlandi, U. Löhnert, M. P. Cadeddu, D. D. Turner, and M.-T. Chen (2014), Absorption properties of supercooled liquid water between 31 and 225 GHz: Evaluation of absorption models using ground-based observations, *J. Appl. Meteorol. Climatol.*, *53*(4), 1028–1045.

Kulie, M. S., M. J. Hiley, R. Bennartz, S. Kneifel, and S. Tanelli (2014), Triple-frequency radar reflectivity signatures of snow: Observations and comparisons with theoretical ice particle scattering models, *J. Appl. Meteorol. Climatol.*, *53*(4), 1080–1098.

Kumjian, M. R., S. A. Rutledge, R. M. Rasmussen, P. C. Kennedy, and M. Dixon (2014), High-resolution polarimetric radar observations of snow-generating cells, *J. Appl. Meteorol. Climatol.*, *53*(6), 1636–1658, doi:10.1175/JAMC-D-13-0312.1.

Leinonen, J., and D. Moisseev (2015), What do triple-frequency radar signatures reveal about aggregate snowflakes?, *J. Geophys. Res. Atmos.*, *120*, 229–239, doi:10.1002/2014JD022072.

Leinonen, J., D. N. Moisseev, V. Chandrasekar, and J. Koskinen (2011), Mapping radar reflectivity values of snowfall between frequency bands, *IEEE Trans. Geosci. Remote Sens.*, *49*, 3047–3058, doi:10.1109/TGRS.2011.2117432.

Leinonen, J., S. Kneifel, D. Moisseev, J. Tyynelä, S. Tanelli, and T. Nousiainen (2012), Evidence of nonspheroidal behavior in millimeter-wavelength radar observations of snowfall, *J. Geophys. Res.*, *117*, D18205, doi:10.1029/2012JD017680.

Leinonen, J., D. Moisseev, and T. Nousiainen (2013), Linking snowflake microstructure to multi-frequency radar observations, *J. Geophys. Res. Atmos.*, *118*, 3259–3270, doi:10.1002/jgrd.50163.

Liljegren, J. C., S. -A. Boukabara, K. Cady-Pereira, and S. A. Clough (2005), The effect of the half-width of the 22-GHz water vapor line on retrievals of temperature and water vapor profiles with a 12-channel microwave radiometer, *IEEE Trans. Geosci. Remote Sens.*, *43*(5), 1102–1108.

Liu, G. (2008), A database of microwave single-scattering properties for nonspherical ice particles, *Bull. Amer. Meteor. Soc.*, *89*(10), 1563–1570, doi:10.1175/2008BAMS2486.1.

Locatelli, J., and P. Hobbs (1974), Fall speeds and masses of solid precipitation particles, *J. Geophys. Res.*, *79*(15), 2185–2197.

Löffler-Mang, M., and U. Blahak (2001), Estimation of the equivalent radar reflectivity factor from measured snow size spectra, *J. Appl. Meteorol.*, *40*, 843–849, doi:10.1175/1520-0450(2001)040<0843;EOTERR>2.0.CO;2.

Löffler-Mang, M., and J. Joss (2000), An optical disdrometer for measuring size and velocity of hydrometeors, *J. Atmos. Oceanic Technol.*, *17*, 130–139, doi:10.1175/1520-0426(2000)017<0130;AODFMS>2.0.CO;2.

Marshall, J. S. (1953), Precipitation trajectories and patterns, *J. Meteorol.*, *10*(1), 25–29, doi:10.1175/1520-0469(1953)010<0025:PTAP>2.0.CO;2.

Matrosov, S. Y. (1992), Radar reflectivity in snowfall, *IEEE Trans. Geosci. Remote Sens.*, *30*(3), 454–461, doi:10.1109/36.142923.

Matrosov, S. Y. (1998), A dual-wavelength radar method to measure snowfall rate, *J. Appl. Meteorol.*, *37*(11), 1510–1521.

Matrosov, S. Y. (2007), Modeling backscatter properties of snowfall at millimeter wavelengths, *J. Atmos. Sci.*, *64*(5), 1727–1736.

Matrosov, S. Y., A. J. Heymsfield, and Z. Wang (2005), Dual-frequency radar ratio of nonspherical atmospheric hydrometeors, *Geophys. Res. Lett.*, *32*, L13816, doi:10.1029/2005GL023210.

Nemarich, J., R. Wellman, and J. Lacombe (1988), Backscatter and attenuation by falling snow and rain 96, 140, and 225 GHz, *IEEE Trans. Geosci. Remote Sens.*, *26*(3), 319–329.

Newman, A. J., P. A. Kucera, and L. F. Bliven (2009), Presenting the snowflake video imager (SVI), *J. Atmos. Oceanic Technol.*, *26*, 167–179.

Nowell, H., G. Liu, and R. Honeyager (2013), Modeling the microwave single-scattering properties of aggregate snowflakes, *J. Geophys. Res. Atmos.*, *118*, 7873–7885, doi:10.1002/jgrd.50620.

Ori, D., T. Maestri, R. Rizzi, D. Cimini, M. Montopoli, and F. S. Marzano (2014), Scattering properties of modeled complex snowflakes and mixed-phase particles at microwave and millimeter frequencies, *J. Geophys. Res. Atmos.*, *119*, 9931–9947, doi:10.1002/2014JD021616.

Petty, G. W., and W. Huang (2010), Microwave backscatter and extinction by soft ice spheres and complex snow aggregates, *J. Atmos. Sci.*, *67*(3), 769–787, doi:10.1175/2009JAS3146.1.

Rasmussen, R., and H. R. Pruppacher (1982), A wind-tunnel and theoretical study of the melting behavior of atmospheric ice particles. I: A wind-tunnel study of frozen drops of radius less than 500 mu-m, *J. Atmos. Sci.*, *39*(1), 152–158, doi:10.1175/1520-0469(1982)039<0152:AWTATS>2.0.CO;2.

Rasmussen, R., et al. (2012), How well are we measuring snow: The NOAA/FAA/NCAR winter precipitation test bed, *Bull. Am. Meteorol. Soc.*, *93*, 811–829.

Rosenkranz, P. W. (1998), Water vapor microwave continuum absorption: A comparison of measurements and models, *Radio Sci.*, *33*, 919–928.

Silverman, B. W. (1986), *Density Estimation for Statistics and Data Analysis*, Chapman and Hall, London, U. K.

Turner, D. D., M. P. Cadeddu, U. Lohnert, S. Crewell, and A. M. Vogelmann (2009), Modifications to the water vapor continuum in the microwave suggested by ground-based 150-GHz observations, *IEEE Trans. Geosci. Remote Sens.*, *47*(10), 3326–3337.

Tyynelä, J., and V. Chandrasekar (2014), Characterizing falling snow using multifrequency dual-polarization measurements, *J. Geophys. Res. Atmos.*, *119*, 8268–8283, doi:10.1002/2013JD021369.

Tyynelä, J., J. Leinonen, D. Moisseev, and T. Nousiainen (2011), Radar backscattering from snowflakes: Comparison of fractal, aggregate, and soft spheroid models, *J. Atmos. Oceanic Technol.*, *28*(11), 1365–1372, doi:10.1175/JTECH-D-11-00004.1.

Tyynelä, J., J. Leinonen, C. D. Westbrook, D. Moisseev, and T. Nousiainen (2013), Applicability of the Rayleigh-Gans approximation for scattering by snowflakes at microwave frequencies in vertical incidence, *J. Geophys. Res. Atmos.*, *118*, 1826–1839, doi:10.1002/jgrd.50167.

Verlinde, J., M. P. Rambukkange, E. E. Clothiaux, G. M. McFarquhar, and E. W. Eloranta (2013), Arctic multilayered, mixed-phase cloud processes revealed in millimeter-wave cloud radar Doppler spectra, *J. Geophys. Res. Atmos.*, *118*, 13,199–13,213, doi:10.1002/2013JD020183.

Wood, N. B., T. S. L'Ecuyer, A. J. Heymsfield, G. L. Stephens, D. R. Hudak, and P. Rodriguez (2014), Estimating snow microphysical properties using collocated multisensor observations, *J. Geophys. Res. Atmos.*, *119*, 8941–8961, doi:10.1002/2013JD021303.

Paper III

AGU PUBLICATIONS

JGR

Journal of Geophysical Research: Atmospheres

RESEARCH ARTICLE
10.1002/2016JD026272

Key Points:

- Rime mass fraction and unrimed snow mass-size relation are derived
- Riming is responsible for 5% to 40% of snowfall mass
- Depending on particle size, riming can either increase or decrease the differential reflectivity

Correspondence to:
D. Moisseev,
dmitri.moisseev@helsinki.fi

Citation:
Moisseev, D., A. von Lerber, and J. Tiira (2017), Quantifying the effect of riming on snowfall using ground-based observations, *J. Geophys. Res. Atmos.*, *122*, 4019–4037, doi:10.1002/2016JD026272.

Received 18 NOV 2016
Accepted 28 MAR 2017
Accepted article online 4 APR 2017

Quantifying the effect of riming on snowfall using ground-based observations

Dmitri Moisseev[1,2], **Annakaisa von Lerber**[2], **and Jussi Tiira**[1]

[1]Department of Physics, University of Helsinki, Helsinki, Finland, [2]Finnish Meteorological Institute, Helsinki, Finland

Abstract Ground-based observations of ice particle size distribution and ensemble mean density are used to quantify the effect of riming on snowfall. The rime mass fraction is derived from these measurements by following the approach that is used in a single ice-phase category microphysical scheme proposed for the use in numerical weather prediction models. One of the characteristics of the proposed scheme is that the prefactor of a power law relation that links mass and size of ice particles is determined by the rime mass fraction, while the exponent does not change. To derive the rime mass fraction, a mass-dimensional relation representative of unrimed snow is also determined. To check the validity of the proposed retrieval method, the derived rime mass fraction is converted to the effective liquid water path that is compared to microwave radiometer observations. Since dual-polarization radar observations are often used to detect riming, the impact of riming on dual-polarization radar variables is studied for differential reflectivity measurements. It is shown that the relation between rime mass fraction and differential reflectivity is ambiguous, other factors such as change in median volume diameter need also be considered. Given the current interest on sensitivity of precipitation to aerosol pollution, which could inhibit riming, the importance of riming for surface snow accumulation is investigated. It is found that riming is responsible for 5% to 40% of snowfall mass. The study is based on data collected at the University of Helsinki field station in Hyytiälä during U.S. Department of Energy Biogenic Aerosols Effects on Clouds and Climate (BAECC) field campaign and the winter 2014/2015. In total 22 winter storms were analyzed, and detailed analysis of two events is presented to illustrate the study.

1. Introduction

In middle to high latitudes majority of precipitation originates from snow [*Field and Heymsfield*, 2015]. Ice particles grow by vapor deposition, aggregation, and riming. Riming is an important precipitation process, given that a large percentage of cloud systems contain supercooled liquid water [*Hogan et al.*, 2003; *Moss and Johnson*, 1994]. *Borys et al.* [2003, 2000] have shown that in midlatitude orographic clouds both riming and snowfall rates are affected by anthropogenic aerosol pollution. *Saleeby et al.* [2013] have further investigated this phenomenon and found that the local aerosol effect on snowfall can be significant, though synoptic conditions may have larger influence. *Lohmann* [2004] has shown that the aerosol impact on riming could have climatic implications. Given this potential sensitivity of precipitation and climate, there is a need to quantify how important riming is for surface precipitation. *Mitchell et al.* [1990] and *Harimaya and Sato* [1989] have shown that riming could explain 30% to 100% of surface snowfall mass. Furthermore, *Grazioli et al.* [2015] have found that there is also an apparent positive correlation between a precipitation rate and riming occurrence during winter storms.

Typically, riming is quantified either by using manual observations of individual snow particles [e.g., *Mitchell et al.*, 1990; *Harimaya and Sato*, 1989; *Mosimann et al.*, 1994] or by utilizing automatic optical observations [*Garrett and Yuter*, 2014; *Grazioli et al.*, 2015]. From automatic optical observations riming is detected by identifying visual particle features that are caused by riming. For example, by visually inspecting rime coverage of an ice particle surface, *Mosimann et al.* [1994] introduced the degree of riming, a parameter that defines what part of the particle surface is covered by frozen drops. They have also shown a connection between the degree of riming and rime mass fraction, which is used in numerical weather prediction models.

Dual-polarization radar observations are often used to identify ice precipitation regions affected by riming [e.g., *Straka et al.*, 2000; *Liu and Chandrasekar*, 2000; *Chandrasekar et al.*, 2013; *Giangrande et al.*, 2016]. Accurate identification of such regions would improve our understanding of precipitation processes as well as improve aviation safety [*Ellis et al.*, 2012], among other applications. Unfortunately, the connection between dual-polarization radar observations and riming is not always unambiguous and further studies are needed to establish a better link.

Recently, a new microphysical scheme based on a single ice-phase category was proposed for the use in numerical weather prediction models [*Morrison and Grabowski*, 2008; *Morrison and Milbrandt*, 2015]. This new microphysical scheme allows a continuous representation of changes of ice particle properties and avoids abrupt and artificial transition from one ice particle type to another. The scheme assumes that during riming, particle maximum dimension stays the same, while mass increases [*Heymsfield*, 1982; *Erfani and Mitchell*, 2017]. The particle maximum dimension will eventually increase by riming, but this will happen at the graupel stage. *Morrison and Grabowski* [2008], *Morrison and Milbrandt* [2015], and *Erfani and Mitchell* [2017] have explained that this conceptual model would result in a power law mass-dimensional relation, $m = \alpha D^{\beta}$, where the exponent, β, remains constant, while the prefactor, α, increases. Therefore, the mass-dimensional relation can be written as a function of the rime mass fraction.

This paper presents analysis of 22 events observed during two consecutive winters, 2013/2014 and 2014/2015. The assumption that only the prefactor of the $m(D)$ relation is reacting to riming is converted to a method to retrieve rime mass fraction from surface-based snowfall measurements. As a part of the developed method, a mass-size relation that can be treated as representative of unrimed snowflakes is also determined. The validity of the proposed retrieval method is checked by estimating particle-effective liquid water paths that correspond to the computed rime mass fractions and comparing these to microwave radiometer observations. Furthermore, the computed rime mass fraction in combination with precipitation rate and accumulation observations are used to quantify impact of riming on precipitation mass. Finally, the impact of riming on dual-polarization radar variables is investigated.

2. Data and Methods

2.1. Observations

This study is based on observations carried out during the Biogenic Aerosols Effects on clouds and Climate (BAECC) field experiment [*Petäjä et al.*, 2016] and the winter of 2014/2015. During the experiment U.S. Department of Energy Atmospheric Radiation Measurement (ARM) deployed the second ARM mobile facility (AMF2) to the University of Helsinki Research Station located in Hyytiälä, Finland (61°50′37′′N, 24°17′16′′E). In addition to the remote sensing instruments of the AMF2, an extensive suite of surface-based precipitation instrumentation was placed at the measurement site 20–30 m away from the remote sensors. A part of the surface-based precipitation instrumentation is provided by the NASA Global Precipitation Mission Validation program.

Data from two AMF2 remote sensing instruments are used in this study. Microwave radiometer (MWR)-retrieved liquid water path (LWP) [*Cadeddu et al.*, 2013] is used to cross validate the derived rime mass fraction. High spectral resolution lidar (HSRL) observations of backscatter and linear depolarization ratio are employed for detection of embedded supercooled-liquid water layers [e.g., *Hogan et al.*, 2003; *Shupe et al.*, 2006; *Westbrook and Illingworth*, 2011], which appear as thin bright layers in the backscatter coefficient measurements.

In addition to the AMF2 remote sensors, data from Finnish Meteorological Institute (FMI) C band dual-polarization weather radar are employed in this study. The FMI radar, which is located in Ikaalinen about 64 km west of the measurement site, performed range height indicator scans over the measurement site every 15 min. From these observations vertical profiles of reflectivity and differential reflectivity are computed. To compute these profiles, reflectivity and differential reflectivity measurements for each ray were averaged using range gates located within 1 km ground range of the measurement site. It should be noted that because of the availability of the range height indicator (RHI) scans, quasi-vertical profiles [*Ryzhkov et al.*, 2016] were not used.

The presented method and data analysis is based on observations of volume flux weighted ensemble mean density and particle size distribution parameters of falling snow. These observations started in December 2013 and being carried continuously since. The ensemble mean density is retrieved using particle volume flux computed from NASA Particle Imaging Package (PIP) and liquid water equivalent (LWE) precipitation rate measured by a weighing gauge [*Tiira et al.*, 2016]. The particle size distribution (PSD) parameters are computed from PIP observations. Because the density retrieval is sensitive to precipitation accumulation, the PSD parameters and ensemble mean density values are retrieved from observations which were collected with a temporal resolution determined by the precipitation accumulation. It was required that the precipitation accumulation exceeds 0.1 mm. This way it was insured that the retrieval error is minimized [*Tiira et al.*, 2016]. The PSD parameters were computed using a standard technique, [see, e.g., *Bringi and Chandrasekar*, 2001; *Leinonen et al.*, 2012].

Prior to 24 November 2016, the date on which the PIP software was updated, the PIP diameter bin size was set to 0.25 mm. After the date it was set to 0.2 mm. This also affected the minimum recorded particle size: before the software update it was 0.25 mm, and it became 0.2 mm. *Tiira et al.* [2016] have shown the impact of the PSD truncation on the retrieved density. It is shown that for cases where the median volume diameter, D_0, is less than 1 mm, the density is expected to be overestimated by at most 20%. For larger D_0 cases this error becomes smaller than 5%.

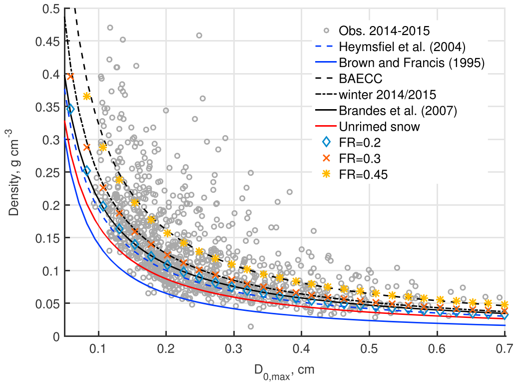

Figure 1. Scatterplot of volume flux weighted ensemble mean snow density, ρ, versus median volume diameter D_0 as retrieved by *Tiira et al.* [2016]. For the comparison, computed mean snow density—D_0 curves based on m-D relations of *Brown and Francis* [1995] (blue solid line), *Heymsfield et al.* [2004] (blue dashed line), and *Brandes et al.* [2007] (black solid line) ρ-D_0 relations are also plotted. The black dashed and dash-dotted lines depict ρ-D_0 relations found for BAECC and 2014/2015 winters. The blue diamonds, red crosses, and yellow stars show relations for rime mass fraction, FR, values of 0.2, 0.3, and 0.45, respectively.

The PIP records video with 380 fps, which means that typically more than two observations of the same particle are recorded. From these records the particle fall velocity is computed. It should be noted that the number of records is determined not only by the vertical velocity of the particles but also by horizontal wind. During all of our observations wind speeds did not exceed 4 m/s. The observed relation between the snow density and median volume diameter is shown in Figure 1. The density and PSD parameters are derived from observations from winters of 2013/2014 and 2014/2015 as discussed in *Tiira et al.* [2016].

Since PIP records snowflake shadows on a single side plane only, the observed particle dimensions are not necessarily matching the true ones [*Wood et al.*, 2013; *Tiira et al.*, 2016]. The PIP-measured diameter is the equivalent area diameter, which is the diameter of a circle with the same area as the area of a particle shadow. Following *Tiira et al.* [2016], in this study the PIP-observed diameter is converted to the volume equivalent diameter, D_{veq}, and to the maximum particle diameter D_{max}. The conversion is done by applying a correction factor of 1/0.92 for D_{pip} to D_{veq} conversion. *Tiira et al.* [2016] found that this correction factor is suitable for the data set used in this study and represents the average particle shape, which can be assumed to be spheroidal with the axis ratio, AR, of 0.6. The D_{max} is computed from the D_{veq} as follows:

$$D_{max} = 0.6^{-1/3} D_{veq}. \tag{1}$$

This yields that $D_{pip} \approx 0.8 D_{max}$, which is similar to what *Wood et al.* [2013] have derived.

There are two reasons why we assume that snowflakes can be modeled as spheroids with the axis ratio, AR, of 0.6, which is a good model for mature snow aggregates as was shown by analyzing multifrequency radar observations [*Matrosov et al.*, 2005] and through theoretical studies of the aggregation process [*Westbrook et al.*, 2004]. First, the goal of this study is to investigate the connection between riming and snowfall accumulation. During the studied events, highest precipitation rates were recorded during the periods where relatively large snowflakes were observed. These snowflakes are typically aggregates or rimed aggregates. Second, as will be discussed later in the paper, the largest uncertainty in the rime mass fraction retrieval occurs during the cases where majority of precipitation occurs in the form of crystals. In these cases, the error caused by the assumption of the particle shape is relatively minor compared to the other error sources.

2.2. Method

A particle video imager, such as the PIP, measures particle size distribution and fall velocity. These observations can be used to compute the particle volume flux. The volume flux in combination with precipitation rate measurements yield a bulk density [*Brandes et al.*, 2007] or ensemble mean density of snow [*Tiira et al.*, 2016]. It should be noted that the snow densities derived by *Brandes et al.* [2007] and *Tiira et al.* [2016] are the same, despite having different names. The notation, ensemble mean density, was adopted by *Tiira et al.* [2016] to be consistent with numerous aircraft studies, see, for example, *Heymsfield et al.* [2004]. In these studies the notation bulk density is reserved for a density of individual ice particle and not to the mean density of a distribution of snowflakes.

Assuming that snow PSD can be represented in a Gamma functional form

$$N(D) = N_0 D^{\mu} \exp(-\Lambda D) = N_0 D^{\mu} \exp\left(-\frac{3.67 + \mu}{D_0} D\right), \tag{2}$$

where N_0 is the intercept parameter, D_0 is the median volume diameter, and μ is the shape parameter; the particle volume flux, F_v, can be expressed as a function of PSD parameters, N_0 and Λ, and the parameters of a velocity-dimensional, $v(D)$, relation:

$$F_V = \frac{\pi}{6} \int \mathrm{AR} \cdot D^3 \cdot a_v D^{b_v} \cdot N_0 D^{\mu} \exp(-\Lambda D) \mathrm{d}D = \frac{\pi}{6} \cdot \mathrm{AR} \cdot a_v N_0 \cdot \frac{\Gamma(4 + b_v + \mu)}{\Lambda^{4+b_v+\mu}} \quad (\mathrm{cms^{-1}}), \tag{3}$$

where a_v and b_v are the prefactor and exponent of the $v(D)$ relation. Here and later in the text D stands for $D_{\max}$; therefore, the particle axis ratio AR is used to compute the volume. Following the same notation, the precipitation rate, or the mass flux F_m, can be expressed as

$$F_m = \int \alpha D^{\beta} \cdot a_v D^{b_v} \cdot N_0 D^{\mu} \exp(-\Lambda D) \mathrm{d}D = \alpha a_v N_0 \cdot \frac{\Gamma(\beta + b_v + \mu + 1)}{\Lambda^{\beta+b_v+\mu+1}} \quad (\mathrm{g\ cm^{-2} s^{-1}}) \tag{4}$$

This equation is derived expressing the mass-size relation in the power law form $m = \alpha D^{\beta}$.

Heymsfield [1982] have proposed a conceptual model that describes how ice particle properties evolve during riming. At the initial stage, a particle, a planar ice crystal or an aggregate, is formed. The second stages, the first stage of riming growth for the planar ice crystal and aggregate, are different. The ice crystal growth mainly occurs by riming at the underside, which changes the aspect ratio of the particle while maintaining the maximum dimension. Given tumbling and gyration of aggregates, the aggregates grow by filing an imaginary spherical shell. At this stage the shell diameter is the particle maximum dimension, which stays constant. Both for the crystal and aggregate the second growth stage ends when the particles reach spherical shapes. At the last stage, the particles continue to grow in a spherical form and from this stage $D_{\max}$ starts to increase. This stage manifests the beginning of the graupel growth stage.

We are proposing a small modification to this conceptual model. This modification concerns with the transformation of the aggregate shape during the second growth stage. We assume that the shape of an aggregate during this stage does not change. The riming just fills unoccupied places while not affecting the snowflake shape, as summarized in Table 1. This assumption can be tested, since it has a direct implication for dual-polarization radar observations. It would mean that values of dual-polarization radar variables would increase due to riming, as will be presented later in more detail. As was discussed by *Erfani and Mitchell* [2017], *Morrison and Grabowski* [2008], and *Morrison and Milbrandt* [2015], snowflake growth during the first riming stage will lead to a snowflake mass-size relation where the exponent remains constant, while the prefactor changes. Therefore, the $m(D)$ relation can be written as a function of the rime mass fraction, FR, as

$$m = \alpha D^{\beta} = \frac{\alpha_{\mathrm{us}}}{1 - \mathrm{FR}} D^{\beta} \quad (\mathrm{g}), \tag{5}$$

where $m_{\mathrm{us}} = \alpha_{\mathrm{us}} D^{\beta}$ is the mass-dimensional relation of unrimed snowflakes. The rime mass fraction is the ratio of the rime mass to the snowflake mass, $\mathrm{FR} = m_{\mathrm{rime}}/m = (m - m_{\mathrm{us}})/m$. By combining (3)–(5) and assuming the FR is independent of size, we can express the ensemble mean density as a function of the rime mass fraction:

$$\rho = \frac{F_m}{F_V} = \frac{6}{\pi} \frac{\alpha_{\mathrm{us}}}{1 - \mathrm{FR}} \frac{\Gamma(\beta + b_v + \mu + 1)}{\mathrm{AR} \cdot \Gamma(4 + \mu + b_v)} \Lambda^{3-\beta} \quad (\mathrm{gcm^{-3}}) \tag{6}$$

Table 1. Schematic Summary of Riming Growth Stages and Expected Changes in Particle Maximum Dimension, D_{max}, and Aspect Ratio, AR

	Crystal	Aggregate
Stage 0	*Crystal Formation and Growth*	
	—	Aggregation
Stage 1	*Riming: Fill-In Stage*	
	D_{max} is preserved	D_{max} and AR are preserved
	AR increases	
Stage 2	*Riming: Graupel Growth Stage*	
	D_{max} increases	D_{max} and AR increase

This leads to the expression of the rime mass fraction as a function of the retrieved ensemble mean snow density, Λ, the exponent of the *v-D* relation and coefficients of the unrimed snow $m(D)$ relation.

$$\mathrm{FR} = 1 - \frac{6}{\pi} \cdot \frac{\alpha_{us}}{\rho} \frac{\Gamma(\beta + b_v + \mu + 1)}{\mathrm{AR} \cdot \Gamma(4 + \mu + b_v)} \Lambda^{3-\beta} \quad (7)$$

The exponent of the $v(D)$ relation varies between 0.217 and 0.256 as was presented by *Tiira et al.* [2016]. However, the derived FR values depend weakly on b_v. The FR value changes by less than 1% due to changes in b_v. Therefore, b_v can be assumed to be constant. It was selected to be equal to 0.22. This value is close to what was found by *Zawadzki et al.* [2010]. To derive the rime mass fraction, given observations of ρ and Λ, parameters α_{us} and β have to be estimated.

Using observations from two winters the ensemble mean snow density and median volume diameter were estimated [*Tiira et al.*, 2016]. The scatterplot between the two is shown in Figure 1. From these observations a mass-size relation of unrimed snow is defined as follows. It is assumed that snow particles with the smallest mass for a given diameter represent unrimed snow. This means that the lowest edge of the scatterplot in Figure 1 should correspond to unrimed snow. To take into account possible uncertainties in the retrievals of ρ and D_0, we have split the data into D_0 intervals ranging between 0.1 and 0.6 cm with a step of 0.02 cm. For each interval, data that have density values belonging to the lowest 5% were selected. Using equation (6), where FR = 0, the parameters of the mass-dimensional relation were estimated using a linear fit in the logρ-logD_0 space. It was found that the relation $m = 0.0075D_{veq}^{2.05}$, or $m = 0.0053D_{max}^{2.05}$ if expressed as a function of D_{max}, represents the unrimed snow. It should be noted that the assumed value of b_v has a negligible error on the retrieved relation. *Tiira et al.* [2016] have discussed impact of PSD truncation on the retrieval of ρ. This discussion also applies here. It was found that for D_0 values larger than 0.1 cm the bias in the computed ensemble mean density values, due to the small size truncation of PSD [*Moisseev and Chandrasekar*, 2007], is less than 5%. Therefore, it is expected that the derived $m(D)$ overestimates unrimed snowflake masses by a maximum of 5%. Of course, there is a possibility that during collected observations that span over two winters, no unrimed snowflakes were observed. This possibility is difficult to quantify, given the lack of other supporting observations.

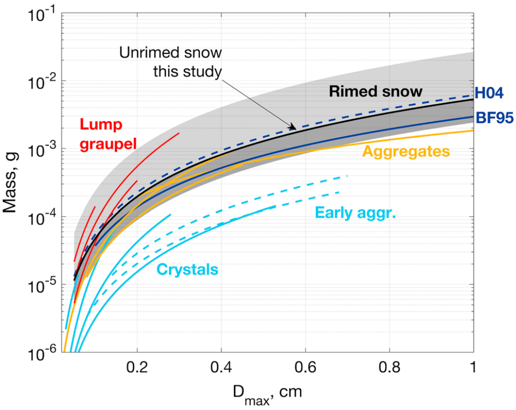

Figure 2. The $m(D)$ relations reported in literature are shown by lines: light blue lines show relations for crystals and early aggregates, yellow lines for aggregates, and red lines for graupel. The dark gray-shaded region presents the ad hoc $m(D)$ region representative of aggregates. The light gray region depicts the region of rimed particles as retrieved in this study. Two dark blue lines are *Heymsfield et al.* [2004] and *Brown and Francis* [1995] relations which are also used in Figure 1.

The comparison of the derived $m(D)$ to other relations presented in Figure 1 shows a relatively good agreement. The derived relation represents heavier ice particles than those observed by *Brown and Francis* [1995], for example. It can be seen in Figure 1 that the vast majority of our observations are located above *Brown and Francis* [1995] curve. The relation found by *Heymsfield et al.* [2004], on the other hand, is very close.

To assess the potential uncertainty associated with the selection of the unrimed snow $m(D)$ relation, a comparison of relations reported in literature is performed and summarized in Figure 2. The figure shows $m(D)$ relations for crystals (P1e, P1a, P1c, and C1h according to *Magono and Nakamura* [1965] classification) [*Pruppacher and Klett*, 1996], early aggregates (P1e and P1a) [*Kajikawa*, 1989], lump graupel [*Locatelli and Hobbs*, 1974], aggregates of planar polycrystals and aggregates of side planes [*Mitchell*, 1996], aggregates of unrimed assemblages of dendrites [*Locatelli and Hobbs*, 1974], and relations of *Brown and Francis* [1995] and *Heymsfield et al.* [2004]. If the relations for different particle types are considered separately, the biggest spread of masses for a given $D_{\max}$ is given by crystals. The masses of aggregates fall within a much narrow range of values shown by the dark gray-shaded region. The *Brown and Francis* [1995] curve (dark blue solid line) falls well within this region, while our relation depicted by the black line and *Heymsfield et al.* [2004] relation (dark blue dashed line) can be considered as the upper boundaries of the aggregate region. The boundaries of this ad hoc region can be given by the prefactor values of $m(D)$, which vary between 0.0024 and 0.0053. Here we are assuming that $\beta = 2.05$.

This analysis indicates that if the proposed relation for unrimed snow is used and riming is detected, i.e., FR is larger than zero, then there is a very high probability that riming actually occurs. The amount of riming may be underestimated. Since higher precipitation rates are typically associated with larger particles, in stratiform precipitation systems these particles are mainly aggregates at various stages of riming. In these cases the retrieval uncertainty is contained to the range of α values defined by the aggregation region.

Given the derived mass-dimensional relation for the unrimed snow and utilizing equation (7), the observed spread in the ρ-D_0 scatterplot can be explained in terms of the rime mass fraction. For example, the ρ-D_0 relation proposed by *Brandes et al.* [2007] matches well with the relation derived using $m_{\mathrm{us}}(D)$ and FR $= 0.2$, as shown by the blue diamonds in Figure 1. In a similar way, observations collected during BAECC campaign match well with FR $= 0.45$ curve. The snow during winter 2014/2015 was less dense, FR $= 0.3$, and closer to the one recorded in Colorado by *Brandes et al.* [2007]. The maximum observed value measured during our observation period lies in the range between 0.7 and 0.8.

To summarize, the proposed method can be presented as the following steps:

1. At the first step, the ensemble mean density should be retrieved from observations of PSD, $v(D)$, and snowfall rate, *SR*, as described in *Tiira et al.* [2016] or *Brandes et al.* [2007].
2. At the second step, a mass-dimensional relation of unrimed snow should be estimated for a given climate or geographical location. This step can be potentially omitted and the relation $m_{\mathrm{us}} = 0.0053 D_{\max}^{2.05}$ derived in this study can be used instead.
3. At the third step, the retrieved mean density, $m_{\mathrm{us}}(D)$, μ, Λ, and the exponent of $v(D)$ relation are applied to equation (7) to retrieve the rime mass fraction. It should be noted that changes in μ and the exponent of $v(D)$ values have a minor effect on FR. They can be fixed to be 0 and 0.22, respectively, without making a significant error.

3. Results

3.1. Case Studies

3.1.1. The 21 February 2014 Event

To demonstrate how the retrieved rime mass fraction relates to the other falling snow microphysical parameters, analysis of two events is performed. The first analyzed snowfall case took place on 21 February 2014. A wide low-pressure area from the North Atlantic was approaching Scandinavia with a trough and an associated frontal system passing over Hyytiälä from the southwest during the night of 21–22 February. Around midnight UTC, the occlusion point of the system passed near the southwestern coast of Finland where also largest snow accumulations were recorded. In Figure 3, time series of PSD parameters, snowfall rate, the ensemble mean snow density, and rime mass fraction are presented. Analyses of parts of this storm are already presented in literature [*Kneifel et al.*, 2015; *Petäjä et al.*, 2016; *Kalesse et al.*, 2016]. *Kneifel et al.* [2015] have studied triple-frequency radar signatures and coinciding surface observations to infer a connection between multi-frequency radar and microphysical properties of snow. As a part of the presented analysis, it was found that around 2300 UTC there is a transition from light, graupel-like snowfall to a moderate aggregate snowfall. This transition is also clearly visible in Figure 3. The FR reaches 0.7 at 2305 UTC, meaning that 70% of the particle mass is determined by collected supercooled liquid drops. This indicates very heavy riming. At the same time D_0 value is not very high, 0.15 cm, that is a characteristic value for relatively small ice particles. Just a few minutes later, D_0 value doubles and at the same time the liquid water equivalent (LWE) precipitation rate

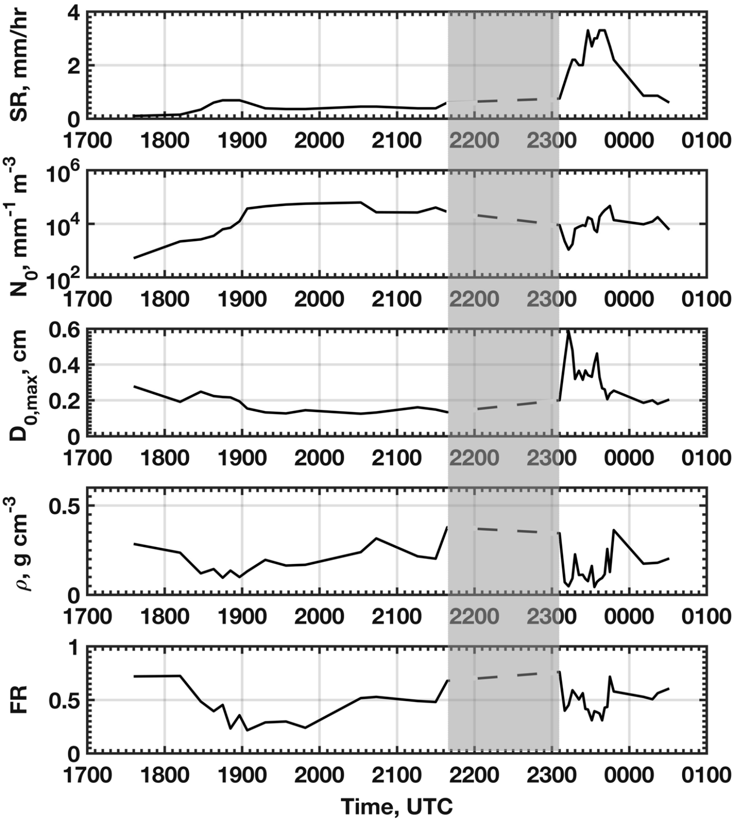

Figure 3. Overview of the precipitation event that took place on 21 February 2014. The panels show measurements of snowfall LWE rate, SR, PSD intercept parameter, N_0, median volume diameter, D_0, bulk density, ρ, and rime mass fraction, FR. The shaded area shows the time period during which the precipitation rate was low, and the density and correspondingly FR retrieval were not stable.

exceeds 3 mm/h. During this period, which ends at around 2350 UTC, the retrieved rime mass fraction value drops below 0.5, and at some instances it goes below 0.2. At the same time there is also a reduction in Doppler velocity values, at the low levels, which also supports the idea of lower FR values. After 2350 UTC the FR increases again.

This short period of relatively heavy snowfall and lower FR values coincides with ice phase seeder-feeder process [*Hobbs*, 1978; *Matejka et al.*, 1980] discussed in *Petäjä et al.* [2016] and can be seen in Figure 4. The ice particles falling out of the cirrus cloud seed lower clouds, where riming is taking place. The evidence of riming is reported in *Kalesse et al.* [2016], who have used a combination of radar Doppler spectra, microwave radiometer, and riming model to analyze a part of this event. The intensive seeder-feeder process depletes supercooled water and almost halts riming. The HSRL measured backscatter coefficient, presented in Figure 4, shows smaller values during this period supporting the conclusion that the liquid layer is depleted. At the same time, aggregation growth of snowflakes becomes more active [*Moisseev et al.*, 2015; *Hobbs et al.*, 1974]. The seeding stops just before 0 UTC, as can be seen in Figure 4, and the supercooled water starts to restore and riming replaces aggregation as the dominating snow growth process.

Before the discussed period, the rime mass fraction was steadily increasing starting from 1900 UTC. It should be noted that between 2130 and 2305 UTC, the shaded area in Figure 3, the precipitation rate was rather low and the density retrieval was unreliable. Because of this, the FR values are also unreliable, and the values

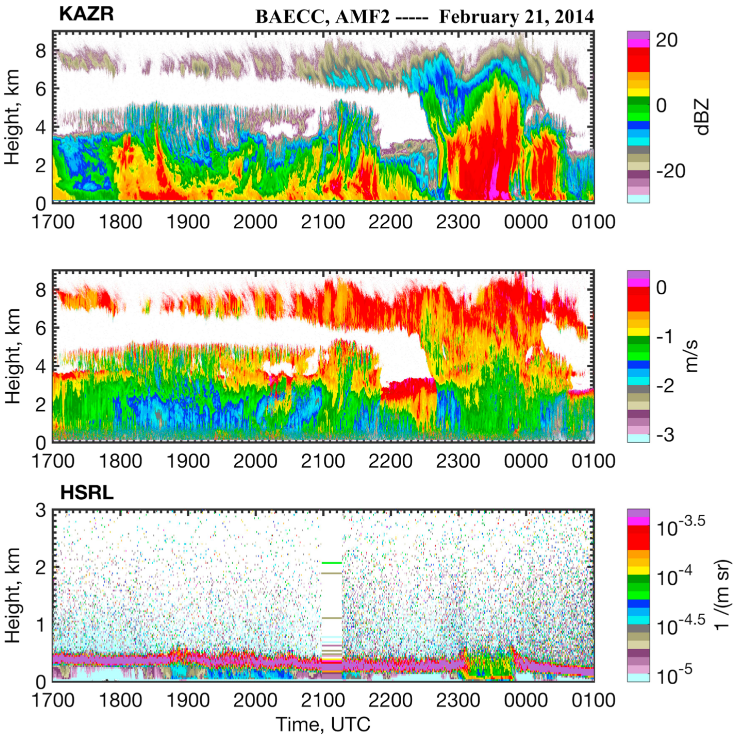

Figure 4. KAZR reflectivity, Doppler velocity, and HSRL measurements for 21 – 22 February 2014 event.

presented in the figure are just a linear interpolation between the values retrieved immediately before and after the above mentioned period. It should be noted that most of the precipitation accumulation during this event was between 2300 and 0000 UTC, when aggregation was taking place.

3.1.2. The 20 March 2014 Event

The second case study is of the snowfall event that took place on 20 March 2014. The total precipitation accumulation during this event is 4.3 mm. The event is a textbook example of a typical winter precipitation event in Southern Finland, where similarly to the 21 February event, there is a wide low-pressure area approaching Scandinavia from the west, and an associated frontal system passes over the Gulf of Finland from the southwest. The heaviest snowfall in Hyytiälä originated from the thick cloud area associated with a warm front reaching the area in the evening.

In Figure 5 the summary of derived snow microphysical properties is shown. As can be seen the ensemble mean snow density varies between 0.1 and 0.3 g/cm^3. In many cases the high values are reached during the time periods when the median volume diameter approaches 0.1 cm. Furthermore, the low-density values coincide with periods when relatively large snowflakes are observed. This pattern is the same for the previously discussed event. The rime mass fraction values do not exhibit a correlation with D_0. This mean density behavior is not surprising, since it is the function not only of FR but also of D_0.

The radar and lidar observations recorded during this event are presented in Figure 6. The KAZR vertical Doppler velocity shows particle fall velocities ranging from 1.5 to 2 m/s between 1730 and 1830 UTC and after 1900 UTC. These velocities indicate that the snowflakes observed during these periods are rimed [*Mosimann*, 1995; *Barthazy and Schefold*, 2006]. The rime mass fraction shows a local maximum of 0.2 starting just before 1630 and lasting until 1720 UTC, after which FR decreases to zero. At 1800 UTC the FR starts to increase again and continues until the end of the event, where it reaches the value of 0.7. The comparison of FR and Doppler

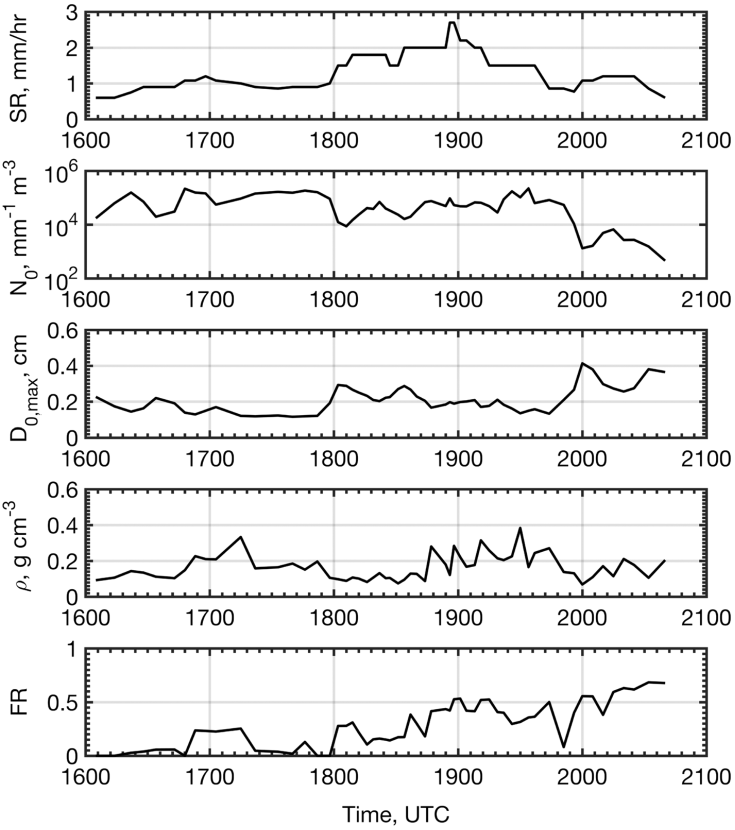

Figure 5. Similar to Figure 3 but for 20 March 2014.

velocity indicates that even though both observations indicate the presence of rimed particles at about the same times, these times do not match exactly.

3.2. Connection Between FR and LWP

The proposed retrieval procedure relies on the assumption that differences in snowflake masses for particles of the same dimensions are due to different rime mass fractions. This assumption explicitly ignores possible changes in a particle mass linked to the presence of different crystal habits; the associated uncertainty is discussed in section 2. To test how viable this approximation is, a connection between derived FR and another measurable quantity needs to be established. Given that the rime mass is determined by the mass of swept supercooled liquid droplets, FR can be expressed as a function of the effective liquid water path, ELWP, which can be written as

$$\mathrm{ELWP} = \frac{m_{\mathrm{rime}}}{E_r(\pi/4)D_{\max}^2} = \frac{\alpha_{\mathrm{us}} D_{\max}^{\beta}}{E_r(\pi/4)D_{\max}^2} \cdot \frac{\mathrm{FR}}{1-\mathrm{FR}} \approx \frac{4}{\pi}\alpha_{\mathrm{us}}\frac{\mathrm{FR}}{1-\mathrm{FR}} \quad (\mathrm{g\ cm^{-2}}) \tag{8}$$

where m_{rime} is the change in the particle mass due to riming and E_r is the riming efficiency. The final equation is derived assuming that $E_r = 1$. It is known that E_r is likely to vary considerably depending on cloud conditions, which may account for some discrepancies between ELWP and LWP values, which will be shown later. Also, it is assumed that the area perpendicular to the direction of fall is circular, which is a reasonable approximation for planar crystals and aggregates. Given that the exponent of $m(D)$ relation is very close to 2, dependence of (8) on $D_{\max}$ is also ignored.

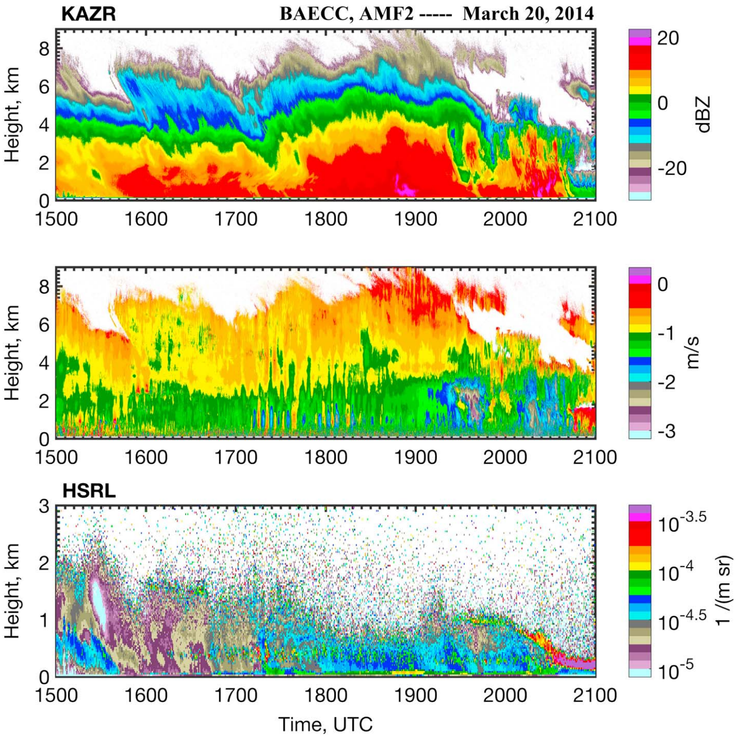

Figure 6. KAZR reflectivity, Doppler velocity, and HSRL measurements for 20 March 2014 event.

Following (8) ELWP values were computed for the two case studies. In Figure 7 the ELWP is plotted for the 21–22 February 2014 event. For the comparison, LWP observations by the AMF2 MWR are also presented in the figure. Overall, the ELWP and LWP agree rather well. The ELWP is lower, but follows LWP, two curves raise and fall at about the same time. It is not surprising that the ELWP is lower. First, the actual E_r is probably lower than 1. Second, the path of a falling particle is different from the vertical path used in MWR observations. This also explains why ELWP and LWP curves sometimes behave differently as, for example, before 2000 UTC. The difference in paths could also explain a slight temporal shift between the curves; this is clearly visible in areas of large LWP gradients.

The observations of 20 March 2014 also show a relatively good agreement, as can be seen in Figure 8. The temporal shift between the curves is larger in this case. It was found that if the ELWP curve is shifted by 30 min, the agreement with LWP is much better. As in the February case, LWP and ELWP are correlated. Not all features visible in the LWP curve can be found in the ELWP. The temporal resolutions are different, and paths where particles travel in the atmosphere are expected to be different from the vertical. It should be noted that the applied temporal shift also improves the comparison with the radar observations, as was discussed in the previous section. It is interesting to see that LWP values below or close to the MWR detection limit can produce detectable riming signatures as can be observed in Figure 8 around 1700 UTC. There is a clear peak in FR reaching 0.2, but both ELWP and LWP values are smaller than 30 g m^{-2}. This indicates that for detection of riming, a dual-channel MWR should be used with care.

A comparison of FR, ELWP, and LWP was performed for all BAECC cases. The results of this comparison are presented in Figure 9. As was noted from the case studies, both FR and ELWP are related to LWP. The correlations between ELWP and LWP or FR and LWP are not very high, the presented scatterplots are rather wide. This is not surprising, however, since no temporal adjustments to match the observations were performed. Nonetheless, the presented analysis show that the derived rime mass fraction reacts to the changes in LWP indicating

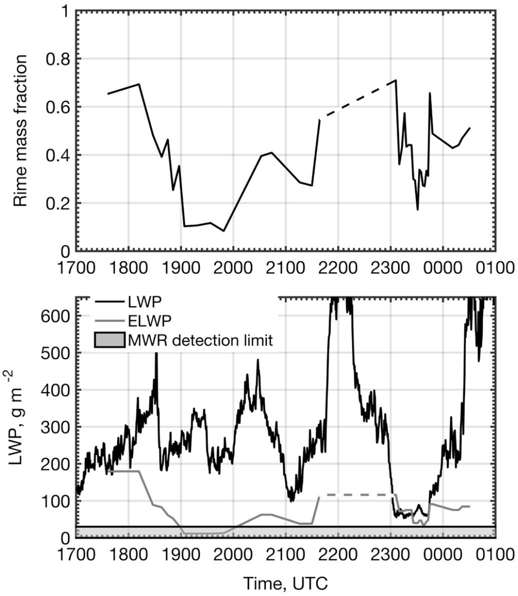

Figure 7. Comparison of rime mass fraction,FR, derived effective liquid water path (ELWP), and microwave radiometer measured LWP for the event of 21 – 22 February 2014.

that both represent same processes that take place in the cloud system. The computed ELWP is about 2 times lower than LWP. It can also be seen that if LWP values exceed 400 g m^{-2}, then we can expect heavily rimed ice particles with rime mass fractions exceeding 0.6.

3.3. Impact of Riming on Surface Precipitation

From observations of two snow events that took place in the Sierra Nevada mountains, *Mitchell et al.* [1990] have found that riming is responsible for 30% to 40% of accumulated snow mass. *Harimaya and Sato* [1989]

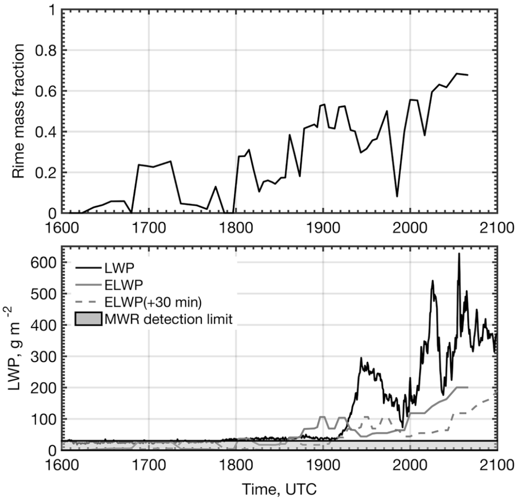

Figure 8. Same as Figure 7 but for the event of 20 March 2014.

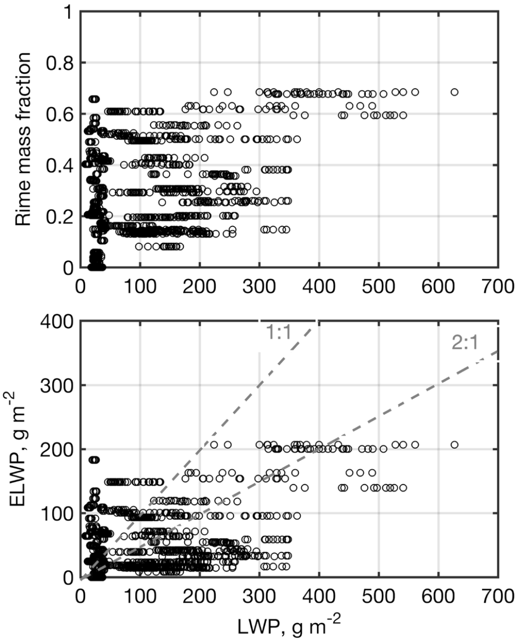

Figure 9. Scatterplots of FR versus LWP and ELWP versus LWP for all BAECC events.

Table 2. Summary of the Studied Events[a]

Event	Date	LWE (mm)	T_{min} (°C)	T_{max} (°C)
1	2014 Feb 1 00:00–03:30	3.9	−9.8	−8.9
2	2014 Feb 12 05:30–07:45	0.6	−1	0
3	2014 Feb 15 21:50 to Feb 16 01:00	2.3	−2.1	−1
4	2014 Feb 21 17:30 to Feb 22 05:00	4.7	−2.7	0
5	2014 Mar 18 08:50–18:45	4.3	−3.8	−1.8
6	2014 Mar 20 16:05–20:40	5.4	−4.3	−1.3
7	2014 Nov 6 19:15 to Nov 7 13:50	9.9	−2.4	−1.6
8	2014 Dec 18 15:00–18:40	2.4	−2.3	−0.8
9	2014 Dec 24 08:45–12:45	1.2	−9.2	−8.9
10	2014 Dec 30 02:50–13:50	6.1	−10.4	−0.6
11	2015 Jan 3 09:35–23:30	7.2	−3.9	0
12	2015 Jan 7 02:00–20:00	3.7	−6.5	−0.8
13	2015 Jan 8 09:00–13:30	2.6	−1.9	0
14	2015 Jan 9 19:55 to Jan 10 03:50	2.9	−3.7	−0.2
15	2015 Jan 12 22:00 to Jan 13 07:50	11.9	−15.7	−9.0
16	2015 Jan 14 02:15–04:20	2.0	−8.0	−0.3
17	2015 Jan 16 01:50–07:30	5.8	−1.3	−0.6
18	2015 Jan 18 16:15–20:45	1.8	−2.4	−0.3
19	2015 Jan 22 21:15 to Jan 23 03:30	2.1	−13.3	−12.5
20	2015 Jan 23 16:00–22:30	1.2	−10.1	−8.8
21	2015 Jan 25 09:00–15:45	2.7	−2.4	−1.7
22	2015 Jan 31 13:40–23:15	6.4	−1.9	−0.4

[a] For each event a total LWE accumulation, minimum and maximum temperatures are given. The first six events were recorded during the BAECC experiment.

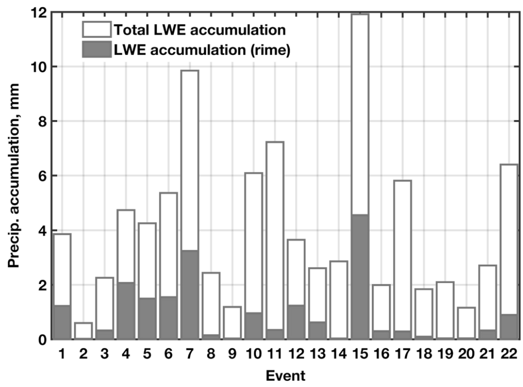

Figure 10. Precipitation liquid water equivalent (LWE) accumulations and rime precipitation fractions for all analyzed events.

estimate that this value is higher for the coastal region of Japan and ranges between 50% and 100%. *Grazioli et al.* [2015] have shown that there seems to be a correlation between occurrence of riming and precipitation accumulation.

To analyze the impact of riming on snowfall, we have computed total precipitation accumulations, A, for the recorded 22 events, summarized in Table 2, and corresponding rime precipitation accumulation, A_{FR}. The total accumulation and rime precipitation accumulation are defined as

$$\begin{aligned} A &= \sum_j \mathrm{SR}_j \cdot \Delta T_j \\ A_{\mathrm{FR}} &= \sum_j \mathrm{FR}_j \cdot \mathrm{SR}_j \cdot \Delta T_j \end{aligned} \tag{9}$$

where j stands for a time integration period during which PSD parameters, SR and FR are estimated and ΔT_j is the corresponding integration time.

In Figure 10 the accumulations for all events are shown. The observations show that riming is an important factor and responsible for 5% to 40% of snow mass accumulation. The found rime precipitation accumulation fraction, A_{FR}/A, is in line with the *Mitchell et al.* [1990] finding and is lower than that found by *Harimaya and Sato* [1989]. There also appears to be a tendency that the higher accumulation events have larger rime precipitation accumulations, for example, events 15 and 7. There are exceptions as well, events 10, 11, 17, and 22 have above average accumulations, close or exceeding 6 mm, while having below average A_{FR}. The Pearson correlation coefficient between A and A_{FR} is 0.83 as shown in Figure 11. It could be higher, if events like 10, 11, 17, and 22 can be considered outliers, or it can be significantly lower if events like 15 and 7 are rare. Given that the conclusion whether presence of riming would enhance precipitation accumulation depends very much on a few events, it is too early to make a decisive statement. It should further be noted that the correlation between average precipitation rate, A, divided by the event duration and A_{FR}/A is much smaller. The Pearson correlation coefficient is just 0.33, see Figure 11. This seems to point to the conclusion that riming does not enhance precipitation, at least in Southern Finland.

3.4. Riming and Dual-Polarization Radar Observations

Dual-polarization radar variables depend on hydrometeor shape and refractive index [*Bringi and Chandrasekar*, 2001]. In the case of an ice particle, the refractive index is directly related to the particle density [*Sihvola*, 1999]. We should note that in the radar community the definition of particle density is different

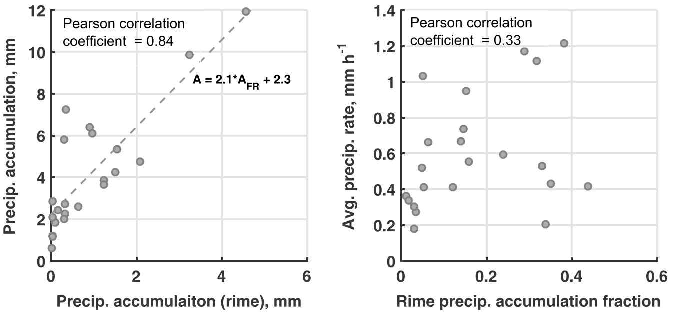

Figure 11. Scatterplots showing relations (left) between rime precipitation accumulation and precipitation accumulations and (right) between rime precipitation accumulation fraction and average precipitation rate.

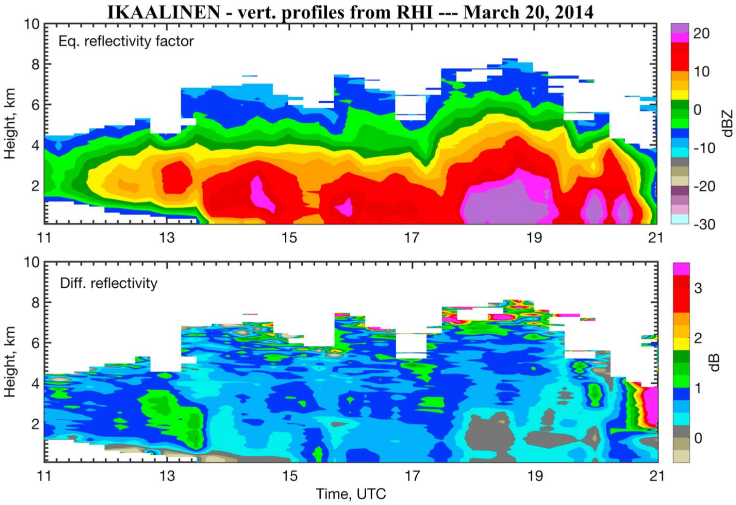

Figure 12. Ikaalinen radar VPT plots of reflectivity and differential reflectivity for 20 March 2014 case. The VPT plots are generated from the RHI scans that were carried out every 15 min.

from the bulk density used in connection with aircraft studies. The particle density, used to compute the particle refractive index and radar variables, is the mass of the particle divided by the volume of a prolate or oblate spheroid. The length of a spheroid major axis typically coincided with the particle maximum dimension. The minor axis is determined such that the spheroid closely approximates the particle shape, see, e.g., *Hogan et al.* [2012] for the discussion on how the spheroidal dimensions can be defined. The particle density defined in this way is typically larger than the bulk density and can be used for computations of the particle refractive index.

During the fill-in stage of riming growth, see Table 1, the particle mass is increasing while the maximum dimension stays constant. If the particle shape is also not changing as was hypothesized to be the case for aggregates, the measured differential reflectivity, Z_{dr}, should increase as FR increases, see *Bringi and Chandrasekar* [2001, p. 63] for an explanation of the connection between the particle density and values of dual-polarization radar variables. On the other hand, if the particle becomes more spherical, as expected to be the case for crystals, the Z_{dr} should decrease with an increase in FR. Therefore, dual-polarization radar observations can be used to test the conceptual model describing the evolution of particle shape during riming growth.

To test the conceptual model, Ikaalinen radar observations of reflectivity, Z, and differential reflectivity are compared to FR, mean snow density, and computed differential reflectivity values for the two analyzed events. From the RHI measurements that are performed every 15 min, a time series of vertical profiles (VPT) of reflectivity and differential reflectivity above the measurement site were constructed. Both the reflectivity factor and differential reflectivity values were averaged over 1 km range. Time series of Z and Z_{dr} values were also computed from observations of PSD and FR. To compute the radar variables *Leinonen* [2014] implementation of T-matrix code [*Mishchenko and Travis*, 1994; *Wielaard et al.*, 1997] is utilized. Since the dual-polarization radar observations are sensitive to particle aspect ratios, AR, the computation are performed for various AR values.

In Figure 12 VPT observations of reflectivity and differential reflectivity for the 20 March 2014 event are shown. From the lowest reliable altitude, which is about 500 m above the ground, time series of measured Z and Z_{dr} values are selected. These values are then compared to the computed ones as shown in Figure 13. It can be seen that the computed and measured reflectivity values agree rather well. In this case, the computed reflectivity values did not change much with AR and the ones computed using $AR = 0.6$ are shown. The differential reflectivity, as expected, reacts strongly to changes in AR. In the figure two curves with AR of 0.4 and 0.6 are

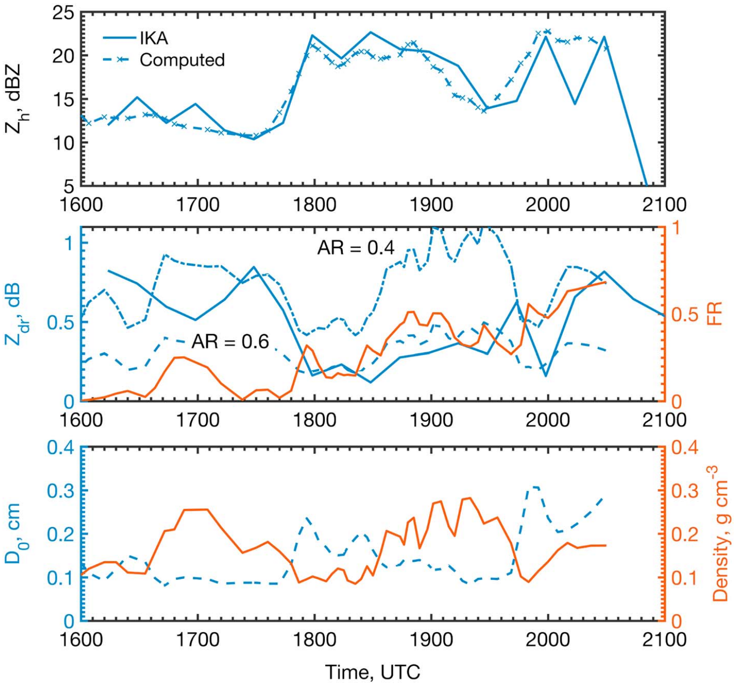

Figure 13. Comparison of Z_{dr}, FR, D_0, and ensemble mean density. The Z_{dr} time series are taken from the lowest reliable height, which is about 500 m above the measurement station.

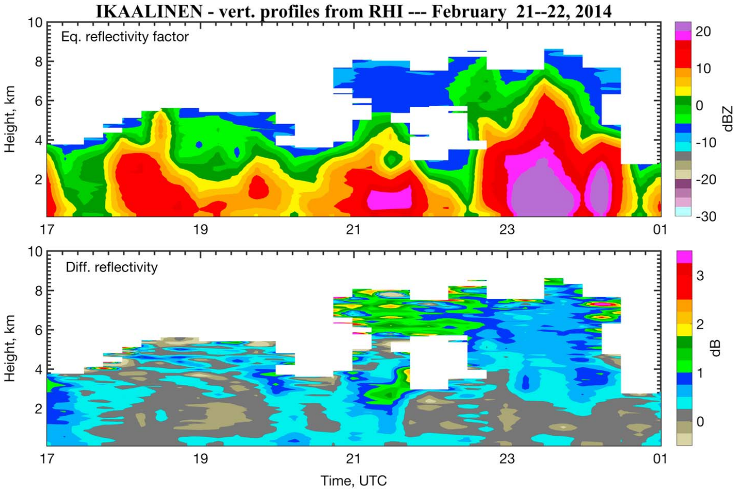

Figure 14. Same as Figure 12 but for the case of 21 February 2014.

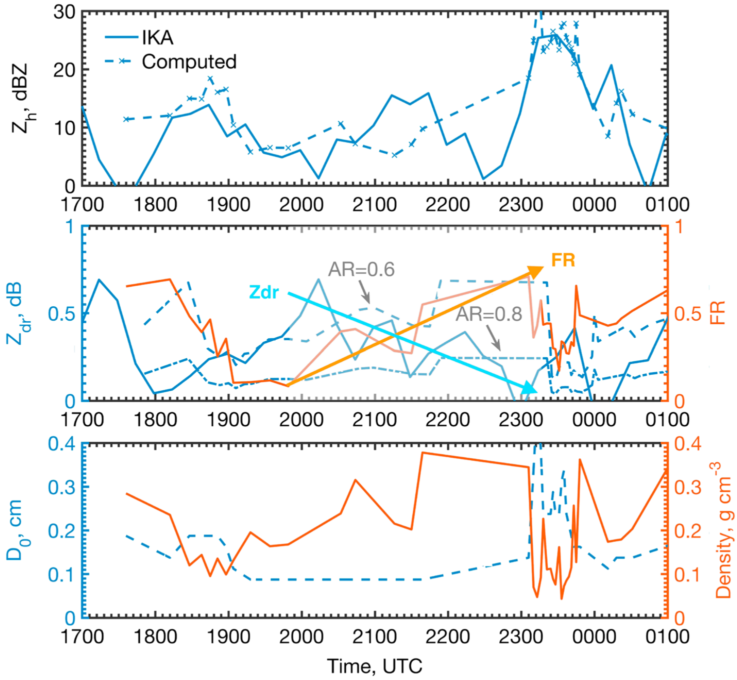

Figure 15. Same as Figure 13 but for 21 February 2014. The gray shading shows the time where graupel growth is detected, Z_{dr} decreases while FR increases.

shown. Between 1600 and 1800 UTC, the Z_{dr} curve computed with $AR = 0.4$ agrees better with the measurements. Between 1800 and 2000 UTC the 0.6 curve is in better agreement with the data. During this time the FR was steadily increasing from 0.1 to 0.5, while at the same time Z_{dr} has also increased. The Z_{dr} computations show that this increase in Z_{dr} is due to the change in density, which is partially caused by the change in FR. Furthermore, the computations show that the particle shape stays constant during this time. This observation supports the conceptual model of riming growth of snow aggregates.

A different story can be deduced from 21 to 22 February 2014 event. The corresponding observations are presented in Figures 14 and 15. The agreement between measured and computed reflectivity values are not as good as for the 20 March event. It should be noted, however, that the agreement during the heavy precipitation period, between 2300 and 0000 UTC, is rather good. The other interesting time period is between just before 2000 UTC and just after 2300 UTC, this period is marked by gray shading in the Z_{dr} plot. During this period the Z_{dr} decreases while FR increases. The Z_{dr} computations indicate that this decrease is due to the change in AR, which changes from 0.6 to 0.8 during this time period. This pattern is consistent with riming growth of planar crystals, as was hypothesized in the conceptual model. During this period the observed D_0 values are close to 1 mm, which are also consistent with presence of crystals/rimed crystals.

Often, it is assumed that differential reflectivity and other dual-polarization radar variables should decrease because of riming [*Straka et al.*, 2000; *Liu and Chandrasekar*, 2000; *Giangrande et al.*, 2016]. The motivation for this is that heavy riming would transform an ice particle to graupel. A graupel particle typically would have a quasi-spherical shape, and therefore, the differential reflectivity will become smaller. The presented analysis indicates that care should be taken while making conclusions about riming presence from the analysis of dual-polarization radar measurements, since riming growth of aggregates could produce the opposite to the expected pattern.

4. Discussion and Conclusions

Following the assumption proposed for a new ice particle property-based microphysical scheme [*Morrison and Grabowski*, 2008; *Morrison and Milbrandt*, 2015], the ice particle rime mass fraction was retrieved from ensemble mean snow density measurements. At the first step of the retrieval, a reference $m(D)$ relation, deviations from which could be interpreted as snowflake mass growth by riming, was determined. The relation represents particles with the masses belonging to the fifth percentile for a given dimension. The selection of the particles is somewhat arbitrary, but follows a rule that these particles should be the lightest observed. The derived relation $m = 0.0053D_{\mathrm{max}}^{2.05}$ can be treated as a relation of unrimed snowflakes. Since the relation is computed from observations recorded during 22 events that took place in Southern Finland, we cannot exclude potential differences, if one uses it for a characterization of snowfall taking place in a different geographical region. It should also be noted that the relation is different from the ones listed in literature. For example, it gives heavier particles than *Brown and Francis* [1995] but agrees relatively well with *Heymsfield et al.* [2004].

To verify the proposed rime mass fraction retrieval approach, a method to link FR and microwave radiometer liquid water path observations was proposed. Given that the exponent of the retrieved $m(D)$ is very close to 2, the dependence of the computed effective liquid water path on D can be ignored. The comparison between ELWP and LWP showed that they react to the same processes that take place in the observed precipitation systems. The computed ELWP is about half of LWP. There are also differences in timings and appearances of certain features, which could be attributed to the deviation of effective paths of snowflakes from the vertical.

Using the derived rime mass fraction, analysis of riming mass growth effects on snowfall was analyzed. From observations of 22 events, it was found that riming is responsible for 5% to 40% of precipitation mass. Furthermore, a correlation between rime precipitation fraction and precipitation accumulation was observed. This correlation, however, is determined by just two events and may not be statistically significant. A much weaker correlation between the average precipitation rate and rime precipitation fraction also points in the direction that there is no strong link between average precipitation amount and riming for an event.

The comparison of dual-polarization radar observations and retrieved snowflake microphysical properties was also carried out. It was shown that this comparison can be used to test the validity of the conceptual riming model. In this study the conceptual model of *Heymsfield* [1982] was modified slightly by hypothesizing that shapes of aggregates would not change during riming. Therefore, it is expected that Z_{dr} should increase with riming, as was observed on 20 March 2014. For crystals, on the other hand, the opposite is expected and was observed on 21 February between 2000 and 2300 UTC where the Z_{dr} was decreasing while FR was increasing. This behavior is expected to be more common for smaller ice particles. The overall connection between dual-polarization radar observations and riming is therefore expected to be more complex than currently expected. In some cases Z_{dr} will increase, while in the other it will decrease, depending on initial particle sizes.

Acknowledgments
We would like to acknowledge the Hyytiälä station and University of Helsinki personnel for the daily tasks with measurements, especially mentioning Matti Leskinen and Janne Levula. The research of J.T. and D.M. was supported by Academy of Finland (grant 305175) and the Academy of Finland Finnish Center of Excellence program (grant 3073314). A.v.L. was funded by grant of the Vilho, Yrjö and Kalle Väisälä Foundation and by SESAR Joint Undertaking Horizon 2020 grant agreement 699221 (PNOWWA). The instrumentation used in this study was supported by NASA Global Precipitation Measurement Mission ground validation program and by the Office of Science U.S. Department of Energy ARM program. The BAECC data used in this study are available from DOE ARM archives. The data from winter 2014/2015 are available by request from the first author (dmitri.moisseev@helsinki.fi).

References

Barthazy, E., and R. Schefold (2006), Fall velocity of snowflakes of different riming degree and crystal types, *Atmos. Res.*, *82*(1), 391–398.

Borys, R. D., D. H. Lowenthal, and D. L. Mitchell (2000), The relationships among cloud microphysics, chemistry, and precipitation rate in cold mountain clouds, *Atmos. Environ.*, *34*(16), 2593–2602.

Borys, R. D., D. H. Lowenthal, S. A. Cohn, and W. O. J. Brown (2003), Mountaintop and radar measurements of anthropogenic aerosol effects on snow growth and snowfall rate, *Geophys. Res. Lett.*, *30*(10), 1538, doi:10.1029/2002GL016855.

Brandes, E. A., K. Ikeda, G. Zhang, M. Schönhuber, and R. M. Rasmussen (2007), A statistical and physical description of hydrometeor distributions in Colorado snowstorms using a video disdrometer, *J. Appl. Meteorol. Clim.*, *46*(5), 634–650.

Bringi, V. N., and V. Chandrasekar (2001), *Polarimetric Doppler Weather Radar: Principles and Applications*, Cambridge Univ. Press, New York.

Brown, P. R. A., and P. N. Francis (1995), Improved measurements of the ice water content in cirrus using a total-water probe, *J. Atmos. Oceanic Technol.*, *12*(2), 410–414, doi:10.1175/1520-0426(1995)012<0410:IMOTIW>2.0.CO;2.

Cadeddu, M. P., J. C. Liljegren, and D. D. Turner (2013), The Atmospheric Radiation Measurement (ARM) program network of microwave radiometers: Instrumentation, data, and retrievals, *J. Atmos. Meas. Tech*, *6*(9), 2359–2372, doi:10.5194/amt-6-2359-2013.

Chandrasekar, V., R. Keranen, S. Lim, and D. Moisseev (2013), Recent advances in classification of observations from dual polarization weather radars, *Atmos. Res.*, *119*, 97–111, doi:10.1016/j.atmosres.2011.08.014.

Ellis, S., et al. (2012), Towards the detection of aircraft icing conditions using operational dual-polarimetric radar, in *Proceedings of the 7th European Conference On Radar In Meteorology And Hydrology*, pp. 24–29, ERAD, Toulouse, France.

Erfani, E., and D. L. Mitchell (2017), Growth of ice particle mass and projected area during riming, *Atmos. Chem. Phys.*, *17*(2), 1241–1257, doi:10.5194/acp-17-1241-2017.

Field, P. R., and A. J. Heymsfield (2015), Importance of snow to global precipitation, *Geophys. Res. Lett.*, *42*, 9512–9520, doi:10.1002/2015GL065497.

Garrett, T. J., and S. E. Yuter (2014), Observed influence of riming, temperature, and turbulence on the fallspeed of solid precipitation, *Geophys. Res. Lett.*, *41*, 6515–6522, doi:10.1002/2014GL061016.

Giangrande, S. E., T. Toto, A. Bansemer, M. R. Kumjian, S. Mishra, and A. V. Ryzhkov (2016), Insights into riming and aggregation processes as revealed by aircraft, radar, and disdrometer observations for a 27 April 2011 widespread precipitation event, *J. Geophys. Res. Atmos.*, *121*, 5846–5863, doi:10.1002/2015JD024537.

Grazioli, J., G. Lloyd, L. Panziera, C. R. Hoyle, P. J. Connolly, J. Henneberger, and A. Berne (2015), Polarimetric radar and in situ observations of riming and snowfall microphysics during CLACE 2014, *Atmos. Chem. Phys.*, *15*(23), 13,787–13,802, doi:10.5194/acp-15-13787-2015.

Harimaya, T., and M. Sato (1989), Measurement of the riming amount on snowflakes, *J. Fac. Sci. Hokkaido Univ.*, *8*(4), 355–366.

Heymsfield, A. J. (1982), A comparative study of the rates of development of potential graupel and hail embryos in high plains storms, *J. Atmos. Sci.*, *39*(12), 2867–2897, doi:10.1175/1520-0469(1982)039<2867:ACSOTR>2.0.CO;2.

Heymsfield, A. J., A. Bansemer, C. Schmitt, C. Twohy, and M. R. Poellot (2004), Effective ice particle densities derived from aircraft data, *J. Atmos. Sci.*, *61*(9), 982–1003, doi:10.1175/1520-0469(2004)061<0982:EIPDDF>2.0.CO;2.

Hobbs, P. V. (1978), Organization and structure of clouds and precipitation on the mesoscale and microscale in cyclonic storms, *Rev. Geophys.*, *16*(4), 741–755, doi:10.1029/RG016i004p00741.

Hobbs, P. V., S. Chang, and J. D. Locatelli (1974), The dimensions and aggregation of ice crystals in natural clouds, *J. Geophys. Res.*, *79*(15), 2199–2206, doi:10.1029/JC079i015p02199.

Hogan, R. J., P. N. Francis, H. Flentje, A. J. Illingworth, M. Quante, and J. Pelon (2003), Characteristics of mixed-phase clouds. I: Lidar, radar and aircraft observations from CLARE'98, *Q. J. R. Meteorol. Soc.*, *129*(592), 2089–2116, doi:10.1256/rj.01.208.

Hogan, R. J., L. Tian, P. R. A. Brown, C. D. Westbrook, A. J. Heymsfield, and J. D. Eastment (2012), Radar scattering from ice aggregates using the horizontally aligned oblate spheroid approximation, *J. Appl. Meteorol. Climatol.*, *51*(3), 655–671, doi:10.1175/JAMC-D-11-074.1.

Kajikawa, M. (1989), Observation of the falling motion of early snowflakes. 2. On the variation of falling velocity, *J. Meteorol. Soc. Jpn*, *67*(5), 731–738.

Kalesse, H., W. Szyrmer, S. Kneifel, P. Kollias, and E. Luke (2016), Fingerprints of a riming event on cloud radar Doppler spectra: Observations and modeling, *Atmos. Chem. Phys.*, *16*(5), 2997–3012, doi:10.5194/acp-16-2997-2016.

Kneifel, S., A. von Lerber, J. Tiira, D. Moisseev, P. Kollias, and J. Leinonen (2015), Observed relations between snowfall microphysics and triple-frequency radar measurements, *J. Geophys. Res. Atmos.*, *120*, 6034–6055, doi:10.1002/2015JD023156.

Leinonen, J. (2014), High-level interface to T-matrix scattering calculations: Architecture, capabilities and limitations, *Opt. Express*, *22*(2), 1655–1660, doi:10.1364/OE.22.001655.

Leinonen, J., D. Moisseev, M. Leskinen, and W. A. Petersen (2012), A climatology of disdrometer measurements of rainfall in Finland over five years with implications for global radar observations, *J. Appl. Meteorol. Climatol.*, *51*(2), 392–404, doi:10.1175/JAMC-D-11-056.1.

Liu, H., and V. Chandrasekar (2000), Classification of hydrometeors based on polarimetric radar measurements: Development of fuzzy logic and neuro-fuzzy systems, and in situ verification, *J. Atmos. Oceanic Technol.*, *17*(2), 140–164, doi:10.1175/1520-0426(2000)017<0140:COHBOP>2.0.CO;2.

Locatelli, J. D., and P. V. Hobbs (1974), Fall speeds and masses of solid precipitation particles, *J. Geophys. Res.*, *79*(15), 2185–2197.

Lohmann, U. (2004), Can anthropogenic aerosols decrease the snowfall rate?, *J. Atmos. Sci.*, *61*(20), 2457–2468, doi:10.1175/1520-0469(2004)061<2457:CAADTS>2.0.CO;2.

Magono, C., and T. Nakamura (1965), Aerodynamic studies of falling snowflakes, *J. Meteorol. Soc. Jpn. Ser. II*, *43*(3), 139–147.

Matejka, T. J., R. A. Houze, and P. V. Hobbs (1980), Microphysics and dynamics of clouds associated with mesoscale rainbands in extratropical cyclones, *Q. J. R. Meteorol. Soc.*, *106*(447), 29–56, doi:10.1002/qj.49710644704.

Matrosov, S. Y., A. J. Heymsfield, and Z. Wang (2005), Dual-frequency radar ratio of nonspherical atmospheric hydrometeors, *Geophys. Res. Lett.*, *32*(13), L13816, doi:10.1029/2005GL023210.

Mishchenko, M. I., and L. D. Travis (1994), T-matrix computations of light scattering by large spheroidal particles, *Opt. Commun.*, *109*(1), 16–21, doi:10.1016/0030-4018(94)90731-5.

Mitchell, D. L. (1996), Use of mass- and area-dimensional power laws for determining precipitation particle terminal velocities, *J. Atmos. Sci.*, *53*(12), 1710–1723, doi:10.1175/1520-0469(1996)053<1710:UOMAAD>2.0.CO;2.

Mitchell, D. L., R. Zhang, and R. L. Pitter (1990), Mass-dimensional relationships for ice particles and the influence of riming on snowfall rates, *J. Appl. Meteor.*, *29*(2), 153–163, doi:10.1175/1520-0450(1990)029<0153:MDRFIP>2.0.CO;2.

Moisseev, D. N., and V. Chandrasekar (2007), Examination of the μ-Λ relation suggested for drop size distribution parameters, *J. Atmos. Oceanic Technol.*, *24*(5), 847–855, doi:10.1175/JTECH2010.1.

Moisseev, D. N., S. Lautaportti, J. Tyynela, and S. Lim (2015), Dual-polarization radar signatures in snowstorms: Role of snowflake aggregation, *J. Geophys. Res. Atmos.*, *120*(24), 12,644–12,655, doi:10.1002/2015JD023884.

Morrison, H., and W. W. Grabowski (2008), A novel approach for representing ice microphysics in models: Description and tests using a kinematic framework, *J. Atmos. Sci.*, *65*(5), 1528–1548, doi:10.1175/2007JAS2491.1.

Morrison, H., and J. A. Milbrandt (2015), Parameterization of cloud microphysics based on the prediction of bulk ice particle properties. Part I: Scheme description and idealized tests, *J. Atmos. Sci.*, *72*(1), 287–311, doi:10.1175/JAS-D-14-0065.1.

Mosimann, L. (1995), An improved method for determining the degree of snow crystal riming by vertical Doppler radar, *Atmos. Res.*, *37*(4), 305–323, doi:10.1016/0169-8095(94)00050-N.

Mosimann, L., E. Weingartner, and A. Waldvogel (1994), An analysis of accreted drop sizes and mass on rimed snow crystals, *J. Atmos. Sci.*, *51*(11), 1548–1558, doi:10.1175/1520-0469(1994)051<1548:AAOADS>2.0.CO;2.

Moss, S., and D. Johnson (1994), Aircraft measurements to validate and improve numerical model parametrisations of ice to water ratios in clouds, *Atmos. Res.*, *34*(1), 1–25, doi:10.1016/0169-8095(94)90078-7.

Petäjä, T., et al. (2016), BAECC: A field campaign to elucidate the impact of biogenic aerosols on clouds and climate, *Bull. Amer. Meteor. Soc.*, *97*(10), 1909–1928, doi:10.1175/BAMS-D-14-00199.1.

Pruppacher, H., and J. Klett (1996), *Microphysics of Clouds and Precipitation*, Atmos. and Oceanogr. Sci. Libr., Springer, Netherlands.

Ryzhkov, A., P. Zhang, H. Reeves, M. Kumjian, T. Tschallener, S. Trömel, and C. Simmer (2016), Quasi-vertical profiles—A new way to look at polarimetric radar data, *J. Atmos. Oceanic Technol.*, *33*(3), 551–562, doi:10.1175/JTECH-D-15-0020.1.

Saleeby, S. M., W. R. Cotton, D. Lowenthal, and J. Messina (2013), Aerosol impacts on the microphysical growth processes of orographic snowfall, *J. Appl. Meteorol. Climatol.*, *52*(4), 834–852, doi:10.1175/JAMC-D-12-0193.1.

Shupe, M. D., S. Y. Matrosov, and T. Uttal (2006), Arctic mixed-phase cloud properties derived from surface-based sensors at SHEBA, *J. Atmos. Sci.*, *63*(2), 697–711, doi:10.1175/JAS3659.1.

Sihvola, A. (1999), *Electromagnetic Mixing Formulas and Applications*, Inst. of Electrical Eng., London.

Straka, J., D. Zrnić, and A. Ryzhkov (2000), Bulk hydrometeor classification and quantification using polarimetric radar data: Synthesis of relations, *J. App. Meteorol.*, *39*(8), 1341–1372, doi:10.1175/1520-0450(2000)039<1341:BHCAQU>2.0.CO;2.

Tiira, J., D. N. Moisseev, A. von Lerber, D. Ori, A. Tokay, L. F. Bliven, and W. Petersen (2016), Ensemble mean density and its connection to other microphysical properties of falling snow as observed in Southern Finland, *Atmos. Meas. Tech.*, *9*(9), 4825–4841, doi:10.5194/amt-9-4825-2016.

Westbrook, C. D., and A. J. Illingworth (2011), Evidence that ice forms primarily in supercooled liquid clouds at temperatures −27°C, *Geophys. Res. Lett.*, *38*, L14808, doi:10.1029/2011GL048021.

Westbrook, C. D., R. C. Ball, P. R. Field, and A. J. Heymsfield (2004), Universality in snowflake aggregation, *Geophys. Res. Lett.*, *31*, L15104, doi:10.1029/2004GL020363.

Wielaard, D. J., M. I. Mishchenko, A. Macke, and B. E. Carlson (1997), Improved T-matrix computations for large, nonabsorbing and weakly absorbing nonspherical particles and comparison with geometrical-optics approximation, *Appl. Opt.*, *36*(18), 4305–4313, doi:10.1364/AO.36.004305.

Wood, N. B., T. S. L'Ecuyer, F. L. Bliven, and G. L. Stephens (2013), Characterization of video disdrometer uncertainties and impacts on estimates of snowfall rate and radar reflectivity, *Atmos. Meas. Tech.*, *6*(12), 3635–3648, doi:10.5194/amt-6-3635-2013.

Zawadzki, I., E. Jung, and G. Lee (2010), Snow studies. Part I: A study of natural variability of snow terminal velocity, *J. Atmos. Sci.*, *67*(5), 1591–1604, doi:10.1175/2010JAS3342.1.

Paper IV

Atmos. Meas. Tech., 13, 1227–1241, 2020
https://doi.org/10.5194/amt-13-1227-2020

Atmospheric Measurement Techniques
Open Access

Unsupervised classification of vertical profiles of dual polarization radar variables

Jussi Tiira[1] **and Dmitri Moisseev**[1,2]

[1]Institute for Atmospheric and Earth System Research/Physics, Faculty of Science, University of Helsinki, Helsinki, Finland
[2]Finnish Meteorological Institute, Helsinki, Finland

Correspondence: Jussi Tiira (jussi.tiira@helsinki.fi)

Received: 9 August 2019 – Discussion started: 20 August 2019
Revised: 21 January 2020 – Accepted: 2 February 2020 – Published: 13 March 2020

Abstract. Vertical profiles of polarimetric radar variables can be used to identify fingerprints of snow growth processes. In order to systematically study such manifestations of precipitation processes, we have developed an unsupervised classification method. The method is based on k-means clustering of vertical profiles of polarimetric radar variables, namely reflectivity, differential reflectivity and specific differential phase. For rain events, the classification is applied to radar profiles truncated at the melting layer top. For the snowfall cases, the surface air temperature is used as an additional input parameter. The proposed unsupervised classification was applied to 3.5 years of data collected by the Finnish Meteorological Institute Ikaalinen radar. The vertical profiles of radar variables were computed above the University of Helsinki Hyytiälä station, located 64 km east of the radar. Using these data, we show that the profiles of radar variables can be grouped into 10 and 16 classes for rainfall and snowfall events, respectively. These classes seem to capture most important snow growth and ice cloud processes. Using this classification, the main features of the precipitation formation processes, as observed in Finland, are presented.

1 Introduction

Globally, the majority of precipitation during both winter and summer originates from ice clouds (Field and Heymsfield, 2015). At higher latitudes winter precipitation occurs in the form of snow, which can have a dramatic impact on human life (Juga et al., 2012). There are a number of challenges in remote sensing of winter precipitation or ice clouds, i.e., quantitative estimation of ice water content or precipitation rate (von Lerber et al., 2017), identification of dangerous weather conditions, etc. To address these challenges, advances in identifying and documenting the processes that take place in ice clouds are needed.

There are several pathways by which ice particles grow, such as vapor deposition, aggregation and riming. Occurrence of these processes depends on environmental conditions. Interpretation of radar observations is based on our understanding of the link between microphysical and scattering properties of hydrometeors. By identifying particle types in observations, we may conclude what processes took place. Currently, dual-polarization radar observations are used in fuzzy logic classification to identify the dominant hydrometeor type present in a radar volume (e.g., Chandrasekar et al., 2013; Thompson et al., 2014). Such methods work very well for classification of hydrometeors of summer precipitations and some features of winter precipitation types. The main challenge is the lack of distinction in dual-polarization radar variables between some ice particle habits. For example, large low-density aggregates and graupel may have similar radar characteristics. Furthermore, these methods perform classification on radar volume by volume basis, without taking into account surrounding observations. Recently, a modification for the hydrometeor classifiers was proposed to make the algorithms aware of the surroundings by incorporating measurements from neighboring radar volumes (Bechini and Chandrasekar, 2015; Grazioli et al., 2015b). This step has greatly improved classification robustness, but it aims to identify particle types instead of fingerprints of microphysical processes.

In the past 10 years, a number of studies reported signatures of ice growth processes in dual-polarization radar observations. Kennedy and Rutledge (2011) have reported bands of increased values of specific differential phase, K_{dp}, and differential reflectivity, Z_{DR}, in Colorado snowstorms. These bands took place at altitudes where ambient air temperature was around −15 °C and their occurrence was attributed to growth of dendritic crystals. Andrić et al. (2013) have implemented a simple steady-state single-column snow growth model to explain the main features of the bands. It was also observed that the occurrence of K_{dp} bands can be linked to heavier surface precipitation (Kennedy and Rutledge, 2011; Bechini et al., 2013). Moisseev et al. (2015) have advocated that the K_{dp} bands occur only in precipitation systems with high enough cloud-top heights, where a large number of ice crystals can be generated by either heterogeneous or homogeneous ice nucleation. Using a larger dataset, Griffin et al. (2018) have shown that the K_{dp} bands can be linked to formation of ice by homogeneous ice nucleation at cloud tops. Furthermore, it was shown that the K_{dp} bands can be linked to onset of aggregation (Moisseev et al., 2015), which tends to occur more frequently in environments with higher water vapor content (Schneebeli et al., 2013). In addition to the above-listed studies, different aspects of these bands were presented by Trömel et al. (2014), Oue et al. (2018), and Kumjian and Lombardo (2017). Besides K_{dp} bands in the dendritic growth zone, several studies (e.g., Grazioli et al., 2015a; Sinclair et al., 2016; Kumjian et al., 2016; Giangrande et al., 2016) have reported K_{dp} observations in the temperature region where Hallett–Mossop (H–M; Hallett and Mossop, 1974) rime-splintering secondary ice production takes place (Field et al., 2016). Sinclair et al. (2016) have shown that such observations can be used to test representation of the secondary ice production in numerical weather prediction models. Other dual-polarization observations that show notable features are high-Z_{DR} regions surrounding the cores of snow-generating cells (Kumjian et al., 2014) and at the top of ice clouds which can be linked to the presence of planar crystals and further to the presence of supercooled liquid water, providing very favorable conditions for their growth at these temperatures (Williams et al., 2015; Oue et al., 2016).

As presented above, the fingerprints of snow growth processes can occur in the form of bands in stratiform clouds, either embedded in the precipitation or on top of a cloud, or in the form of convective generating cells. To identify and document such features, a classification method that uses vertical profiles of dual-polarization radar observations can be used. In this study, we have developed such an unsupervised classification method based on k-means clustering of vertical profiles of polarimetric radar variables, namely reflectivity, differential reflectivity and specific differential phase. The proposed classification is applied to 3.5 years of data collected with the Finnish Meteorological Institute Ikaalinen radar.

The paper is structured as follows. Section 2 describes polarimetric radar and temperature data and their preprocessing. The unsupervised classification method is presented in Sect. 3. Section 4 is dedicated to the analysis and interpretation of the classification results and Sect. 5 presents the conclusions.

2 Data

In this study, we use vertical profiles of polarimetric radar observables of precipitation over the Hyytiälä forestry station in Juupajoki, Finland, collected using Ikaalinen weather radar, hereafter IKA. The radar is located 64 km west from the station. The measurements were performed between January 2014 and May 2017, partly during the Biogenic Aerosols – Effects on Clouds and Climate (BAECC; Petäjä et al., 2016) field campaign which took place at the measurement site in 2014.

The classification training material includes all precipitation events from this period, where, after preprocessing (see Sect. 2.2), there were no major data quality problems identified. Since synoptic conditions may be similar even in cases where there are gaps in observed precipitation, we define any two precipitation events to be separate from each other if a continuous gap in reflectivity between them exceeds 12 h. See Sect. 4 for more discussion. During the observation period, we identified 74 snow and 123 rain events that meet these conditions. Generally, the full temporal extent of an event includes radar profiles in which precipitation has not reached the ground. A list of the precipitation events is given in the Supplement.

In order to link features identified in vertical profiles of radar variables to precipitation processes, information on the ambient temperature is needed. For this purpose we use vertical profiles of temperature from the National Center for Environmental Prediction (NCEP) Global Data Assimilation System (GDAS) output for Hyytiälä interpolated to match the temporal and vertical resolution of the vertical profiles of radar variables used in this study. The original temporal resolution of the NCEP GDAS data over Hyytiälä is 3 h, and the vertical resolution is 25 hPa between the 1000 and 900 hPa levels and 50 hPa elsewhere.

2.1 Vertical profiles of dual-polarization radar observables

The radar profiles are extracted from IKA C-band radar range height indicator (RHI) measurements. IKA performs RHI scans directly towards Hyytiälä station every 15 min. The values of the radar profiles above Hyytiälä are estimated as horizontal medians over a range of 1 km from the station. The medians are taken over constant altitudes using linear spatial interpolation between the rays. The target bin size of the height interpolation is 50 m.

In this investigation, vertical profiles of equivalent reflectivity factor, Z_{e}, differential reflectivity, Z_{DR}, and specific differential phase, K_{dp}, are considered in the classification.

The K_{dp} values were computed using the Maesaka et al. (2012) method as implemented in the Python ARM Radar Toolkit (Py-ART; Helmus and Collis, 2016). The method assumes that propagation differential phase, ϕ_{DP}, increases monotonically with increasing range from the radar. In this study, we mainly focus on precipitation processes typically occurring in stratiform precipitation, where negative K_{dp} is not important. The Maesaka et al. (2012) algorithm should be avoided when studying precipitation events with lightning activity, where negative K_{dp} may occur due to electrification (Caylor and Chandrasekar, 1996). Negative K_{dp} has also been reported during events of conical graupel which have been linked to observations of generating cells (Oue et al., 2015). The total fraction of profiles analyzed in this study where conical graupel appear or which represent strong convective cells with a possibility for lightning activity is expected to be marginal, as discussed further in Sect. 4.

2.2 Radar data preprocessing

Prior to training or using the polarimetric radar vertical profile data for the classification, noise and clutter filtering is applied to the binned profiles, which is followed by normalization and smoothing. Additionally, there are different preprocessing procedures for rain and snow events that allow ambient temperature to be taken into account in the classification. This section describes the mentioned preprocessing steps in more detail.

2.2.1 Profile truncation

This paper focuses on identifying, characterizing and investigating the frequencies of different types of vertical structures of dual-polarization radar variables specifically from the perspective of detecting, documenting and studying ice processes. Therefore, before the classification, vertical profiles of radar variables are truncated at the top of the melting layer (ML), if one is present. Cases where melting layer signatures were not identified and surface air temperature was 1 °C or lower are placed in the snowfall category and investigated separately.

Following Wolfensberger et al. (2015), who have used gradient detection on a combination of normalized Z_{H} and ρ_{hv} for ML detection, we combine ρ_{hv} and standardized Z_{e} and Z_{DR} into a melting layer indicator:

$$I_{\mathrm{ML}} = \hat{Z}_{\mathrm{e}} \hat{Z}_{\mathrm{DR}} (1 - \rho_{\mathrm{hv}}). \tag{1}$$

The same standardization of Z_{e} and Z_{DR} is used here as in classification, as described in Sect. 3.1. In this study, instead of gradient detection, we use peak detection on smoothed I_{ML} to find the ML. Peaks are defined as any sample whose direct neighbors have a smaller amplitude and are found in three steps.

1. Peak detection is performed with thresholds for absolute peak amplitude and prominence ($H_{I_{\mathrm{ML}}}$, as described below), with chosen values of 2 and 0.3, respectively. The SciPy (version 1.3; Virtanen et al., 2020) implementation of the peak detection algorithm[1] is used here.

2. Median ML height, $\tilde{h}_{\mathrm{ML}}$, is computed as the weighted median of the peak altitudes, h_i, using the product of peak absolute amplitude and $H_{I_{\mathrm{ML}}}$ as weights. Peaks above a chosen height threshold of $h_{\mathrm{thresh}} = 4200\,\mathrm{m}$ are ignored in this step.

3. Step 1 is run again, this time only considering data within $\tilde{h}_{\mathrm{ML}} \pm \Delta h_{\mathrm{ML}}$ with a chosen Δh_{ML} value of 1500 m. If multiple peaks exceed the threshold values within a profile, the one with the highest amplitude is used.

The ML top height $h_{\mathrm{ML,top}}$ is estimated as the altitude corresponding to the $0.3 H_{I_{\mathrm{ML}}}$ upper contour of the peak. Peak prominence, H, is a measure of how much a peak stands out from the surrounding baseline value and is defined as the difference between the peak value and its baseline. The baseline is the lowest contour line of the peak encircling it but containing no higher peak (Virtanen et al., 2020).

It should be noted that in steps 2 and 3, the analysis height is limited to reflect the climatology of temperature profiles on the measurement site. In step 2, we assume the ML to be always below h_{thresh}, and in step 3 we expect melting layer height not to change more than Δh_{ML} during an event. Such use of domain knowledge allows more robust ML detection in situations where I_{ML} has high values elsewhere. This may occur in the dendritic growth layer (DGL), for example, where the crystals can be pristine enough to cause a significant increase in Z_{DR} and a decrease in ρ.

Sensitivity of the retrieved $h_{\mathrm{ML,top}}$ is tested for small changes in peak detection parameters discarding inconsistent values. A moving window median threshold filter is applied on time series of $h_{\mathrm{ML,top}}$ in order to discard rapid high-amplitude fluctuations caused by noise in Z_{DR}, for example. A rolling triangle mean with a window size of five profiles, corresponding to 1 h, is used for smoothing. Finally, linear interpolation and constant extrapolation is applied to $h_{\mathrm{ML,top}}$ on a per-precipitation-event basis to make the estimate continuous. This robust, albeit fairly complex, procedure produces a smooth estimate for melting layer top height. The results from the ML detection were analyzed manually and the events with errors were discarded. In 90 % of events in the original dataset, the ML was detected without errors.

The analysis of rain profiles is limited to a layer from $\Delta h_{\mathrm{margin}} = 300\,\mathrm{m}$ to 10 km above $h_{\mathrm{ML,top}}$. The purpose of the margin $\Delta h_{\mathrm{margin}}$ is to prevent properties of the melting layer from leaking to the clustering features. The truncation described in this section has no effect on the height bin size.

---

[1] Function scipy.signal.find_peaks.

Table 1. Standardization of radar variables, $[a, b] \to [0, 1]$.

	Rainfall		Snowfall	
	a	b	a	b
Z_e, dBZ	−10	38	−10	34
Z_{DR}, dB	0	3.1	0	3.3
K_{dp}, $^\circ$ km^{-1}	0	0.25	0	0.11

2.2.2 Absence of melting layer

Cutting the rain profiles at the top of the melting layer effectively provides information about the ambient temperature at the profile base. As temperature is a key factor driving the ice processes, such information should also be included in the classification process when there is no ML present. In order to introduce corresponding information on ambient temperature at the profile base, we use surface temperature as an extra classification parameter for events with snowfall on the surface. While it would be possible to use whole temperature profiles from soundings or numerical models as classification parameters, we feel that this may not be feasible for many potential key use cases of the classification method. With the wide availability of surface temperature observations in high temporal resolution and in real time, presumably this choice makes the classification method more accessible, especially for operational applications.

The analysis of snow profiles is limited to a layer between 0.2 and 10 km above ground level.

3 Classification method

The unsupervised classification method used in this study is based on clustering of dual-polarization radar observations, namely vertical profiles of K_{dp}, Z_{DR} and Z_e. Feature extraction is performed by applying principal component analysis (PCA) on standardized profiles. Clustering is applied to the principal components of the profiles using the k-means method (Lloyd, 1982). A flowchart of the whole process is shown in Fig. 1.

While the core method is identical for processing of all radar profiles, information on temperature is included in a slightly different way based on if it is raining or snowing on the surface. These differences are explained in Sect. 2.2.1 and 2.2.2 and highlighted in Fig. 1: for rain events, the profiles are cut at the top of the melting layer, and for events without a ML surface temperature is included as an extra classification variable. Using this approach, information on profile base ambient temperature is included in the classification process, and the analysis is limited to ice processes.

3.1 Feature extraction

The vertical resolution of the interpolated data is 50 m with bins from 200 m to 10 km altitude for snow events and from 300 m to 10 km above the melting layer top for rain events. Thus, with the three radar variables, each profile is described by a vector of 588 and 582 dimensions for snow and rain events, respectively. In this study, we apply PCA to standardized profiles of the polarimetric radar variables to extract features for the clustering phase.

A standardization of the preprocessed polarimetric radar data is performed to allow adequate weights for each variable in clustering. This was done separately for the snow and rain datasets in order to account for seasonal differences in the average values. We used standardization similar to that of Wolfensberger et al. (2015), normalizing typical ranges of values $[a, b] \to [0, 1]$, with the additional condition that the standardized variables should have approximately equal variances. The values a, b used in this study are listed in Table 1. The values of the standardized variables are not capped, but values greater than 1 are allowed when the unscaled values exceed b. Without the standardization, the dominance of each variable in classification would be determined by their variance.

The number of components explaining a significant portion of the total variance for the two training datasets was determined considering the scree test (Cattell, 1966), the Kaiser method, and the component and cumulative explained variance criteria. However, these criteria alone would allow such a low number of components that the inverse transformation from principal component space to the original would result in unrealistic profiles. Thus, the number of components was increased such that, visually, the inverse transformed profiles presented the significant features in the original profiles, up to the point where adding more components seemed to start explaining trivial features such as noise. For both rain and snow profile classification, the first 30 components are used as features. The high number of significant components suggests that reducing the dimensionality of radar observations is not trivial. An advantage of using PCA over simply sampling the profiles is that the former interconnects data from different heights and radar variables such that the components effectively represent features in the profile shapes, while sampling would rather be driven by absolute values at the individual sampling heights.

With snow profile classification, a proxy of the surface temperature, $P(T_s) = aT_s$, where a is a scaling parameter, is used as an additional feature. Thus, essentially, σ_{T_s} within a cluster is decreased with increasing a. In this study, the value of a was determined in an iterative process during the clustering phase, described in Sect. 3.2, such that, over the clusters, $\mathrm{median}(2\sigma_{T_s}) \approx 3\,^\circ$C. Thus, assuming T_s is normally distributed within a given cluster, approximately 95 % of the values of T_s would be typically within a range of 3 °C

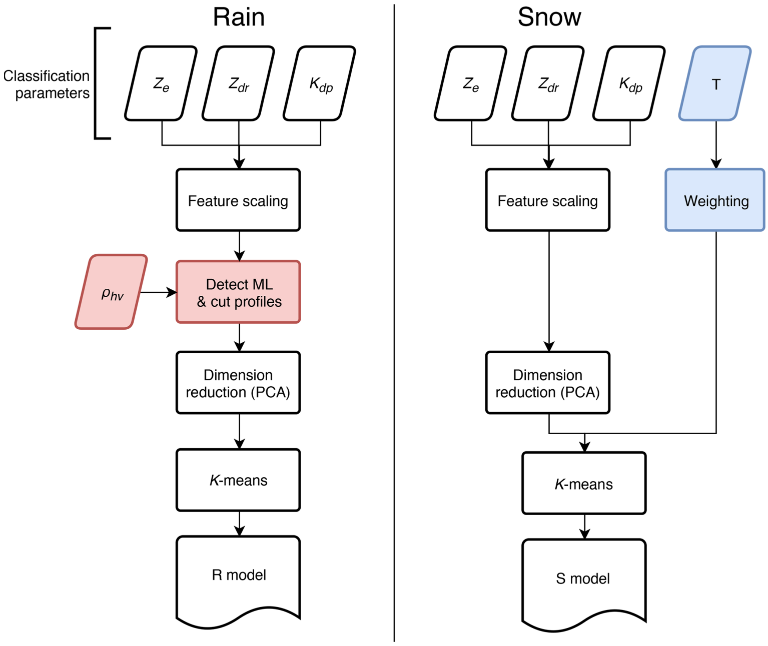

Figure 1. Vertical profile clustering method for creating classification models for rain and snow events.

from the cluster mean. A value of $a = 0.75$ was used in this study.

3.2 Clustering

In the present study, the widely used k-means method was chosen for clustering. The algorithm is known for its speed and easy implementation and interpretation. Limitations of the method include the assumption of isotropic data space, sensitivity to outliers (Raykov et al., 2016) and the possibility to converge into a local minimum which may result in counterintuitive results. In our analysis, the anisotropy of the data space is partly mitigated by the PCA transformation. After the transformation, there is still anisotropy, but the transitions in density of the data points in PCA space are smooth (not shown), such that the k-means method seems to produce clusters of meaningful sizes and shapes. The problem of local minima is addressed using the k-means++ method (Arthur and Vassilvitskii, 2007) to distribute the initial cluster seeds in a way that optimizes their spread. The k-means++ is repeated 40 times and the best result in terms of the sum of squared distances of samples from their closest cluster center is used for seeding.

3.3 Selecting the number of classes

An important consideration in using k-means clustering is the choice of number of clusters, k. A good model should explain the data well while being simple. Several methods exist for estimating the optimal number of classes. Nevertheless, often domain- and problem-specific criteria have to be applied for the best results.

The optimal number of clusters depends on variability in the data and correlations between different variables. The more variability and degrees of freedom, the more clusters are generally needed to describe different features in a dataset. Since one important use case for the method is ice process detection, particular attention is paid in separation of fingerprints of different processes between classes. An optimal set of classes would maximize this separation without introducing too many classes to make their interpretation complicated.

As the problem of the number of classes is complex, it is difficult to find an unambiguous quantitative measure for evaluating the correct number of classes. Attempts to create a scoring function for optimizing the separation of ice processes alone did not yield satisfactory results, but were rather used to support the manual selection process.

Silhouette analysis (Rousseeuw, 1987), which is a method for measuring how far each sample is from other clusters (separation) compared to its own cluster (cohesion), was also considered for selecting k. The metric, silhouette coefficient s, takes values between -1 and 1. The higher the value, the better the profile represents the cluster it is assigned to. A profile with $s = 0$ would be a borderline case between clusters, and negative values indicate that the profiles might have been assigned to wrong clusters. Silhouette score $\overline{s} = \frac{1}{k}\sum_{i=1}^{k} s_i$ can generally be used for choosing k. Unfortunately, when applied to the radar profile clustering results, $\overline{s}$ decreases almost monotonically with increasing k in the ranges of k analyzed and thus did not prove very useful for this purpose. Rather, in this study, we calculate s for each profile classification result individually as a measure of how well the profile represents the class it is assigned to.

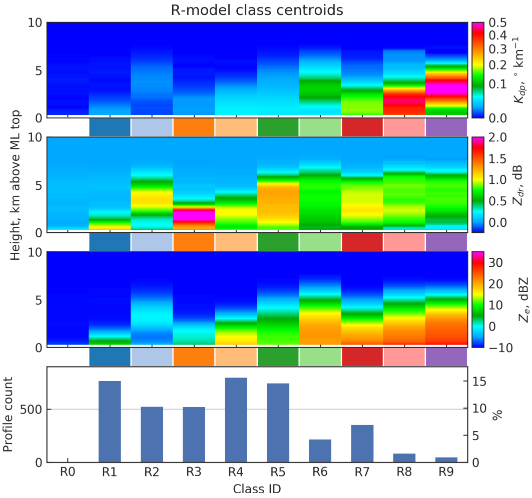

Figure 2. Class centroid profiles of the R model. Profile counts per class are shown at the bottom omitting the count for low-reflectivity class R0. Between the panes, each class has been assigned a color code.

The process of selecting the number of rain and snow profile clusters, k_R and k_S, respectively, was as follows. First, the k-means clustering was repeated 12 times for each k in $[5, 21]$ with 40 k-means++ initializations. This is where the above-described silhouette analysis was performed for each set of clusters and the stability of the initialization process was analyzed for each k. Between the 12 repetitions, the clustering converges to identical results for each $k_\mathrm{R} < 12$ and $k_\mathrm{S} < 10$. With higher values of k, there are multiple solutions to the clustering problem with only minor differences between them. Moreover, the properties of the cluster centroids are not highly sensitive to k. Clustering performed with $k = k_0$ and $k = k_0 + 1$ would typically result in sets of clusters sharing $k_0 - 1$ to k_0 very similar centroids.

This stability of the clustering results makes it convenient to select k manually. In the second stage, we analyzed each separate clustering solution for differences between the clusters from the point of view of snow processes and surface precipitation. Specifically, an important criterion was to separate the typical K_dp signatures of dendritic growth (e.g., Kennedy and Rutledge, 2011) and the H–M process (Field et al., 2016) into different classes. On the other hand, the use of an unsupervised classification method should also allow us to discover previously undocumented features in the radar profiles if they are present in the data in significant numbers.

The goal in this step is to find as many significant unique fingerprints with as low k as possible by manual evaluation. Significant differences between clusters in this context include variations in profile shapes and altitudes of characteristics such as peaks, clear differences in echo-top heights or differences of cluster centroid T_s of more than 3 °C. The most common trivial difference between a pair of clusters was a difference in the intensity of polarimetric radar variables while the shapes of the cluster centroid profiles were almost identical. Altitude differences between fingerprints of overhanging precipitation were also considered trivial.

During this process, allowing some profile classes with only trivial characteristics was inevitable in order to include others with significant unique fingerprints. For this reason, some classes likely reflect natural variability of the same microphysical process rather than unique processes and need to be combined. However, the optimal way of combining the classes may depend on the application. Thus, we present the classes uncombined in this paper.

In snow profile clustering, T_s as an extra classification parameter adds a significant additional degree of freedom. Thus, a larger number of snow profile classes are needed to meet the criteria described above. In clustering, there is a distinguishable separation between clusters representing T_s close to 0 °C and around −10 °C. The vast majority of profiles belong to the warmer group.

Taking all the mentioned considerations into account, we chose to use 10 and 16 classes for rain and snow profiles, respectively. In 12 of the snow profile class centroids, $T_\mathrm{s} > -5\,^\circ\mathrm{C}$. In this paper, the rain and snow profile classification models are termed the R model and S model, respectively.

In this section we have described our approach for optimizing the number of classes with the main criteria of separating the main profile characteristics and the fingerprints of ice processes into individual classes. It should be noted, however, that there is a large spectrum of research problems and operational applications where an unsupervised profile classification method such as the one described in this paper could be potentially useful. The optimal number of classes may depend on the application.

4 Results

Class centroids of rain and snow profile classes are shown in Figs. 2 and 3, respectively. The centroid profiles of dual-polarization radar variables are inverse transformed from corresponding centroids in PCA space. Classes are numbered in the ascending order by the value of the first principal component in the class centroids. By definition, the first component has the largest variance and therefore has the biggest influ-

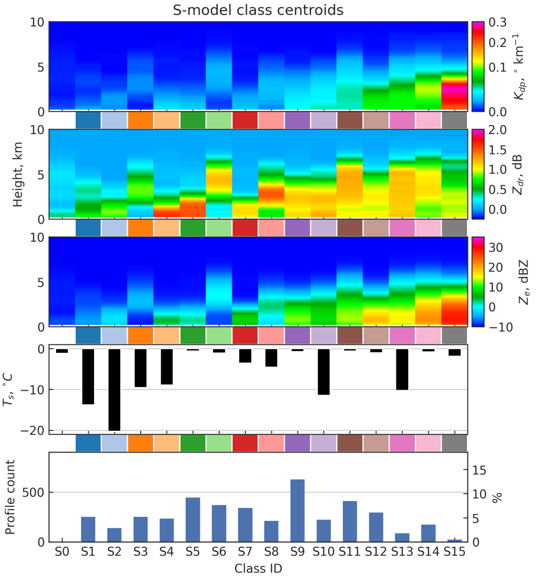

Figure 3. Class centroid profiles of the S model. The top panel shows class centroid surface temperatures. Profile counts per class are shown at the bottom omitting the count for low-reflectivity class S0. Between the panes, each class has been assigned a color code.

ence on the clustering and classification results. The value of this component is strongly correlated with intensities of K_{dp} and Z_{e}.

A number of class centroids in both classification models display distinct features in dual-polarization radar variables often linked to snow processes, such as peaks and gradients in K_{dp} and Z_{DR}. Such features and their connection to other characteristics in the vertical structure of the profiles and finally to the precipitation processes are discussed in this section.

As a general pattern in Figs. 2 and 3 we see that the highest values of Z_{DR} are associated with low echo tops while the highest K_{dp} values occur in deeper clouds. This is in line with the previously reported findings (Kennedy and Rutledge, 2011; Bechini et al., 2013; Moisseev et al., 2015; Schrom et al., 2015; Griffin et al., 2018) that echo tops in the DGL are associated with high Z_{DR} and low K_{dp} in the layer, whereas high K_{dp} in the DGL with low Z_{DR} is associated with echo tops in $T < -37$ °C where homogeneous freezing occurs. Using the NCEP GDAS model output, we analyzed the echo top temperatures, T_{top}, of each vertical profile radar observation. The results, grouped by profile class, are visualized in Fig. 4. It should be noted that in the summer cold echo tops may be caused by strong updrafts in convection, whereas during the winter, echo tops colder than approximately -37 °C are a more unambiguous indication of homogenous freezing. Inspecting the class centroids in Figs. 2 and 3, and comparing them to echo top heights in Fig. 4, it is evident that K_{dp} layers, especially elevated ones, are strongly associated with high echo tops.

The clustering results expose a prominent seasonal difference in K_{dp} intensity: consistently lower values are present in snow events. There are four rain profile classes in contrast to only two snow profile classes with peak cluster centroid K_{dp} exceeding 0.1 ° km^{-1}. They represent total fractions of 13 % and 4 % of rain and snow profiles, respectively. Corresponding to this difference, in Figs. 2 and 3, as well as in Figs. 7 and 8 introduced later, K_{dp} is visualized in different ranges in relation to rain and snow profiles. The seasonal differences in Z_{DR} and Z_{e} intensities are less prominent. High K_{dp} in the summer may be linked to higher water content during the season. Additionally, the seasonal variability of vertical motion could impact the Z_{DR} and K_{dp} enhancements.

Convection in the summer, especially in the presence of hail, is linked to extreme values of radar variables and high echo tops (Voormansik et al., 2017), which may also have a small contribution to the seasonal differences (Mäkelä et al., 2014). However, convective rainstorms are of short duration and thus typically present in just a couple of profiles per convective cell. Therefore, their impact on the class properties is expected to be limited. Manual analysis revealed that classes R6 and R9 have the highest and R5 the lowest fractions of profiles measured in convective cells. Further details of this analysis are presented in Sect. 4.2.

Class frequencies are presented in the bottom panels of Figs. 2 and 3. Classes S0 and R0 represent very low values of Z_{e} throughout the column, i.e., profiles with very weak or no echoes. Therefore their frequencies depend merely on the subjective selection of observation period boundaries and are thus omitted in the figures. Boundaries of the precipitation events are partly based on these two 0 classes. Events are considered independent and separate if between them there are profiles classified as S0 or R0 continuously for at least 12 h.

With respect to K_{dp} intensity, classes in the R model can be divided into four categories: R0 through R3 with negligible K_{dp}, low-K_{dp} classes R4 and R5 with $\max(K_{\mathrm{dp,c}}) \approx 0.04$ ° km^{-1}, high-K_{dp} classes R6 and R7 with $\max(K_{\mathrm{dp,c}}) > 0.11$ ° km^{-1}, and classes R8 and R9 representing extreme values ($\max(K_{\mathrm{dp,c}}) \approx 0.5$ ° km^{-1}). The subscript "c" denotes a class centroid value as opposed to values in individual profiles. The peak $K_{\mathrm{dp,c}}$ of both R6 and R9 is at 3 km, corresponding to class mean GDAS temperatures of -16 and -18 °C, respectively. Essentially, these two classes represent clear K_{dp} features in the DGL.

Classes R7 and R8 feature considerable K_{dp} in 2–3 km thick layers right above the ML, with centroid values slightly below 0.2 ° km^{-1} and around 0.4 ° km^{-1}, respectively. Essentially, both classes represent K_{dp} signatures in both the DGL and temperatures favored by the H–M process. Sinclair et al. (2016) found that the typical K_{dp} values for the H–M process are capped at 0.2…0.3 ° km^{-1} for the C band due to

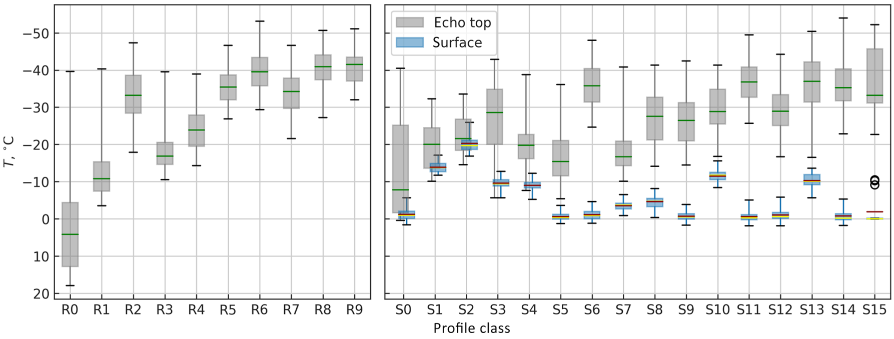

Figure 4. Cloud-top temperature distributions by class (gray) with the green line marking the medians. For S classes, surface temperature distribution is also shown (blue) with red lines marking the class centroid and yellow lines marking the median. Boxes extend between the first and the third quantiles, and whiskers cover 95 % of the data.

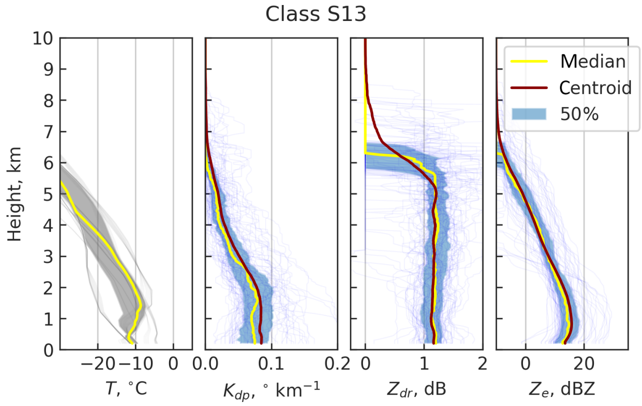

Figure 5. The class S13 centroid is visualized in the three rightmost panes. Individual class member profiles are marked with thin lines. The pane on the left shows corresponding NCEP GDAS temperature profiles. The areas between the first and the third quantiles are shaded, radar data is in blue and GDAS is in gray.

onset of aggregation. Based on this, it can be argued that R7 is a more likely indicator of H–M than R8.

Classes R3 and R4 were found to often coexist in precipitation events. Both are characterized by low K_{dp} and a layer of Z_{DR} in the DGL. In Fig. 4, we see that the echo tops are lower for the R3 profiles, typically in the DGL. Therefore, we would expect growth of pristine crystals in low number concentrations and consequently with no significant aggregation. This would explain why peak Z_{DR} values from 3 to 5 dB are common in relation with R3. Profiles classified as R4, on the other hand, have slightly higher echo tops ($T < -20\,°\mathrm{C}$), which are expected to result in higher number concentrations, leading to aggregation. The R4 profiles are characterized by much lower Z_{DR} values.

In the S model (Fig. 3), classes S0 through S3 represent profiles with low values of all three radar variables, each with $\max(Z_{\mathrm{e,c}}) < 0$ dBZ, $\max(Z_{\mathrm{DR,c}}) < 1$ dB and $\max(K_{\mathrm{dp,c}}) < 0.01\,°\,\mathrm{km}^{-1}$. These four low-reflectivity classes represent different surface temperatures, which is likely a major driver for the separation of these classes in the clustering process. Classes S4 and S5 represent low echo top profiles with high Z_{DR}, with class centroid surface temperatures of -9.0 and -0.6 °C, respectively. Further analysis of NCEP GDAS temperature profiles reveals that, across the board, there is an inversion layer present where radar profiles are classified as S4, typically with temperatures below -10 °C within the lowest kilometer. This corresponds well with the bump in $Z_{\mathrm{DR,c}}$ close to the surface, suggesting possible growth of pristine dendrites within a strong inversion layer. In contrast, there is no inversion in connection with profiles belonging to S5, and the enhancement in Z_{DR} occurs already at 2 to 3 km above the surface, where the median NCEP GDAS temperature for S5 profiles is roughly between -18 and -10 °C. S5 is the second most common class in S-model classification results.

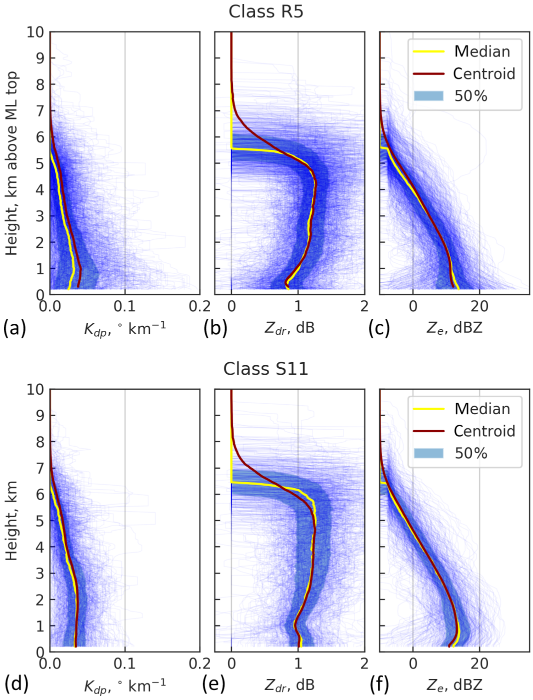

Figure 6. Comparing classes R5 **(a, b, c)** and S11 **(d, e, f)** shows evident similarities. Individual class member profiles are marked with thin blue lines and the areas between the first and the third quantiles are shaded with blue.

Classes S6 and S8 represent situations where precipitation is detached from the surface. These types of profiles are typically present in association with approaching frontal systems before the onset of surface precipitation. The most frequent class of the S model is S9 covering 13 % of the profiles. It represents moderate values of polarimetric radar variables and cloud-top height. The most extreme values of reflectivity and K_{dp} values in the S model are represented by classes S14 and S15. For both classes, $K_{\mathrm{dp,c}}$ peaks above 3 km, suggesting dendritic growth in the member profiles. Values of $Z_{\mathrm{DR,c}}$ are significantly lower compared to other high echo top classes with weaker $K_{\mathrm{dp,c}}$. Class S15 can be seen as a more extreme variant of S14 with much stronger $K_{\mathrm{dp,c}}$ and $Z_{\mathrm{e,c}}$. In addition, S15 represents lower values of Z_{DR} near the DGL, having slightly elevated values in the bottom 3 km instead. These differences are likely due to even higher ice number concentrations in S15 profiles, which lead to more intense aggregation.

Comparing class centroid T_{s} and class frequencies in Fig. 3 it can be seen that most snowfall occurs at $T_{\mathrm{s}} \approx 0\,°\mathrm{C}$. Further analysis of GDAS temperature profiles for the snow events revealed that typically cold surface temperatures ($T_{\mathrm{s}} < -6\,°\mathrm{C}$) are heavily contributed to by strong inversion layers. The centroid and members of S13 are visualized in Fig. 5, along with the member GDAS temperature profiles. The profile class is characterized by a thick layer of considerable K_{dp} from 2 to 3 km to the surface, and $T_{\mathrm{s}} \approx -10\,°\mathrm{C}$. As seen in the left panel of Fig. 5, S13 represents conditions where T typically falls below $-10\,°\mathrm{C}$ close to the surface. This finding suggests that a second DGL may occur in a strong inversion layer.

Using the double-moment Morrison microphysics scheme (Morrison et al., 2005), Sinclair et al. (2016) showed that K_{dp} at the -8 to $-3\,°\mathrm{C}$ temperature range can be used for identifying the H–M process. Such fingerprints are present in particular in profiles classified as R7 or S12. However, manual analysis of the profile data revealed that both of these classes represent a mixture of fingerprints indicating H–M, dendritic growth or the co-presence of both processes. In several events, there were continuous time frames of profiles classified as either R7 or S12 during which the altitude of the K_{dp} signal was changing from profile to profile between the DGL and 0 °C level and was occasionally bimodal. One example of such a time frame is shown in Fig. 7 and discussed further in Sect. 4.1.1. Some bimodality is also present in the centroid $K_{\mathrm{dp,c}}$ of both classes, suggesting that the elevated $K_{\mathrm{dp,c}}$ values in the H–M region cannot be explained solely by sedimenting planar crystals generated aloft but are contributed by the H–M process.

While there are no classes with clear-cut $K_{\mathrm{dp,c}}$ peaks at altitudes corresponding to temperatures preferred by the H–M process in either rain or snow profile classification, there are, in contrast, several classes with strong elevated $K_{\mathrm{dp,c}}$ layers. The proposal of Sinclair et al. (2016) that K_{dp} fingerprints of the H–M process are not very pronounced may explain the tendency of the classification method not to produce more pure H–M classes. Nevertheless, R7 and S12 can be used as indicators for conditions where H–M may occur.

Despite the differences in the classification methods for rain and snow profiles, there are prominent similarities between the two models and profile classes therein. Archetypal classes such as high echo tops in the presence of elevated K_{dp} layers (R6, R9, S14, S15) or high Z_{DR} in shallow precipitation (R3, S4, S5) exist in both classification models. Frequent classes R5 and S11, visualized side by side in Fig. 6, can be considered direct counterparts of each other. The vertical structure of polarimetric radar variables above the ML in R5 match strikingly well with S11. The two classes are characterized by weak K_{dp} and typical values of Z_{DR} slightly above 1 dB aloft, decreasing towards the altitude corresponding to 0 °C. Presumably, this indicates the presence of aggregation.

4.1 Case studies

In Figs. 2 and 3, each class is assigned a color code (between the panels). This color coding is used in Figs. 7 and 8 to mark classification results in a rain and a snow case, respectively.

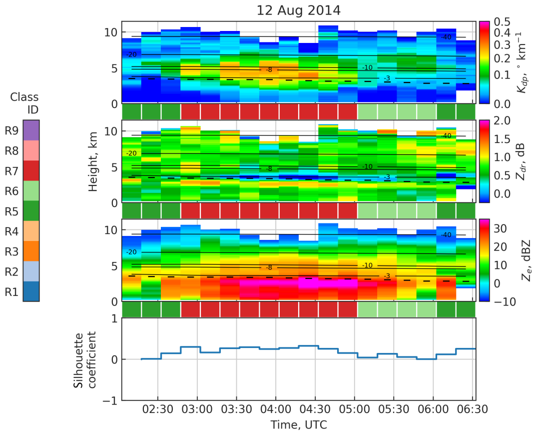

Figure 7. Classification analysis of a rain case with silhouette scores. The automatically detected melting layer is marked with a dashed line, the solid lines show the NCEP GDAS temperature contours and the colors between the panes denote classification results.

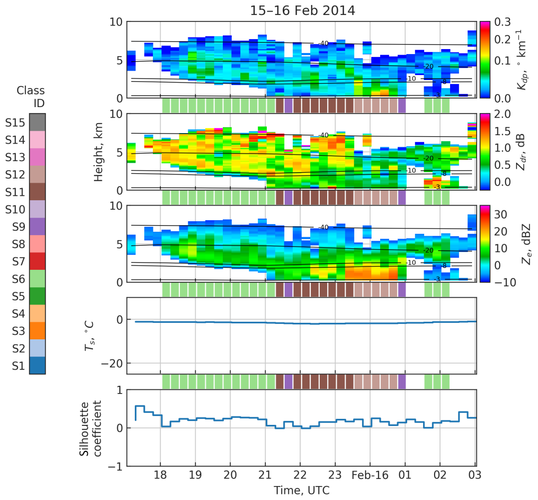

Figure 8. Classification analysis of a snow case with silhouette scores. Solid lines show the NCEP GDAS temperature contours and the colors between the panes denote classification results.

Note that the same set of colors is used for denoting rain and snow profile classification, but they should not be confused with each other.

4.1.1 12 August 2014

In Fig. 7, rain profile classification has been applied to a precipitation event from 12 August 2014. During this event, echo tops repeatedly exceed 10 km. Only the parts of the profiles above the melting layer top are analyzed here, since everything below that level is invisible to the classifier. The first two and the last two profiles shown in the figure are characterized by low Z_e and low K_{dp}, while Z_{DR} has values around 1 dB. These profiles are classified as R5 (dark green). Between 02:30 and 03:00 UTC, a significant increase in K_{dp} occurs, followed by an increase in reflectivity and decrease in Z_{DR}. The temperature (altitude) of the downward increase in K_{dp} varies from the −20 °C level to closer to the ML. In this phase, there is also a small increase in Z_{DR} in the DGL whenever the increase in K_{dp} also occurs in the DGL. This phase in the event is sustained until around 05:00 UTC and is classified as R7 (dark red). It is followed by approximately an hour of a weaker elevated K_{dp} layer at around 4 to 6 km altitude with profiles classified as class R6 (light green). The silhouette coefficient is positive throughout the event indicating good confidence of the classification results. The silhouette of the profiles classified as R6 is not very high, though, which is likely due to lower values of Z_e compared to the class centroid.

Similar analysis of more rain events in the dataset reveals that, similar to the 12 August event, R7 typically coincides with an increase in K_{dp} in the DGL, H–M layer or both, often with varying altitude. Without in situ observations or analysis of Doppler spectra, it is not trivial to tell whether this variability is due to co-presence of dendritic growth and H–M or simply fall streaks. Class R6, on the other hand, is more specific to a K_{dp} fingerprint in the DGL. The more infrequent profiles with clear K_{dp} bands above the DGL are typically also classified as R6 or R9.

4.1.2 15–16 February 2014

Classification results for 15–16 February 2014 are shown in Fig. 8. The event has a clear structure of an approaching frontal system. Between 17:00 and 18:00 UTC Z_e is very low, corresponding to class S0, which is marked with white color between the panels. Between 18:00 and 21:00 UTC, the event starts with overhanging precipitation, classified as S6 (light green). This is followed by light precipitation with echo tops at roughly 7 to 8 km and relatively high Z_{DR} near the echo top, decreasing downwards. This corresponds well with class S11 (dark brown). After 23:30 UTC, The echo top height is decreased to roughly 6 km, Z_{DR} is decreased and K_{dp} signals appear close to ground level. The increase in K_{dp} occurs within the −8 to −3 °C temperature range, suggesting the presence of the H–M process. Indeed, Kneifel et al. (2015) report needles, needle aggregates and rimed particles on the surface at the measurement site during this period and favorable conditions for rime splintering. Further, using the Weather Research and Forecast (WRF) model, Sinclair et al. (2016) showed that secondary ice processes are needed to explain the observed number concentrations during this time period. The corresponding profiles are classified as S12 (light brown). Within this case study, two profiles, marked with dark purple, are classified as S9, likely due to the momentary absence of any strong K_{dp} or Z_{DR} signals.

4.2 Statistics

Frequency statistics of the profile classes are presented in Fig. 9. We analyzed a subset of rain events as either convective or stratiform using a number of sources of publicly available satellite and numerical model data. Out of 70 events analyzed, 15 were convective and 55 stratiform. Panel (a_2) in Fig. 9 shows the ratios of the number of profiles in convective cases per class to the expected value in uniform distribution. On average, twice as many profiles are classified as R6 and R9 in convective situations compared to their average frequencies. Both classes are characterized by high echo tops and elevated K_{dp} bands. On the other hand, classes R7 and R8, also representing high K_{dp} values, but closer to the melting layer than R6 and R9, appear in lower-than-average frequency in convective situations. Class R5 is most pronouncedly characteristic for stratiform events, with frequency in convective events roughly one-third of the average value.

Panels (a_3) and (b_3) of Fig. 9 show the fractions of independent precipitation events in which each class occurs. With rain events, this frequency correlates inversely with $K_{\mathrm{dp,c}}$. Rain profiles classified as R8 and R9, which represent the strongest K_{dp} signatures, occur in 20 % and 19 % of the events, respectively, with at least one of the two occurring in 25 % of the events. Classes R6 and R7, representing more modest K_{dp} features, occur in 45 % and 57 % of cases, respectively, and the rest of the classes between 67 % and 92 % of the cases.

With snow events, the likelihood of a given class occurring within an event correlates not only with peak $K_{\mathrm{dp,c}}$ but also with surface temperature. Any class representing low K_{dp} values and surface temperature close to 0 °C occurs in more than half of the snow events.

The per precipitation event class persistence is visualized in the bottom panels of Fig. 9. Profile classes representing the highest values of Z_{e} at the surface, namely R6–R9, S12, S14 and S15, are short-lived, whereas snow profile classes characterized by cold surface temperatures are the most persistent. Profiles classified as R0 or S0 omitted, the median durations of rain and snow events in the dataset are 5.5 and 11.5 h, respectively. This difference explains why S classes are on average more persistent than R classes.

5 Conclusions

A novel method of dual-polarization radar profile classification for investigating vertical structure of snow processes in the profiles was presented in this paper. The method is based on clustering of PCA components of vertical profiles of K_{dp}, Z_{DR} and Z_{e} and surface temperature. It was applied to vertical profile data extracted from C-band RHI scans over Hyytiälä measurement station in southern Finland. We applied separate versions of the method based on if surface precipitation type was rain (R model) or snow (S model). In the R model, profiles are truncated at the melting layer top, and in the S model surface temperature is used as an additional classification feature. The content of the vertical profile classes was manually interpreted.

In the present investigation, some class centroids resembled textbook examples of previously documented snow process fingerprints, while others may represent a mixture of different conditions. If temperature profiles from either soundings or numerical models are available, the interpretation can be done in the absence of surface crystal type reports. Notably, this is prerequisite in cases of rainfall when direct observations of crystal types cannot be performed at the surface.

The year-round variability in the vertical structure of K_{dp}, Z_{DR} and Z_{e} can be described using a total of 26 profile classes: 10 and 16 in the presence and absence of the ML, respectively. One of the main goals of this study was to associate profile classes with snow processes for their automated identification. It should be noted, though, that the profile classification is not based on expressly selected characteristics of radar fingerprints of the processes, but rather the general, complete structure of the profiles. Nevertheless, some profile classes seem to be strong indicators of specific processes or their combinations within the vertical profiles. From both classification models we can identify a total of seven archetypes with the following characteristics.

1. Profiles have a strong K_{dp} peak in the DGL, while the peak in Z_{DR} is not pronounced. This archetype appears in deep precipitation systems with homogeneous freezing at the cloud top. It is associated with intensified dendritic growth leading to aggregation and high precipitation rate. (Classes R6, R9, S14, S15)

2. There is a K_{dp} signature between the DGL and the 0 °C level, possibly due to simultaneous occurrence of dendritic growth and secondary ice production. Homogeneous freezing occurs at the cloud top. (R7, R8, S12)

3. Profiles are characterized by high echo tops, negligible K_{dp}, and $Z_{\mathrm{DR}} > 1$ dB, which decreases closer to the melting level due to aggregation. Typically, $Z_{\mathrm{e}} <$ 20 dBZ. (R5, S11)

4. The cloud top is between the -30 and -20 °C levels, and there is only a weak Z_{DR} band present at the -15 °C level. Z_{e} is moderate at roughly 20–30 dBZ, and K_{dp} is weak. (R4, S9)

5. Z_{DR} is typically higher than 1.5 dB at the cloud to at around -15 °C and is associated with the growth of pristine planar crystals in low number concentrations.

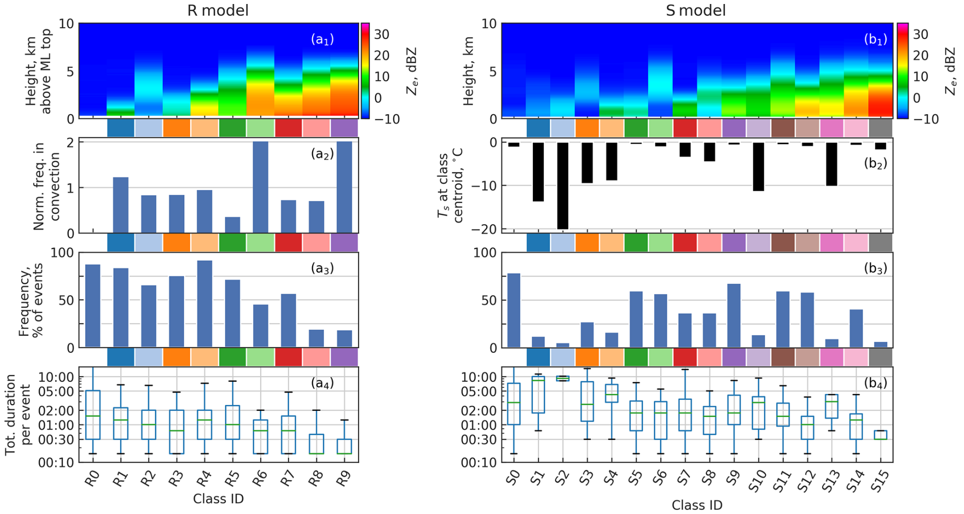

Figure 9. Statistics on frequency of each profile class. Classes are identified by class centroid Z_e **(a1, b1)** and class centroid T_s for snow profile classes **(b2)**, with color codes between the panels and class IDs at the bottom. Panel **(a2)** has the ratios of the number of profiles in convective cases per class to the expected value in uniform distribution. In **(a4, b4)**, the class frequencies are given as percentage of events **(a3, b3)** and total durations **(a4, b4)** within events.

No K_{dp} is present, and low values of Z_e indicate the absence of aggregation. (R3, S5)

6. The radar echo is detached from the surface either due to snow particles not having reached the surface yet or because they are sublimating due to a dry layer. (R2, S3, S6, S8)

7. Z_e is weak throughout the profile. (R0, S0–S2)

In addition to these archetypes found in both summer and winter storms, there are S classes representing situations where strong inversions interfere with snow processes. Notably, we found indications of dendritic growth in strong inversion layers, manifested as class S13. As the colder arctic air mass seldom occurs in southern Finland, $T_s < -10\,°C$ can usually be attributed to a strong lower-level inversion. Such inversions may have an important effect on the frequency of occurrence of some ice processes. Further, this implies that temperature information near the surface is necessary in order to determine whether a low altitude K_{dp} signature in the winter is an implication of the H–M process or dendritic growth.

Our approach to the classification problem is pronouncedly data-driven. This way, if the training material represents the climatology of ice processes and their radar signatures, as was the aim in this study, the resulting classes will reflect the statistical properties of this climatology. Hand picking the training material, on the other hand, would introduce human bias into the class boundaries.

However, there are possible drawbacks in the data-driven approach. The typical radar fingerprints of the H–M process were found to be much more scarce than those of dendritic growth, and often less pronounced. This negatively affects how the typical fingerprints of the H–M process are represented in the classes. This could be enhanced by introducing a larger fraction of H–M profiles in the training data.

Another disadvantage in the data-driven approach is that covering a meaningful collection of unique fingerprints requires a large number of clusters, some of which do not represent unique microphysical processes. This problem may be mitigated to some extent by further optimizing the scaling of the radar variables such that the clustering would be less driven by differences in the intensities of the signatures in contrast to their shapes. Another way to address this issue is to simply combine classes that seem to represent the same processes, in like manner of the archetypes presented above. Reducing the number of classes by simply choosing a smaller k in the k-means clustering would reduce the amount of manual work involved in defining the class boundaries at the cost of decreased detail and accuracy in separating the processes. With a smaller k, the clustering would be driven by more general features of the profiles such as the overall shape and intensity of the polarimetric radar variables, whereas especially the typical characteristics of the H–M process fingerprints involve a higher level of detail.

The classification method presented in this study should be considered a starting point in studying vertical profiles of radar variables using unsupervised classification. As such, there is a vast range of potentially useful opportunities for further development of the method. The method is built on reasoned use of well-known, proven algorithms such as PCA and k-means. We showed that this combination of machine learning algorithms allows both identification of known fingerprints and a more explorative approach in studying the characteristics of a regional climatology of precipitation processes. Limitations of the k-means method include the spherical shape and similar area occupied by the clusters, which involve a risk of suboptimal separation of the microphysical processes to different classes. In this study, we addressed these limitations by allowing a rather large number of initial classes and combining similar ones by identifying the archetypes based on known fingerprints of the processes. Another possible approach would be to explore the numerous alternative clustering methods for a more optimal separation of the precipitation processes. A comprehensive comparison of such methods, however, is outside the scope of this study.

In the present classification method, ambient temperature is known only at the profile base. Compared to the use of full temperature profiles, this simplifies the method and, perhaps even more importantly, the requirements for the input data. However, future studies should investigate if the use of full temperature profiles allows more accurate separation of precipitation processes into different classes.

The unsupervised nature of the classification method is expected to allow extension of its application to the detection of ice processes not covered in this study. Recently, Li et al. (2018) showed that certain combinations of Z_e, Z_DR and K_dp signatures can potentially be used for detecting heavy riming. Furthermore, the process is frequently observed in Finland, highlighting the potential of using an unsupervised method for its identification.

It should be noted that wind shear effects induce differential advection of hydrometeors at different altitudes, affecting the gradients in the vertical profiles of radar variables (Lauri et al., 2012). Therefore caution should be used in interpreting microphysical processes corresponding to class centroid profiles. The wind shear effects are difficult to correct for using vertical profile or RHI radar observations due to the limitations in horizontal sampling. Such adjustments become more viable if classification is performed on profiles extracted from volume scans, which will be investigated in future work.

The ability to describe a climatology of vertical structure of dual-polarization radar variables and, further, precipitation processes using a finite number of classes has evident potential in improving quantitative precipitation estimation. We anticipate that automated detection of ice processes may allow the development of adaptive relation for snowfall rate $S = S(Z_\mathrm{e})$, in which the parameters could be chosen based on the profile classification result. Adaptive $S(Z_\mathrm{e})$ relations, in turn, have potential in improving the vertical profile of reflectivity correction methods. Future work will be devoted to investigating the use of unsupervised profile classification in such applications.

Data availability. The FMI radar and surface temperature data are available from the Finnish Meteorological Institute (2019) open data portal: https://en.ilmatieteenlaitos.fi/open-data-sets-available (last access: 1 October 2019).

Supplement. The supplement related to this article is available online at: https://doi.org/10.5194/amt-13-1227-2020-supplement.

Author contributions. The study was designed by both authors. JT implemented and ran the classification and made the figures. JT wrote the manuscript, with contributions from DM. Both authors discussed the results and commented on the manuscript.

Competing interests. The authors declare that they have no conflict of interest.

Acknowledgements. We would like to thank the personnel of Hyytiälä station and Matti Leskinen for their support in field observation.

Financial support. This research has been supported by the Academy of Finland's Center of Excellence (CoE) (grant no. 307331). The research of Jussi Tiira has been supported by the Doctoral Programme in Atmospheric Sciences (ATM-DP, University of Helsinki).

Open access funding provided by Helsinki University Library.

Review statement. This paper was edited by S. Joseph Munchak and reviewed by two anonymous referees.

References

Andrić, J., Kumjian, M. R., Zrnić, D. S., Straka, J. M., and Melnikov, V. M.: Polarimetric Signatures above the Melting Layer in Winter Storms: An Observational and Modeling Study, J. Appl. Meteorol. Clim., 52, 682–700, https://doi.org/10.1175/JAMC-D-12-028.1, 2013.

Arthur, D. and Vassilvitskii, S.: k-means++: The advantages of careful seeding, 1027–1035, Society for Industrial and Applied Mathematics, 2007.

Bechini, R. and Chandrasekar, V.: A Semisupervised Robust Hydrometeor Classification Method for Dual-Polarization Radar Applications, J. Atmos. Ocean. Tech., 32, 22–47, https://doi.org/10.1175/JTECH-D-14-00097.1, 2015.

Bechini, R., Baldini, L., and Chandrasekar, V.: Polarimetric Radar Observations in the Ice Region of Precipitating Clouds at C-Band

and X-Band Radar Frequencies, J. Appl. Meteorol. Clim., 52, 1147–1169, https://doi.org/10.1175/JAMC-D-12-055.1, 2013.

Cattell, R. B.: The Scree Test For The Number Of Factors, Multivar. Behav. Res., 1, 245–276, 1966.

Caylor, I. and Chandrasekar, V.: Time-varying ice crystal orientation in thunderstorms observed with multiparameter radar, IEEE T. Geosci. Remote Sens., 34, 847–858, https://doi.org/10.1109/36.508402, 1996.

Chandrasekar, V., Keränen, R., Lim, S., and Moisseev, D.: Recent advances in classification of observations from dual polarization weather radars, Atmos. Res., 119, 97–111, https://doi.org/10.1016/j.atmosres.2011.08.014, 2013.

Field, P. R. and Heymsfield, A. J.: Importance of snow to global precipitation: IMPORTANCE OF SNOW TO PRECIPITATION, Geophys. Res. Lett., 42, 9512–9520, https://doi.org/10.1002/2015GL065497, 2015.

Field, P. R., Lawson, R. P., Brown, P. R. A., Lloyd, G., Westbrook, C., Moisseev, D., Miltenberger, A., Nenes, A., Blyth, A., Choularton, T., Connolly, P., Buehl, J., Crosier, J., Cui, Z., Dearden, C., DeMott, P., Flossmann, A., Heymsfield, A., Huang, Y., Kalesse, H., Kanji, Z. A., Korolev, A., Kirchgaessner, A., Lasher-Trapp, S., Leisner, T., McFarquhar, G., Phillips, V., Stith, J., and Sullivan, S.: Chapter 7. Secondary Ice Production – Current State of the Science and Recommendations for the Future, Meteorol. Monogr., 58, 7.1–7.20, https://doi.org/10.1175/AMSMONOGRAPHS-D-16-0014.1, 2016.

Finnish Meteorological Institute: The Finnish Meteorological Institute's open data, available at: https://en.ilmatieteenlaitos.fi/open-data, last access: 1 October 2019.

Giangrande, S. E., Toto, T., Bansemer, A., Kumjian, M. R., Mishra, S., and Ryzhkov, A. V.: Insights into riming and aggregation processes as revealed by aircraft, radar, and disdrometer observations for a 27 April 2011 widespread precipitation event: Insights into Riming and Aggregation, J. Geophys. Res.-Atmos., 121, 5846–5863, https://doi.org/10.1002/2015JD024537, 2016.

Grazioli, J., Lloyd, G., Panziera, L., Hoyle, C. R., Connolly, P. J., Henneberger, J., and Berne, A.: Polarimetric radar and in situ observations of riming and snowfall microphysics during CLACE 2014, Atmos. Chem. Phys., 15, 13787–13802, https://doi.org/10.5194/acp-15-13787-2015, 2015a.

Grazioli, J., Tuia, D., and Berne, A.: Hydrometeor classification from polarimetric radar measurements: a clustering approach, Atmos. Meas. Tech., 8, 149–170, https://doi.org/10.5194/amt-8-149-2015, 2015b.

Griffin, E. M., Schuur, T. J., and Ryzhkov, A. V.: A Polarimetric Analysis of Ice Microphysical Processes in Snow, Using Quasi-Vertical Profiles, J. Appl. Meteorol. Clim., 57, 31–50, https://doi.org/10.1175/JAMC-D-17-0033.1, 2018.

Hallett, J. and Mossop, S. C.: Production of secondary ice particles during the riming process, Nature, 249, 26–28, https://doi.org/10.1038/249026a0, 1974.

Helmus, J. J. and Collis, S. M.: The Python ARM Radar Toolkit (Py-ART), a Library for Working with Weather Radar Data in the Python Programming Language, Journal of Open Research Software, 4, e25, https://doi.org/10.5334/jors.119, 2016.

Juga, I., Hippi, M., Moisseev, D., and Saltikoff, E.: Analysis of weather factors responsible for the traffic "Black Day" in Helsinki, Finland, on 17 March 2005, Met. Apps, 19, 1–9, https://doi.org/10.1002/met.238, 2012.

Kennedy, P. C. and Rutledge, S. A.: S-Band Dual-Polarization Radar Observations of Winter Storms, J. Appl. Meteorol. Clim., 50, 844–858, https://doi.org/10.1175/2010JAMC2558.1, 2011.

Kneifel, S., von Lerber, A., Tiira, J., Moisseev, D., Kollias, P., and Leinonen, J.: Observed relations between snowfall microphysics and triple-frequency radar measurements: Triple Frequency Signatures of Snowfall, J. Geophys. Res.-Atmos., 120, 6034–6055, https://doi.org/10.1002/2015JD023156, 2015.

Kumjian, M. R. and Lombardo, K. A.: Insights into the Evolving Microphysical and Kinematic Structure of Northeastern U.S. Winter Storms from Dual-Polarization Doppler Radar, Mon. Weather Rev., 145, 1033–1061, https://doi.org/10.1175/MWR-D-15-0451.1, 2017.

Kumjian, M. R., Rutledge, S. A., Rasmussen, R. M., Kennedy, P. C., and Dixon, M.: High-Resolution Polarimetric Radar Observations of Snow-Generating Cells, J. Appl. Meteorol. Clim., 53, 1636–1658, https://doi.org/10.1175/JAMC-D-13-0312.1, 2014.

Kumjian, M. R., Mishra, S., Giangrande, S. E., Toto, T., Ryzhkov, A. V., and Bansemer, A.: Polarimetric radar and aircraft observations of saggy bright bands during MC3E: SAGGY BRIGHT BANDS, J. Geophys. Res.-Atmos., 121, 3584–3607, https://doi.org/10.1002/2015JD024446, 2016.

Lauri, T., Koistinen, J., and Moisseev, D.: Advection-Based Adjustment of Radar Measurements, Mon. Weather Rev., 140, 1014–1022, https://doi.org/10.1175/MWR-D-11-00045.1, 2012.

Li, H., Moisseev, D., and von Lerber, A.: How Does Riming Affect Dual-Polarization Radar Observations and Snowflake Shape?, J. Geophys. Res.-Atmos., 123, 6070–6081, https://doi.org/10.1029/2017JD028186, 2018.

Lloyd, S.: Least squares quantization in PCM, IEEE T. Informa. Theory, 28, 129–137, https://doi.org/10.1109/TIT.1982.1056489, 1982.

Maesaka, T., Iwanami, K., and Maki, M.: Non-negative K DP estimation by monotone increasing Φ DP assumption below melting layer, in: Extended Abstracts, Seventh European Conf. on Radar in Meteorology and Hydrology, 3 June 2012, Toulouse, France, 2012.

Moisseev, D. N., Lautaportti, S., Tyynela, J., and Lim, S.: Dual-polarization radar signatures in snowstorms: Role of snowflake aggregation, J. Geophys. Res.-Atmos., 120, 12644–12655, https://doi.org/10.1002/2015jd023884, 2015.

Morrison, H., Curry, J. A., and Khvorostyanov, V. I.: A New Double-Moment Microphysics Parameterization for Application in Cloud and Climate Models. Part I: Description, J. Atmos. Sci., 62, 1665–1677, https://doi.org/10.1175/JAS3446.1, 2005.

Mäkelä, A., Enno, S.-E., and Haapalainen, J.: Nordic Lightning Information System: Thunderstorm climate of Northern Europe for the period 2002–2011, Atmos. Res., 139, 46–61, https://doi.org/10.1016/j.atmosres.2014.01.008, 2014.

Oue, M., Kumjian, M. R., Lu, Y., Jiang, Z., Clothiaux, E. E., Verlinde, J., and Aydin, K.: X-Band Polarimetric and Ka-Band Doppler Spectral Radar Observations of a Graupel-Producing Arctic Mixed-Phase Cloud, J. Appl. Meteorol. Clim., 54, 1335–1351, https://doi.org/10.1175/JAMC-D-14-0315.1, 2015.

Oue, M., Galletti, M., Verlinde, J., Ryzhkov, A., and Lu, Y.: Use of X-Band Differential Reflectivity Measurements to Study Shallow Arctic Mixed-Phase Clouds, J. Appl. Meteorol. Clim., 55, 403–424, https://doi.org/10.1175/JAMC-D-15-0168.1, 2016.

Oue, M., Kollias, P., Ryzhkov, A., and Luke, E. P.: Toward Exploring the Synergy Between Cloud Radar Polarimetry and Doppler Spectral Analysis in Deep Cold Precipitating Systems in the Arctic, J. Geophys. Res.-Atmos., 123, 2797–2815, https://doi.org/10.1002/2017JD027717, 2018.

Petäjä, T., O'Connor, E. J., Moisseev, D., Sinclair, V. A., Manninen, A. J., Väänänen, R., von Lerber, A., Thornton, J. A., Nicoll, K., Petersen, W., Chandrasekar, V., Smith, J. N., Winkler, P. M., Krüger, O., Hakola, H., Timonen, H., Brus, D., Laurila, T., Asmi, E., Riekkola, M.-L., Mona, L., Massoli, P., Engelmann, R., Komppula, M., Wang, J., Kuang, C., Bäck, J., Virtanen, A., Levula, J., Ritsche, M., and Hickmon, N.: BAECC A field campaign to elucidate the impact of Biogenic Aerosols on Clouds and Climate, B. Am. Meteorol. Soc., 97, 1909–1928, https://doi.org/10.1175/BAMS-D-14-00199.1, 2016.

Raykov, Y. P., Boukouvalas, A., Baig, F., and Little, M. A.: What to Do When K-Means Clustering Fails: A Simple yet Principled Alternative Algorithm, PLOS ONE, 11, e0162259, https://doi.org/10.1371/journal.pone.0162259, 2016.

Rousseeuw, P. J.: Silhouettes: A graphical aid to the interpretation and validation of cluster analysis, J. Comput. Appl. Math., 20, 53–65, https://doi.org/10.1016/0377-0427(87)90125-7, 1987.

Schneebeli, M., Dawes, N., Lehning, M., and Berne, A.: High-Resolution Vertical Profiles of X-Band Polarimetric Radar Observables during Snowfall in the Swiss Alps, J. Appl. Meteorol. Clim., 52, 378–394, https://doi.org/10.1175/JAMC-D-12-015.1, 2013.

Schrom, R. S., Kumjian, M. R., and Lu, Y.: Polarimetric Radar Signatures of Dendritic Growth Zones within Colorado Winter Storms, J. Appl. Meteorol. Clim., 54, 2365–2388, https://doi.org/10.1175/JAMC-D-15-0004.1, 2015.

Sinclair, V. A., Moisseev, D., and von Lerber, A.: How dual-polarization radar observations can be used to verify model representation of secondary ice, J. Geophys. Res.-Atmos., 121, 10954–10970, https://doi.org/10.1002/2016JD025381, 2016.

Thompson, E. J., Rutledge, S. A., Dolan, B., Chandrasekar, V., and Cheong, B. L.: A Dual-Polarization Radar Hydrometeor Classification Algorithm for Winter Precipitation, J. Atmos. Ocean. Tech., 31, 1457–1481, https://doi.org/10.1175/JTECH-D-13-00119.1, 2014.

Trömel, S., Ryzhkov, A. V., Zhang, P., and Simmer, C.: Investigations of Backscatter Differential Phase in the Melting Layer, J. Appl. Meteorol. Clim., 53, 2344–2359, https://doi.org/10.1175/JAMC-D-14-0050.1, 2014.

Virtanen, P., Gommers, R., Oliphant, T. E., Haberland, M., Reddy, T., Cournapeau, D., Burovski, E., Peterson, P., Weckesser, W., Bright, J., van der Walt, S. J., Brett, M., Wilson, J., Millman, K. J., Mayorov, N., Nelson, A. R. J., Jones, E., Kern, R., Larson, E., Carey, C. J., Polat, İ, Feng, Y., Moore, E. W., VanderPlas, J., Laxalde, D., Perktold, J., Cimrman, R., Henriksen, I., Quintero, E. A., Harris, C. R., Archibald, A. R., Ribeiro, A. H., Pedregosa, F., van Mulbregt, P., and SciPy 1.0 Contributors: SciPy 1.0: fundamental algorithms for scientific computing in Python, Nat. Methods, 17, 261–272, https://doi.org/10.1038/s41592-019-0686-2, 2020.

von Lerber, A., Moisseev, D., Bliven, L. F., Petersen, W., Harri, A.-M., and Chandrasekar, V.: Microphysical Properties of Snow and Their Link to Ze–S Relations during BAECC 2014, J. Appl. Meteorol. Clim., 56, 1561–1582, https://doi.org/10.1175/JAMC-D-16-0379.1, 2017.

Voormansik, T., Rossi, P. J., Moisseev, D., Tanilsoo, T., and Post, P.: Thunderstorm hail and lightning detection parameters based on dual-polarization Doppler weather radar data, Met. Apps, 24, 521–530, https://doi.org/10.1002/met.1652, 2017.

Williams, E. R., Smalley, D. J., Donovan, M. F., Hallowell, R. G., Hood, K. T., Bennett, B. J., Evaristo, R., Stepanek, A., Bals-Elsholz, T., Cobb, J., Ritzman, J., Korolev, A., and Wolde, M.: Measurements of Differential Reflectivity in Snowstorms and Warm Season Stratiform Systems, J. Appl. Meteorol. Clim., 54, 573–595, https://doi.org/10.1175/JAMC-D-14-0020.1, 2015.

Wolfensberger, D., Scipion, D., and Berne, A.: Detection and characterization of the melting layer based on polarimetric radar scans, Q. J. Roy. Meteor. Soc., 142, 108–124, https://doi.org/10.1002/qj.2672, 2015.

Paper V

Atmos. Chem. Phys., 20, 9547–9562, 2020
https://doi.org/10.5194/acp-20-9547-2020

Atmospheric Chemistry and Physics
Open Access

Towards the connection between snow microphysics and melting layer: insights from multifrequency and dual-polarization radar observations during BAECC

Haoran Li[1], **Jussi Tiira**[1], **Annakaisa von Lerber**[2], **and Dmitri Moisseev**[1,2]

[1]Institute for Atmospheric and Earth System Research/Physics, Faculty of Science, University of Helsinki, Helsinki, Finland
[2]Finnish Meteorological Institute, Helsinki, Finland

Correspondence: Haoran Li (haoran.li@helsinki.fi)

Received: 9 January 2020 – Discussion started: 3 April 2020
Revised: 7 July 2020 – Accepted: 8 July 2020 – Published: 14 August 2020

Abstract. In stratiform rainfall, the melting layer (ML) is often visible in radar observations as an enhanced reflectivity band, the so-called bright band. Despite the ongoing debate on the exact microphysical processes taking place in the ML and on how they translate into radar measurements, both model simulations and observations indicate that the radar-measured ML properties are influenced by snow microphysical processes that take place above it. There is still, however, a lack of comprehensive observations to link the two. To advance our knowledge of precipitation formation in ice clouds and provide new insights into radar signatures of snow growth processes, we have investigated this link. This study is divided into two parts. Firstly, surface-based snowfall measurements are used to develop a new method for identifying rimed and unrimed snow from X- and Ka-band Doppler radar observations. Secondly, this classification is used in combination with multifrequency and dual-polarization radar observations collected during the Biogenic Aerosols – Effects on Clouds and Climate (BAECC) experiment in 2014 to investigate the impact of precipitation intensity, aggregation, riming and dendritic growth on the ML properties. The results show that the radar-observed ML properties are highly related to the precipitation intensity. The previously reported bright band "sagging" is mainly connected to the increase in precipitation intensity. Ice particle riming plays a secondary role. In moderate to heavy rainfall, riming may cause additional bright band sagging, while in light precipitation the sagging is associated with unrimed snow. The correlation between ML properties and dual-polarization radar signatures in the snow region above appears to be arising through the connection of the radar signatures and ML properties to the precipitation intensity. In addition to advancing our knowledge of the link between ML properties and snow processes, the presented analysis demonstrates how multifrequency Doppler radar observations can be used to get a more detailed view of cloud processes and establish a link to precipitation formation.

1 Introduction

Stratiform precipitation is prevalent in middle to high latitudes. In such precipitation systems, ice particles nucleated at the cloud top descend and grow on their way down by going through various microphysical processes, e.g., vapor deposition, aggregation and/or riming (Lamb and Verlinde, 2011). In the case of rainfall, these ice particles transform into raindrops in the melting layer (ML). The melting of ice particles is capable of modulating the thermal structure of the ML through the exchange of latent heat with the environment (Stewart et al., 1984; Carlin and Ryzhkov, 2019) and, as a result, can change the dynamics of precipitation (e.g., Heymsfield, 1979; Szeto et al., 1988; Fabry and Zawadzki, 1995). It has shown that ML properties are modified by the ambient environment such as relative humidity (RH; Willis and Heymsfield, 1989; Battaglia et al., 2003; Carlin and Ryzhkov, 2019), as well as microphysical processes taking place in the ML (Heymsfield et al., 2015), and by snow microphysical processes occurring above, e.g., aggregation and riming (Stewart et al., 1984; Klaassen, 1988; Fabry and

Zawadzki, 1995; Zawadzki et al., 2005; von Lerber et al., 2014; Kumjian et al., 2016; Xie et al., 2016; Wolfensberger et al., 2016; Trömel et al., 2019). In addition, the microwave attenuation in the ML is sensitive to the parameterization of snow microphysics (von Lerber et al., 2014) and can be significant at millimeter wavelengths (Matrosov, 2008; Haynes et al., 2009; Li and Moisseev, 2019).

To centimeter-wavelength weather radars, the ML appears as a band of the increased reflectivity, the so-called bright band, while to millimeter-wavelength radars, such an appearance is less distinct (e.g., Lhermitte, 1988; Sassen et al., 2005; Kollias and Albrecht, 2005). Properties of the ML and its radar manifestation bright band are influenced by cloud dynamics and microphysics, which can be directly probed by aircraft-mounted in situ measurements (e.g., Stewart et al., 1984; Willis and Heymsfield, 1989; Heymsfield et al., 2015) despite the inability to conduct continuous long-term operations with such setups. Remote sensing of the ML with radars dates back to the 1940s (Ryde, 1946). Atlas (1957) has found that the strength of the bright band is weakened when melting graupel particles are present, which was further confirmed by Klaassen (1988) and Zawadzki et al. (2005). A comprehensive long-term analysis of the ML appearance in vertically pointing X-band radar and ultra high frequency (UHF) wind profiler observations has been performed by Fabry and Zawadzki (1995). They have compiled a record of the main ML features that were later used in modeling studies (e.g., Szyrmer and Zawadzki, 1999; Zawadzki et al., 2005; von Lerber et al., 2014). As the ML bridges snow and rain, the raindrop size distributions below the ML seem to be related to the bright band's reflectivity values (Huggel et al., 1996; Sarma et al., 2016). As presented by Wolfensberger et al. (2016), the thickness of the ML depends on riming, particle fall velocities and the bright band intensity. Meanwhile, the downward extension of the bright band, called the saggy bright band, may be linked to riming as suggested by previous studies (Trömel et al., 2014; Kumjian et al., 2016; Ryzhkov et al., 2016; Xie et al., 2016; Erlingis et al., 2018). Recently, Carlin and Ryzhkov (2019) have incorporated the cooling effects of melting snowflakes in the ML model and proposed that the saggy bright band may be explained by a combination of processes instead of a single factor. From the perspective of observation, there seems to be a lack of statistical studies untangling the impacts of snow growth processes on the observed ML properties.

Over the last few years, multifrequency radar measurements of clouds and precipitation have become more easily attainable, which has led to the proliferation of studies demonstrating the advantages of using these observations for the investigation of snow microphysical processes (e.g., Kneifel et al., 2011, 2015; Leinonen et al., 2012a; Leinonen et al., 2013, 2018; Tyynelä and Chandrasekar, 2014; Leinonen and Moisseev, 2015; Leinonen and Szyrmer, 2015; Grecu et al., 2018; Chase et al., 2018; Mason et al., 2018, 2019). The potential dependence of dual-wavelength ratios (DWRs) at Ka–W-bands and X–Ka-bands on riming was observed by Kneifel et al. (2015). Dias Neto et al. (2019) have presented the strong aggregation signatures close to the ML using multifrequency radar observations. This rapid aggregation could manifest itself as a dark band in W-band cloud radar observations, namely the dip in radar reflectivity just above the ML top (Lhermitte, 1988; Sassen et al., 2005, 2007; Heymsfield et al., 2008). Such a reflectivity dip just above the ML may even be present in X-band radar measurements of light precipitation (Fabry and Zawadzki, 1995) but has not been well addressed. Mason et al. (2018) have incorporated the Doppler velocity and radar reflectivity observations from vertically pointing Ka- and W-band radars into an optimal estimation scheme to infer the riming fraction, among other parameters. In addition to multifrequency radar observations, dual-polarization radar measurements show promise in improving our understanding of ice precipitation processes (e.g., Bechini et al., 2013; Giangrande et al., 2016; Kumjian et al., 2016; Ryzhkov et al., 2016; Moisseev et al., 2015, 2017; Li et al., 2018; Oue et al., 2018; Vogel and Fabry, 2018; Moisseev et al., 2019; Tiira and Moisseev, 2020). Therefore, the utilization of collocated multifrequency and dual-polarization radar observations may pave the way for a better understanding of the connection between dry and melting snow microphysics.

The detailed properties of ice particles are complex as manifested by the extraordinary variety in their habit, size, mass and concentration (Korolev et al., 2000, 2003; Bailey and Hallett, 2009). This complexity is exacerbated by the diversity of ice growth processes that take place in ice clouds (Li et al., 2018; Oue et al., 2018; Barrett et al., 2019; Moisseev et al., 2015, 2017, 2019; Tiira and Moisseev, 2020). Despite the recent attempts to resolve the ice microphysics (e.g., Mason et al., 2018, 2019; Barrett et al., 2019), direct characterization of ice particles and their growth processes is still challenging. In some cases, ML properties could emphasize radar signatures of such processes (Zawadzki et al., 2005; Kumjian et al., 2016; Li and Moisseev, 2020) and therefore provide additional information. However, there is an ongoing debate on the link between snow growth processes, such as riming and aggregation, their radar signatures and ML properties (e.g., Kumjian et al., 2016; Carlin and Ryzhkov, 2019; Heymsfield et al., 2015). This study aims to advance our understanding of the link and resolve at least some of the discussed topics. During the Biogenic Aerosols – Effects on Clouds and Climate (BAECC) experiment (Petäjä et al., 2016), vertically pointing X-, Ka- and W-band cloud radars were deployed at the University of Helsinki research station in Hyytiälä, Finland. These observations were supplemented by range–height indicator (RHI) scans carried out by the Finnish Meteorological Institute (FMI) C-band dual-polarization radar, providing a set of unique synergistic observations ideally suited for studying the connection between the growth and melting processes of snowflakes.

The paper is organized as follows. Section 2 introduces the instrumentation used in this study, followed by the illustration of detecting the ML and separating unrimed and rimed snow in Sect. 3. A sanity check of the snow classification and the statistical results of multifrequency and dual-polarization radar observations are provided in Sect. 4. Conclusions are presented in Sect. 5.

2 Measurements

The BAECC field campaign was conducted at the University of Helsinki's Hyytiälä Station from February to September 2014 (Petäjä et al., 2016). This experiment provides comprehensive vertically pointing multifrequency radar rainfall observations, which are used in this study. A 2D video disdrometer (2DVD) was used to measure rain rate and calibrate X-band radar reflectivity. The collocated observations were aided by the FMI C-band dual-polarization weather radar. In addition to the radar setup during BAECC, long-term snow observations were made by a National Aeronautics and Space Administration (NASA) Particle Imaging Package (PIP; Newman et al., 2009; Tiira et al., 2016; von Lerber et al., 2017).

2.1 2DVD and vertically pointing radars

The Atmospheric Radiation Measurement 2DVD (ARM 2DVD) used in this study is the new generation of the one described in Kruger and Krajewski (2002). It relies on two cameras and two light sources placed in orthogonal directions and records image projections of raindrops as they fall cross the cameras' field of view. The 2DVD is often used for recording the size distributions, fall velocities and shapes of raindrops. Based on this information, the rain rate and reflectivity at a given radar frequency can be derived.

The X- and Ka-band scanning ARM cloud radar (X/Ka-SACR) and W-band ARM cloud radar (MWACR) have the range gate spacing of 25, 25 and 30 m, respectively (Kollias et al., 2014; Kneifel et al., 2015; Falconi et al., 2018). The original time resolution of 2 s was averaged to 10 s for these radars. The half-power beam widths of X-SACR, Ka-SACR and MWACR are 1.27, 0.33 and 0.38°, respectively. X- and Ka-SACR are dual-polarization radar systems installed on the same pedestal, recording the co-polar (e.g., ρ_{hv}, Z_{dr}) and cross-polar (e.g., cross-polar correlation coefficient and linear depolarization ratio, LDR) measurements, respectively. MWACR had a small antenna pointing error of 0.5 to 1°, which may lead to significant error in the vertical Doppler velocity but which does not affect reflectivity measurements.

To mitigate the potential attenuation from wet radome and raindrops, the simulated X-band radar reflectivity from 2DVD data was used to match the measured X-band reflectivity at 500 m where the near-field effect is minimized (Sekelsky, 2002; Falconi et al., 2018). As the Ka-band reflectivity can be significantly affected by the attenuation from the ML, rain and a wet radome (Li and Moisseev, 2019), the relative calibration was made at precipitation top where the Rayleigh assumption can be applied at Ka- and X-bands. During BAECC, a radiosonde was launched four times per day, out of which the temporally closest one was used as input to the millimeter-wavelength propagation model (Liebe, 1985) to correct for the gaseous attenuation at all radar frequencies.

2.2 Dual-polarization weather radar

The FMI C-band dual-polarization weather radar located in Ikaalinen, 64 km west from the Hyytiälä station, operates in the simultaneous transmission and receiving mode (Doviak et al., 2000). This radar performs RHI scans over the measurement site every 15 min. The range and azimuth resolutions are 500 m and 1°, respectively. The dual-polarization measurements used in this study are Z_{dr}, which was calibrated during light rainfalls (Bringi and Chandrasekar, 2001; Li et al., 2018). For data analysis, the Python ARM Radar Toolkit (Helmus and Collis, 2016) was used.

2.3 NASA particle imaging package

The PIP is an improved version of the Snowflake Video Imager (Newman et al., 2009), which uses a high frame rate camera operating at 380 frames per second to record the silhouettes of precipitation particles. The field of view of this camera is 48 mm×64 mm with a spatial resolution of 0.01 mm^2. The focal plane of this camera is 1.3 m. Because the measurement volume is not enclosed, the wind-induced effects on the measurements are minimized (Newman et al., 2009). The data-processing software defines the size of each particle using the disk-equivalent diameter (D_{deq}), which is the diameter of a disk with the same area of a particle shadow. Particle size distribution (PSD) and fall velocity are recorded as a function of D_{deq} in the PIP software. Based on these PIP products, von Lerber et al. (2017) have derived particle mass and fall velocity as a function of the observed maximum particle diameter ($D_{\mathrm{max,ob}}$), which is obtained by fitting an ellipsoid model to each particle. Here and hereafter, D represents $D_{\mathrm{max,ob}}$. The snowfall measurements started as part of the BAECC field campaign were continued, and data collected during the experiment and an additional three winters were used in this study. The collected data were processed using the method by von Lerber et al. (2017).

3 Methods

3.1 Detection of ML boundaries

The height where melting starts ranges from the surface to several kilometers above, mainly depending on the temperature profiles. Thus, prior to addressing the general characteristics of ML, it is important to detect ML boundaries. Fabry and Zawadzki (1995) have employed the gradient of reflectivity to determine the ML boundaries using single-polarization X-band radar measurements. The vertically pointing X- and Ka-band radars used in this study provide dual-polarization observations, i.e., ρ_{hv} and LDR, respectively. These observations supply additional information to estimate the ML boundaries (Giangrande et al., 2008). However, care should be taken in how this information is used. Wolfensberger et al. (2016) have suggested that the use of ρ_{hv} could underestimate the ML top as the significant drop in ρ_{hv} may not happen until a significant amount of ice has already melted. To mitigate this issue, we determined the upper boundary of ML by finding the local minimum of the X-band reflectivity gradient around the ρ_{hv}-detected ML top, which is similar to Wolfensberger et al. (2016). The validity of utilizing the radar reflectivity in determining the ML top is further confirmed in our recent study (Li and Moisseev, 2020). The ML bottom was determined in a similar way to derive the radar reflectivity at the melting bottom. Note that cases in which precipitation fall streaks are significantly slanted, as shown in Fabry and Zawadzki (1995), were excluded.

3.2 Diagnosing snowflake rime mass fraction

The rime mass fraction (FR), defined as the ratio of accreted ice mass by riming to the total snowflake mass, has been used to quantify the riming extent in ice microphysical schemes (Morrison and Milbrandt, 2015) and in observational studies (e.g., Moisseev et al., 2017; Li et al., 2018). The rime mass fraction can be defined as

$$\mathrm{FR} = 1 - \frac{\int_{D_{\min}}^{D_{\max}} N(D) m_{\mathrm{ur}}(D) \mathrm{d}D}{\int_{D_{\min}}^{D_{\max}} N(D) m_{\mathrm{ob}}(D) \mathrm{d}D}, \tag{1}$$

where $D_{\max}$ and $D_{\min}$ are maximum and minimum particle sizes, respectively, $m_{\mathrm{ob}}(D)$ and $m_{\mathrm{ur}}(D)$ are masses of observed and unrimed snowflakes as a function of D, respectively, and $N(D)$ is the PSD. In this study, FR was computed using ground-based observations of PSD and snowflake masses retrieved from PIP observations, as described in von Lerber et al. (2017). The masses of unrimed ice particles were derived assuming the following. Firstly, unrimed snowflakes were present in PIP observations. Secondly, the ice particles belonging to the lightest 5 % are representative of unrimed snowflakes. Following these assumptions, the mass of unrimed snowflakes can be expressed as $m_{\mathrm{ur}}(D) = 0.0053 D^{2.05}$. This relation is similar to the one derived from aircraft measurements (Heymsfield et al., 2004). A further discussion on the definition of $m_{\mathrm{ur}}(D)$ is found in Moisseev et al. (2017) and Li et al. (2018).

Mason et al. (2018) have shown that the extent of riming can be retrieved using radar-measured DWR (Matrosov, 1998; Hogan et al., 2000) and mean Doppler velocity (V). If the radar reflectivity is expressed in decibels (dB), then the DWR can be written as

$$\mathrm{DWR}(\lambda_1, \lambda_2) = Z_{\lambda_1} - Z_{\lambda_2}, \tag{2}$$

where Z_{λ_1} and Z_{λ_2} are observed radar reflectivities at the wavelengths of λ_1 and λ_2, respectively. Z_λ can be expressed as

$$Z_\lambda = 10\log_{10}\left(\int_{D_{\min}}^{D_{\max}} \frac{\lambda^4}{\pi^5 |K_\lambda|^2} N(D) \sigma_{\mathrm{b},\lambda}(D, m_{\mathrm{ob}}(D)) \mathrm{d}D \right), \tag{3}$$

where $|K_\lambda|^2$ is the dielectric constant of liquid water and $\sigma_{\mathrm{b},\lambda}(D, m_{\mathrm{ob}}(D))$ is the backscattering coefficient of snow particles at a given wavelength. In X-SACR, Ka-SACR and MWACR data files, $|K_\lambda|^2$ is set to 0.93, 0.88 and 0.70, respectively. The values of $\sigma_{\mathrm{b},\lambda}$ were taken from the single-scattering databases (Leinonen and Moisseev, 2015; Leinonen and Szyrmer, 2015; Tyynelä and von Lerber, 2019). These three datasets were combined into a single lookup table of ice particle scattering properties defined as a function of maximum diameter and mass. For a given D and m_{ob}, the backscattering cross section was estimated using linear interpolation in the log–log space. The mean Doppler velocity can be derived in the same way:

$$V_\lambda = \frac{\int_{D_{\min}}^{D_{\max}} v(D) N(D) \sigma_{\mathrm{b},\lambda}(D, m_{\mathrm{ob}}(D)) \mathrm{d}D}{\int_{D_{\min}}^{D_{\max}} N(D) \sigma_{\mathrm{b},\lambda}(D, m_{\mathrm{ob}}(D)) \mathrm{d}D}, \tag{4}$$

where $v(D)$ is the fall velocity of snowflakes which was used to derive $m(D)$ (von Lerber et al., 2017). To minimize the impact of varying air density (ρ_{air}), V_λ was adjusted to the air condition of 1000 hPa and 0 °C (air density $\rho_{\mathrm{air},0}$) with a factor of $(\frac{\rho_{\mathrm{air},0}}{\rho_{\mathrm{air}}})^{0.54}$ (Heymsfield et al., 2007). ρ_{air} was derived from the temperature and relative humidity obtained from the temporally closest sounding.

Dias Neto et al. (2019) have shown that the size growth of snowflakes close to the ML is accelerated due to the enhanced aggregation. Therefore, relatively large aggregates are prevalent snow types close to the ML and are better represented by DWR(X, Ka) than DWR(Ka, W) (see the comparison by Barrett et al., 2019). The use of a lower radar frequency (X- and Ka-bands) avoids estimating the non-neglectable W-band attenuation caused by ML, as well as supercooled liquid water (Li and Moisseev, 2019). Therefore, the potential link between FR and simulated Doppler radar measurements at X- and Ka-bands was accessed with the utilization of in situ snowfall observations from BAECC to the winters of 2014–2018.

The dependence of DWR(X, Ka) and V_X on FR can be computed using Eqs. (1), (2) and (4). For comparison, the $m_{\text{ob}} - D$ and $v - D$ relations of aggregates of unrimed radiating assemblages, side planes, bullets, and columns (LH74 unrimed), aggregates of densely rimed radiating assemblages of dendrites (LH74 rimed), and lump graupel (LH74 graupel) presented in Locatelli and Hobbs (1974) were used. To compute the DWR(X, Ka) and V_X using relations from the literature, we assumed that $N(D)$ can be parameterized as

$$N(D) = N_0 e^{-\Lambda D}, \tag{5}$$

where the intercept parameter N_0 is canceled out while computing DWR and V_X, so the radar variables depend on Λ, which controls the average size of ice particles in $N(D)$. We have varied Λ^{-1} between 0 and 11 mm to mimic different snowfall conditions, which is similar to what was done in Leinonen and Szyrmer (2015). Table 1 summaries the fitted expressions of DWR(X, Ka) $= aV_X^b$ for these three particle types. Since snow microphysics and the corresponding radar measurements can significantly change with precipitation intensity (Moisseev et al., 2017), the computed values were separated into four subgroups according to precipitation rate (PR).

Simulations of DWR(X, Ka)-V_X for four groups of precipitation rate are presented in Fig. 1. Most cases with FR ≤ 0.2 are centered around the curve of LH74 unrimed, whose velocity–diameter relation is similar to low-density snowflakes (Tiira et al., 2016). It seems that riming happens more frequently in heavier precipitation. In contrast, far fewer unrimed cases are present in heavier precipitation (Fig. 1c and d). Heavily rimed snowflakes (FR > 0.5; red dots) are characterized by low DWR(X, Ka) and high V_X, contrasting with the unrimed/lightly rimed cases (blue dots). Specifically, snowflakes with large sizes and low velocities usually are rather slightly rimed (FR ≤ 0.2). For the cases where FR exceeds 0.5, most DWR(X, Ka) values are below 3 dB, indicating that heavily rimed particles are usually associated with small snowflakes. Inspired by this distinct feature, we have fitted the DWR(X, Ka) $= aV_X^b$ relations for cases with FR ≤ 0.2 and $0.4 \leq$ FR ≤ 0.6 (shown in Table 1), which separate the observations into three types: unrimed, transitional and rimed snow. For the sake of comparison, the power b for unrimed snow was adopted from the fit for LH74 unrimed. In this study, these fitted relations were employed for classifying unrimed and rimed snow. The presence of supercooled liquid water does not significantly affect X-band reflectivity but may lead to appreciable attenuation at Ka-band which translates to enhanced DWR(X, Ka) after the relative calibration at precipitation top. For the liquid water path of 500 g m^{-2}, the estimated Ka-band attenuation is in the order of 1 dB (Kneifel et al., 2015). Therefore, cases with DWR(X, Ka) $<$ 1 dB were rejected when identifying unrimed snow.

4 Results

To study how ML properties depend on the precipitation intensity, snowflake riming fraction and PSD, all rainfall cases observed during the BAECC experiment were analyzed. Given the need for coinciding multifrequency vertically pointing radar measurements and the radar scans performed during the experiment, we have identified 4147 vertical profiles of observations in 24 stratiform rainfall events corresponding to about 11.5 h. Table 2 summaries the dates used in this study (quicklooks are available at https://doi.org/10.5281/zenodo.3979103). Due to the periodic changes in radar scans, the multifrequency radar measurements recorded in the vertically pointing mode were available only in some inconsecutive time periods for an event. During the analysis, the mean radar Doppler velocity was scaled to the air density at 1000 hPa and 0 °C, as previously described. It should be noted that the RHI scans by the FMI C-band weather radar were performed every 15 min. Therefore, the profiles of specific differential phase and differential reflectivity are recorded much less frequently than the vertically pointing radar observations. The RHI observations are nonetheless presented here in order to link the features observed in this study to the previous reports (Giangrande et al., 2016; Kumjian et al., 2016; Li et al., 2018; Vogel and Fabry, 2018). Figure 2 shows the flow chart of the data process in this study.

4.1 Sanity check of the snow classification

At the first step of our data analysis, the classification of unrimed and rimed snow using DWR(X, Ka)-V_X observations at the ML top, proposed in the previous section, was evaluated against previous studies. As shown in Fig. 3, both DWR(X, Ka) and V_X tend to increase as the precipitation intensifies. Most cases of rimed snow fall in the region of DWR(X, Ka) $<$ 4 dB and V_X being higher than for unrimed snow. The V_X of unrimed snow rarely exceeds 1.5 m s^{-1}. Those outliers of rimed snow in Fig. 1a may be attributed to the local vertical air motions, which contaminate the measured mean Doppler velocity. It should be noted that the snow observations in Fig. 1 are limited to PR $\leq$ 4 mm h^{-1}; namely, the maximum radar reflectivity at the ML bottom ($Z_{\text{X,rain}}$) is around 33 dBZ, as computed by using the localized Z–R relation (Leinonen et al., 2012b).

The reflectivity enhancement in the ML, which is defined as the difference between the Z_X maximum in the ML and the Z_X at the melting bottom ($Z_{\text{X,rain}}$), was also studied. Zawadzki et al. (2005) have analyzed the UHF Doppler wind profiler observations in $V_{\text{UHF,snow}}/V_{\text{UHF,rain}}$ reflectivity en-

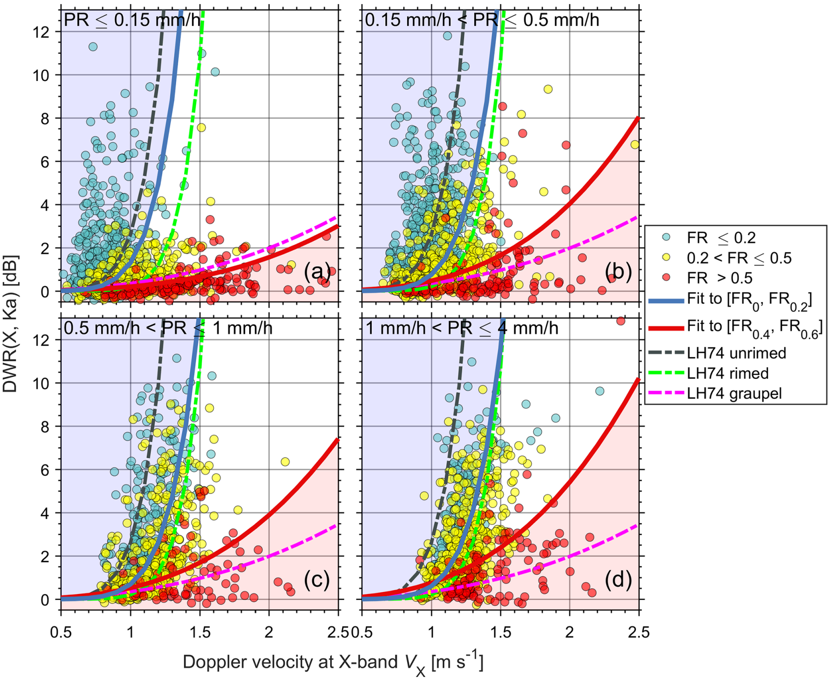

Figure 1. Scatter plot of DWR(X, Ka) versus V_X (1000 hPa and 0 °C) colored with FR. Mass–size and velocity–size relations from Locatelli and Hobbs (1974) are adopted for reference (dashed lines). Observed mass–size and velocity–size relations are derived using the approach developed by von Lerber et al. (2017), and the particle backscattering coefficient $\sigma_{b,\lambda}$ is adopted from Leinonen and Moisseev (2015) and Leinonen and Szyrmer (2015). The solid blue and red curves separate unrimed (light blue shading), transitional (no shading) and rimed snow (light red shading) in our classification scheme.

Table 1. Fitted parameters for $\mathrm{DWR(X,\ Ka)} = aV_X^b$. Aggregates of unrimed radiating assemblages, side planes, bullets, and columns (LH74 unrimed), aggregates of densely rimed radiating assemblages of dendrites (LH74 rimed), and lump graupel (LH74 graupel) in Locatelli and Hobbs (1974) are shown for reference. The last column shows the root mean square error (RMSE) of fitting. The confidence interval is marked by "\" when the parameter is manually fixed.

Fitted parameters		a (95 % confidence interval)	b (95 % confidence interval)	RMSE (dB)
LH74	Unrimed	2.6 (2.2 3)	7.3 (6.1 8.5)	1.9
	Rimed	0.2 (0.09 0.31)	9.8 (8.1 11.5)	1.8
	Graupel	0.35 (0.19 0.51)	2.5 (2.03 2.97)	0.8
$\mathrm{PR} \leq 0.15\,\mathrm{mm\,h^{-1}}$	$\mathrm{FR} \in [0\ 0.2]$	1.3 (1.02 1.58)	7.3 (\)	2
	$\mathrm{FR} \in [0.4\ 0.6]$	0.2 (0.14 0.26)	2.96 (2.26 3.66)	0.5
$0.15\,\mathrm{mm\,h^{-1}} < \mathrm{PR} \leq 0.5\,\mathrm{mm\,h^{-1}}$	$\mathrm{FR} \in [0\ 0.2]$	0.75 (0.64 0.86)	7.3 (\)	2.4
	$\mathrm{FR} \in [0.4\ 0.6]$	0.47 (0.37 0.57)	3.1 (2.7 3.5)	1.1
$0.5\,\mathrm{mm\,h^{-1}} < \mathrm{PR} \leq 1\,\mathrm{mm\,h^{-1}}$	$\mathrm{FR} \in [0\ 0.2]$	0.69 (0.61 0.77)	7.3 (\)	2.2
	$\mathrm{FR} \in [0.4\ 0.6]$	0.52 (0.4 0.64)	2.9 (2.3 3.5)	0.85
$1\,\mathrm{mm\,h^{-1}} < \mathrm{PR} \leq 4\,\mathrm{mm\,h^{-1}}$	$\mathrm{FR} \in [0\ 0.2]$	0.6 (0.59 0.61)	7.3 (\)	2.3
	$\mathrm{FR} \in [0.4\ 0.6]$	0.75 (0.59 0.91)	2.85 (2.16 3.54)	1.2

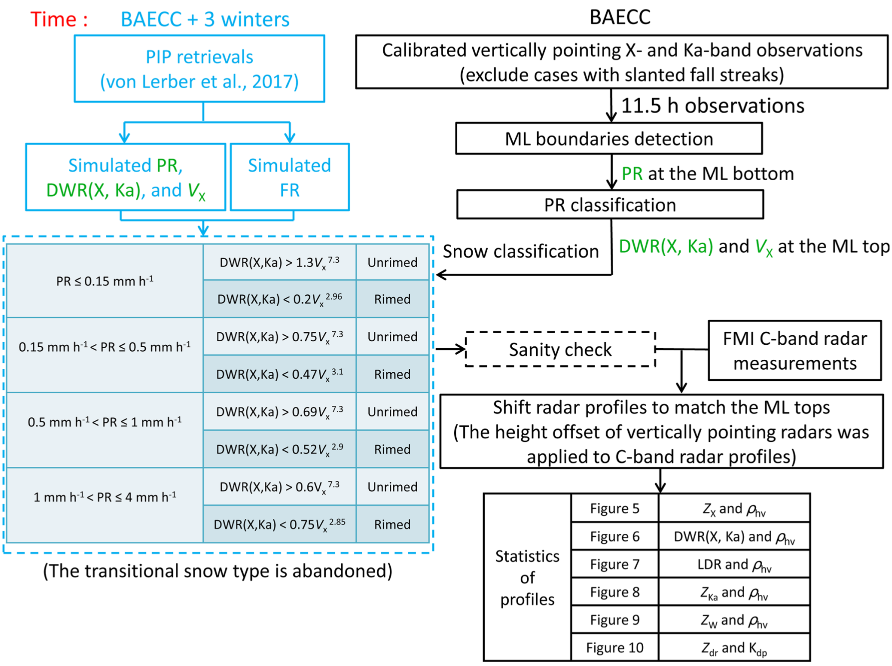

Figure 2. Flow chart of the data process in this study. The snow classification part as discussed in Sect. 3.1 is in light blue. Variables used in snow classification are in green. Radar observations during BAECC are in black. The sanity check in the next section is represented by the dashed black diagram.

Table 2. Summary of the studied events.

Event	Date	Event	Date
1	9 May 2014	13	10 August 2014
2	11 May 2014	14	12 August 2014
3	16 May 2014	15	13 August 2014
4	19 May 2014	16	14 August 2014
5	31 May 2014	17	18 August 2014
6	4 June 2014	18	19 August 2014
7	6 June 2014	19	20 August 2014
8	12 June 2014	20	24 August 2014
9	13 June 2014	21	25 August 2014
10	15 July 2014	22	26 August 2014
11	16 July 2014	23	27 August 2014
12	30 July 2014	24	9 September 2014

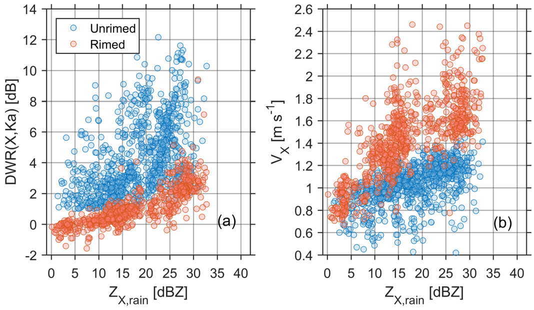

Figure 3. Distribution of **(a)** DWR(X, Ka) and **(b)** V_X above the ML as a function of $Z_{X,rain}$. Note that no transitional snow type between unrimed and rimed is presented.

hancement space and found that the augmentation of rimed snowflake mass can increase $V_{UHF,snow}/V_{UHF,rain}$ and decrease reflectivity enhancement. As shown in Fig. 4, despite the scattered distribution of reflectivity enhancement, the majority of cases with high $V_{X,snow}/V_{X,rain}$ is dominated by rimed snow, while most unrimed cases are below $V_{X,snow}/V_{X,rain} = 0.25$. Such dependence of $V_{X,snow}/V_{X,rain}$ on riming is in line with the results in Zawadzki et al. (2005), indicating the reasonable snow classification employed in this study.

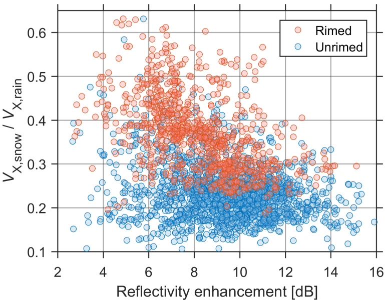

Figure 4. Scatter plot of $V_{\mathrm{X,snow}}/V_{\mathrm{X,rain}}$ versus reflectivity enhancement in the ML. The reflectivity enhancement is defined as the difference between the reflectivity peak in the ML and the reflectivity in rain just below the ML.

4.2 Vertical profiles of multifrequency radar measurements in the ML

To obtain a general idea of how the ML is modulated by riming and aggregation, statistics of vertically pointing radar observations were made. As the ML properties are modulated by precipitation intensity (Fabry and Zawadzki, 1995; Carlin and Ryzhkov, 2019), the observations were grouped by PR. For ease of comparison, the vertical axis is shifted such that the reference height is the ML top.

4.2.1 X-band reflectivity, ρ_{hv} and DWR(X, Ka)

Figure 5 shows the profiles of radar reflectivity and ρ_{hv} measured by X-SACR and grouped by PR. Note that to generalize the observations, the vertical axis is shifted such that the ML top is the reference height of 0 m, and each reflectivity profile was normalized by offsetting the difference between $Z_{\mathrm{X,rain}}$ and the median value of $Z_{\mathrm{X,rain}}$ in the corresponding PR group. The same procedure was made to ρ_{hv} and the following measurements. For most cases, the relative humidity (RH) around the ML top is above 95 % with no dependence on PR. Thus, the effect of dry air infiltration, e.g., decreasing reflectivity and ML thickness and descending dual-polarization measurements (Carlin and Ryzhkov, 2019), should be minimized. Considering the general aspects of Fig. 5, it is clear that the ML thickness and reflectivity peak increase with PR, which is in line with previous results (Fabry and Zawadzki, 1995; Wolfensberger et al., 2016; Trömel et al., 2019).

The ρ_{hv} and radar reflectivity have been used in identifying the bright band sagging (Kumjian et al., 2016; Ryzhkov et al., 2016; Xie et al., 2016). When PR is greater than 1 mm h^{-1}, the level of ρ_{hv} minimum of rimed snow seems to be lower than the unrimed; however, the opposite holds when PR is less than or equal to 1 mm h^{-1}, which seems controversial to the expectation that the bright band sagging is mainly caused by riming (Kumjian et al., 2016). In our observations, both ρ_{hv} dip and reflectivity peak descend with the increase in PR. Therefore, it appears that precipitation intensity is an important factor affecting the formation of the saggy bright band. This finding is in line with a recent simulation study (Carlin and Ryzhkov, 2019), which proposes that the saggy bright band can also be attributed to other factors, such as the aggregation process, the increased precipitation intensity and the sudden decrease in RH. For unrimed snow, the response of ρ_{hv} to the melting is obviously later than X-band reflectivity, which indicates that the utilization of ρ_{hv} for detecting the ML top should be applied with caution.

The reflectivity peak is smaller for rimed snow than unrimed for a given PR provided that the Rayleigh scattering is not violated. When PR is greater than 1 mm h^{-1}, the reflectivity peaks of rimed and unrimed snow are closer, which can be explained by the non-Rayleigh scattering of very large aggregates at X-band, as discussed by Fabry and Zawadzki (1995). Another notable finding is that the Z_{X} at the ML top for rimed snow is smaller than unrimed, which indicates that rimed snowflakes may have smaller sizes for a given PR. This is further confirmed in the DWR(X, Ka) profiles as shown in Fig. 6. From the aggregation region to the ML top, the DWR(X, Ka) of rimed snow is significantly smaller than unrimed snow. In particular, very weak DWR(X, Ka) for rimed snow could be identified just above the ML. This indicates that the aggregation process, the dominating factor of growing snow size close to the ML (Fabry and Zawadzki, 1995), can be heavily suppressed for rimed snow. Heymsfield et al. (2015) have reported the enhanced maximum particle size below the 0 °C isotherm using in situ measurements and attributed it to the continuing aggregation in the ML. Such continuing aggregation in conjunction with the changing scattering properties (the water coating) may be responsible for the continuing increase in DWR(X, Ka) in the ML.

Interestingly, the DWR(X, Ka) profile below the ML is higher for the rimed cases and progressively converges towards the unrimed profile as PR increases. For light precipitation, the rain drops are small enough to be Rayleigh scatterers at Ka-band; thus the difference of DWR(X, Ka) in rain between unrimed and rimed cases is rooted in the differences in attenuation. If the supercooled liquid water attenuation of rimed cases is more significant, the corresponding DWR(X, Ka) in rain would be smaller than the unrimed cases. However, the reverse is observed. von Lerber et al. (2014) have shown that the melting layer attenuation of rimed snowflakes is smaller than unrimed ones, which could possibly explain the larger DWR(X, Ka) of rimed cases in rain. With the increase in precipitation intensity, the DWR(X, Ka) of rimed cases in rain decreases towards the unrimed profile. This can be attributed to several factors, such as the enhanced liquid attenuation above the melting layer and the non-Rayleigh scattering of large raindrops at Ka-band. We hesitate to determine the role of non-Rayleigh scattering in rain since raindrops characterized by

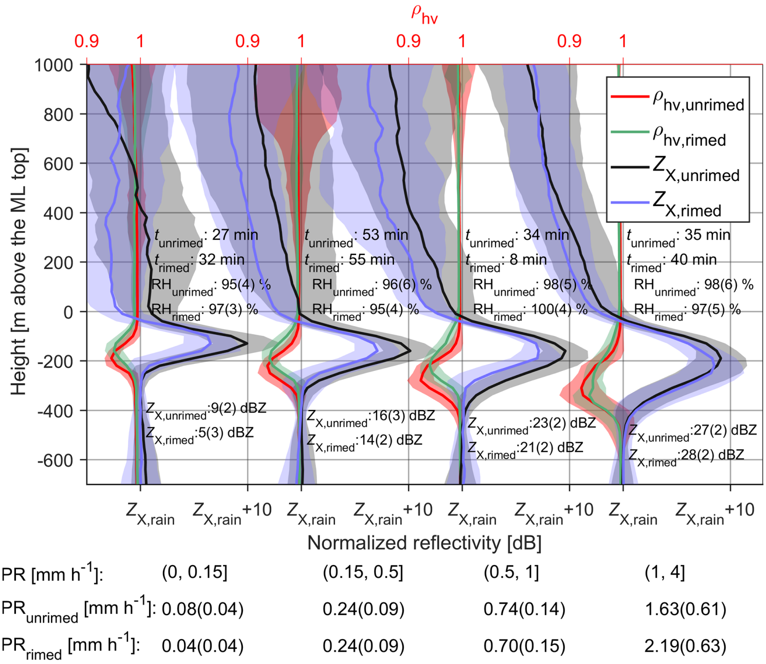

Figure 5. Normalized X-band radar profiles grouped by PR. t_{unrimed} and t_{rimed} indicate the total observing time in each group for unrimed and rimed cases, respectively. The median values of X-band reflectivity at the ML bottom for unrimed ($Z_{\text{X,unrimed}}$) and rimed ($Z_{\text{X,rimed}}$) cases are marked just below the ML bottom with the standard values in brackets. The median and standard deviations (in parentheses) of relative humidity (RH) at the ML top for unrimed ($\text{RH}_{\text{unrimed}}$) and rimed ($\text{RH}_{\text{rimed}}$) cases in each group are presented near the ML top. The median and standard deviations (in parentheses) of PR for unrimed ($\text{PR}_{\text{unrimed}}$) and rimed ($\text{PR}_{\text{rimed}}$) cases in each group are presented in the lower part. Shaded regions represent the standard derivation.

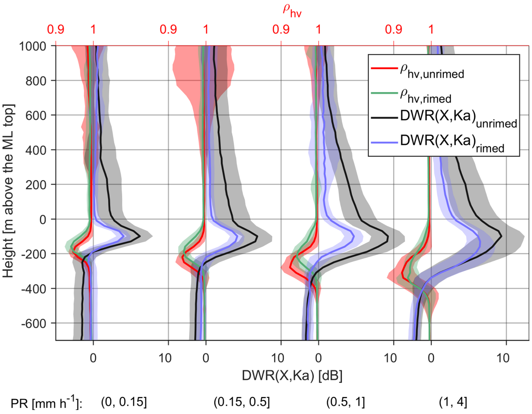

Figure 6. Same as Fig. 5 but for DWR(X, Ka). Note that the radar calibration is made by matching the X- and Ka-band radar reflectivities at precipitation top.

different non-Rayleigh scattering size regions can lead to opposite effects on DWR(X, Ka), as shown by Li and Moisseev (2019).

4.2.2 Ka-band LDR and reflectivity

LDR usually increases in the ML as melting increases the dielectric constant of nonspherical ice particles. Figure 7 shows the profiles of LDR (Ka-SACR) and ρ_{hv} (X-SACR). Both LDR peak and ρ_{hv} dip in rimed snow are lower than unrimed snow when PR is greater than 1 mm h^{-1}, while the reverse is observed for lighter precipitation. Despite the rather good agreement between LDR and ρ_{hv} observations, it appears that LDR systematically reveals a lower ML bottom than ρ_{hv}, indicating that LDR can be suitable in discriminating between rain and melting snow (Illingworth and Thompson, 2011; Dias Neto et al., 2019). The smaller LDR peak for rimed snow is correlated with the smaller X-band reflectivity enhancement as shown in Fig. 5, which is consistent with Illingworth and Thompson (2011) and Sandford et al. (2017).

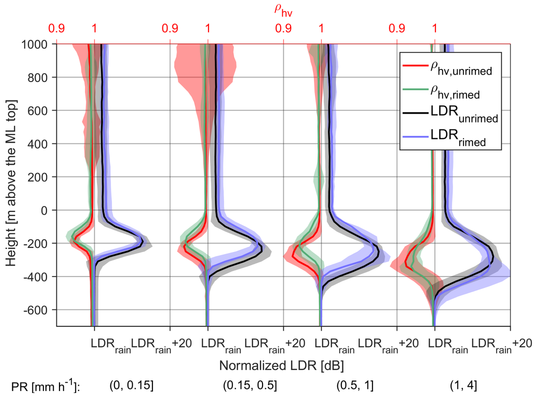

Figure 7. Same as Fig. 5 but for LDR observed by Ka-SACR.

As shown in Fig. 8, the Ka-band reflectivity enhancement in the ML decreases as the precipitation intensifies. This is similar to the observations presented by Fabry and Zawadzki (1995) who found that the reflectivity peak in the ML observed by an X-band radar is less pronounced than that measured by an UHF radar when the reflectivity in rain exceeds 25 dBZ. With the increase in precipitation intensity, the size of snowflakes generally grows. Therefore, there are less hydrometeors satisfying the Rayleigh criteria, and the non-Rayleigh scattering becomes more significant. As a result, the reflectivity peak in the ML is not as pronounced as in the scenario of Rayleigh scattering. In addition, the ML attenuation increases as PR intensifies (Li and Moisseev, 2019), which further impedes the increase in reflectivity in the ML. This also explains the lower reflectivity enhancement in the ML for rimed snow when PR is greater than 0.5 mm h^{-1}. As shown in Fig. 6, rimed snowflakes are usually smaller; thus the non-Rayleigh effect and ML attenuation (von Lerber et al., 2014) are not as significant as the larger unrimed ice particles.

When PR is less than or equal to 0.15 mm h^{-1}, a weak reflectivity dip, the dark band, appears at the top of the ML for unrimed snow, which may also be observed by centimeter-wavelength radars (Fabry and Zawadzki, 1995). In the literature, the dark band has different definitions. For ground-based radars, Kollias and Albrecht (2005) referred the dip in radar reflectivity below the ML top as dark band. The dark band which is present just above the ML top, as observed by the spaceborne W-band radar, can be caused by the strong signal attenuation from large snow aggregates, as discussed in Sassen et al. (2007). Meanwhile, the change of PSD during the aggregation process can also contribute to this reflectivity dip, which is named dark band by Sassen et al. (2005) and dim band by Heymsfield et al. (2008). In this study, the dark band is identified as the decrease in radar reflectivity just above the ML top, as shown in Sassen et al. (2005, 2007) and Heymsfield et al. (2008).

4.2.3 W-band reflectivity

W-band reflectivity can be heavily affected by a wet radome, rain, ML, supercooled liquid water and gaseous attenuation (Kneifel et al., 2015; Li and Moisseev, 2019). Such attenuation coupled with precipitation microphysical processes, as well as the change of particle scattering regimes, can modulate the W-band reflectivity profiles. As shown in Fig. 9, the decrease in W-band reflectivity with height is mainly caused by rain attenuation. This effect is enhanced as PR increases, which has been adopted to retrieve PR (Matrosov, 2007). From dry to melting snow, there is a jump in W-band reflectivity, and the extent of such a jump seems dependent on PR. The bright band signature is partially visible when PR is less than or equal to 0.15 mm h^{-1} but is absent as the precipitation intensifies. This is expected, given the increased non-Rayleigh scattering at W-band for large snowflakes (Sassen et al., 2005). When PR is less than or equal to 0.15 mm h^{-1}, the dark band is present for both unrimed and rimed snow, while the reflectivity dip near the ML top for unrimed snow is stronger than rimed. Below 1 mm h^{-1}, the dark band is present for unrimed snow, in contrast with its absence for rimed snow when PR is greater than 0.15 mm h^{-1}, which may indicate that the dark band is more frequently observed for the scenario of unrimed snow.

Sassen et al. (2005) have proposed that the dark band observed by W-band radars is due to the combination of Rayleigh and non-Rayleigh scattering effects modulated by the PSD. Heymsfield et al. (2008) have pinpointed that such a reflectivity dip is linked to the aggregation process, which consumes small ice while growing large snowflakes whose backscattering cross sections at W-band are much smaller than the scenario of Rayleigh scattering. This statement is evidenced in our statistical results since the dark band feature is more significant for unrimed snow and is more distinct at W-band than at Ka-band. Furthermore, the obscured dark band for rimed snow may indicate that the aggregation of rimed snow can be weaker than unrimed snow.

4.3 Weather radar measurements

Recent studies have demonstrated the potential of polarimetric measurements in revealing cloud microphysics and improving precipitation forecasts (Tiira and Moisseev, 2020; Trömel et al., 2019). Given the importance of precipitation intensity to the ML, it is necessary to address how the dual-polarization observations are dependent on PR. Therefore, we have analyzed the statistical profiles of Z_{dr} and K_{dp} observed by the RHI scan of the FMI C-band dual-polarization radar. The vertical axis of weather radar RHI observations was shifted to the same level as we did for vertically pointing radars.

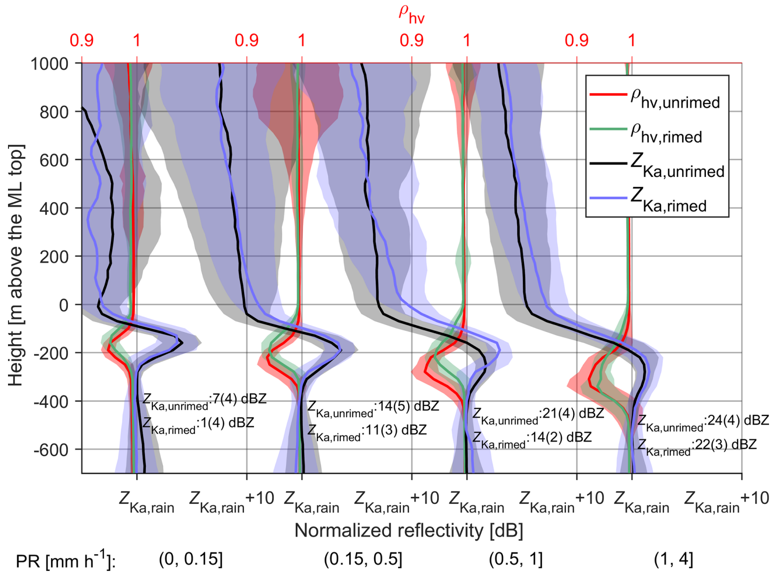

Figure 8. Same as Fig. 5 but for Ka-band radar. Note that the calibration is made by matching the Ka-band reflectivity with X-band at precipitation top, while the attenuation in the profile is not accounted for. To be in line with Fig. 5, ρ_{hv} observed by X-SACR is presented instead of the LDR measured by Ka-SACR.

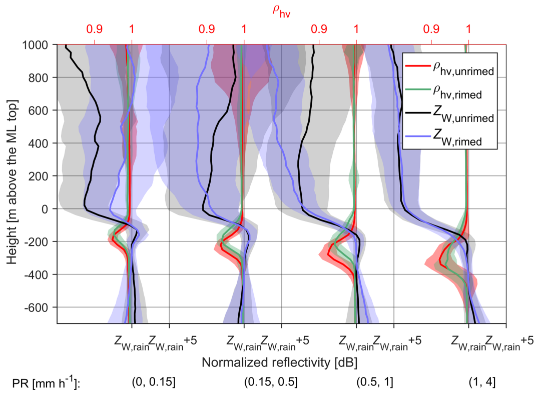

Figure 9. Same as Fig. 5 but for W-band. Note that the reflectivity profiles at W-band are shifted by matching the radar reflectivity at the ML bottom ($Z_{W,rain}$), while the value of $Z_{W,rain}$ is not shown due to the unknown W-band attenuation.

Significant dependence of Z_{dr} and K_{dp} on PR can be found in Fig. 10. In cases when PR is greater than 0.15 mm h^{-1}, Z_{dr} decreases significantly to around 0 dB just above the ML. This is mainly due to the aggregation process, which leads to increased particle size and decreased density. In contrast, Z_{dr} does not change just above the ML when PR is less than or equal to 0.15 mm h^{-1}, indicating that very weak aggregation happens in light precipitation. Li et al. (2018) have shown that Z_{dr} is a function of snow shape, canting angle distribution and density, and it generally decreases with the increase in radar reflectivity. It would be interesting to study the riming impact on Z_{dr} profiles (Vogel and Fabry, 2018); unfortunately, we were not able to perform such a comparison due to the very limited number of RHI profiles during the studied events. It should be noted that the beam width of FMI C-band radar is 1°, resulting in a vertical projection of around 1.1 km over the Hyytiälä station. This explains why the height at which Z_{dr} starts increasing is approximately 500 m higher than the ML top determined by X-SACR.

High K_{dp} values were observed when PR exceeds 1 mm h^{-1}, while no detectable K_{dp} signal can be found when PR is less than or equal to 1 mm h^{-1}. This is in line with the previous finding that the enhanced K_{dp} is indicative of intense precipitation (Bechini et al., 2013). When PR is greater than 1 mm h^{-1}, the enhanced K_{dp} starts at around 3000 m above the ML with the expected temperature of around -20 °C, which is related to the dendritic growth region (Bechini et al., 2013; Moisseev et al., 2015). Overall, these observations indicate that the dependence of ML properties on the dual-polarization signatures above may mainly be due to the correlation of these signatures with precipitation intensity.

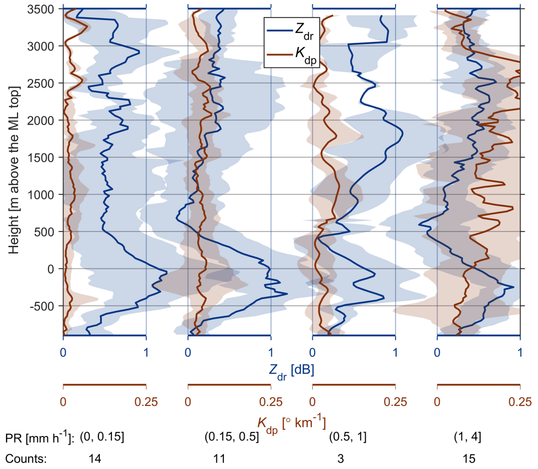

Figure 10. Normalized Z_{dr} and K_{dp} profiles observed by FMI C-band radar with RHI scanning. Number of RHI profiles is presented at the bottom. The ML top (as retrieved from X-SACR observations) is used as the reference height in the vertical axis.

5 Conclusions

In this work, the connection between the precipitation melting layer and snow microphysics was studied using vertically pointing multifrequency Doppler radar and C-band dual-polarization weather radar observations. Using surface-based snowfall measurements collected over five winters at the University of Helsinki measurement station and supplemented by the single particle scattering datasets of aggregated snowflakes and rimed ice particles, a connection between rime mass fraction and radar observations at X- and Ka-bands was established and used in classifying unrimed and rimed snow. The sanity checks show that the results of this classification are consistent with the previous study using single-frequency radar observations (Zawadzki et al., 2005). Statistics of vertically pointing multifrequency dual-polarization radars and RHI scans of C-band polarimetric weather radar show the following.

1. The radar-observed melting layer properties show a detectable connection to the precipitation intensity. The increase in precipitation intensity can lead to the saggy bright band, i.e., the descending of reflectivity peak and ρ_{hv} dip.
2. Riming can affect melting layer properties in the following ways.
   a. In moderate to heavy rainfall, riming may cause additional bright band sagging. However, the opposite effect is observed in light precipitation, namely, such sagging is associated with unrimed snow.
   b. X-band radar reflectivity peak is smaller for rimed snow than unrimed for a given precipitation intensity if the non-Rayleigh scattering effect is not significant.
   c. If the non-Rayleigh scattering effect is distinct, e.g., at Ka- or W-band, the reflectivity peak can be larger for rimed snow.
   d. The reflectivity dip at the melting layer top (dark band) is obscured for rimed snow, while it is pronounced for unrimed snow. This suggests that the aggregation process may be suppressed by riming.
3. The decrease in Z_{dr} towards the melting layer is pronounced in heavy precipitation but is insignificant in light precipitation.

A well-calibrated triple-frequency radar setup has been shown potential in studying the microphysics of snowfall. However, such measurements may not be well suited to rainfall due to the highly uncertain W-band attenuation caused by the melting layer, as well as the supercooled water. The approach presented explores the possibility of adding the Doppler velocity to distinguish between unrimed and rimed conditions and is less affected by the attenuation from supercooled water. Such instrumentation as the X/Ka-SACR mounted on the same platform takes much less effort in pointing alignment. Its application may also be expanded to space-borne radars. For example, instead of launching triple-frequency radars, implementing the Doppler capability with sufficient sensitivity on either of the radars on a dual-wavelength platform may be served as an option.

A coordinated radar setup as employed during BAECC facilitates the synergy of multiple radar frequencies and polarimetric observations at various scan modes. Due to the periodical changes of radar scanning modes during BAECC, the total stratiform rainfall cases are limited to ~ 11.5 h. More of such observations can be utilized to evaluate and consolidate the presented conclusions. If such coordinated measurements with high time resolutions can be obtained in the future, our understanding of snow microphysical processes may be further advanced.

Data availability. Quicklooks of radar observations used in this study are available at https://doi.org/10.5281/zenodo.3979103 (Li, 2020).

The FMI radar data are available from the Atmospheric Radiation Measurement (ARM) Climate Research Facility (https://iop.archive.arm.gov/arm-iop/2014/tmp/baecc/moisseev-radar_cband/?uid=LIH2&st=5f32748d&home=arm-archive, last access: 11 August 2020) (von Lerber, 2020).

The ARM data used in this study are available from Atmospheric Radiation Measurement (ARM) Climate Research Facility (ARM Climate Research Facility, 2006, 2010, 2011).

PIP data are available from https://doi.org/10.5281/zenodo.3977959 (Moisseev, 2020).

Author contributions. HL and DM designed and conceptualized the study. HL performed the investigation and did the data analysis. DM contributed with the research supervision. JT processed the FMI C-band radar raw data. AvL developed the snow retrieval algorithm based on PIP products. HL wrote the original paper. All coauthors contributed to reviewing and editing this paper.

Competing interests. The authors declare that they have no conflict of interest.

Acknowledgements. We would like to thank the personnel of Hyytiälä Station for their support in field observations. We especially thank Matti Leskinen for his help in data analysis. The research of Haoran Li, Jussi Tiira and Dmitri Moisseev was supported by the Academy of Finland's Centers of Excellence program (grant 307331) and ERA-PLANET's transnational project iCUPE (grant agreement 689443), funded under the EU Horizon 2020 framework program. Annakaisa von Lerber was funded by the Academy of Finland (postdoc grant 333901). Haoran Li was also funded by the China Scholarship Council. The instrumentation used in this study was supported by NASA's Global Precipitation Measurement Mission ground validation program and by the US Department of Energy's Office of Science ARM program.

Financial support. This research has been supported by the Academy of Finland (grant no. 307331), the European Commission (grant no. ERA-PLANET (689443)) and the China Scholarship Council (grant no. 201603170181).

Open-access funding was provided by Helsinki University Library.

Review statement. This paper was edited by Jui-Yuan Christine Chiu and reviewed by Andrew Heymsfield and two anonymous referees.

References

ARM Climate Research Facility: Marine W-Band (95 GHz) ARM Cloud Radar (MWACR). 2014-01-15 to 2014-09-13, ARM Mobile Facility (TMP) U. of Helsinki Research Station (SMEAR II), Hyytiala, Finland; AMF2 (M1), Compiled by: Isom, B., Bharadwaj, N., Lindenmaier, I., Nelson, D., Hardin, J., and Matthews, A., Atmospheric Radiation Measurement (ARM) Climate Research Facility Data Archive, Oak Ridge, Tennessee, USA, https://doi.org/10.5439/1150242, 2006.

ARM Climate Research Facility: Ka-Band Scanning ARM Cloud Radar (KASACRVPT). 2014-01-15 to 2014-09-13, ARM Mobile Facility (TMP) U. of Helsinki Research Station (SMEAR II), Hyytiala, Finland; AMF2 (M1), Compiled by: Isom, B., Bharadwaj, N., Lindenmaier, I., Nelson, D., Hardin, J., and Matthews, A., Atmospheric Radiation Measurement (ARM) Climate Research Facility Data Archive, Oak Ridge, Tennessee, USA, https://doi.org/10.5439/1046201, 2010.

ARM Climate Research Facility: X-Band Scanning ARM Cloud Radar (XSACRVPT). 2014-01-15 to 2014-09-13, ARM Mobile Facility (TMP) U. of Helsinki Research Station (SMEAR II), Hyytiala, Finland; AMF2 (M1), Compiled by: Isom, B., Bharadwaj, N., Lindenmaier, I., Nelson, D., Hardin, J., and Matthews, A., Atmospheric Radiation Measurement (ARM) Climate Research Facility Data Archive, Oak Ridge, Tennessee, USA, https://doi.org/10.5439/1150303, 2011.

Atlas, D.: Drop size and radar structure of a precipitation streamer, J. Meteorol., 14, 261–271, 1957.

Bailey, M. P. and Hallett, J.: A comprehensive habit diagram for atmospheric ice crystals: confirmation from the laboratory, AIRS II, and other field studies, J. Atmos. Sci., 66, 2888–2899, 2009.

Barrett, A. I., Westbrook, C. D., Nicol, J. C., and Stein, T. H. M.: Rapid ice aggregation process revealed through triple-wavelength Doppler spectrum radar analysis, Atmos. Chem. Phys., 19, 5753–5769, https://doi.org/10.5194/acp-19-5753-2019, 2019.

Battaglia, A., Kummerow, C., Shin, D.-B., and Williams, C.: Constraining microwave brightness temperatures by radar brightband observations, J. Atmos. Ocean. Tech., 20, 856–871, 2003.

Bechini, R., Baldini, L., and Chandrasekar, V.: Polarimetric radar observations in the ice region of precipitating clouds at C-band and X-band radar frequencies, J. Appl. Meteorol. Clim., 52, 1147–1169, 2013.

Bringi, V. N. and Chandrasekar, V.: Polarimetric Doppler weather radar: principles and applications, Cambridge University Press, Cambridge, 2001.

Carlin, J. T. and Ryzhkov, A. V.: Estimation of melting-layer cooling rate from dual-polarization radar: spectral bin model simulations, J. Appl. Meteorol. Clim., 58, 1485–1508, 2019.

Chase, R. J., Finlon, J. A., Borque, P., McFarquhar, G. M., Nesbitt, S. W., Tanelli, S., Sy, O. O., Durden, S. L., and Poellot, M. R.: Evaluation of triple-frequency radar retrieval of snowfall properties using coincident airborne in situ observations during OLYMPEX, Geophys. Res. Lett., 45, 5752–5760, 2018.

Dias Neto, J., Kneifel, S., Ori, D., Trömel, S., Handwerker, J., Bohn, B., Hermes, N., Mühlbauer, K., Lenefer, M., and Simmer, C.: The TRIple-frequency and Polarimetric radar Experiment for improving process observations of winter precipitation, Earth Syst. Sci. Data, 11, 845–863, https://doi.org/10.5194/essd-11-845-2019, 2019.

Doviak, R., Bringi, V., Ryzhkov, A., Zahrai, A., and Zrnić, D.: Considerations for polarimetric upgrades to operational WSR-88D radars, J. Atmos. Ocean. Tech., 17, 257–278, 2000.

Erlingis, J. M., Gourley, J. J., Kirstetter, P.-E., Anagnostou, E. N., Kalogiros, J., Anagnostou, M. N., and Petersen, W.: Evaluation of operational and experimental precipitation algorithms and microphysical insights during IPHEx, J. Hydrometeorol., 19, 113–125, 2018.

Fabry, F. and Zawadzki, I.: Long-term radar observations of the melting layer of precipitation and their interpretation, J. Atmos. Sci., 52, 838–851, 1995.

Falconi, M. T., von Lerber, A., Ori, D., Marzano, F. S., and Moisseev, D.: Snowfall retrieval at X, Ka and W bands: consistency of backscattering and microphysical properties using BAECC ground-based measurements, Atmos. Meas. Tech., 11, 3059–3079, https://doi.org/10.5194/amt-11-3059-2018, 2018.

Giangrande, S. E., Krause, J. M., and Ryzhkov, A. V.: Automatic designation of the melting layer with a polarimetric prototype of the WSR-88D radar, J. Appl. Meteorol. Clim., 47, 1354–1364, 2008.

Giangrande, S. E., Toto, T., Bansemer, A., Kumjian, M. R., Mishra, S., and Ryzhkov, A. V.: Insights into riming and aggregation processes as revealed by aircraft, radar, and disdrometer observations for a 27 April 2011 widespread precipitation event, J. Geophys. Res.-Atmos., 121, 5846–5863, 2016.

Grecu, M., Tian, L., Heymsfield, G. M., Tokay, A., Olson, W. S., Heymsfield, A. J., and Bansemer, A.: Nonparametric methodology to estimate precipitating ice from multiple-frequency radar reflectivity observations, J. Appl. Meteorol. Clim., 57, 2605–2622, 2018.

Haynes, J. M., L'Ecuyer, T. S., Stephens, G. L., Miller, S. D., Mitrescu, C., Wood, N. B., and Tanelli, S.: Rainfall retrieval over the ocean with spaceborne W-band radar, J. Geophys. Res.-Atmos., 114, D00A22, https://doi.org/10.1029/2008JD009973, 2009.

Helmus, J. J. and Collis, S. M.: The Python ARM Radar Toolkit (Py-ART), a library for working with weather radar data in the Python programming language, J. Open Res. Softw., 4, e25, https://doi.org/10.5334/jors.119, 2016.

Heymsfield, A. J., Bansemer, A., Schmitt, C., Twohy, C., and Poellot, M. R.: Effective ice particle densities derived from aircraft data, J. Atmos. Sci., 61, 982–1003, 2004.

Heymsfield, A. J., Bansemer, A., and Twohy, C. H.: Refinements to ice particle mass dimensional and terminal velocity relationships for ice clouds. Part I: Temperature dependence, J. Atmos. Sci., 64, 1047–1067, 2007.

Heymsfield, A. J., Bansemer, A., Matrosov, S., and Tian, L.: The 94-GHz radar dim band: Relevance to ice cloud properties and CloudSat, Geophys. Res. Lett., 35, L03802, https://doi.org/10.1029/2007GL031361, 2008.

Heymsfield, A. J., Bansemer, A., Poellot, M. R., and Wood, N.: Observations of ice microphysics through the melting layer, J. Atmos. Sci., 72, 2902–2928, 2015.

Heymsfield, G. M.: Doppler radar study of a warm frontal region, J. Atmos. Sci., 36, 2093–2107, 1979.

Hogan, R. J., Illingworth, A. J., and Sauvageot, H.: Measuring crystal size in cirrus using 35-and 94-GHz radars, J. Atmos. Ocean. Tech., 17, 27–37, 2000.

Huggel, A., Schmid, W., and Waldvogel, A.: Raindrop size distributions and the radar bright band, J. Appl. Meteorol., 35, 1688–1701, 1996.

Illingworth, A. and Thompson, R.: Radar bright band correction using the linear depolarisation ratio, in: Proceedings of the 8th International Symposium on Weather Radar and Hydrology, April 2011, Exeter, UK, 64–68, 2011.

Klaassen, W.: Radar observations and simulation of the melting layer of precipitation, J. Atmos. Sci., 45, 3741–3753, 1988.

Kneifel, S., Kulie, M., and Bennartz, R.: A triple-frequency approach to retrieve microphysical snowfall parameters, J. Geophy. Res.-Atmos., 116, D11203, https://doi.org/10.1029/2010JD015430, 2011.

Kneifel, S., Lerber, A., Tiira, J., Moisseev, D., Kollias, P., and Leinonen, J.: Observed relations between snowfall microphysics and triple-frequency radar measurements, J. Geophy. Res.-Atmos., 120, 6034–6055, 2015.

Kollias, P. and Albrecht, B.: Why the melting layer radar reflectivity is not bright at 94 GHz, Geophys. Res. Lett., 32, L24818, https://doi.org/10.1029/2005GL024074, 2005.

Kollias, P., Jo, I., Borque, P., Tatarevic, A., Lamer, K., Bharadwaj, N., Widener, K., Johnson, K., and Clothiaux, E. E.: Scanning ARM cloud radars. Part II: Data quality control and processing, J. Atmos. Ocean. Tech., 31, 583–598, 2014.

Korolev, A., Isaac, G., and Hallett, J.: Ice particle habits in stratiform clouds, Q. J. Roy. Meteorol. Soc., 126, 2873–2902, 2000.

Korolev, A. V., Isaac, G. A., Cober, S. G., Strapp, J. W., and Hallett, J.: Microphysical characterization of mixed-phase clouds, Q. J. Roy. Meteorol. Soc., 129, 39–65, 2003.

Kruger, A. and Krajewski, W. F.: Two-dimensional video disdrometer: A description, J. Atmos. Ocean. Tech., 19, 602–617, 2002.

Kumjian, M. R., Mishra, S., Giangrande, S. E., Toto, T., Ryzhkov, A. V., and Bansemer, A.: Polarimetric radar and aircraft observations of saggy bright bands during MC3E, J. Geophys. Res.-Atmos., 121, 3584–3607, 2016.

Lamb, D. and Verlinde, J.: Physics and chemistry of clouds, Cambridge University Press, Cambridge, 2011.

Leinonen, J. and Moisseev, D.: What do triple-frequency radar signatures reveal about aggregate snowflakes?, J. Geophys. Res.-Atmos., 120, 229–239, 2015.

Leinonen, J. and Szyrmer, W.: Radar signatures of snowflake riming: A modeling study, Earth Space Sci., 2, 346–358, 2015.

Leinonen, J., Kneifel, S., Moisseev, D., Tyynelä, J., Tanelli, S., and Nousiainen, T.: Evidence of nonspheroidal behavior in millimeter-wavelength radar observations of snowfall, J. Geophys. Res.-Atmos., 117, D18205, https://doi.org/10.1029/2012JD017680, 2012a.

Leinonen, J., Moisseev, D., Leskinen, M., and Petersen, W. A.: A climatology of disdrometer measurements of rainfall in Finland over five years with implications for global radar observations, J. Appl. Meteorol. Clim., 51, 392–404, 2012b.

Leinonen, J., Moisseev, D., and Nousiainen, T.: Linking snowflake microstructure to multi-frequency radar observations, J. Geophys. Res.-Atmos., 118, 3259–3270, 2013.

Leinonen, J., Lebsock, M. D., Tanelli, S., Sy, O. O., Dolan, B., Chase, R. J., Finlon, J. A., von Lerber, A., and Moisseev, D.:

Retrieval of snowflake microphysical properties from multifrequency radar observations, Atmos. Meas. Tech., 11, 5471–5488, https://doi.org/10.5194/amt-11-5471-2018, 2018.

Lhermitte, R. M.: Observation of rain at vertical incidence with a 94 GHz Doppler radar: An insight on Mie scattering, Geophys. Res. Lett., 15, 1125–1128, 1988.

Li, H. and Moisseev, D.: Melting layer attenuation at Ka- and W-bands as derived from multi-frequency radar Doppler spectra observations, J. Geophys. Res.-Atmos., 124, 9520–9533, https://doi.org/10.1029/2019JD030316, 2019.

Li, H.: Quicklooks of X-SACR data during BAECC – stratiform rainfall, zenodo, https://doi.org/10.5281/zenodo.3979103, 2020.

Li, H. and Moisseev, D.: Two layers of melting ice particles within a single radar bright band: Interpretation and implications, Geophys. Res. Lett., 47, e2020GL087499, https://doi.org/10.1029/2020GL087499, 2020.

Li, H., Moisseev, D., and von Lerber, A.: How does riming affect dual-polarization radar observations and snowflake shape?, J. Geophys. Res.-Atmos., 123, 6070–6081, 2018.

Liebe, H. J.: An updated model for millimeter wave propagation in moist air, Radio Sci., 20, 1069–1089, 1985.

Locatelli, J. D. and Hobbs, P. V.: Fall speeds and masses of solid precipitation particles, J. Geophys. Res., 79, 2185–2197, 1974.

Mason, S., Chiu, C., Hogan, R., Moisseev, D., and Kneifel, S.: Retrievals of riming and snow density from vertically pointing doppler radars, J. Geophys. Res.-Atmos., 123, 13807–13834, 2018.

Mason, S. L., Hogan, R. J., Westbrook, C. D., Kneifel, S., Moisseev, D., and von Terzi, L.: The importance of particle size distribution and internal structure for triple-frequency radar retrievals of the morphology of snow, Atmos. Meas. Tech., 12, 4993–5018, https://doi.org/10.5194/amt-12-4993-2019, 2019.

Matrosov, S. Y.: A dual-wavelength radar method to measure snowfall rate, J. Appl. Meteorol., 37, 1510–1521, 1998.

Matrosov, S. Y.: Potential for attenuation-based estimations of rainfall rate from CloudSat, Geophys. Res. Lett., 34, L05817, https://doi.org/10.1029/2006GL029161, 2007.

Matrosov, S. Y.: Assessment of radar signal attenuation caused by the melting hydrometeor layer, IEEE T. Geosci. Remote., 46, 1039–1047, 2008.

Moisseev, D.: Snow microphysical properties retrieved from PIP observations collected in Hyytiälä on 2014–2015, zenodo, https://doi.org/10.5281/zenodo.3977959, 2020.

Moisseev, D., von Lerber, A., and Tiira, J.: Quantifying the effect of riming on snowfall using ground-based observations, J. Geophys. Res.-Atmos., 122, 4019–4037, 2017.

Moisseev, D., Lautaportti, S., Alku, L., Tabakova, K., O'Connor, E. J., Leskinen, M., and Kulmala, M.: Inadvertent Localized Intensification of Precipitation by Aircraft, J. Geophys. Res.-Atmos., 124, 2094–2104, https://doi.org/10.1029/2018JD029449, 2019.

Moisseev, D. N., Lautaportti, S., Tyynela, J., and Lim, S.: Dual-polarization radar signatures in snowstorms: Role of snowflake aggregation, J. Geophys. Res.-Atmos., 120, 12644–12655, 2015.

Morrison, H. and Milbrandt, J. A.: Parameterization of cloud microphysics based on the prediction of bulk ice particle properties. Part I: Scheme description and idealized tests, J. Atmos. Sci., 72, 287–311, 2015.

Newman, A. J., Kucera, P. A., and Bliven, L. F.: Presenting the snowflake video imager (SVI), J. Atmos. Ocean. Tech., 26, 167–179, 2009.

Oue, M., Kollias, P., Ryzhkov, A., and Luke, E. P.: Toward exploring the synergy between cloud radar polarimetry and Doppler spectral analysis in deep cold precipitating systems in the Arctic, J. Geophys. Res.-Atmos., 123, 2797–2815, 2018.

Petäjä, T., O'Connor, E. J., Moisseev, D., Sinclair, V. A., Manninen, A. J., Väänänen, R., von Lerber, A., Thornton, J. A., Nicoll, K., Petersen, W., Chandrasekar, V., Smith, J. N., Winkler, P. M., Krüger, O., Hakola, H., Timonen, H., Brus, D., Laurila, T., Asmi, E., Riekkola, M. L., Mona, L., Massoli, P., Engelmann, R., Komppula, M., Wang, J., Kuang, C. G., Back, J., Virtanen, A., Levula, J., Ritsche, M., and Hickmon, N.: BAECC: A field campaign to elucidate the impact of biogenic aerosols on clouds and climate, B. Am. Meteorol. Soc., 97, 1909–1928, 2016.

Ryde, J.: The attenuation and radar echoes produced at centimeter wavelengths by various meteorological phenomena, in: Meteorological Factors in Radio Wave Propagation, Physical Society, London, 169–189, 1946.

Ryzhkov, A., Zhang, P., Reeves, H., Kumjian, M., Tschallener, T., Trömel, S., and Simmer, C.: Quasi-vertical profiles – A new way to look at polarimetric radar data, J. Atmos. Ocean. Tech., 33, 551–562, 2016.

Sandford, C., Illingworth, A., and Thompson, R.: The potential use of the linear depolarization ratio to distinguish between convective and stratiform rainfall to improve radar rain-rate estimates, J. Appl. Meteorol. Clim., 56, 2927–2940, 2017.

Sarma, A. C., Deshamukhya, A., Narayana Rao, T., and Sharma, S.: A study of raindrop size distribution during stratiform rain and development of its parameterization scheme in the framework of multi-parameter observations, Meteorol. Appl., 23, 254–268, 2016.

Sassen, K., Campbell, J. R., Zhu, J., Kollias, P., Shupe, M., and Williams, C.: Lidar and triple-wavelength Doppler radar measurements of the melting layer: A revised model for dark- and brightband phenomena, J. Appl. Meteorol., 44, 301–312, 2005.

Sassen, K., Matrosov, S., and Campbell, J.: CloudSat spaceborne 94 GHz radar bright bands in the melting layer: An attenuation-driven upside-down lidar analog, Geophys. Res. Lett., 34, L16818, https://doi.org/10.1029/2007GL030291, 2007.

Sekelsky, S. M.: Near-field reflectivity and antenna boresight gain corrections for millimeter-wave atmospheric radars, J. Atmos. Ocean. Tech., 19, 468–477, 2002.

Stewart, R. E., Marwitz, J. D., Pace, J. C., and Carbone, R. E.: Characteristics through the melting layer of stratiform clouds, J. Atmos. Sci., 41, 3227–3237, 1984.

Szeto, K. K., Lin, C. A., and Stewart, R. E.: Mesoscale circulations forced by melting snow. Part I: Basic simulations and dynamics, J. Atmos. Sci., 45, 1629–1641, 1988.

Szyrmer, W. and Zawadzki, I.: Modeling of the melting layer. Part I: Dynamics and microphysics, J. Atmos. Sci., 56, 3573–3592, 1999.

Tiira, J. and Moisseev, D.: Unsupervised classification of vertical profiles of dual polarization radar variables, Atmos. Meas. Tech., 13, 1227–1241, https://doi.org/10.5194/amt-13-1227-2020, 2020.

Tiira, J., Moisseev, D. N., von Lerber, A., Ori, D., Tokay, A., Bliven, L. F., and Petersen, W.: Ensemble mean density and its connection to other microphysical properties of falling snow as observed in Southern Finland, Atmos. Meas. Tech., 9, 4825–4841, https://doi.org/10.5194/amt-9-4825-2016, 2016.

Trömel, S., Ryzhkov, A. V., Zhang, P., and Simmer, C.: Investigations of backscatter differential phase in the melting layer, J. Appl. Meteorol. Clim., 53, 2344–2359, 2014.

Trömel, S., Ryzhkov, A. V., Hickman, B., Mühlbauer, K., and Simmer, C.: Polarimetric radar variables in the layers of melting and dendritic growth at X band – implications for a nowcasting strategy in stratiform rain, J. Appl. Meteorol. Clim., 58, 2497–2522, 2019.

Tyynelä, J. and Chandrasekar, V.: Characterizing falling snow using multifrequency dual-polarization measurements, J. Geophys. Res.-Atmos., 119, 8268–8283, 2014.

Tyynelä, J. and von Lerber, A.: Validation of microphysical snow models using in-situ, multi-frequency and dual-polarization radar measurements in Finland, J. Geophys. Res.-Atmos., 124, 13273–13290, https://doi.org/10.1029/2019JD030721, 2019.

Vogel, J. M. and Fabry, F.: Contrasting polarimetric observations of stratiform riming and nonriming events, J. Appl. Meteorol. Clim., 57, 457–476, 2018.

von Lerber, A.: Finnish Meteorological Institute Dual-Pol C-band Weather Radar, Ikaalinen, available at: https://iop.archive.arm.gov/arm-iop/2014/tmp/baecc/moisseev-radar_cband/?uid=LIH2&st=5f32748d&home=arm-archive, last access: 11 August 2020.

von Lerber, A., Moisseev, D., Leinonen, J., Koistinen, J., and Hallikainen, M. T.: Modeling radar attenuation by a low melting layer with optimized model parameters at C-band, IEEE T. Geosci. Remote., 53, 724–737, 2014.

von Lerber, A., Moisseev, D., Bliven, L. F., Petersen, W., Harri, A.-M., and Chandrasekar, V.: Microphysical properties of snow and their link to Ze–S relations during BAECC 2014, J. Appl. Meteorol. Clim., 56, 1561–1582, 2017.

Willis, P. T. and Heymsfield, A. J.: Structure of the melting layer in mesoscale convective system stratiform precipitation, J. Atmos. Sci., 46, 2008–2025, 1989.

Wolfensberger, D., Scipion, D., and Berne, A.: Detection and characterization of the melting layer based on polarimetric radar scans, Q. J. Roy. Meteorol. Soc., 142, 108–124, 2016.

Xie, X., Evaristo, R., Simmer, C., Handwerker, J., and Trömel, S.: Precipitation and microphysical processes observed by three polarimetric X-band radars and ground-based instrumentation during HOPE, Atmos. Chem. Phys., 16, 7105–7116, https://doi.org/10.5194/acp-16-7105-2016, 2016.

Zawadzki, I., Szyrmer, W., Bell, C., and Fabry, F.: Modeling of the melting layer. Part III: The density effect, J. Atmos. Sci., 62, 3705–3723, 2005.